HOW TO KILL CANCER: STARVE IT AND SHOOT IT

Sanne van Lith

HOW TO KILL CANCER: STARVE IT AND SHOOT IT

Proefschrift

ter verkrijging van de graad van doctor
aan de Radboud Universiteit Nijmegen
op gezag van de rector magnificus prof. dr. J.H.J.M. van Krieken,
volgens besluit van het college van decanen
in het openbaar te verdedigen op woensdag 28 augustus 2019
om 14.30 uur precies

door
Sanne Anna Maria van Lith
geboren op 13 augustus 1988
te Arnhem

Promotoren
Prof. dr. R.E. Brock
Prof. dr. P. Wesseling

Copromotor:
Dr. W.P.J. Leenders

Manuscriptcommissie:
Prof. dr. J. Bussink
Prof. dr. O.C. Boerman
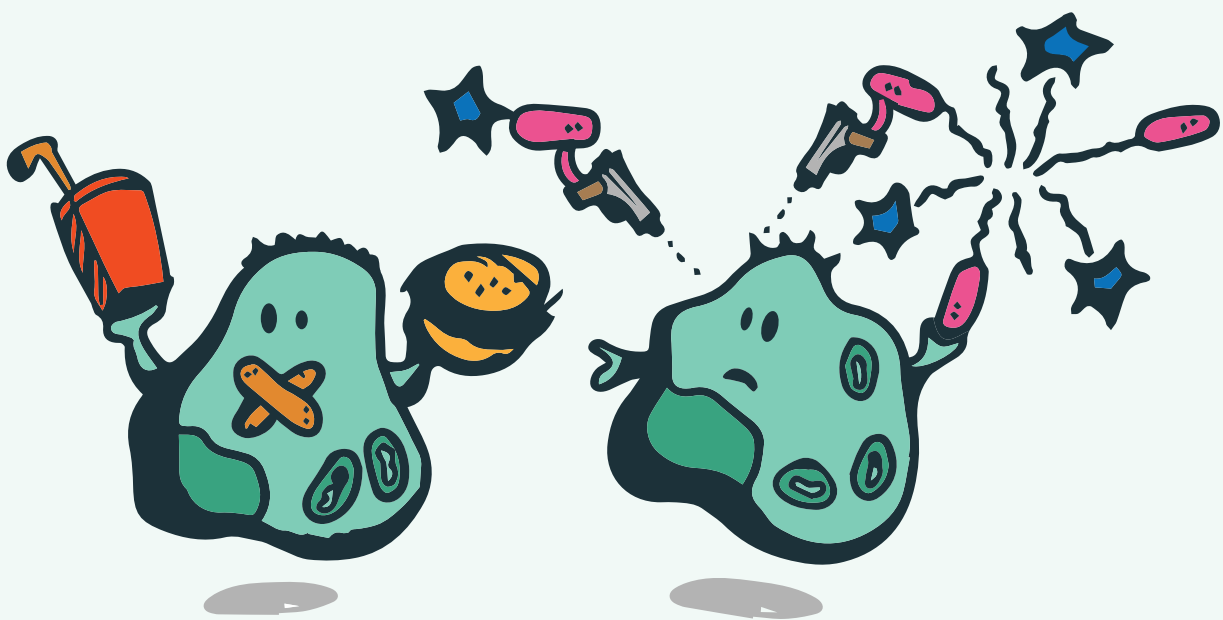Prof. dr. C. Herold-Mende (Universität Heidelberg, Duitsland)

Paranimfen:
Kelly M. van Lith
Krissie Lenting

TABLE OF CONTENTS

CHAPTER 1

General introduction

Sanne A.M. van Lith[1], Anna C. Navis[1], Kiek Verrijp[1], Simone P. Niclou[2], Rolf Bjerkvig[3],
Pieter Wesseling[1,4], Bastiaan Tops[1], Remco Molenaar[5], Cornelis J.F. van Noorden[5],
William P.J. Leenders[1]

[1]Department of Pathology, Radboud institute of Molecular Life Sciences, Radboudumc Nijmegen, The Netherlands
[2]NorLux Neuro-oncology Laboratory, CRP-Santé Luxembourg, Luxembourg
[3]NorLux Neuro-oncology, Department of biomedicine, University of Bergen, Norway
[4]Department of Pathology, VU University Medical Center, Amsterdam, The Netherlands [5]Department of Cell Biology and Histology, Academic Medical Center, Amsterdam, The Netherlands

Oncogenesis

Cancer is one of the most prevalent multifactorial diseases, characterized by the loss of physiological control associated with malignant transformation. Tumor cells show biological characteristics that are considered to be drivers of malignancy, and these are described as the hallmarks of cancer[1]. These hallmarks provide an organizing principle for rationalizing the complexity of cancers, and they include sustained proliferative signaling, evasion of growth suppressors, avoidance of immune destruction, replicative immortality, tumor promoting inflammation, activation of invasion and metastasis, induction of angiogenesis, genome instability and mutations, resistance to cell death and deregulation of cellular metabolism (Figure 1). It is becoming clear that besides a tumor promoting environment (e.g. hypoxia), these hallmarks are the result of a range of mutational events that alter signaling pathways. Multiple drugs that inhibit the various hallmarks of cancer have been developed. However, increasing efforts in high-throughput next generation sequencing show that the mutational load of tumors is larger and more heterogeneous than previously thought, and therefore it is questionable if blocking individual oncogenic signaling molecules is a practical therapeutic strategy.

Alterations in cellular metabolism can be regarded as a hallmark of cancer that is absolutely required for malignant transformation. In this thesis, both targeting of tumor metabolism and development of a nanomedicine platform for targeting of active signaling pathways are described. In the future they could be used in combination therapies to achieve synthetic lethality[2].
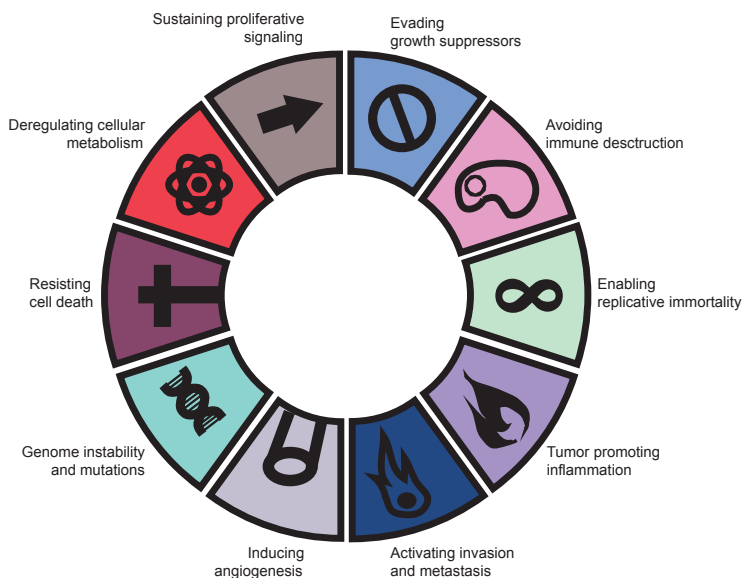

Figure 1. Hallmarks of cancer, adapted from Hanahan, Cell, 2011.

Tumor metabolism

Cancer cells are different from normal cells because they maintain a high growth rate, enabled by altered cellular metabolism. Glucose has been the central metabolite in studies on cancer metabolism for a long time, especially since Otto Warburg found that cancer cells often show increased glucose consumption and increased lactate production, regardless of oxygen availability. This phenomenon was termed the Warburg effect, or aerobic glycolysis[3-4], and it was thought to be a consequence of compromised mitochondrial function of cancer cells rather than a driver of tumorigenesis.

Now it is apparent that the metabolic rewiring in cancer cells goes beyond the Warburg effect, since cancer cells have been shown to maintain mitochondrial respiration for ATP production[5-7], and that this is essential for cancer cell survival[8]. Furthermore other metabolic pathways, like the pentose phosphate pathway (PPP), glutaminolysis and fatty acid synthesis, are reprogrammed in cancer cells as well. So far, the focus has been on the role of activation of oncogenes and inactivation of tumor suppressor genes in this metabolic rewiring. However, an increasing number of mutations is found in metabolic genes, and some of these are directly involved in tumorigenesis.

Activation of oncogenes and inactivation of tumor suppressor genes in tumor metabolism
Tumor metabolic reprogramming can be a direct result of altered intracellular pathways due to mutations in oncogenes and tumor suppressor genes. Tumors frequently contain mutations that lead to sustained high signaling levels of the PI3K-AKT-mTORC1 pathway without external growth factor stimulation[9] (Figure 2). This pathway promotes an anabolic program resulting in increased protein synthesis, and increased glycolytic flux and lipid synthesis through activation of transcription factors hypoxia inducible factor 1 (HIF-1) and sterol regulatory element-binding protein (SREBP), respectively[10].

Furthermore, gain of function of the transcription factor Myc is often seen. This change is known to enhance glycolysis through increased expression of glucose transporters and glycolytic enzymes. In addition it promotes lactate production and export, mitochondrial oxidative metabolism, nucleotide synthesis and glutaminolysis[11-12]. Besides oncogenes, tumor suppressor genes can also regulate metabolism. Loss of function of tumor suppressor p53 contributes to the increased glycolytic flux and inhibition of oxidative phosphorylation (OXPHOS) to maintain anabolism and redox balance in tumor cells[13].

Some tumors display constitutive activation of HIF-1 even under normoxic conditions. This can be caused by various mechanisms, among which mTORC1 hyperactivation or the loss of von Hippel-Lindau (VHL) function. The *VHL* suppressor gene encodes pVHL, part of a multi-protein complex that targets the α subunits of HIF-1 and HIF-2 for ubiquitin-mediated degradation, an oxygen mediated process[14]. Lack of pVHL function results in increased HIF-1 levels, leading to increased glycolytic flux and decreased mitochondrial metabolism.
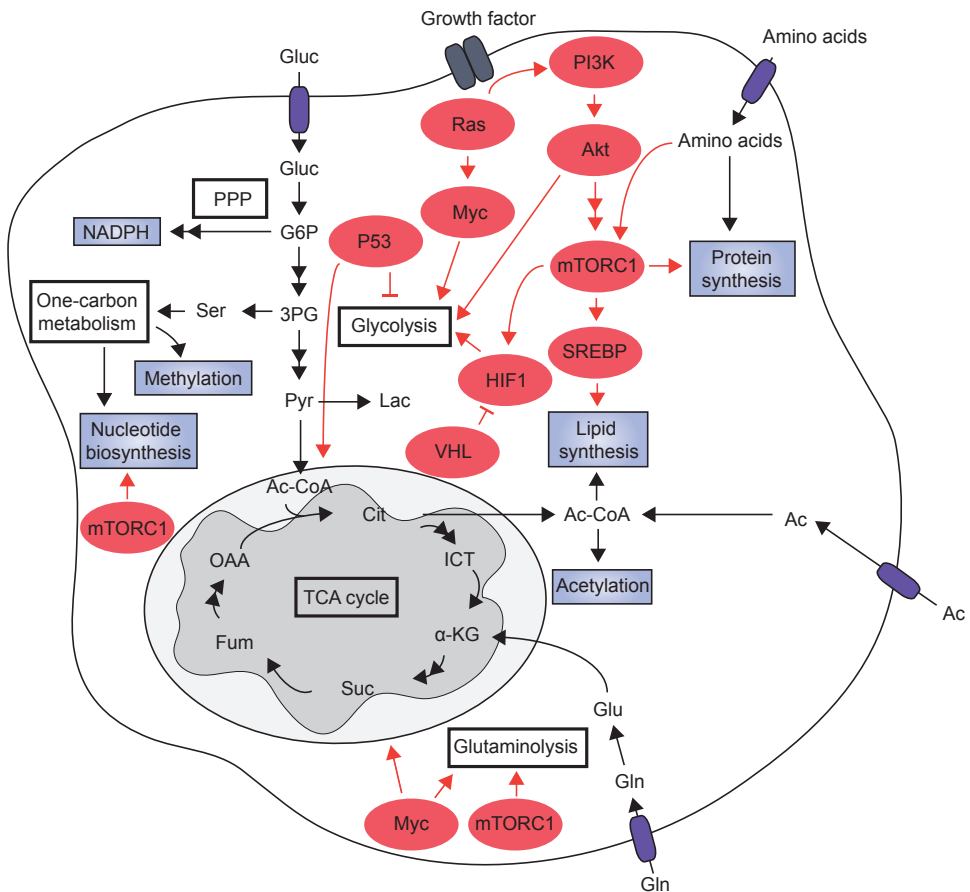
Figure 2. Signaling pathways that regulate cancer metabolism. Tumor cells have aberrant activation of mTORC1 that induces an anabolic growth program resulting in nucleotide, protein and lipid synthesis. Loss of tumor suppressors like p53 and pVHL or activation of oncogenes like Myc further promotes anabolism through transcriptional regulation of metabolic genes (Gluc = glucose, G6P = glucose-6-phosphate, 3PG = 3-phosphoglycerate, Ser = serine, Lac = lactate, Pyr = pyruvate, Ac-CoA = acetyl coenzyme A, Cit = citrate, ICT = isocitrate, α-KG = α-ketoglutarate, Suc = succinate, Fum = fumarate, OAA = oxalo-acetate, Ac = acetate, Gln = glutamine, Glu= glutamate). Red ovals depict transcription factors and other genes involved in regulation of metabolic pathways, white rectangles depict metabolic processes and purple rectangles depict products of these processes (Adapted from DeBerardinis, Science Advances, 2016).

Mutations in metabolic genes in tumor metabolism and oncometabolites

Although a combination of loss of tumor suppressor genes and activation of oncogenes can dysregulate cellular metabolism, an increasing number of genes encoding metabolic enzymes have now been found to carry cancer-inducing mutations. In 2008, genome-sequencing efforts in gliomas, the most frequent cancers originating from the brain parenchyma itself, led to detection of mutations in genes encoding the key metabolic enzymes isocitrate dehydrogenase (IDH) 1 or 2[15] (Figure 3). IDH enzymes catalyze the oxidative decarboxylation of isocitrate to α-ketoglutarate (α-KG) and CO_2. Three IDH isoforms exist, IDH1 and 2 are $NADP^+$ dependent, and IDH3 is NAD^+ dependent. IDH1 is found exclusively in the cytoplasm and peroxisomes, whereas IDH2 and IDH3 are found in the mitochondria. Mutations are found commonly in grade II and III diffuse gliomas and secondary glioblastomas (GBMs)[15-16], acute myeloid leukemia (AML)[17], and a limited number of other tumor types[18-19]. In gliomas, mutations in *IDH1* are most common[16] whereas *IDH1* and *IDH2* mutations occur with equal frequency in AML[20]. The mutations are somatic and monoallelic, and the large majority of mutations involve an arginine to histidine mutation at position 132 in the catalytic site of IDH1, while IDH2 mutations mostly involve R172[15-16]. IDH2 mutations in AML can also involve R140, again in the enzymatically active site[17].

The mutations cause a decrease in the affinity of the enzyme for isocitrate, but an increase in the affinity for α-KG[21]. Additionally the mutant enzymes have acquired a novel function by reducing α-KG into D-2-hydroxyglutarate (D-2-HG) with concomitant NADPH oxidation[22]. D-2-HG can rise up to millimolar levels, and it interferes with a number of enzymes for which α-KG is an essential co-factor, such as the TET (Ten-Eleven-Translocation) family of hydroxymethylases and Jumonji-C-domain-containing histone demethylases (JHDMs)[23-24]. These changes ultimately lead to global DNA and histone hypermethylation, altered gene expression and inhibition of differentiation[25]. In addition, D-2-HG serves as a cofactor for Egg Laying defective Nine (EGLN), a member of the family of prolyl hydroxylases (PHDs) that hydroxylates specific proline residues of HIF-1α, inducing ubiquitination and degradation[26] (Figure 3). HIF-1α is a transcription factor that regulates expression of a number of hypoxia-related genes such as glucose transporter 1 and 3 (GLUT-1, GLUT-3) and vascular endothelial growth factor-A (VEGF-A)[27], and is a central modulator of angiogenesis and vascular hyperpermeability. Increased HIF-1α degradation by D-2-HG fits with the notion that IDH mutations are frequent in grade II/III glioma that grow very diffusely and lack hypoxic signaling and angiogenesis[28-29]. Indeed, low-grade IDH-mutant gliomas show less edema and contrast enhancement in MRI. As D-2-HG results in increased cell proliferation and exogenous addition of D-2-HG results in epigenetic alterations and HIF-1α degradation comparable to the situation in *IDH1* mutants, at least in leukemic cells[30], D-2-HG is now considered to be an oncometabolite.

Secondly, loss-of-function mutations have been identified in genes encoding the enzymes fumarate hydratase (FH) and the succinate dehydrogenase complex (SDH), that catalyze sequential steps in the tricarboxylic acid (TCA) cycle[31-32] (Figure 3). These mutations not only

impair TCA cycle flux, they also cause accumulation of their substrates fumarate and succinate which share structural similarities with α-KG. Both fumarate and succinate inhibit α-KG dependent PHDs, resulting in normoxic stabilization of HIF subunits and constitutive activation of HIF targets[33-34].

Another example is the genomic amplification of phosphoglycerate dehydrogenase (*PHGDH*) which is found in breast cancer and melanoma[35-36] (Figure 3). PHGDH catalyzes the conversion of 3-phosphoglycerate (3PG) to 3-phosphohydroxypyruvate (3POHPyr) as the first step of serine metabolism. Serine may donate a methyl group to the one-carbon pool, and is thereby converted to glycine. Together these amino acids contribute to nucleotide synthesis, methylation reactions and NADPH production, and an accelerated flux through this biosynthetic pathway may contribute to oncogenesis.
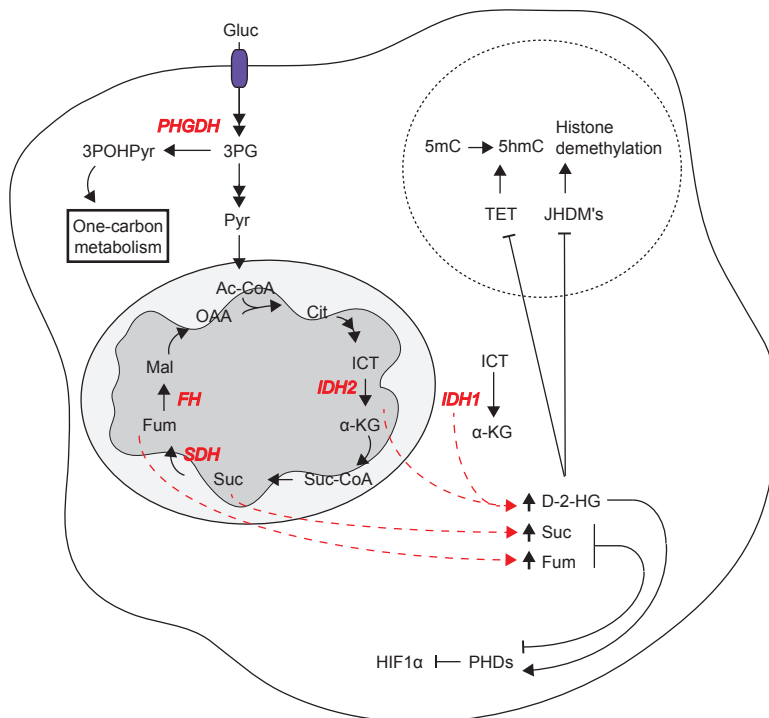
Figure 3. The effects of mutations in metabolic enzymes. Mutations in genes encoding FH and SDH cause accumulation of the substrates fumarate and succinate, respectively, whereas IDH1/2 mutant enzymes have acquired a novel function of reducing α-KG to D-2-HG. D-2-HG, succinate and fumarate bind competitively to α-KG dependent enzymes, thereby reducing activity. Inhibition of TET hydroxymethylases leads to hypermethylation of CpG islands in the genome, and inhibition of JHMDs leads to hypermethylation of lysines in histone H3. This hypermethylated phenotype results in altered gene expression and a dedifferentiated phenotype of the cell. Succinate and fumarate are known to inhibit PHDs, thereby increasing HIF-mediated expression of genes, whereas for D-2-HG stimulation of the PDH EGLN has

been suggested (Gluc = glucose, 3PG = 3-phosphoglycerate, 3POHPyr = 3-phosphohydroxypyruvate, Pyr = pyruvate, Ac-CoA = acetyl coenzyme A, Cit = citrate, ICT = isocitrate, α-KG = α-ketoglutarate, Suc-CoA = succinyl-CoA, Suc = succinate, Fum = fumarate, Mal = malate, OAA = oxalo-acetate, D-2-HG = D-2-hydroxyglutarate, 5mC = 5-methylcytosine, 5hmC = 5-hydroxymethylcytosine) (Adapted from van Lith, BBA reviews on cancer, 2014).

Rewiring in metabolism

Increasing evidence suggests that tumor cells have rewired their metabolism to create a phenotype that enables tumor cells to generate ATP and molecules for biosynthesis while maintaining cellular redox balance, processes that are essential for proliferation and survival. These changes include altered fluxes among major metabolic pathways like glycolysis, the PPP, the TCA cycle and glutaminolysis via altered expression or post-translational modification of metabolic enzymes. Two examples are metabolic changes induced by VHL inactivation and *IDH* mutations.

VHL inactivation

50%-80% of sporadic clear cell renal cell carcinomas (ccRCC) show biallelic loss of *VHL*[37-38] due to frameshift insertions, missense and nonsense mutations, promoter hypermethylation, contralateral allele loss or loss of heterozygosity. This inactivation of pVHL causes sustained accumulation of HIF-1α and/or HIF-2α, even under normoxic conditions[39]. This leads to constitutive expression of HIF-α target genes that, amongst others, regulate angiogenesis, apoptosis and metabolism[40-42]. In normal cells, glucose is converted to pyruvate for entry in the TCA cycle, however, HIF increases expression of glucose transporters needed for glucose internalization, glycolytic enzymes, and lactate dehydrogenase A (LDHA) and monocarboxylic acid transporters (MCTs) that promote lactate production and efflux, thereby favoring aerobic glycolysis (Figure 4). Furthermore HIF dependent induction of pyruvate dehydrogenase kinase 1 (PDK1) leads to pyruvate dehydrogenase (PDH) inhibition, thus disconnecting the TCA cycle from glycolysis. Although most metabolic pathways besides high glycolytic rate are still maintained in most cancers, VHL-deficient renal cell carcinoma has been shown to downregulate energy production through the TCA cycle[43]. To compensate for the reduced conversion of glucose to citrate, a source for fatty acid production, via the TCA, VHL inactivated cells use glutamine for production of cytosolic Ac-CoA (Figure 4). This occurs through operation of the mitochondrial IDH2 in the reductive direction of the TCA cycle[44]. An additional cytoplasmic route of reductive carboxylation is mediated by IDH1[45-46]. Metabolic flux analyses have demonstrated that the glutamine-driven reductive carboxylation is increased by hypoxia and dependent on HIF, however, the exact mechanism is still unclear.

HIF-1α and HIF-2α are highly similar in structure, but HIF-1α is ubiquitously expressed while HIF-2α is limited to several organs like, the kidney[47]. In ccRCC differential expression of HIF-1α and HIF-2α is observed, with tumors expressing either both subtypes or exclusively HIF-2α. Recently, it has been shown that HIF-1 is lost during progression to higher disease stages[48].

Part of the effects of HIF-1α and HIF-2α are overlapping, but they also regulate expression of distinct genes. Examples are the unique involvement of HIF-1α in altering glucose metabolism, while HIF-2α plays a role in cell cycle regulation and glutamine metabolism[49-50].
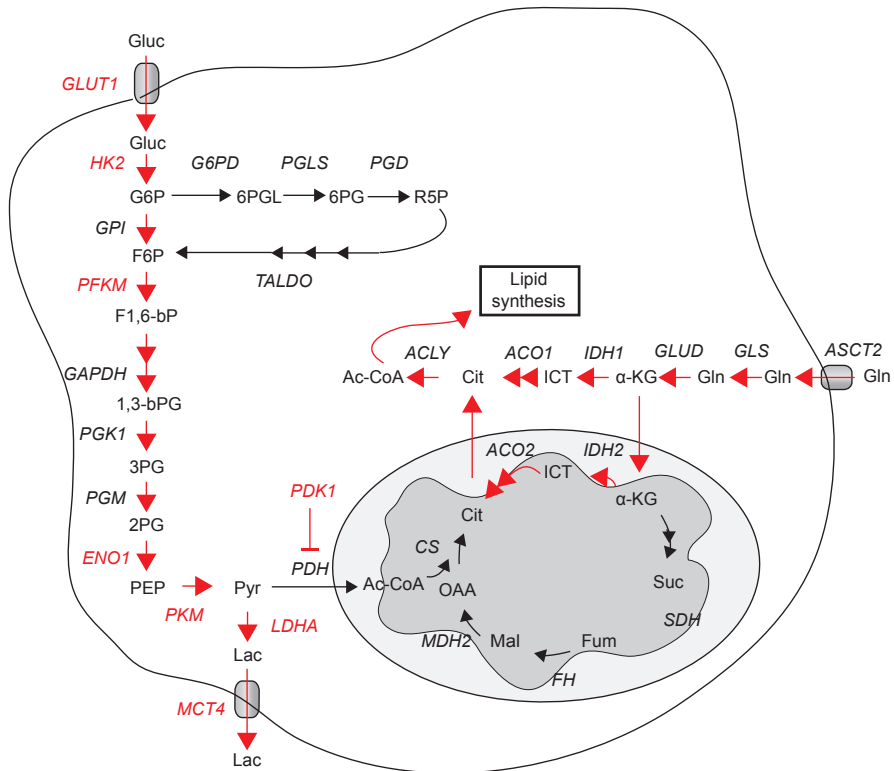
Figure 4. Metabolic rewiring induced by VHL inactivation and HIF-mediated pseudohypoxia. In normal cells, glucose is converted to pyruvate, which enters the TCA cycle. Glucose derived citrate is then shuttled into the cytosol for lipid synthesis. Increased activity of HIF in VHL-inactivated cells drives aerobic glycolysis by activating expression of glycolytic proteins including GLUT-1, HK2, PFKM, ENO, PKM, LDHA and MCT4, thereby stimulating production and excretion of lacate. HIF also uncouples aerobic glycolysis from the TCA cycle by activating PDK1, which phosphorylates and inhibits PDH, the key enzyme converting pyruvate to Ac-CoA. To compensate for the reduced flux of glucose to citrate, reductive carboxylation of glutamine generates cytosolic citrate for lipid synthesis. Red proteins indicate HIF target genes, and red arrows indicate upregulated pathways induced by HIF activation. (Gluc = glucose, G6P = glucose-6-phosphate, F6P = fructose-6-phosphate, F1,6-bPG = fructose 1,6-biphosphate, 1,3-bPG = 1,3-biphosphoglycerate, 3PG = 3-phosphoglycerate, 2PG = 2-phosphoglycerate, PEP = phosphoenolpyruvate, Lac = lactate, Pyr = pyruvate, Ac-CoA = acetyl coenzyme A, Cit = citrate, ICT = isocitrate, α-KG = α-ketoglutarate, Suc = succinate, Fum = fumarate, Mal = malate, OAA = oxalo-acetate, Gln = glutamine).

IDH mutations

Besides the described non-metabolic role of D-2-HG in gliomagenesis, *IDH1*-mutant cells also have decreased IDH-mediated cytosolic NADPH production[51], ~ 65% of which is produced by IDH1 in the human brain[52]. NADPH is the major metabolite needed for detoxification processes that, among others, protect cells from reactive oxygen species (ROS) which are produced especially during radiotherapy and chemotherapy[53].
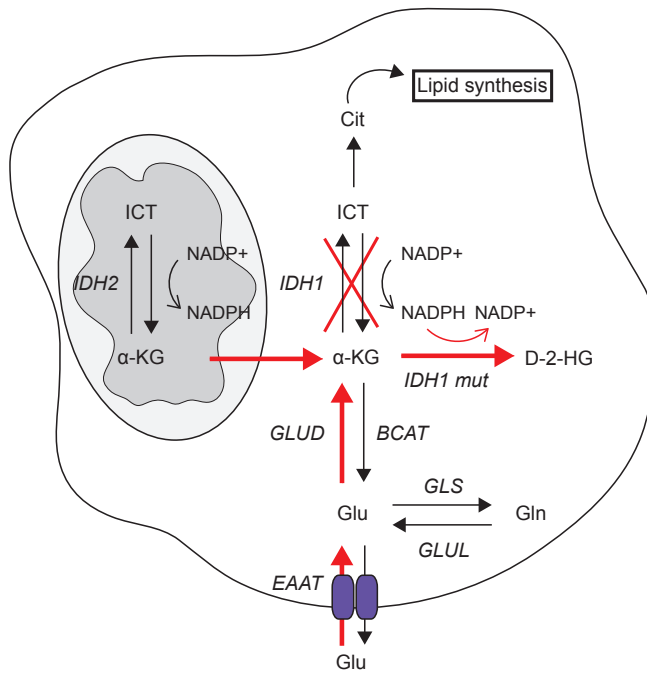
Figure 5. Described anaplerotic pathways of α-KG production. Pathways which may rescue metabolic defects in *IDH1*-mutated tumors are depicted as red arrows. Mutant IDH1 converts α-KG to D-2-HG. Since the cytosolic α-KG pool is depleted, and this metabolite is essential for tumor cell proliferation, compensatory mechanisms must occur. First, α-KG which is formed in the mitochondria by IDH2 can be transported to the cytosol via the malate-α-KG antiporter. Additionally, glutamate may be imported from the microenvironment via the EAAT2 glutamate importer which is expressed in low-grade glioma. Glutamate can then be converted to α-KG by GLUD. (ICT = isocitrate, α-KG = α-ketoglutarate, Cit = citrate, Glu = glutamate, Gln = glutamine, D-2-HG = D-2-hydroxyglutarate). (Adapted from van Lith, BBA reviews on cancer, 2014).

Furthermore, the excessive consumption of α-KG impairs the reverse reductive carboxylation of α-KG to isocitrate, which is subsequently used for the generation of citrate, a precursor of acetyl-CoA that reacts with NADPH to generate fatty acids and lipids[44,54]. Since IDH1-R132H lacks the reverse activity[22,55], *IDH1*-mutant cells need to use alternative anaplerotic pathways to maintain α-KG production (Figure 5). One of these salvage pathways may be the formation of α-KG by the mitochondrial IDH2[56]. Another compensatory mechanisms is the upregulation of glutamine import and glutaminase (GLS) activity[57]. Furthermore, since the effect of GLS inhibition on proliferation of IDH1-R132H cells is only modest[58] and since low grade glioma cells (>80% of which are IDH1-mutant) express the glutamate importer excitatory amino acid transporter 2 (EEAT2)[59], we proposed previously that import and direct usage of glutamate is an efficient anaplerotic pathway for production of α-KG via activity of glutamate dehydrogenase (GLUD)[60].

Targeting tumor metabolism

Cancer associated metabolic alterations have been studied as druggable targets, and molecules that selectively target cancer cells based on metabolic alterations are now entering clinical trials. Since glycolysis is a key metabolic feature, many studies have focused on inhibiting enzymes controlling this pathway [e.g. hexokinase-2 (HK2), Pyruvate kinase (PKM)][61]. Inhibition of key enzymes in the PPP like glucose-6-phosphate-dehydrogenase (G6PD) and transketolase (TKT) has also shown promising results[62].

IDH1-mutant cells have been described to exhibit decreased IDH mediated production of NADPH. Upon radiation therapy this led to increased ROS levels and double strand DNA breaks[51], when compared to *IDH*-wildtype cells. Recently, a specific inhibitor of IDH1-R132H was developed. It promoted differentiation of an IDH1-R132H cell line *in vitro*, and inhibited growth of a subcutaneously grown IDH1-R132H glioma xenograft[63]. However, these inhibitors also desensitized *IDH1*-mutant cells to radiotherapy, probably due to inhibition of D-2-HG formation and increase in NADPH levels[51].

There is increasing interest in the inhibition of the glutaminolysis pathway, which has been shown to be upregulated as an anaplerotic pathway for citrate and lipid synthesis in VHL-impaired and *IDH1*-mutant tumors. Small molecule inhibitors against GLS have been developed, that exhibit anti-tumor activity in numerous pre-clinical studies and in various tumor types[58,64-65]. Another enzyme in the glutaminolysis pathway that could be inhibited is GLUD. This is an NAD(P)+-dependent enzyme that converts glutamate to α-KG. Epigallo-catechin-3-gallate (EGCG), a component of green tea, is a known inhibitor of NADP+-dependent enzymes[66]. It does not only interfere with glutaminolysis flux but also with NADPH levels, and thus the redox capacity in cells, probably increasing sensitivity to ROS dependent therapies like radiotherapy (Rtx) or photodynamic therapy (PDT).

Other means of tumor targeting

As described above, tumor initiation and progression are dependent on multiple factors besides alterations in metabolism. During the past decades a wealth of information has been collected on the role of membrane receptor tyrosine kinases and the signaling pathways they initiate. In order to inhibit these pathways, molecules that target such proteins have been developed.

Antibodies

One of the more successful immunotherapies developed for treatment of tumors relies on tumor-targeting monoclonal antibodies (mAbs). The effector functions of these antibodies may rely on several mechanisms: 1) direct action of the mAb (receptor agonist/antagonist activity); 2) immune-mediated cell killing (antibody-dependent cellular toxicity (ADCC) or complement-dependent cellular toxicity (CDC); 3) effects on tumor vasculature and stroma.

Though unmodified mAbs may show some therapeutic potency, in most cases they are not curative. Therefore mAbs conjugated to drugs, toxins or radionuclides have been developed. There are, however, some complex issues. Drugs or radionuclides can degrade or decay before the tumor cells are reached and conjugation can change binding characteristics, pharmacokinetics and biodistribution. Currently, two mAb conjugates are FDA and EMA approved for cancer therapies; brentuximab-vedotin, targeting CD30[67-68] and trastuzumab-emtasine (T-DM1), targeting human epidermal growth factor receptor 2 (HER2)[69]. Furthermore over 30 additional mAb conjugates have entered clinical development[70-71]. Though these antibodies and antibody drug conjugates have found their way to the clinic, their distribution and tumor penetration are limited due to size (~150 kDa, 10-15 nm long and 7-9 nm wide). Furthermore, the long half-life (days to weeks) causes high background levels in molecular imaging, and in addition toxicity and immune responses are still an issue.

VHHs

An interesting alternative for standard antibodies are the variable heavy chain domains of single chain llama antibodies, called VHHs or nanobodies (Figure 6). VHHs typically have a molecular weight of ~15 kDa and can bind target antigens with affinities down to the low picomolar range. The ease of genetic engineering and handling combined with other advantages such as high water solubility, low production cost, small size, low immunogenicity in humans and high thermo- and pH-stability, make this a highly interesting class of antibody fragments[72]. A number of VHHs with high specificity and affinity against tumor targets (e.g. epidermal growth factor receptor (EGFR), tyrosine-protein kinase Met (c-Met), HER2) have been developed[73-75], as well as VHHs against cognate receptor ligands (e.g. hepatocyte growth factor (HGF), vascular endothelial growth factor (VEGF))[76-78].

Therapeutically, VHHs can be used as neutralizing agents, as receptor-ligand antagonists and as vehicles for effector delivery or targeted vehicle-based drug therapy[79-80]. Some VHHs that have been developed as antagonist of extracellular targets are now undergoing phase I, II and III clinical trials by Ablynx (www.ablynx.com).
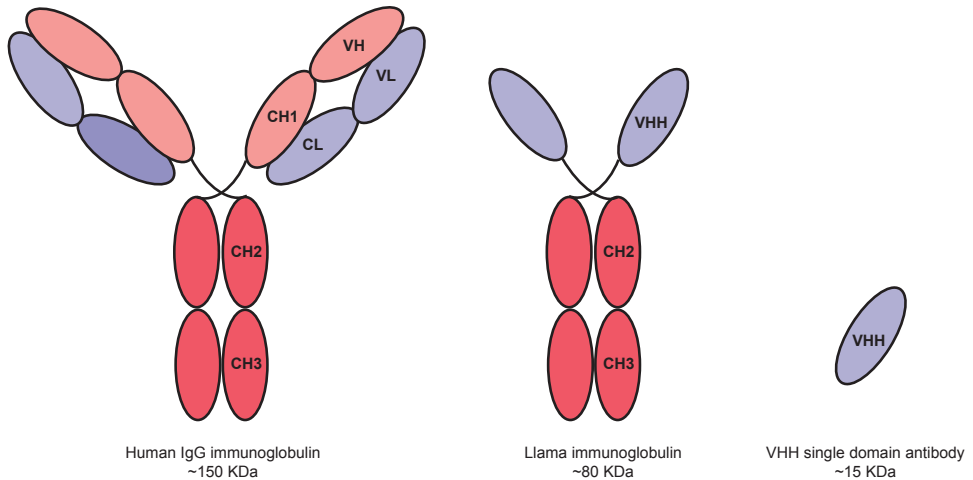
Figure 6. Domain structures of a conventional human immunoglobulin, a heavy chain only llama immunoglobulin and a VHH. A conventional IgG antibody is a dimeric molecule consisting of two heavy chains and two light chains. The heavy chain consists of the constant domains (CH1, CH2, CH3) and the variable domain (VH). The llama immunoglobulin lacks the light chain and contains only one antigen binding domain (VHH).

Non-specific conjugation strategies
Currently, the most common method for covalently conjugating agents to antibodies are cross-linking agents, which can conjugate functional groups such as amines, thiols and carboxyl groups[81]. Since these reactive groups are usually present in high abundance in targeting ligands, this reaction is generally very fast and easy, however, if the conjugation involves residues that are critical for antigen binding, functionality can be impaired. Furthermore, labeling leads to a heterogeneous population of proteins with various amounts of introduced moieties. Carbohydrate side chains of the constant heavy domains are also being used for conjugation, however this method cannot be applied to VHHs of which 90% do not contain glycosylation sites[82], or which are not glycosylated when produced in bacterial expression systems.

Site-specific conjugation strategies

Site-specific chemical conjugation methods employ introduction of functional groups that are not present in natural amino acids, like ketones and azides. Furthermore unnatural amino acids can be incorporated[83], but this method faces practical limitations in terms of scalability and efficacy. Approaches to conjugate VHHs without compromising functionality include intein-based ligation[84], the site-specific introduction of a carboxyterminal cysteine allowing maleimide chemistry[85] and sortase A transpeptidation[86].

Staphylococcal Sortase A is a bacterial transpeptidase that recognizes substrate proteins containing a Leucine-Proline-X-Threonine-Glycine (LPXTG) amino acid sequence (Figure 7). Sortase A harbors a catalytic cysteine residue that cleaves the pentapeptide between the threonine and glycine, generating a thioacyl-intermediate. This intermediate is resolved by creation of a new peptide bond with the N-terminus of a oligoglycine nucleophile[87-89]. Since recombinantly expressed proteins can easily be equipped with either an N-terminal or C-terminal LPXTG tag, the sortase A chemistry is increasingly exploited for site-specific conjugations. It allows incorporation of functional moieties that cannot be introduced by genetic engineering, and furthermore it offers the possibility of generation of N-N or C-C dimer proteins, which could be advantageous for reactivity of both subunits. Sortase A has also been used to incorporate strain-promoted alkyne-azide cycloaddition (SPAAC) click handles to enable further modification by cycloaddition click reactions[86,90].
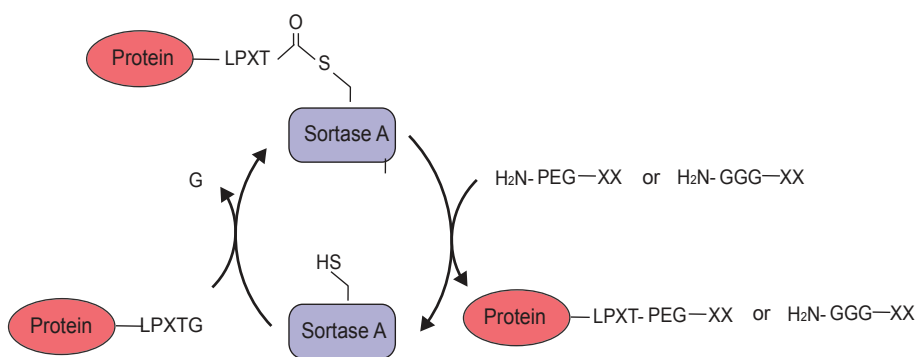

Figure 7. Sortagging principle. A substrate protein containing an LPXTG motif is cleaved between the threonine and the glycine by Sortase A. The formed acyl-enzyme intermediate can be resolved by an (oligo)glycine or PEG containing nucleophile, resulting in the release of Sortase A and the formation of a substrate-nucleophile ligation product.

VHH mediated drug delivery

Encapsulation of drugs can overcome numerous issues like poor solubility, limited stability and rapid clearance[91-92], therefore efforts are undertaken in the field of nanoparticles. Several therapeutic nanoparticle platforms (eg. liposomes, albumin nanoparticles, polymeric micelles) have already been approved for cancer therapy[93].

Nanoparticles decorated with VHHs have also been expoited as conduits for delivering toxins or drugs to tumor cells. Carriers that have been used are liposomes[94-95], micelles[96], albumin-based nanoparticles (NANAPs)[75] and polymer-based polymersomes[97]. Two nanoparticle systems that are exploited in this thesis are polycaprolactone (PCL) diblock polymer micelles and elastin like peptide (ELP) micelles.

PCL based micelles

One attractive class of carriers for therapeutic and diagnostic agents are polymeric micelles. They are formed by the self-assembly of amphiphilic block copolymers in aqueous solutions. Several micellar formulations are now being evaluated in clinical trials. Because of their small size (10-200 nm) they are able to passively target tumors via extravasation and the enhanced permeation and retention (EPR) effect. However, to actively target these particles to tumor cells, or to induce receptor mediated uptake of the particles, they can also be functionalized with antibodies or VHHs[96].

ELP based micelles

ELPs are an artificial biomimetic class of protein polymers, inspired by the hydrophobic motifs of the extracellular matrix protein tropoelastin[98]. They are composed of repeating pentameric glycine-X-glycine-valine-proline (GXGVP) units, in which X can be any amino acid[99-100]. One quality of ELPs is that they can reversibly transform from a soluble disordered state below their transition temperature to an aggregated state above this transition temperature[101]. This transition temperature highly depends on the nature of the guest residue X, ELP length, concentration and presence of salts[102]. ELP-based nanoparticles have been prepared out of amphiphilic block copolymers, either by employing ELP diblock polypeptides with different guest residues and hence different transition temperatures, or by coupling ELPs with low transition temperature to hydrophilic polymers such as polyethylene glycol[103].

VHHs against intracellular targets

VHHs do not suffer from reducing intracellular environments, and therefore they could be used for targeting or inhibition of intracellular proteins (e.g. metabolic enzymes) if applied systemically. The therapeutic effect would, however, be minimal since VHHs show limited membrane penetration. There are several strategies that could be used for the intracellular delivery of a protein, such as the use of nanoparticles, disruption of the membrane and cell-penetrating peptides (CPPs). CPPs are a class of peptides that can cross the plasma membrane,

and they have been used for intracellular delivery of siRNA, small molecules, proteins and other peptides[104]. CPPs vary in amino acid composition and 3D structure, leading to different modes of uptake. Endocytosis and direct translocation are the major uptake mechanisms. The mode of uptake depends on e.g. CPP concentration and composition of the lipid bilayer of the cell, as well as on the cargo that is conjugated to the CPP.

VHHs and photodynamic therapy

In photodynamic therapy, a photosensitizer (PS) is administered and activated with light of a certain wavelength. Upon activation, the PS gets into an excited triplet state and upon return to its ground state energy is released and transmitted to molecular oxygen, leading to the formation of reactive oxygen species (ROS)[105]. ROS damage cellular constituents, ultimately leading to cell death[106]. Because of the local character of this treatment, PDT is more selective compared to other therapies like chemotherapy. Various PSs are approved as PDT drugs (Photofrin, Visudyne, Levulan, Metvixia, Bremachlorin and Foscan). Problems with the non-targeted PDT approach, however, are the low water solubility of the currently used PSs, and the targeting to healthy tissues leading to side effects like phototoxicity of the skin. Part of these problems could be solved by conjugation of the PS to a tumor targeting moiety (e.g. antibody, VHH) for so-called photoimmunotherapy (PIT).

THESIS OUTLINE

Aims of this thesis were to identify and target altered metabolic pathways in cancer cells, and to develop and test a VHH-based nanomedicine platform for targeted therapy.

The last years, increasing amount of mutations in genes important in cell metabolism were found, like mutations in genes encoding the enzymes active in the tricarboxylic acid (TCA) cycle succinate dehydrogenase (SDH), fumarate hydratase (FH) and isocitrate dehydrogenase (IDH). The majority of mutations in *IDH* genes are point mutations involving Arg132 in *IDH1* and Arg172 or Arg140 in *IDH2*. In **chapter two**, we present a novel heterozygous *IDH1* mutation, *IDH1^{R314C}*, which is identified by targeted next generation sequencing of a high grade glioma. IDH1^{R314C} lacks isocitrate-to-α-KG conversion activity due to reduced affinity for NADP$^+$, and differs from the IDH1^{R132} mutants in that it does not produce the oncometabolite D-2-HG.

Another protein which is often mutated in renal cancer, and causes a rewiring in cellular metabolism, is the VHL tumor suppressor protein. In **chapter three**, we describe the analysis of the metabolism of two VHL impaired RCC cell lines. Metabolic phenotypes of the cells are identified, and we show that cells have differential sensitivity to metabolic inhibitors of the glutaminolysis and PPP.

Interesting molecules for tumor targeting are the heavy domains of single chain only antibodies (VHHs or nanobodies). They are ten times smaller than conventional antibodies and can be easily expressed as recombinant proteins. In **chapter four**, we describe a novel tumor targeting VHH; C-C7, which is identified via *in vivo* biopanning of a llama VHH phage display library in an orthotopic glioma mouse model. We show that it binds dynactin-1-p150^{Glued} on activated endothelial cells and macrophages.

Conjugation of VHHs with diagnostic or therapeutic nanoparticles, peptides or proteins could greatly improve targeted therapy or diagnostics. In **chapter five,** we discuss a modular approach for VHH conjugations, employing sortase A transPEGylation and maleimide chemistry for introduction of a chemical click moiety and a fluorescent label, respectively. The resulting clickable VHHs are then used for conjugation to other groups employing the Cu$^+$-independent strain-promoted alkyne-azide cycloadition (SPAAC) reaction. Using this approach, tail-to-tail bispecific VHHs and VHH-targeted nanoparticles are generated without affecting VHH functionality.

To endow the VHH with the capacity to enter the cell, we use the optimized sortase A transpeptidation protocols to couple a human lactoferrin-derived cell-penetrating peptide (CPP) (hLF$^{38-59}$) to the EGFR specific VHH 7D12 in **chapter six**. We observe increased uptake of the VHH-CPP complex in EGFR expressing cells compared to VHH alone. Furthermore, the conjugate blocks EGF-mediated EGFR activation with higher efficacy than both modalities alone, which is caused by both effective receptor blockade and internalization.

Besides CPPs all kinds of therapeutic and diagnostic handles can be conjugated to VHHs with the described conjugation strategies. One of them are photosensitizers. These molecules

cause instant cell death via induction of ROS after illumination with light of a specific wave length. In **chapter seven**, we conjugate 7D12 and 7D12-CPP to a photosensitizer. Using these conjugates, we induce EGFR specific phototoxicity *in vitro* in tumor cell lines and tumor cell spheres, and in clinical ascites samples from women diagnosed with serous ovarian carcinoma, a cancer type that is accessible to light via laparoscopy. Internalization is disadvantageous, since the membrane bound 7D12 variant is more effective than 7D12-CPP.

In **chapter eight**, we report the use of an ELP diblock (ELP^{DB}) polypeptide for creation of VHH-decorated nanoparticles that reversibly self-assemble upon heating. The 7D12-decorated ELP^{DB} micelles are able to selectively target tumor cells that (over)express EGFR. Upon incorporation of a third ELP^{DB} to which the photosensitizer IRDye700DX is conjugated, the nanoparticles can be used for highly effective and specific photoimmunotherapy (PIT).

REFERENCES

1. Hanahan, D.; Weinberg, R. A., Hallmarks of cancer: the next generation. *Cell* 2011, *144* (5), 646-74.

2. O'Neil, N. J.; Bailey, M. L.; Hieter, P., Synthetic lethality and cancer. *Nat Rev Genet* **2017,** *18* (10), 613-623.

3. Warburg, O., On the origin of cancer cells. *Science* **1956,** *123* (3191), 309-14.

4. Warburg, O., On respiratory impairment in cancer cells. *Science* **1956,** *124* (3215), 269-70.

5. Ward, P. S.; Thompson, C. B., Metabolic reprogramming: a cancer hallmark even warburg did not anticipate. *Cancer Cell* **2012,** *21* (3), 297-308.

6. Schulze, A.; Harris, A. L., How cancer metabolism is tuned for proliferation and vulnerable to disruption. *Nature* **2012,** *491* (7424), 364-73.

7. Koppenol, W. H.; Bounds, P. L.; Dang, C. V., Otto Warburg's contributions to current concepts of cancer metabolism. *Nat Rev Cancer* **2011,** *11* (5), 325-37.

8. Wallace, D. C., Mitochondria and cancer. *Nat Rev Cancer* **2012,** *12* (10), 685-98.

9. Yuan, T. L.; Cantley, L. C., PI3K pathway alterations in cancer: variations on a theme. *Oncogene* **2008,** *27* (41), 5497-510.

10. Dibble, C. C.; Manning, B. D., Signal integration by mTORC1 coordinates nutrient input with biosynthetic output. *Nat Cell Biol* **2013,** *15* (6), 555-64.

11. DeBerardinis, R. J.; Chandel, N. S., Fundamentals of cancer metabolism. *Sci Adv* **2016,** *2* (5), e1600200.

12. Tarrado-Castellarnau, M.; de Atauri, P.; Cascante, M., Oncogenic regulation of tumor metabolic reprogramming. *Oncotarget* **2016,** *7* (38), 62726-62753.

13. Kruiswijk, F.; Labuschagne, C. F.; Vousden, K. H., p53 in survival, death and metabolic health: a lifeguard with a licence to kill. *Nat Rev Mol Cell Biol* **2015,** *16* (7), 393-405.

14. Kaelin, W. G., Jr., The von Hippel-Lindau tumor suppressor protein and clear cell renal carcinoma. *Clinical cancer research : an official journal of the American Association for Cancer Research* **2007,** *13* (2 Pt 2), 680s-684s.

15. Parsons, D. W.; Jones, S.; Zhang, X.; Lin, J. C.; Leary, R. J.; Angenendt, P.; Mankoo, P.; Carter, H.; Siu, I. M.; Gallia, G. L.; Olivi, A.; McLendon, R.; Rasheed, B. A.; Keir, S.; Nikolskaya, T.; Nikolsky, Y.; Busam, D. A.; Tekleab, H.; Diaz, L. A., Jr.; Hartigan, J.; Smith, D. R.; Strausberg, R. L.; Marie, S. K.; Shinjo, S. M.; Yan, H.; Riggins, G. J.; Bigner, D. D.; Karchin, R.; Papadopoulos, N.; Parmigiani, G.; Vogelstein, B.; Velculescu, V. E.; Kinzler, K. W., An integrated genomic analysis of human glioblastoma multiforme. *Science* **2008,** *321* (5897), 1807-12.

16. Yan, H.; Parsons, D. W.; Jin, G.; McLendon, R.; Rasheed, B. A.; Yuan, W.; Kos, I.; Batinic-Haberle, I.; Jones, S.; Riggins, G. J.; Friedman, H.; Friedman, A.; Reardon, D.; Herndon, J.; Kinzler, K. W.; Velculescu, V. E.; Vogelstein, B.; Bigner, D. D., IDH1 and IDH2 mutations in gliomas. *N Engl J Med* **2009,** *360* (8), 765-73.

17. Ward, P. S.; Patel, J.; Wise, D. R.; Abdel-Wahab, O.; Bennett, B. D.; Coller, H. A.; Cross, J. R.; Fantin, V. R.; Hedvat, C. V.; Perl, A. E.; Rabinowitz, J. D.; Carroll, M.; Su, S. M.; Sharp, K. A.; Levine, R. L.; Thompson, C. B., The common feature of leukemia-associated IDH1 and IDH2 mutations is a neomorphic enzyme activity converting alpha-ketoglutarate to 2-hydroxyglutarate. *Cancer Cell* **2010,** *17* (3), 225-34.

18. Amary, M. F.; Bacsi, K.; Maggiani, F.; Damato, S.; Halai, D.; Berisha, F.; Pollock, R.; O'Donnell, P.; Grigoriadis, A.; Diss, T.; Eskandarpour, M.; Presneau, N.; Hogendoorn, P. C.; Futreal, A.; Tirabosco, R.; Flanagan, A. M., IDH1 and IDH2 mutations are frequent events in central chondrosarcoma and central and periosteal chondromas but not in other mesenchymal tumours. *The Journal of pathology* **2011,** *224* (3), 334-43.

19. Cairns, R. A.; Mak, T. W., Oncogenic isocitrate dehydrogenase mutations: mechanisms, models, and clinical opportunities. *Cancer discovery* **2013,** *3* (7), 730-41.

20. Mardis, E. R.; Ding, L.; Dooling, D. J.; Larson, D. E.; McLellan, M. D.; Chen, K.; Koboldt, D. C.; Fulton, R. S.; Delehaunty, K. D.; McGrath, S. D.; Fulton, L. A.; Locke, D. P.; Magrini, V. J.; Abbott, R. M.; Vickery, T. L.; Reed, J. S.; Robinson, J. S.; Wylie, T.; Smith, S. M.; Carmichael, L.; Eldred, J. M.; Harris, C. C.; Walker, J.; Peck, J. B.; Du, F.; Dukes, A. F.; Sanderson, G. E.; Brummett, A. M.; Clark, E.; McMichael, J. F.; Meyer, R. J.; Schindler, J. K.; Pohl, C. S.; Wallis, J. W.; Shi, X.; Lin, L.; Schmidt, H.; Tang, Y.; Haipek, C.; Wiechert, M. E.; Ivy, J. V.; Kalicki, J.; Elliott, G.; Ries, R. E.; Payton, J. E.; Westervelt, P.; Tomasson, M. H.; Watson, M. A.; Baty, J.; Heath, S.; Shannon, W. D.; Nagarajan, R.; Link, D. C.; Walter, M. J.; Graubert, T. A.; DiPersio, J. F.; Wilson, R. K.; Ley, T. J., Recurring mutations found by sequencing an acute myeloid leukemia genome. *N Engl J Med* **2009,** *361* (11), 1058-66.

21. Yang, B.; Zhong, C.; Peng, Y.; Lai, Z.; Ding, J., Molecular mechanisms of "off-on switch" of activities of human IDH1 by tumor-associated mutation R132H. *Cell Res* **2010,** *20* (11), 1188-200.

22. Dang, L.; White, D. W.; Gross, S.; Bennett, B. D.; Bittinger, M. A.; Driggers, E. M.; Fantin, V. R.; Jang, H. G.; Jin, S.; Keenan, M. C.; Marks, K. M.; Prins, R. M.; Ward, P. S.; Yen, K. E.; Liau, L. M.; Rabinowitz, J. D.; Cantley, L. C.; Thompson, C. B.; Vander Heiden, M. G.; Su, S. M., Cancer-associated IDH1 mutations produce 2-hydroxyglutarate. *Nature* **2009,** *462* (7274), 739-44.

23. Xu, W.; Yang, H.; Liu, Y.; Yang, Y.; Wang, P.; Kim, S. H.; Ito, S.; Yang, C.; Wang, P.; Xiao, M. T.; Liu, L. X.; Jiang, W. Q.; Liu, J.; Zhang, J. Y.; Wang, B.; Frye, S.; Zhang, Y.; Xu, Y. H.; Lei, Q. Y.; Guan, K. L.; Zhao, S. M.; Xiong, Y., Oncometabolite 2-hydroxyglutarate is a competitive inhibitor of alpha-ketoglutarate-dependent dioxygenases. *Cancer Cell* **2011,** *19* (1), 17-30.

24. Chowdhury, R.; Yeoh, K. K.; Tian, Y. M.; Hillringhaus, L.; Bagg, E. A.; Rose, N. R.; Leung, I. K.; Li, X. S.; Woon, E. C.; Yang, M.; McDonough, M. A.; King, O. N.; Clifton, I. J.; Klose, R. J.; Claridge, T. D.; Ratcliffe, P. J.; Schofield, C. J.; Kawamura, A., The oncometabolite 2-hydroxyglutarate inhibits histone lysine demethylases. *EMBO reports* **2011,** *12* (5), 463-9.

25. Lu, C.; Ward, P. S.; Kapoor, G. S.; Rohle, D.; Turcan, S.; Abdel-Wahab, O.; Edwards, C. R.; Khanin, R.; Figueroa, M. E.; Melnick, A.; Wellen, K. E.; O'Rourke, D. M.; Berger, S. L.; Chan, T. A.; Levine, R. L.; Mellinghoff, I. K.; Thompson, C. B., IDH mutation impairs histone demethylation and results in a block to cell differentiation. *Nature* **2012,** *483* (7390), 474-8.

26. Koivunen, P.; Lee, S.; Duncan, C. G.; Lopez, G.; Lu, G.; Ramkissoon, S.; Losman, J. A.; Joensuu, P.; Bergmann, U.; Gross, S.; Travins, J.; Weiss, S.; Looper, R.; Ligon, K. L.; Verhaak, R. G.; Yan, H.; Kaelin, W. G., Jr., Transformation by the (R)-enantiomer of 2-hydroxyglutarate linked to EGLN activation. *Nature* **2012,** *483* (7390), 484-8.

27. Harris, A. L., Hypoxia--a key regulatory factor in tumour growth. *Nat Rev Cancer* **2002,** *2* (1), 38-47.

28. Rong, Y.; Durden, D. L.; Van Meir, E. G.; Brat, D. J., 'Pseudopalisading' necrosis in glioblastoma: a familiar morphologic feature that links vascular pathology, hypoxia, and angiogenesis. *J Neuropathol Exp Neurol* **2006,** *65* (6), 529-39.

29. Svensson, K. J.; Kucharzewska, P.; Christianson, H. C.; Skold, S.; Lofstedt, T.; Johansson, M. C.; Morgelin, M.; Bengzon, J.; Ruf, W.; Belting, M., Hypoxia triggers a proangiogenic pathway involving cancer cell microvesicles and PAR-2-mediated heparin-binding EGF signaling in endothelial cells. *Proc Natl Acad Sci U S A* **2011,** *108* (32), 13147-52.

30. Losman, J. A.; Looper, R. E.; Koivunen, P.; Lee, S.; Schneider, R. K.; McMahon, C.; Cowley, G. S.; Root, D. E.; Ebert, B. L.; Kaelin, W. G., Jr., (R)-2-hydroxyglutarate is sufficient to promote leukemogenesis and its effects are reversible. *Science* **2013,** *339* (6127), 1621-5.

31. Tomlinson, I. P.; Alam, N. A.; Rowan, A. J.; Barclay, E.; Jaeger, E. E.; Kelsell, D.; Leigh, I.; Gorman, P.; Lamlum, H.; Rahman, S.; Roylance, R. R.; Olpin, S.; Bevan, S.; Barker, K.; Hearle, N.; Houlston, R. S.; Kiuru, M.; Lehtonen, R.; Karhu, A.; Vilkki, S.; Laiho, P.; Eklund, C.; Vierimaa, O.; Aittomaki, K.; Hietala, M.; Sistonen, P.; Paetau, A.; Salovaara, R.; Herva, R.; Launonen, V.; Aaltonen, L. A.; Multiple Leiomyoma, C., Germline mutations in FH predispose to dominantly inherited uterine fibroids, skin leiomyomata and papillary renal cell cancer. *Nature genetics* **2002,** *30* (4), 406-10.

32. Baysal, B. E.; Ferrell, R. E.; Willett-Brozick, J. E.; Lawrence, E. C.; Myssiorek, D.; Bosch, A.; van der Mey, A.; Taschner, P. E.; Rubinstein, W. S.; Myers, E. N.; Richard, C. W., 3rd; Cornelisse, C. J.; Devilee,

P.; Devlin, B., Mutations in SDHD, a mitochondrial complex II gene, in hereditary paraganglioma. *Science* **2000,** *287* (5454), 848-51.

33. Selak, M. A.; Armour, S. M.; MacKenzie, E. D.; Boulahbel, H.; Watson, D. G.; Mansfield, K. D.; Pan, Y.; Simon, M. C.; Thompson, C. B.; Gottlieb, E., Succinate links TCA cycle dysfunction to oncogenesis by inhibiting HIF-alpha prolyl hydroxylase. *Cancer Cell* **2005,** *7* (1), 77-85.

34. Isaacs, J. S.; Jung, Y. J.; Mole, D. R.; Lee, S.; Torres-Cabala, C.; Chung, Y. L.; Merino, M.; Trepel, J.; Zbar, B.; Toro, J.; Ratcliffe, P. J.; Linehan, W. M.; Neckers, L., HIF overexpression correlates with biallelic loss of fumarate hydratase in renal cancer: novel role of fumarate in regulation of HIF stability. *Cancer Cell* **2005,** *8* (2), 143-53.

35. Locasale, J. W.; Grassian, A. R.; Melman, T.; Lyssiotis, C. A.; Mattaini, K. R.; Bass, A. J.; Heffron, G.; Metallo, C. M.; Muranen, T.; Sharfi, H.; Sasaki, A. T.; Anastasiou, D.; Mullarky, E.; Vokes, N. I.; Sasaki, M.; Beroukhim, R.; Stephanopoulos, G.; Ligon, A. H.; Meyerson, M.; Richardson, A. L.; Chin, L.; Wagner, G.; Asara, J. M.; Brugge, J. S.; Cantley, L. C.; Vander Heiden, M. G., Phosphoglycerate dehydrogenase diverts glycolytic flux and contributes to oncogenesis. *Nature genetics* **2011,** *43* (9), 869-74.

36. Possemato, R.; Marks, K. M.; Shaul, Y. D.; Pacold, M. E.; Kim, D.; Birsoy, K.; Sethumadhavan, S.; Woo, H. K.; Jang, H. G.; Jha, A. K.; Chen, W. W.; Barrett, F. G.; Stransky, N.; Tsun, Z. Y.; Cowley, G. S.; Barretina, J.; Kalaany, N. Y.; Hsu, P. P.; Ottina, K.; Chan, A. M.; Yuan, B.; Garraway, L. A.; Root, D. E.; Mino-Kenudson, M.; Brachtel, E. F.; Driggers, E. M.; Sabatini, D. M., Functional genomics reveal that the serine synthesis pathway is essential in breast cancer. *Nature* **2011,** *476* (7360), 346-50.

37. Gnarra, J. R.; Tory, K.; Weng, Y.; Schmidt, L.; Wei, M. H.; Li, H.; Latif, F.; Liu, S.; Chen, F.; Duh, F. M.; et al., Mutations of the VHL tumour suppressor gene in renal carcinoma. *Nature genetics* **1994,** *7* (1), 85-90.

38. Foster, K.; Prowse, A.; van den Berg, A.; Fleming, S.; Hulsbeek, M. M.; Crossey, P. A.; Richards, F. M.; Cairns, P.; Affara, N. A.; Ferguson-Smith, M. A.; et al., Somatic mutations of the von Hippel-Lindau disease tumour suppressor gene in non-familial clear cell renal carcinoma. *Hum Mol Genet* **1994,** *3* (12), 2169-73.

39. Kim, W.; Kaelin, W. G., Jr., The von Hippel-Lindau tumor suppressor protein: new insights into oxygen sensing and cancer. *Current opinion in genetics & development* **2003,** *13* (1), 55-60.

40. Majmundar, A. J.; Wong, W. J.; Simon, M. C., Hypoxia-inducible factors and the response to hypoxic stress. *Molecular cell* **2010,** *40* (2), 294-309.

41. Semenza, G. L., HIF-1 mediates metabolic responses to intratumoral hypoxia and oncogenic mutations. *The Journal of clinical investigation* **2013,** *123* (9), 3664-71.

42. Baldewijns, M. M.; van Vlodrop, I. J.; Vermeulen, P. B.; Soetekouw, P. M.; van Engeland, M.; de Bruine, A. P., VHL and HIF signalling in renal cell carcinogenesis. *The Journal of pathology* **2010,** *221* (2), 125-38.

43. Wettersten, H. I.; Aboud, O. A.; Lara, P. N., Jr.; Weiss, R. H., Metabolic reprogramming in clear cell renal cell carcinoma. *Nat Rev Nephrol* **2017,** *13* (7), 410-419.

44. Wise, D. R.; Ward, P. S.; Shay, J. E.; Cross, J. R.; Gruber, J. J.; Sachdeva, U. M.; Platt, J. M.; DeMatteo, R. G.; Simon, M. C.; Thompson, C. B., Hypoxia promotes isocitrate dehydrogenase-dependent carboxylation of alpha-ketoglutarate to citrate to support cell growth and viability. *Proc Natl Acad Sci U S A* **2011,** *108* (49), 19611-6.

45. Metallo, C. M.; Gameiro, P. A.; Bell, E. L.; Mattaini, K. R.; Yang, J.; Hiller, K.; Jewell, C. M.; Johnson, Z. R.; Irvine, D. J.; Guarente, L.; Kelleher, J. K.; Vander Heiden, M. G.; Iliopoulos, O.; Stephanopoulos, G., Reductive glutamine metabolism by IDH1 mediates lipogenesis under hypoxia. *Nature* **2011,** *481* (7381), 380-4.

46. Mullen, A. R.; Wheaton, W. W.; Jin, E. S.; Chen, P. H.; Sullivan, L. B.; Cheng, T.; Yang, Y.; Linehan, W. M.; Chandel, N. S.; DeBerardinis, R. J., Reductive carboxylation supports growth in tumour cells with defective mitochondria. *Nature* **2011,** *481* (7381), 385-8.

47. Wiesener, M. S.; Jurgensen, J. S.; Rosenberger, C.; Scholze, C. K.; Horstrup, J. H.; Warnecke, C.; Mandriota, S.; Bechmann, I.; Frei, U. A.; Pugh, C. W.; Ratcliffe, P. J.; Bachmann, S.; Maxwell, P. H.; Eckardt, K. U., Widespread hypoxia-inducible expression of HIF-2alpha in distinct cell populations of different organs. *FASEB J.* **2003**, *17* (2), 271-3.

48. Shen, C.; Beroukhim, R.; Schumacher, S. E.; Zhou, J.; Chang, M.; Signoretti, S.; Kaelin, W. G., Jr., Genetic and functional studies implicate HIF1alpha as a 14q kidney cancer suppressor gene. *Cancer discovery* **2011,** *1* (3), 222-35.

49. Biswas, S.; Troy, H.; Leek, R.; Chung, Y. L.; Li, J. L.; Raval, R. R.; Turley, H.; Gatter, K.; Pezzella, F.; Griffiths, J. R.; Stubbs, M.; Harris, A. L., Effects of HIF-1alpha and HIF2alpha on Growth and Metabolism of Clear-Cell Renal Cell Carcinoma 786-0 Xenografts. *J Oncol* **2010,** *2010*, 757908.

50. Gameiro, P. A.; Yang, J.; Metelo, A. M.; Perez-Carro, R.; Baker, R.; Wang, Z.; Arreola, A.; Rathmell, W. K.; Olumi, A.; Lopez-Larrubia, P.; Stephanopoulos, G.; Iliopoulos, O., In vivo HIF-mediated reductive carboxylation is regulated by citrate levels and sensitizes VHL-deficient cells to glutamine deprivation. *Cell metabolism* **2013,** *17* (3), 372-85.

51. Molenaar, R. J.; Botman, D.; Smits, M. A.; Hira, V. V.; van Lith, S. A.; Stap, J.; Henneman, P.; Khurshed, M.; Lenting, K.; Mul, A. N.; Dimitrakopoulou, D.; van Drunen, C. M.; Hoebe, R. A.; Radivoyevitch, T.; Wilmink, J. W.; Maciejewski, J. P.; Vandertop, W. P.; Leenders, W. P.; Bleeker, F. E.; van Noorden, C. J., Radioprotection of IDH1-Mutated Cancer Cells by the IDH1-Mutant Inhibitor AGI-5198. *Cancer Res* **2015,** *75* (22), 4790-802.

52. Bleeker, F. E.; Atai, N. A.; Lamba, S.; Jonker, A.; Rijkeboer, D.; Bosch, K. S.; Tigchelaar, W.; Troost, D.; Vandertop, W. P.; Bardelli, A.; Van Noorden, C. J., The prognostic IDH1(R132) mutation is associated with reduced NADP+-dependent IDH activity in glioblastoma. *Acta Neuropathol* **2010,** *119* (4), 487-94.

53. Baldewpersad Tewarie, N. M.; Burgers, I. A.; Dawood, Y.; den Boon, H. C.; den Brok, M. G.; Klunder, J. H.; Koopmans, K. B.; Rademaker, E.; van den Broek, H. B.; van den Bersselaar, S. M.; Witjes, J. J.; Van Noorden, C. J.; Atai, N. A., NADP+ -dependent IDH1 R132 mutation and its relevance for glioma patient survival. *Med Hypotheses* **2013,** *80* (6), 728-31.

54. Metallo, C. M.; Gameiro, P. A.; Bell, E. L.; Mattaini, K. R.; Yang, J.; Hiller, K.; Jewell, C. M.; Johnson, Z. R.; Irvine, D. J.; Guarente, L.; Kelleher, J. K.; Vander Heiden, M. G.; Iliopoulos, O.; Stephanopoulos, G., Reductive glutamine metabolism by IDH1 mediates lipogenesis under hypoxia. *Nature* **2012,** *481* (7381), 380-4.

55. Leonardi, R.; Subramanian, C.; Jackowski, S.; Rock, C. O., Cancer-associated isocitrate dehydrogenase mutations inactivate NADPH-dependent reductive carboxylation. *J. Biol. Chem.* **2012,** *287* (18), 14615-20.

56. Navis, A. C.; Niclou, S. P.; Fack, F.; Stieber, D.; van Lith, S.; Verrijp, K.; Wright, A.; Stauber, J.; Tops, B.; Otte-Holler, I.; Wevers, R. A.; van Rooij, A.; Pusch, S.; von Deimling, A.; Tigchelaar, W.; van Noorden, C. J.; Wesseling, P.; Leenders, W. P., Increased mitochondrial activity in a novel IDH1-R132H mutant human oligodendroglioma xenograft model: in situ detection of 2-HG and alpha-KG. *Acta neuropathologica communications* **2013,** *1*, 18.

57. Grassian, A. R.; Parker, S. J.; Davidson, S. M.; Divakaruni, A. S.; Green, C. R.; Zhang, X.; Slocum, K. L.; Pu, M.; Lin, F.; Vickers, C.; Joud-Caldwell, C.; Chung, F.; Yin, H.; Handly, E. D.; Straub, C.; Growney, J. D.; Vander Heiden, M. G.; Murphy, A. N.; Pagliarini, R.; Metallo, C. M., IDH1 mutations alter citric acid cycle metabolism and increase dependence on oxidative mitochondrial metabolism. *Cancer Res* **2014,** *74* (12), 3317-31.

58. Seltzer, M. J.; Bennett, B. D.; Joshi, A. D.; Gao, P.; Thomas, A. G.; Ferraris, D. V.; Tsukamoto, T.; Rojas, C. J.; Slusher, B. S.; Rabinowitz, J. D.; Dang, C. V.; Riggins, G. J., Inhibition of glutaminase preferentially slows growth of glioma cells with mutant IDH1. *Cancer Res* **2010,** *70* (22), 8981-7.

59. de Groot, J. F.; Liu, T. J.; Fuller, G.; Yung, W. K., The excitatory amino acid transporter-2 induces apoptosis and decreases glioma growth in vitro and in vivo. *Cancer Res* **2005,** *65* (5), 1934-40.

60. van Lith, S. A.; Navis, A. C.; Verrijp, K.; Niclou, S. P.; Bjerkvig, R.; Wesseling, P.; Tops, B.; Molenaar, R.; van Noorden, C. J.; Leenders, W. P., Glutamate as chemotactic fuel for diffuse glioma cells: Are they glutamate suckers? *Biochim. Biophys. Acta* **2014,** *1846* (1), 66-74.

61. Yu, L.; Chen, X.; Wang, L.; Chen, S., The sweet trap in tumors: aerobic glycolysis and potential targets for therapy. *Oncotarget* **2016,** *7* (25), 38908-38926.

62. Lucarelli, G.; Galleggiante, V.; Rutigliano, M.; Sanguedolce, F.; Cagiano, S.; Bufo, P.; Lastilla, G.; Maiorano, E.; Ribatti, D.; Giglio, A.; Serino, G.; Vavallo, A.; Bettocchi, C.; Selvaggi, F. P.; Battaglia, M.; Ditonno, P., Metabolomic profile of glycolysis and the pentose phosphate pathway identifies the central role of glucose-6-phosphate dehydrogenase in clear cell-renal cell carcinoma. *Oncotarget* **2015,** *6* (15), 13371-86.

63. Rohle, D.; Popovici-Muller, J.; Palaskas, N.; Turcan, S.; Grommes, C.; Campos, C.; Tsoi, J.; Clark, O.; Oldrini, B.; Komisopoulou, E.; Kunii, K.; Pedraza, A.; Schalm, S.; Silverman, L.; Miller, A.; Wang, F.; Yang, H.; Chen, Y.; Kernytsky, A.; Rosenblum, M. K.; Liu, W.; Biller, S. A.; Su, S. M.; Brennan, C. W.; Chan, T. A.; Graeber, T. G.; Yen, K. E.; Mellinghoff, I. K., An inhibitor of mutant IDH1 delays growth and promotes differentiation of glioma cells. *Science* **2013,** *340* (6132), 626-30.

64. Gross, M. I.; Demo, S. D.; Dennison, J. B.; Chen, L.; Chernov-Rogan, T.; Goyal, B.; Janes, J. R.; Laidig, G. J.; Lewis, E. R.; Li, J.; Mackinnon, A. L.; Parlati, F.; Rodriguez, M. L.; Shwonek, P. J.; Sjogren, E. B.; Stanton, T. F.; Wang, T.; Yang, J.; Zhao, F.; Bennett, M. K., Antitumor activity of the glutaminase inhibitor CB-839 in triple-negative breast cancer. *Mol Cancer Ther* **2014,** *13* (4), 890-901.

65. Jacque, N.; Ronchetti, A. M.; Larrue, C.; Meunier, G.; Birsen, R.; Willems, L.; Saland, E.; Decroocq, J.; Maciel, T. T.; Lambert, M.; Poulain, L.; Hospital, M. A.; Sujobert, P.; Joseph, L.; Chapuis, N.; Lacombe, C.; Moura, I. C.; Demo, S.; Sarry, J. E.; Recher, C.; Mayeux, P.; Tamburini, J.; Bouscary, D., Targeting glutaminolysis has antileukemic activity in acute myeloid leukemia and synergizes with BCL-2 inhibition. *Blood* **2015,** *126* (11), 1346-56.

66. Shin, E. S.; Park, J.; Shin, J. M.; Cho, D.; Cho, S. Y.; Shin, D. W.; Ham, M.; Kim, J. B.; Lee, T. R., Catechin gallates are NADP+-competitive inhibitors of glucose-6-phosphate dehydrogenase and other enzymes that employ NADP+ as a coenzyme. *Bioorg. Med. Chem.* **2008,** *16* (7), 3580-6.

67. Senter, P. D.; Sievers, E. L., The discovery and development of brentuximab vedotin for use in relapsed Hodgkin lymphoma and systemic anaplastic large cell lymphoma. *Nat. Biotechnol.* **2012,** *30* (7), 631-7.

68. Younes, A.; Yasothan, U.; Kirkpatrick, P., Brentuximab vedotin. *Nature reviews. Drug discovery* **2012,** *11* (1), 19-20.

69. Lambert, J. M.; Chari, R. V., Ado-trastuzumab Emtansine (T-DM1): an antibody-drug conjugate (ADC) for HER2-positive breast cancer. *J. Med. Chem.* **2014,** *57* (16), 6949-64.

70. Beck, A.; Goetsch, L.; Dumontet, C.; Corvaia, N., Strategies and challenges for the next generation of antibody-drug conjugates. *Nature reviews. Drug discovery* **2017,** *16* (5), 315-337.

71. Mullard, A., Maturing antibody-drug conjugate pipeline hits 30. *Nature reviews. Drug discovery* **2013,** *12* (5), 329-32.

72. Harmsen, M. M.; De Haard, H. J., Properties, production, and applications of camelid single-domain antibody fragments. *Appl. Microbiol. Biotechnol.* **2007,** *77* (1), 13-22.

73. Moghimi, S. M.; Rahbarizadeh, F.; Ahmadvand, D.; Parhamifar, L., Heavy Chain Only Antibodies: A New Paradigm in Personalized HER2+ Breast Cancer Therapy. *Bioimpacts* **2013,** *3* (1), 1-4.

74. Roovers, R. C.; Laeremans, T.; Huang, L.; De Taeye, S.; Verkleij, A. J.; Revets, H.; de Haard, H. J.; van Bergen en Henegouwen, P. M., Efficient inhibition of EGFR signaling and of tumour growth by antagonistic anti-EFGR Nanobodies. *Cancer immunology, immunotherapy : CII* **2007,** *56* (3), 303-317.

75. Heukers, R.; Altintas, I.; Raghoenath, S.; De Zan, E.; Pepermans, R.; Roovers, R. C.; Haselberg, R.; Hennink, W. E.; Schiffelers, R. M.; Kok, R. J.; van Bergen en Henegouwen, P. M., Targeting hepatocyte growth factor receptor (Met) positive tumor cells using internalizing nanobody-decorated albumin nanoparticles. *Biomaterials* **2014,** *35* (1), 601-10.

76. Vosjan, M. J.; Vercammen, J.; Kolkman, J. A.; Stigter-van Walsum, M.; Revets, H.; van Dongen, G. A., Nanobodies targeting the hepatocyte growth factor: potential new drugs for molecular cancer therapy. *Mol Cancer Ther* **2012,** *11* (4), 1017-25.

77. Kazemi-Lomedasht, F.; Behdani, M.; Bagheri, K. P.; Habibi-Anbouhi, M.; Abolhassani, M.; Arezumand, R.; Shahbazzadeh, D.; Mirzahoseini, H., Inhibition of angiogenesis in human endothelial cell using VEGF specific nanobody. *Mol Immunol* **2015,** *65* (1), 58-67.

78. Ebrahimizadeh, W.; Mousavi Gargari, S. L.; Javidan, Z.; Rajabibazl, M., Production of Novel VHH Nanobody Inhibiting Angiogenesis by Targeting Binding Site of VEGF. *Appl. Biochem. Biotechnol.* **2015,** *176* (7), 1985-95.

79. Kijanka, M. M.; van Brussel, A. S.; van der Wall, E.; Mali, W. P.; van Diest, P. J.; van Bergen En Henegouwen, P. M.; Oliveira, S., Optical imaging of pre-invasive breast cancer with a combination of VHHs targeting CAIX and HER2 increases contrast and facilitates tumour characterization. *EJNMMI Res* **2016,** *6* (1), 14.

80. Van Audenhove, I.; Gettemans, J., Nanobodies as Versatile Tools to Understand, Diagnose, Visualize and Treat Cancer. *EBioMedicine* **2016,** *8*, 40-48.

81. Kalia, J.; Raines, R. T., Advances in Bioconjugation. *Curr. Org. Chem.* **2010,** *14* (2), 138-147.

82. Harmsen, M. M.; Ruuls, R. C.; Nijman, I. J.; Niewold, T. A.; Frenken, L. G.; de Geus, B., Llama heavy-chain V regions consist of at least four distinct subfamilies revealing novel sequence features. *Mol Immunol* **2000,** *37* (10), 579-90.

83. Wang, L.; Schultz, P. G., Expanding the genetic code. *Angew. Chem. Int. Ed. Engl.* **2004,** *44* (1), 34-66.

84. Debets, M. F.; Leenders, W. P.; Verrijp, K.; Zonjee, M.; Meeuwissen, S. A.; Otte-Holler, I.; van Hest, J. C., Nanobody-functionalized polymersomes for tumor-vessel targeting. *Macromolecular bioscience* **2013,** *13* (7), 938-45.

85. Massa, S.; Xavier, C.; De Vos, J.; Caveliers, V.; Lahoutte, T.; Muyldermans, S.; Devoogdt, N., Site-specific labeling of cysteine-tagged camelid single-domain antibody-fragments for use in molecular imaging. *Bioconjug Chem* **2014,** *25* (5), 979-88.

86. Witte, M. D.; Cragnolini, J. J.; Dougan, S. K.; Yoder, N. C.; Popp, M. W.; Ploegh, H. L., Preparation of unnatural N-to-N and C-to-C protein fusions. *Proc Natl Acad Sci U S A* **2012,** *109* (30), 11993-8.

87. Ton-That, H.; Mazmanian, S. K.; Alksne, L.; Schneewind, O., Anchoring of surface proteins to the cell wall of Staphylococcus aureus. Cysteine 184 and histidine 120 of sortase form a thiolate-imidazolium ion pair for catalysis. *J. Biol. Chem.* **2002,** *277* (9), 7447-52.

88. Ton-That, H.; Liu, G.; Mazmanian, S. K.; Faull, K. F.; Schneewind, O., Purification and characterization of sortase, the transpeptidase that cleaves surface proteins of Staphylococcus aureus at the LPXTG motif. *Proc Natl Acad Sci U S A* **1999,** *96* (22), 12424-9.

89. Mazmanian, S. K.; Liu, G.; Ton-That, H.; Schneewind, O., Staphylococcus aureus sortase, an enzyme that anchors surface proteins to the cell wall. *Science* **1999,** *285* (5428), 760-3.

90. Alt, K.; Paterson, B. M.; Westein, E.; Rudd, S. E.; Poniger, S. S.; Jagdale, S.; Ardipradja, K.; Connell, T. U.; Krippner, G. Y.; Nair, A. K.; Wang, X.; Tochon-Danguy, H. J.; Donnelly, P. S.; Peter, K.; Hagemeyer, C. E., A Versatile Approach for the Site-Specific Modification of Recombinant Antibodies Using a Combination of Enzyme-Mediated Bioconjugation and Click Chemistry. *Angew. Chem. Int. Ed. Engl.* **2015**.

91. Arias, J. L.; Unciti-Broceta, J. D.; Maceira, J.; Del Castillo, T.; Hernandez-Quero, J.; Magez, S.; Soriano, M.; Garcia-Salcedo, J. A., Nanobody conjugated PLGA nanoparticles for active targeting of African Trypanosomiasis. *Journal of controlled release : official journal of the Controlled Release Society* **2015,** *197*, 190-8.

92. Van de Broek, B.; Devoogdt, N.; D'Hollander, A.; Gijs, H. L.; Jans, K.; Lagae, L.; Muyldermans, S.; Maes, G.; Borghs, G., Specific cell targeting with nanobody conjugated branched gold nanoparticles for photothermal therapy. *ACS nano* **2011,** *5* (6), 4319-28.

93. Shi, J.; Kantoff, P. W.; Wooster, R.; Farokhzad, O. C., Cancer nanomedicine: progress, challenges and opportunities. *Nat Rev Cancer* **2017,** *17* (1), 20-37.

94. Oliveira, S.; Schiffelers, R. M.; van der Veeken, J.; van der Meel, R.; Vongpromek, R.; van Bergen En Henegouwen, P. M.; Storm, G.; Roovers, R. C., Downregulation of EGFR by a novel multivalent

nanobody-liposome platform. *Journal of controlled release : official journal of the Controlled Release Society* **2010,** *145* (2), 165-75.

95. van der Meel, R.; Oliveira, S.; Altintas, I.; Haselberg, R.; van der Veeken, J.; Roovers, R. C.; van Bergen en Henegouwen, P. M.; Storm, G.; Hennink, W. E.; Schiffelers, R. M.; Kok, R. J., Tumor-targeted Nanobullets: Anti-EGFR nanobody-liposomes loaded with anti-IGF-1R kinase inhibitor for cancer treatment. *Journal of controlled release : official journal of the Controlled Release Society* **2012,** *159* (2), 281-9.

96. Talelli, M.; Rijcken, C. J.; Oliveira, S.; van der Meel, R.; van Bergen En Henegouwen, P. M.; Lammers, T.; van Nostrum, C. F.; Storm, G.; Hennink, W. E., Nanobody-shell functionalized thermosensitive core-crosslinked polymeric micelles for active drug targeting. *Journal of controlled release : official journal of the Controlled Release Society* **2011,** *151* (2), 183-92.

97. Zou, T.; Dembele, F.; Beugnet, A.; Sengmanivong, L.; de Marco, A.; Li, M. H., Nanobody-functionalized polymersomes. *Journal of controlled release : official journal of the Controlled Release Society* **2015,** *213*, e79-80.

98. Meyer, D. E.; Chilkoti, A., Purification of recombinant proteins by fusion with thermally-responsive polypeptides. *Nat. Biotechnol.* **1999,** *17* (11), 1112-5.

99. Soon, A. S.; Smith, M. H.; Herman, E. S.; Lyon, L. A.; Barker, T. H., Development of self-assembling mixed protein micelles with temperature-modulated avidities. *Advanced healthcare materials* **2013,** *2* (7), 1045-55.

100. Urry, D. W.; Gowda, D. C.; Parker, T. M.; Luan, C. H.; Reid, M. C.; Harris, C. M.; Pattanaik, A.; Harris, R. D., Hydrophobicity scale for proteins based on inverse temperature transitions. *Biopolymers* **1992,** *32* (9), 1243-50.

101. Li, N. K.; Garcia Quiroz, F.; Hall, C. K.; Chilkoti, A.; Yingling, Y. G., Molecular description of the LCST behavior of an elastin-like polypeptide. *Biomacromolecules* **2014,** *15* (10), 3522-30.

102. McDaniel, J. R.; Radford, D. C.; Chilkoti, A., A unified model for de novo design of elastin-like polypeptides with tunable inverse transition temperatures. *Biomacromolecules* **2013,** *14* (8), 2866-72.

103. van Eldijk, M. B.; Smits, F. C.; Vermue, N.; Debets, M. F.; Schoffelen, S.; van Hest, J. C., Synthesis and self-assembly of well-defined elastin-like polypeptide-poly(ethylene glycol) conjugates. *Biomacromolecules* **2014,** *15* (7), 2751-9.

104. Milletti, F., Cell-penetrating peptides: classes, origin, and current landscape. *Drug Discov Today* **2012,** *17* (15-16), 850-60.

105. Henderson, B. W.; Dougherty, T. J., How does photodynamic therapy work? *Photochem. Photobiol.* **1992,** *55* (1), 145-57.

106. Moan, J.; Berg, K., The photodegradation of porphyrins in cells can be used to estimate the lifetime of singlet oxygen. *Photochem. Photobiol.* **1991,** *53* (4), 549-53.

CHAPTER 2

Identification of a novel inactivating mutation in Isocitrate Dehydrogenase 1 (IDH1-R314C) in a high grade astrocytoma

Sanne A.M. van Lith[1], Anna C. Navis[1], Krissie Lenting[1], Kiek Verrijp[1], Jan T.G. Schepens[2], Wiljan J.A.J. Hendriks[2], Nil A. Schubert[1], Hanka Venselaar[3], Ron A. Wevers[4], Arno van Rooij[4], Pieter Wesseling[1,5], Remco J. Molenaar[6], Cornelis J.F. van Noorden[6], Stefan Pusch[7], Bastiaan Tops[1] and William P.J. Leenders[1*]

[1]Department of Pathology, Radboud Institute for Molecular Life Sciences, Radboudumc Nijmegen, The Netherlands
[2]Department of Cell Biology, Radboud Institute for Molecular Life Sciences, The Netherlands, [3]Centre for Molecular and Biomolecular Informatics, Radboud Institute for Molecular Life Sciences, The Netherlands
[4]Translational Metabolic Laboratory, Department Laboratory Medicine, Radboudumc Nijmegen, The Netherlands
[5]Department of Pathology, VU University Medical Center, Amsterdam, The Netherlands [6]Department of Cell Biology and Histology, Academic Medical Center, Amsterdam, The Netherlands
[7]Clinical Cooperation Unit Neuropathology, German Cancer Center (DKFZ) , Heidelberg, Germany

ABSTRACT

The majority of low-grade and secondary high-grade gliomas carry heterozygous hotspot mutations in cytosolic isocitrate dehydrogenase 1 (*IDH1*) or the mitochondrial variant *IDH2*. These mutations mostly involve Arg132 in IDH1, and Arg172 or Arg140 in IDH2. Whereas IDHs convert isocitrate to alpha-ketoglutarate (α-KG) with simultaneous reduction of $NADP^+$ to NADPH, these IDH mutants reduce α-KG to D-2-hydroxyglutarate (D-2-HG) while oxidizing NADPH. D-2-HG is a proposed oncometabolite, acting via competitive inhibition of α-KG-dependent enzymes that are involved in metabolism and epigenetic regulation. However, much less is known about the implications of the metabolic stress, imposed by decreased α-KG and NADPH production, for tumor biology.

We here present a novel heterozygous *IDH1* mutation, $IDH1^{R314C}$, which was identified by targeted next generation sequencing of a high grade glioma from which a mouse xenograft model and a cell line were generated. $IDH1^{R314C}$ lacks isocitrate-to-α-KG conversion activity due to reduced affinity for $NADP^+$, and differs from the $IDH1^{R132}$ mutants in that it does not produce D-2-HG. Because $IDH1^{R314C}$ is defective in producing α-KG and NADPH, without concomitant production of the D-2-HG, it represents a valuable tool to study the effects of IDH1-dysfunction on cellular metabolism in the absence of this oncometabolite.

INTRODUCTION

Diffuse gliomas are primary tumors of the brain that are thought to develop from (precursors of) astrocytes or oligodendrocytes. Based on histopathology and according to WHO guidelines, these cancers are classified as grade II-IV astrocytomas or grade II-III oligodendrogliomas[1-2]. The disease is essentially incurable and median overall survival of patients with grade IV astrocytoma (glioblastoma, the most malignant variant) is only 15 months, despite chemo- and radiotherapy[3].

In 2008, somatic mutations in the isocitrate dehydrogenase genes *IDH1* and *IDH2* were identified in the large majority of low grade gliomas and secondary glioblastomas[4]. These mutations are always heterozygous and mostly involve the same amino acid residues; Arg132 in the cytosolic IDH1 and Arg172 or Arg140 in the mitochondrial IDH2[5-7]. In glioma, the majority of *IDH* mutations are found in *IDH1*, and about 90% are *IDH1[R132H]*. Extensive research has revealed that these mutations are neomorphic gain-of-function mutations, resulting in the conversion of α-ketoglutarate (α-KG), the normal product of IDH-mediated decarboxylation of isocitrate, to D-2-hydroxyglutarate (D-2-HG) which can accumulate to millimolar concentrations[8]. During the conversion of α-KG to D-2-HG by the mutant enzyme, NADPH is oxidized.

Because of the molecular similarity between α-KG and D-2-HG, the latter can competitively inhibit the activity of a range of α-KG-dependent dioxygenases, of which over 60 have been identified[9-10]. Most important examples are the Ten-Eleven-Translocation 2 (TET2) DNA demethylases (resulting in the CpG-island hypermethylator phenotype in *IDH[MUT]* cells) and Jumonji-C (JMJC) histone demethylases (resulting in histone hypermethylation)[11-13]. The net result is a transcriptional profile that contributes to tumorigenesis via mechanisms that are still poorly understood. Although this has been matter of debate, consensus is now that D-2-HG can promote degradation of the transcription factor hypoxia-inducible factor (HIF-1α), possibly after non-enzymatic oxidation to α-KG[14]. How this exactly contributes to oncogenesis is still an active field of investigation[15-17].

The effects of expression of IDH1-mutants and/or D-2-HG on tumor metabolism have started to receive attention now[18]. It was recently shown that D-2-HG inhibits the tricarboxylic acid (TCA) cycle enzyme succinate dehydrogenase, possibly leading to hypersuccinylation of proteins and anti-apoptotic effects[19]. Because mutant IDH1 lacks isocitrate-to-α-KG conversion activity, normally a predominant source of cytosolic NADPH in the brain[20], *IDH[MUT]* cells are predicted to have lower steady state levels of NADPH, an effect that will be augmented by NADPH-oxidation during D-2-HG production. Thus, *IDH* mutations impact the redox status of glioma cells.

Additionally, *IDH* mutations may affect anabolic pathways: IDH1/2 can reduce α-KG back to isocitrate which may serve as carbon source for fatty acid and lipid synthesis via citrate and acetyl-CoA[21-22] but IDH1[R132H] lacks this reverse activity[23]. It is conceivable therefore, that *IDH[MUT]* tumors need metabolic salvage pathways to allow tumor progression and this is supported

by the finding of relatively normal α-KG levels in a patient-derived orthotopic $IDH1^{R132H}$ oligodendroglioma model[24]. Because $IDH1^{MUT}$ cells display higher sensitivity to glutaminase inhibitors than IDH^{WT} cells[25], glutamine has been proposed to feed in into the mitochondrial TCA cycle as an anaplerotic source of α-KG, via the activities of glutaminase and glutamate dehydrogenase (GLUD). We previously postulated that gliomas may resort to direct import of glutamate, a ubiquitous neurotransmitter in brain, to allow GLUD-mediated α-KG production[26-27]. NADH/NADPH, generated during this reaction would simultaneously supplement the NAD(P)H pool. These metabolic changes could all play a role in tumor cell maintenance and therefore be an Achilles heel and target for therapeutic inhibition. However, uncoupling the metabolic alterations that result from NADPH/α-KG depletion from the pleiotrophic effects of D-2-HG is a difficult task.

In this study we describe a novel heterozygous $IDH1$ mutation which we uncovered by next generation sequencing of a glioblastoma from which a patient-derived xenograft model and corresponding cell line were generated. We show that this IDH1^{R314C} mutant does not convert isocitrate to α-KG, unless at non-physiological concentrations of NADP$^+$, and does not produce D-2-HG. These properties make that IDH1^{R314C} tumor models are valuable tools to study the relevance of α-KG/NADPH depletion versus D-2-HG formation in gliomagenesis and tumor progression.

RESULTS

E98 cells contain a rare heterozygous IDH1R314C mutation located in the NADP+ binding pocket

The patient-derived E98 astrocytoma model carries a number of glioma-typical genetic mutations and is phenotypically similar to clinical glioma when grown as orthotopic xenografts[28-30]. This makes this model of high interest as a prototypical glioblastoma model for testing of targeted therapeutics[31-34]. Because the design of rational targeted therapies requires a detailed analysis of genetic aberrations, we subjected this cell line to targeted genomic next generation sequencing via Ion Torrent analysis using a primer set that allows parallel deep sequencing of 409 genes with known involvement in cancer-related pathways. As we unfortunately did not have access to blood of the E98 donor, SNPs and variants with mean allelic frequency (MAF)>1% were filtered out using sequence data from pooled blood samples as reference. Due to our general interest in $IDH1$, our attention was specifically drawn to a heterozygous C to T mutation at position 940 in the $IDH1$ gene (Figure 1A) which results in the p.Arg314Cys substitution. Presence of this mutation was verified in the original patient material (Figure 1B). To check for the incidence of this mutation, 103 DNA samples from glioma (Table 1) were Sanger sequenced. None of these samples contained the p.R314 mutation. Data mining of the Exome Sequencing Project (ESP) database (www.exac.broadinstitute.org/) revealed that

this variant has not been identified in 121,410 alleles. Mining of the Cosmic database revealed only one reported IDH1 c.941G>A / p.R314H mutation in a gastric carcinoma (mutation ID COSM4090677). Thus, the R314C mutation is a rare mutation.

Since Arg314 is located in the NADP+ binding pocket[35] we studied the experimentally solved structure of IDH1^{WT} and IDH1^{R314C} in complex with NADP+ using YASARA. As shown in Figure 1C, the R314C mutation significantly alters the tertiary structure resulting in an imperfect fit of NADP+ in the binding pocket, mainly due to the lack of interaction between the negatively charged 2´-phosphate of the co-enzyme NADP+ and the positively charged amine group of the arginine, and lack of ionic interactions between the Arg314 and glutamate residues on position 247 and 253 in the other subunit.
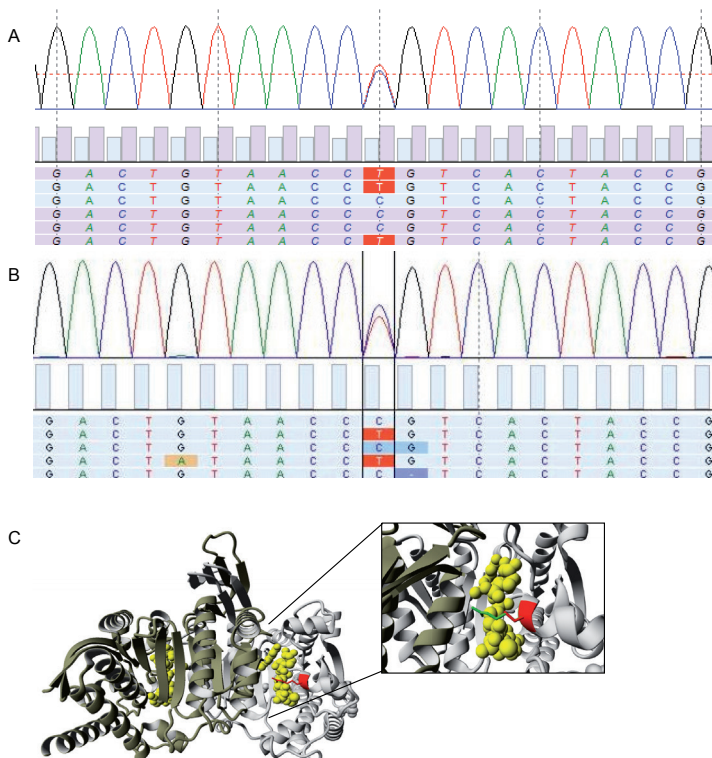
Figure 1. Identification of IDH1^{R314C} in a high grade astrocytoma. A) Sequencing trace showing the heterozygous C to T mutation at position 940 in the *IDH1* gene found in the E98 cell line and B) primary tumor material. This mutation leads to the p.Arg314Cys substitution in the IDH1 protein. C) Display of the 3D- structure of human IDH1^{R314C} generated with YASARA (PDB-file 3inm). The IDH1^{WT} homodimer is displayed with bound cofactor NADP+ (yellow), and the arginine residue on position 314 (red), both subunits are coloured in a different shade of grey. The inset shows the mutated cysteine (red) superimposed on the original arginine (green).

Table 1. Overview of glioma samples used for Sanger sequencing of IDH1[R314C], with diagnosis and IDH1 status.

Diagnosis	Number of samples	Number of samples verified IDH1[R132H]	Number of samples verified IDH1[WT]
GBM	47	1	42
Astrocytoma grade II	13	5	8
Astrocytoma grade III	2	0	1
Oligodendroglioma grade II	18	13	3
Oligodendroglioma grade III	3	0	2
Oligodendroglioma grade IV	1	0	1
Oligoastrocytoma grade II	14	9	3
Oligoastrocytoma grade III	3	0	3
Oligoastrocytoma grade IV	2	2	0

IDH1[R314C] is defective in isocitrate to α-KG conversion

We first examined the activity of purified IDH1[R314C]-GST proteins, using IDH1[WT]-GST and IDH1[R132H]-GST as positive and negative controls. All enzymes could be readily produced and purified (Figure 2A). Under the conditions tested, both IDH1[R132H]-GST and IDH1[R314C]-GST did not show isocitrate-to-α-KG conversion activity whereas IDH1[WT]-GST did (Figure 2B). The absence of α-KG formation by IDH1[R132H]-GST and IDH1[R314C] was confirmed with LC-MS (Figure 2C). Importantly, whereas IDH1[R132H]-GST was active in converting α-KG to D-2-HG (as revealed by oxidation of NADPH) the IDH1[R314C]-GST mutant was completely devoid of this activity (Figure 2D). Thus, IDH1[R314C] homodimers are inactive in converting isocitrate and NADP$^+$ to α-KG and NADPH and, unlike IDH1[R132H]-GST, do not consume NADPH, consistent with the lack of D-2-HG production by E98 xenografts that has already been described before[36].

The IDH1[R132] mutation in human gliomas always occurs in a heterozygous manner, resulting in a theoretical 1:2:1 distribution of IDH[WT/WT], IDH[WT/MUT] and IDH[MUT/MUT] dimers. This stoichiometry may be important for balanced IDH activity, because D-2-HG can only be formed via an intimate crosstalk between wild-type and mutant subunits, for which α-KG is a product and substrate, respectively. To analyze the effects of IDH1[R314C] overexpression in eukaryotic cells we performed enzymatic assays with cell extracts from HEK293T cells, transiently overexpressing IDH1[WT], IDH1[R132H] or IDH1[R314C] as well as lentivirally transduced LN229 and U251 glioma cells, stably expressing the different IDH1 mutants (Figure 3A). To be able to distinguish recombinant from endogenous IDH[WT] and allow statements on IDH[WT/MUT] ratios we equipped the mutated reading frames with a Bap8xHis (biotin-acceptor peptide-8xHis) tag, increasing molecular weight with ~3 kDa. Intriguingly, irrespective of the method of genetic modification (transfection or lentiviral transduction) expression levels of recombinant enzymes were lower than that of the endogenous enzymes, with IDH[R132H]-Baph8xHis consistently being lowest, possibly a result of negative selection for IDH1[R132H]-Bap8xHis overexpression and associated toxic levels of D-2-
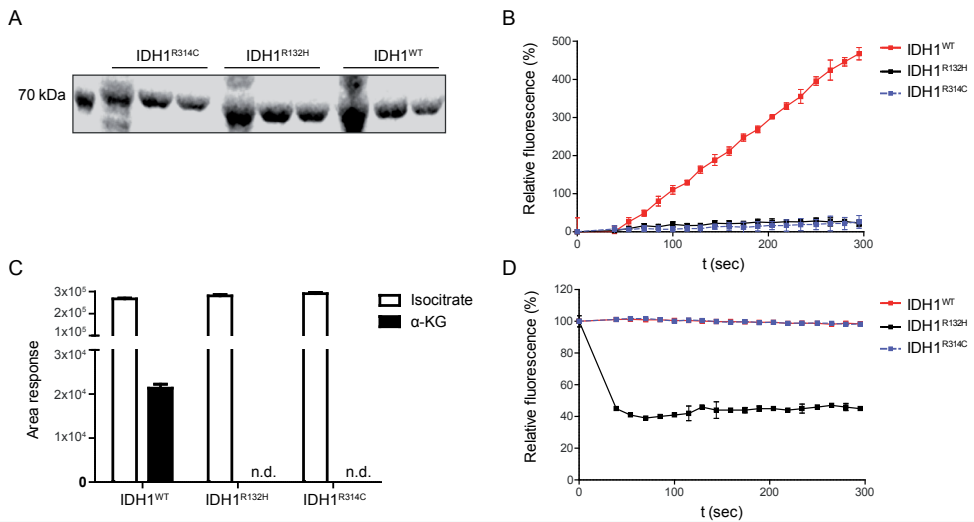
Figure 2. Homodimeric IDH1^{R314C}-GST is defective in the isocitrate-to α-KG reaction and does not produce D-2-HG. A) SDS-page gel stained with coomassie brilliant blue showing expression of purified IDH1-GST constructs. B) Fluorescent monitoring of NADPH formation at 340 nm shows that only purified IDH1^{WT}-GST is capable to convert isocitrate to α-KG under the reaction conditions tested, whereas IDH1^{R132H}-GST and IDH1^{R314C}-GST are inactive. C) α-KG production by IDH1-GST enzymes was measured with LC-MS. Note that only IDH1^{WT}-GST is capable of isocitrate-to-α-KG conversion. (n.d. = non detectable, area<150). D) Fluorescent monitoring of NADPH reduction shows that only purified IDH1^{R132H}-GST is active in the α-KG-to-D-2-HG conversion. Both IDH1^{WT}-GST and IDH1^{R314C}-GST lack the capability to produce D-2-HG.

HG[37]. Consistent with the absence of activity of purified IDH1^{R314C}-GST homodimers (Figure 2B), for all cell lines NADP$^+$-dependent oxidative decarboxylation of isocitrate was significantly lower in IDH1^{R314C}-Bap8xHis expressing cells than in IDH1^{WT}-Bap8xHis cells (Figure 3B). Of note, the reduced activity of IDH1^{R314C}-Bap8xHis in U251 cell extracts could be rescued by performing the enzymatic assay in supraphysiological concentrations of NADP$^+$ (Figure 4), in line with loss of NADP$^+$-affinity as predicted from the solved structure in Yasara, and as described earlier by Lee et. al.[35]. Consistent with this model, the R314C mutation caused an eight-fold increase in Km for NADP$^+$ (318 µM for IDH1^{R314C} vs 38 µM for IDH^{WT}, Figure 3C). This predicts that IDH1^{R314C} is inactive under physiological NADP$^+$ concentrations. Of note, activity of IDH1^{R314C}-GST homodimers at higher concentrations of NADP$^+$ was too low to calculate the Km for isocitrate.

As expected from the lack of NADPH consumption when incubated with α-KG (Figure 2D), IDH1^{R314C}-BAPHIS expressing LN229 and U251 glioblastoma cell lines did not produce 2-HG, in contrast to their IDH1^{R132H}-Bap8xHis counterparts (Figure 3D).
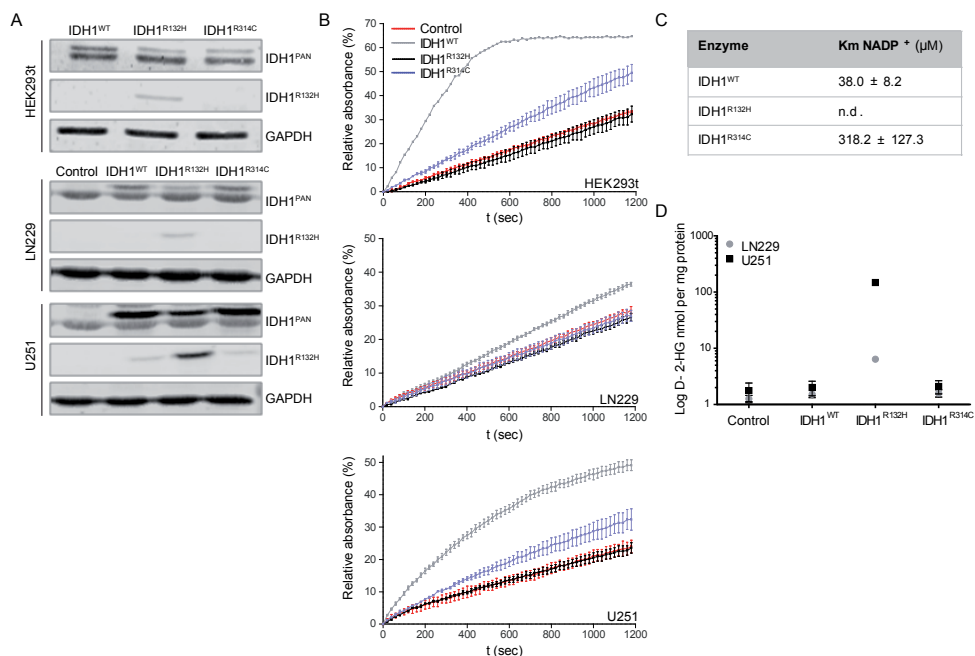
Figure 3. IDH1[R314C]-Bap8xHis expression in glioma cell lines leads to reduced forward activity compared to IDH[WT] expression. A) Western blots showing expression of IDH1-Bap8xHis in transiently transfected HEK293t and lentivirally transduced LN229 and U251 glioma cells. Blots were stained with anti-IDH1[PAN] and anti-IDH1[R132H] as indicated, or with anti-GAPDH as a loading control. Since the recombinant proteins are ~3 kDa larger than endogenous IDH1 they can be distinguished from the endogenous IDH1. Control LN229 and U251 were transduced with empty vector virus (EV). B) Monitoring of NADPH formation after isocitrate/NADP$^+$ addition to extracts from transfected/transduced cell lines. NADPH formation was monitored by absorbance measurements at 340 nm. Note that IDH1[R314C]-Bap8xHis was far less effective in oxidative carboxylation of isocitrate than IDH1[WT]-Bap8xHis. C) Km values of IDH1-GST for NADP$^+$. The Km value for NADP$^+$ for IDH1[R132H]-GST could not be determined. D) D-2-HG production by IDH1-Bap8xHis expressing cell lines was measured with LC-MS. Only IDH1[R132H]-Bap8xHis expressing cells were capable of D-2-HG production.
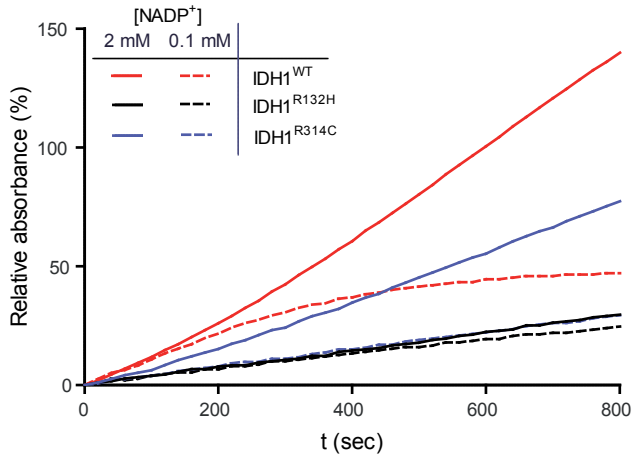
Figure 4. IDH1^{R314C} activity can be rescued by supraphysiological NADP+ levels. Extracts of U251-IDH1^{R314C} U251-IDH1^{R132H} or U251-IDH1^{WT} were incubated with isocitrate and 100 μM or 2 mM NADP+, and NADPH formation was measured in real time by 340 nm absorbance. The activity of IDH1^{R314C}-Bap8xHis but not IDH1^{R132H}-Bap8xHis was partly rescued by increasing NADP+ concentrations to 2 mM.
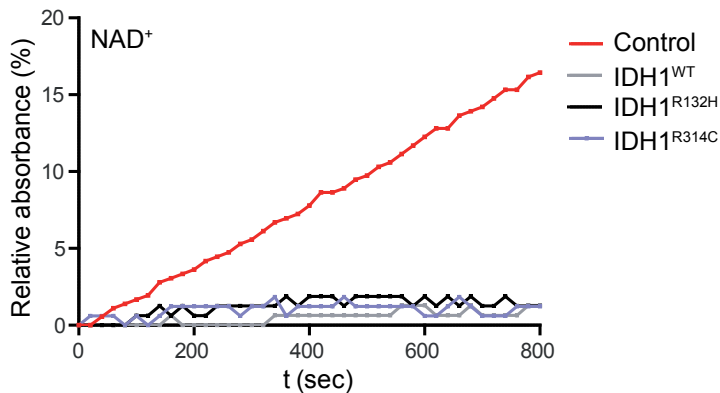
Figure 5. The R314C mutation does not shift the cofactor dependency from NADP+ to NAD+. IDH1^{MUT}-GST enzymes were incubated with isocitrate and NAD+, and NADH formation was measured by 340 nm absorbance. All IDH1 enzymes were inactive in the presence of NAD+. As a positive control a liver extract was used.

DISCUSSION

Since their discovery, hotspot mutations in IDH enzymes have become a major focus of research. The oncogenic potential of IDH1[R132H] has been attributed to epigenetic alterations, resulting from the production of the alleged oncometabolite D-2-HG[9-10,38]. Furthermore it has been shown that proliferation of *IDH1[R132H]* cells requires metabolic rescue programs that depend on *in vivo* tumor-stroma interactions, possibly involving glutamate import[26].

We here identify and characterize IDH1[R314C], a novel and rare mutation in IDH1 in a high grade astrocytoma which has not been reported before. We show that IDH1[R314C] has a greatly reduced affinity for NADP+, in agreement with a previous structure-function relationship study on porcine IDH1[35] and is consequently defective in oxidizing isocitrate to α-KG. The R314C mutation did not shift the cofactor dependency from NADP+ to NAD+ (Figure 5) as was previously reported for mutated IDH1 from the halobacterium *Haloferax Volcanii* [39].

To define an exact role for IDH1[R314C] in tumor formation and biological behavior of cancer cells is impossible in the context of the many more mutations that are found in E98[40]. To study this further, isogenic E98 cell lines with a repaired IDH1[R314R] allele are required and such technically challenging cell lines are not yet available.

The decreased potential of *IDH1[R314C]* cells to produce α-KG and NADPH in the cytosol may directly impact on redox potential, lipid synthesis and membrane production and may explain the slow growth rates of E98 cells *in vitro* (doubling time of 46 hrs, data not shown). Interestingly, despite these very slow growth rates, *in vivo* E98 xenografts represent the most aggressive diffuse infiltrative brain tumor model in our lab, killing mice within 4-5 weeks after intracerebral implantation[28]. This illustrates that the brain micro-environment is crucially involved in allowing growth of E98 cells. Since the redox status of cells may particularly impact on cell migration[41] it would be of high interest to investigate how relatively low NADPH/NADP+ ratios in E98 cells *In vivo* are associated with active cell migration, leading to the diffuse infiltrative phenotype. Further unraveling of the specific *in vivo* metabolic salvage pathways that are adapted by E98 cells and may be involved in its aggressive behavior may lead to potential novel ways for therapeutic intervention.

In oncology, most NGS protocols aim for detection of actionable hot spot mutations in known genes only, leaving a potentially huge amount of mutations with significance for tumor biology, undetected and this is the reason why we only now recognized that E98 cells carry the IDH1[R314C] mutation[24]. Alterations in genes encoding metabolic enzymes may be directly or indirectly involved in tumorigenesis based on subtle distortions in equilibria between metabolic intermediates and/or oxidative milieu.

In conclusion, we identified a novel IDH1[R314C] mutant that shares with the common IDH1[R132H] mutant a defect in isocitrate-to-α-KG conversion activity, but lacks the capacity to produce D-2-HG. Future comparative profiling studies using isogenic cell lines expressing IDH[WT], IDH1[R132H]

or IDH1[R314C] will allow us to distinguish between epigenetic and metabolic alterations, resulting from NADPH/α-KG depletion or D-2-HG accumulation.

METHODS

E98

Generation of the E98 model which was derived from a grade IV astrocytoma, was described before[28]. All animal experimental work was performed in accordance with the guidelines of and was approved by the local ethical committee for animal experimentation of Radboud University. An adherent E98 cell line was generated from mouse xenografts via routine procedures[29,40] and cultured in DMEM (Lonza, Basel, Switzerland) supplemented with 10% FCS (Gibco, ThermoFisher Scientific, Watlham, MA, USA) and 40 µg/ml gentamycin (Centrafarm, Etten-Leur The Netherlands).

Next generation sequencing

Genomic DNA from E98 cells and from original tumor material was analyzed by semi-conductor sequencing (IonPGM, Life Technologies, ThermoFisher Scientific, Watlham, MA, USA) using the comprehensive cancer panel (Life Technologies, ThermoFisher Scientific, Waltham, MA, USA) detecting copy number variations and mutations in 409 cancer-related genes. An IonPGM E98 library was generated according to the manufacturer's protocol. In short, 10 ng of DNA per pool was amplified in 21 cycles by PCR using the Ion AmpliSeqTM mastermix, followed by barcode and adapter ligation. Amplified products were purified with Agencourt AMPure XP beads (Beckman Coulter Genomics, High Wycombe, UK). The library was diluted to 20 pM and emulsion PCR was performed using the Ion OneTouchTM 200 Template kit following the manufacturer's protocol. Next, Ion Sphere Particles (ISPs) were recovered and enriched for template positive ISPs using Dynabeads MyOne Streptavidin C1 beads (Life Technologies, ThermoFisher Scientific, Waltham, MA, USA) in the Ion OneTouchTM ES instrument (Life Technologies, ThermoFisher Scientific, Waltham, MA USA). ISP enrichment was quantified using the Qubit 2.0 fluorometer (Life Technologies, ThermoFisher Scientific, MA, USA). Sequencing primer and polymerase were added to the final enriched spheres before loading onto an Ion 318 chip according to the Ion PGMTM 200 sequencing kit protocol. Variants were called using NextGene (JSI) and filtered for common variants (MAF>1%) in the general population.

Visualization of IDH1 structure with YASARA

The structure of human IDH1 has been experimentally solved and can be found in PDB-file 3inm[8]. We used the WHAT IF & YASARA twinset for visualization and analysis[42-43].

PCR and cloning of IDH1 constructs

Total RNA was isolated from cell lines using TRIzol reagent (Life Technologies, ThermoFisher Scientific, Waltham, MA, USA) and converted to cDNA using oligo-dT and MMLV reverse transcriptase (New England Biolabs, Ipswich, MA, USA) using standard protocols. Open reading frames for $IDH1^{WT}$, $IDH1^{R132H}$ and $IDH1^{R314C}$ were PCR amplified from HT29, E478 and E98 cDNA, respectively, using primers IDH-EcoRIFw ['5'-CGAATTCACTGTCAAGGTTTATTGAAGTC-3'] and IDH-AgeIRev [5'-CACCGGTAAGTTTGGCCTGAGCTAG-3'] and Phusion DNA polymerase (Finnzymes, ThermoFisher Scientific, Watlham, MA, USA). PCR products were digested with EcoRI and AgeI (New England Biolabs, Ipswich, MA, USA) and cloned in fusion to a C-terminal biotin-acceptor peptide (BAP) and an 8xhis tag (8xHis) in vector PHLsec-BAPHIS AgeI/EcoRI, derived from PHLsec-HIS (Addgene, Cambridge, MA, USA) using T4 DNA ligase (New England Biolabs, Ipswich, MA, USA). The BAPHIS tags were added to distinguish recombinant from endogenous IDH by molecular weight and to allow Ni-bead purification. Clones containing the respective mutations were selected via Sanger sequencing. For generation of lentiviral constructs, the different ORFs were recloned in vector pENTRY which was recombined with pLENTI using the GATEWAY system via standard procedures. In parallel, IDH ORFs were cloned in fusion with GST in E.coli expression vector pDEST15 as described before[37].

GST fusion protein expression and purification

GST fusion proteins were expressed in E. coli strain ER2566 via standard induction protocols. Briefly, 2xTY medium supplemented with 50 µg/ml ampicillin (Roche, Basel, Switzerland) was inoculated with 1% v/v overnight culture. Protein expression was induced with 1 mM IPTG (Serva, Heidelberg, Germany) at OD_{600}~0.6. After 3 hours at 30°C, bacteria were harvested by centrifugation and resuspended in 300 mM NaCl, 50 mM TRIS/HCL pH 8.0 supplemented with Complete protease inhibitor (Roche, Basel, Switzerland). Cells were lysed by 3 freeze-thaw cycles, followed by sonication (4 x 15 seconds, 25% amplitude, Bioruptor, Diagenode) and centrifugation (3500 rpm, 20 min). Proteins were purified using glutathione beads (Pierce, ThermoFisher Scientific, Waltham, MA, USA), eluted with 10 mM glutathione and dialyzed extensively against 150 mM NaCl, 25 mM TRIS/HCL pH 7.5. Expression and purity were checked by SDS-PAGE gel electrophoresis and Coommassie Brilliant Blue staining.

Transient transfection experiments

HEK293T cells were grown to 30% confluence in 6 wells plates in DMEM supplemented with 10% FCS and 40 µg/ml gentamycin. Cells were transfected with 2 µg pHLsec-IDH1^{MUT}-Bap8xHis, IDH1^{WT}-Bap8xHis or pIRESneo-EGFP using Fugene HD reagent according to the manufacturers' protocol (Roche, Basel, Switzerland). After 2 days, cells were harvested and processed to cell lysates by scraping in 150 µl sucrose buffer (0.32 M sucrose in 10 mM TRIS-HCL pH 7.5) and sonicating on ice (3 cycles of 30 sec max power and 30 sec off in Bioruptor, Diagenode). Lysates were centrifuged (14000 rpm, 10 min, 4°C) and supernatants were subjected to BCA assays

(Pierce, ThermoFisher Scientific, Waltham, MA, USA) for protein concentration measurements and stored at -20°C until further analysis. To quantify IDH1 protein expression, 20 µg of total cytosolic protein was subjected to 10% SDS-PAGE and electroblotted onto a nitrocellulose membrane (Whatman Optitran BA-S85, GE healthcare, Little Chalfont, UK). After blocking in Odyssey Blocking buffer (LI-COR biosciences, Licoln, NE, USA) in PBS (1:1) the membrane was incubated with rabbit-anti-IDH1 (1:1000, HPA035248, Sigma-Aldrich, St. Louis, MO, USA) and mouse-anti-IDH1R132H (1:400, H09L, Dianova, Hamburg, Germany) in blocking buffer, followed by incubation with goat-anti-mouseDyLight800 (1:10.000, ThermoFisher Scientific, Waltham, MA USA) or goat-anti-rabbitAlexa680 (1:10.000, Invitrogen, ThermoFisher Scientific, Waltham, MA, USA). After washing, blots were analyzed on the Odyssey scanner (LI-COR biotechnology, Lincoln, NE, USA).

Generation of stable IDH1^{MUT} overexpression glioma cell lines

LN229 and U251 cells were transduced with lentiviral vectors encoding IDH1^{WT}-Bap8xHis, IDH1^{R132H}-Bap8xHis, IDH1^{R314C}-Bap8xHis or an empty vector (EV) control as described before[44]. Transduced cells were selected using blasticidin and cultured in DMEM supplemented with 10% FCS and 40 µg/ml gentamycin. Cells were grown to 80% confluency in 10 cm ø culture plates (Corning, Corning, NY, USA). Cell culture media were collected and stored at -20°C until later analysis. Cells were collected and cytosolic extracts were prepared in 400 µl sucrosebuffer as described before. Twenty µg of protein was subjected to SDS-PAGE gel electrophoresis and western blot to quantify protein expression.

IDH activity measurements

Isocitrate-to-α-KG and α-KG-to-2-HG conversion rates of the purified IDH1-GST enzymes were determined by monitoring NADPH generation over time. Assays were performed in 100 µl freshly prepared assay solution (2 mM MgCl$_2$ in 100 mM TRIS/HCL pH 7.4) containing 10 mM NADP$^+$ (Sigma-Aldrich, St. Louis, MO, USA) and 10 mM isocitrate (Sigma-Aldrich, St. Louis, MO, USA) (forward assay) or 10 mM NADPH (Sigma-Aldrich, St. Louis, MO, USA) and 10 mM α-KG (Sigma-Aldrich, St. Louis, MO, USA) (reverse assay). Four µg of purified IDH1-GST fusion proteins were incubated with assay solution in a 96 wells plate at 37°C (BD Falcon, Franklin Lakes, USA) and fluorescence (Ex. 340 +/– 10 nm, Em. 440 +/– 10 nm), was measured every 15 seconds over a period of 5 minutes with an Omega FluoStar (BMG Labtech, Ortenberg, Germany). To examine enzyme kinetics in more detail, 4 µg of IDH1-GST proteins were incubated with varying NADP$^+$ concentrations (0-500 µM) and 100 µM isocitrate at 22°C. Absorbance at 340 nm was measured every 20 seconds with a Benchmark Plus Microplate Spectrophotometer (Bio-Rad, Hercules, CA, USA). Non-linear regression analysis (Michaelis-Menten) was performed in Graphpad Prism 5.03.

To determine NAD$^+$ dependency, 4 µg of IDH1-GST proteins were incubated with 100 µl assay solution containing 2 mM MgCl$_2$, 500 µM isocitrate and 2,5 mM NAD$^+$ (Sigma-Aldrich, St.

Louis, MO, USA) in 100 mM TRIS-HCL pH 7.4 at 22°C. A sucrose extract made from human liver was taken as a control. Absorbance at 340 nm was monitored as described.

For enzyme measurements in extracts of eukaryotic cells, 50 µg of total cytosolic protein were incubated with assay solution (2 mM $MgCl_2$, 500 µM isocitrate in 100 mM TRIS/HCL pH 7.4) containing 100 µM $NADP^+$ in 96 wells plates (Greiner) at 22°C and NADPH generation was quantified as described before.

D-2-HG, α-KG and isocitrate measurements by isotope dilution LC-MS

D-2-HG levels in cell culture media were measured using stable isotope dilution liquid chromatography tandem mass spectrometry (LC-MS) as described before[36]. α-KG and isocitrate levels were determined in *in vitro* IDH1 reaction mixtures. 4 µg of IDH1-GST proteins were incubated in 150 µl freshly prepared assay solution (2 mM $MgCl_2$ in 100 mM TRIS/HCL pH 7.4) containing 500 µM isocitrate and 100 µM $NADP^+$. After 20 min incubation at 22°C the reaction was stopped using 20 µl 4% HCOOH. 25 µl of this solution was mixed with 25 µl 9 µM $^{13}C_5$-2-HG stable isotope (Chiralex, Nijmegen, The Netherlands) in deionized water and 75 µl deionized water before passing it through an Amicon Ultra 30 kDa Centrifugal Filter (Merck Millipore, Billerica, MA, USA) by centrifugation (14000 g, 30 min). 2 µl of the filtrate was injected onto a Atlantis T3 HPLC Column (2.1*100 mM dp 3µ) and run with 12.5% MeOH in 87.5% 0.3%HCOOH in water. The column was connected to a Waters Quattro Premier tandem mass spectrometry fitted with an ESI probe operated in negative mode, recording the following MRM transitions, as summarized in Table 2.

Statistics

All experiments were performed in triplicate. Data were processed in Excell (Microsoft, Redmond, WA, USA) and enzyme kinetics were determined by fitting of Michaelis Menten in Graphpad Prism 5.03 (Graphpad Software, La Jolla, CA, USA).

Table 2. MRM transitions for metabolite detection

MRN	Compound name	Cone V (V)	Coll eV (eV)	Ret. Time (min)
191>111	Isocitrate	22	13	1.28
145>101	α-KG	22	8	1.53
147>129	D-2-HG	19	11	1.54
152>134	$^{13}C_5$-2-HG	19	11	1.54
				Note: t0=0.8min

REFERENCES

1. Sahm, F.; Reuss, D.; Koelsche, C.; Capper, D.; Schittenhelm, J.; Heim, S.; Jones, D. T.; Pfister, S. M.; Herold-Mende, C.; Wick, W.; Mueller, W.; Hartmann, C.; Paulus, W.; von Deimling, A., Farewell to oligoastrocytoma: in situ molecular genetics favor classification as either oligodendroglioma or astrocytoma. *Acta Neuropathol* **2014,** *128* (4), 551-9.

2. Louis, D. N., Ohgaki, H., Wiestler, O.D., Cavenee, W.K. , Classification of Tumours of the Central Nervous System. *WHO* **2007**.

3. Stupp, R.; Mason, W. P.; van den Bent, M. J.; Weller, M.; Fisher, B.; Taphoorn, M. J.; Belanger, K.; Brandes, A. A.; Marosi, C.; Bogdahn, U.; Curschmann, J.; Janzer, R. C.; Ludwin, S. K.; Gorlia, T.; Allgeier, A.; Lacombe, D.; Cairncross, J. G.; Eisenhauer, E.; Mirimanoff, R. O.; European Organisation for, R.; Treatment of Cancer Brain, T.; Radiotherapy, G.; National Cancer Institute of Canada Clinical Trials, G., Radiotherapy plus concomitant and adjuvant temozolomide for glioblastoma. *N Engl J Med* **2005,** *352* (10), 987-96.

4. Parsons, D. W.; Jones, S.; Zhang, X.; Lin, J. C.; Leary, R. J.; Angenendt, P.; Mankoo, P.; Carter, H.; Siu, I. M.; Gallia, G. L.; Olivi, A.; McLendon, R.; Rasheed, B. A.; Keir, S.; Nikolskaya, T.; Nikolsky, Y.; Busam, D. A.; Tekleab, H.; Diaz, L. A., Jr.; Hartigan, J.; Smith, D. R.; Strausberg, R. L.; Marie, S. K.; Shinjo, S. M.; Yan, H.; Riggins, G. J.; Bigner, D. D.; Karchin, R.; Papadopoulos, N.; Parmigiani, G.; Vogelstein, B.; Velculescu, V. E.; Kinzler, K. W., An integrated genomic analysis of human glioblastoma multiforme. *Science* **2008,** *321* (5897), 1807-12.

5. Balss, J.; Meyer, J.; Mueller, W.; Korshunov, A.; Hartmann, C.; von Deimling, A., Analysis of the IDH1 codon 132 mutation in brain tumors. *Acta Neuropathol* **2008,** *116* (6), 597-602.

6. Bleeker, F. E.; Lamba, S.; Leenstra, S.; Troost, D.; Hulsebos, T.; Vandertop, W. P.; Frattini, M.; Molinari, F.; Knowles, M.; Cerrato, A.; Rodolfo, M.; Scarpa, A.; Felicioni, L.; Buttitta, F.; Malatesta, S.; Marchetti, A.; Bardelli, A., IDH1 mutations at residue p.R132 (IDH1(R132)) occur frequently in high-grade gliomas but not in other solid tumors. *Hum Mutat* **2009,** *30* (1), 7-11.

7. Hartmann, C.; Meyer, J.; Balss, J.; Capper, D.; Mueller, W.; Christians, A.; Felsberg, J.; Wolter, M.; Mawrin, C.; Wick, W.; Weller, M.; Herold-Mende, C.; Unterberg, A.; Jeuken, J. W.; Wesseling, P.; Reifenberger, G.; von Deimling, A., Type and frequency of IDH1 and IDH2 mutations are related to astrocytic and oligodendroglial differentiation and age: a study of 1,010 diffuse gliomas. *Acta Neuropathol* **2009,** *118* (4), 469-74.

8. Dang, L.; White, D. W.; Gross, S.; Bennett, B. D.; Bittinger, M. A.; Driggers, E. M.; Fantin, V. R.; Jang, H. G.; Jin, S.; Keenan, M. C.; Marks, K. M.; Prins, R. M.; Ward, P. S.; Yen, K. E.; Liau, L. M.; Rabinowitz, J. D.; Cantley, L. C.; Thompson, C. B.; Vander Heiden, M. G.; Su, S. M. C., Cancer-associated IDH1 mutations produce 2-hydroxyglutarate. *Nature* **2009,** *462* (7274), 739-44.

9. Xu, W.; Yang, H.; Liu, Y.; Yang, Y.; Wang, P.; Kim, S. H.; Ito, S.; Yang, C.; Xiao, M. T.; Liu, L. X.; Jiang, W. Q.; Liu, J.; Zhang, J. Y.; Wang, B.; Frye, S.; Zhang, Y.; Xu, Y. H.; Lei, Q. Y.; Guan, K. L.; Zhao, S. M.; Xiong, Y., Oncometabolite 2-hydroxyglutarate is a competitive inhibitor of alpha-ketoglutarate-dependent dioxygenases. *Cancer Cell* **2011,** *19* (1), 17-30.

10. Borodovsky, A.; Seltzer, M. J.; Riggins, G. J., Altered cancer cell metabolism in gliomas with mutant IDH1 or IDH2. *Curr Opin Oncol* **2012,** *24* (1), 83-9.

11. Lu, C.; Ward, P. S.; Kapoor, G. S.; Rohle, D.; Turcan, S.; Abdel-Wahab, O.; Edwards, C. R.; Khanin, R.; Figueroa, M. E.; Melnick, A.; Wellen, K. E.; O'Rourke, D. M.; Berger, S. L.; Chan, T. A.; Levine, R. L.; Mellinghoff, I. K.; Thompson, C. B., IDH mutation impairs histone demethylation and results in a block to cell differentiation. *Nature* **2012,** *483* (7390), 474-8.

12. Chowdhury, R.; Yeoh, K. K.; Tian, Y. M.; Hillringhaus, L.; Bagg, E. A.; Rose, N. R.; Leung, I. K.; Li, X. S.; Woon, E. C.; Yang, M.; McDonough, M. A.; King, O. N.; Clifton, I. J.; Klose, R. J.; Claridge, T. D.; Ratcliffe, P. J.; Schofield, C. J.; Kawamura, A., The oncometabolite 2-hydroxyglutarate inhibits histone lysine demethylases. *EMBO reports* **2011,** *12* (5), 463-9.

13. Xu, W.; Yang, H.; Liu, Y.; Yang, Y.; Wang, P.; Kim, S. H.; Ito, S.; Yang, C.; Wang, P.; Xiao, M. T.; Liu, L. X.; Jiang, W. Q.; Liu, J.; Zhang, J. Y.; Wang, B.; Frye, S.; Zhang, Y.; Xu, Y. H.; Lei, Q. Y.; Guan, K. L.; Zhao, S. M.; Xiong, Y., Oncometabolite 2-hydroxyglutarate is a competitive inhibitor of alpha-ketoglutarate-dependent dioxygenases. *Cancer Cell* **2011,** *19* (1), 17-30.

14. Tarhonskaya, H.; Rydzik, A. M.; Leung, I. K.; Loik, N. D.; Chan, M. C.; Kawamura, A.; McCullagh, J. S.; Claridge, T. D.; Flashman, E.; Schofield, C. J., Non-enzymatic chemistry enables 2-hydroxyglutarate-mediated activation of 2-oxoglutarate oxygenases. *Nat Commun* **2014,** *5*, 3423.

15. Koivunen, P.; Lee, S.; Duncan, C. G.; Lopez, G.; Lu, G.; Ramkissoon, S.; Losman, J. A.; Joensuu, P.; Bergmann, U.; Gross, S.; Travins, J.; Weiss, S.; Looper, R.; Ligon, K. L.; Verhaak, R. G.; Yan, H.; Kaelin, W. G., Jr., Transformation by the (R)-enantiomer of 2-hydroxyglutarate linked to EGLN activation. *Nature* **2012,** *483* (7390), 484-8.

16. Blouw, B.; Song, H.; Tihan, T.; Bosze, J.; Ferrara, N.; Gerber, H. P.; Johnson, R. S.; Bergers, G., The hypoxic response of tumors is dependent on their microenvironment. *Cancer Cell* **2003**, *4* (2), 133-46.

17. Molenaar, R. J.; Radivoyevitch, T.; Maciejewski, J. P.; van Noorden, C. J.; Bleeker, F. E., The driver and passenger effects of isocitrate dehydrogenase 1 and 2 mutations in oncogenesis and survival prolongation. *Biochim. Biophys. Acta* **2014**.

18. Parker, S. J.; Metallo, C. M., Metabolic consequences of oncogenic IDH mutations. *Pharmacology & therapeutics* **2015,** *152,* 54-62.

19. Li, F.; He, X.; Ye, D.; Lin, Y.; Yu, H.; Yao, C.; Huang, L.; Zhang, J.; Wang, F.; Xu, S.; Wu, X.; Liu, L.; Yang, C.; Shi, J.; He, X.; Liu, J.; Qu, Y.; Guo, F.; Zhao, J.; Xu, W.; Zhao, S., NADP-IDH Mutations Promote Hypersuccinylation that Impairs Mitochondria Respiration and Induces Apoptosis Resistance. *Mol Cell* **2015,** *60* (4), 661-675.

20. Bleeker, F. E.; Atai, N. A.; Lamba, S.; Jonker, A.; Rijkeboer, D.; Bosch, K. S.; Tigchelaar, W.; Troost, D.; Vandertop, W. P.; Bardelli, A.; Van Noorden, C. J., The prognostic IDH1(R132) mutation is associated with reduced NADP+-dependent IDH activity in glioblastoma. *Acta Neuropathol* **2010,** *119* (4), 487-94.

21. Wise, D. R.; Ward, P. S.; Shay, J. E.; Cross, J. R.; Gruber, J. J.; Sachdeva, U. M.; Platt, J. M.; DeMatteo, R. G.; Simon, M. C.; Thompson, C. B., Hypoxia promotes isocitrate dehydrogenase-dependent carboxylation of alpha-ketoglutarate to citrate to support cell growth and viability. *Proc Natl Acad Sci U S A* **2011,** *108* (49), 19611-6.

22. Metallo, C. M.; Gameiro, P. A.; Bell, E. L.; Mattaini, K. R.; Yang, J.; Hiller, K.; Jewell, C. M.; Johnson, Z. R.; Irvine, D. J.; Guarente, L.; Kelleher, J. K.; Vander Heiden, M. G.; Iliopoulos, O.; Stephanopoulos, G., Reductive glutamine metabolism by IDH1 mediates lipogenesis under hypoxia. *Nature* **2012,** *481* (7381), 380-4.

23. Leonardi, R.; Subramanian, C.; Jackowski, S.; Rock, C. O., Cancer-associated isocitrate dehydrogenase mutations inactivate NADPH-dependent reductive carboxylation. *J. Biol. Chem.* **2012,** *287* (18), 14615-20.

24. Navis, A. C.; Niclou, S. P.; Fack, F.; Stieber, D.; van Lith, S.; Verrijp, K.; Wright, A.; Stauber, J.; Tops, B.; Otte-Holler, I.; Wevers, R. A.; van Rooij, A.; Pusch, S.; von Deimling, A.; Tigchelaar, W.; van Noorden, C. J.; Wesseling, P.; Leenders, W. P., Increased mitochondrial activity in a novel IDH1-R132H mutant human oligodendroglioma xenograft model: in situ detection of 2-HG and alpha-KG. *Acta Neuropathol Commun* **2013,** *1* (1), 18.

25. Seltzer, M. J.; Bennett, B. D.; Joshi, A. D.; Gao, P.; Thomas, A. G.; Ferraris, D. V.; Tsukamoto, T.; Rojas, C. J.; Slusher, B. S.; Rabinowitz, J. D.; Dang, C. V.; Riggins, G. J., Inhibition of glutaminase preferentially slows growth of glioma cells with mutant IDH1. *Cancer Res* **2010,** *70* (22), 8981-7.

26. van Lith, S. A.; Navis, A. C.; Verrijp, K.; Niclou, S. P.; Bjerkvig, R.; Wesseling, P.; Tops, B.; Molenaar, R.; van Noorden, C. J.; Leenders, W. P., Glutamate as chemotactic fuel for diffuse glioma cells: Are they glutamate suckers? *Biochim. Biophys. Acta* **2014,** *1846* (1), 66-74.

27. van Lith, S. A.; Molenaar, R.; van Noorden, C. J.; Leenders, W. P., Tumor cells in search for glutamate: an alternative explanation for increased invasiveness of IDH1 mutant gliomas. *Neuro Oncol* **2014**.

28. Claes, A.; Schuuring, J.; Boots-Sprenger, S.; Hendriks-Cornelissen, S.; Dekkers, M.; van der Kogel, A. J.; Leenders, W. P.; Wesseling, P.; Jeuken, J. W., Phenotypic and genotypic characterization of

orthotopic human glioma models and its relevance for the study of anti-glioma therapy. *Brain Pathol* **2008,** *18* (3), 423-33.

29. Navis, A. C.; Bourgonje, A.; Wesseling, P.; Wright, A.; Hendriks, W.; Verrijp, K.; van der Laak, J. A.; Heerschap, A.; Leenders, W. P., Effects of dual targeting of tumor cells and stroma in human glioblastoma xenografts with a tyrosine kinase inhibitor against c-MET and VEGFR2. *PloS one* **2013,** *8* (3), e58262.

30. Navis, A. C.; van Lith, S. A.; van Duijnhoven, S. M.; de Pooter, M.; Yetkin-Arik, B.; Wesseling, P.; Hendriks, W. J.; Venselaar, H.; Timmer, M.; van Cleef, P.; van Bergen En Henegouwen, P.; Best, M. G.; Wurdinger, T. D.; Tops, B. B.; Leenders, W. P., Identification of a novel MET mutation in high-grade glioma resulting in an auto-active intracellular protein. *Acta Neuropathol* **2015,** *130* (1), 131-44.

31. Claes, A.; Leenders, W., Vessel normalization by VEGF inhibition. *Cancer Biol Ther* **2008,** *7* (7), 7.

32. Claes, A.; Wesseling, P.; Jeuken, J.; Maass, C.; Heerschap, A.; Leenders, W. P., Antiangiogenic compounds interfere with chemotherapy of brain tumors due to vessel normalization. *Mol Cancer Ther* **2008,** *7* (1), 71-8.

33. Navis, A. C.; Hamans, B. C.; Claes, A.; Heerschap, A.; Jeuken, J. W.; Wesseling, P.; Leenders, W. P., Effects of targeting the VEGF and PDGF pathways in diffuse orthotopic glioma models. *J Pathol* **2011,** *223* (5), 626-34.

34. Hamans, B.; Navis, A. C.; Wright, A.; Wesseling, P.; Heerschap, A.; Leenders, W., Multivoxel 1H MR spectroscopy is superior to contrast-enhanced MRI for response assessment after anti-angiogenic treatment of orthotopic human glioma xenografts and provides handles for metabolic targeting. *Neuro Oncol* **2013,** *15* (12), 1615-1624.

35. Lee, P.; Colman, R. F., Implication by site-directed mutagenesis of Arg314 and Tyr316 in the coenzyme site of pig mitochondrial NADP-dependent isocitrate dehydrogenase. *Arch. Biochem. Biophys.* **2002,** *401* (1), 81-90.

36. Navis, A. C.; Niclou, S. P.; Fack, F.; Stieber, D.; van Lith, S.; Verrijp, K.; Wright, A.; Stauber, J.; Tops, B.; Otte-Holler, I.; Wevers, R.; van Rooij, A.; Pusch, S.; Von Deimling, A.; Tigchelaar, W.; Van Noorden, C. J.; Wesseling, P.; Leenders, W., Increased mitochondrial activity in a novel IDH1-R132H mutant human oligodendroglioma xenograft model: in situ detection of 2-HG and α-KG. *Acta Neuropathol Comm* **2013,** *1*, 18.

37. Pusch, S.; Schweizer, L.; Beck, A. C.; Lehmler, J. M.; Weissert, S.; Balss, J.; Miller, A. K.; von Deimling, A., D-2-Hydroxyglutarate producing neo-enzymatic activity inversely correlates with frequency of the type of isocitrate dehydrogenase 1 mutations found in glioma. *Acta Neuropathol Commun* **2014,** *2*, 19.

38. Loenarz, C.; Schofield, C. J., Expanding chemical biology of 2-oxoglutarate oxygenases. *Nature chemical biology* **2008,** *4* (3), 152-6.

39. Rodriguez-Arnedo, A.; Camacho, M.; Llorca, F.; Bonete, M. J., Complete reversal of coenzyme specificity of isocitrate dehydrogenase from Haloferax volcanii. *The protein journal* **2005,** *24* (5), 259-66.

40. Navis, A. C.; van Lith, S. A.; van Duijnhoven, S. M.; de Pooter, M.; Yetkin-Arik, B.; Wesseling, P.; Hendriks, W. J.; Venselaar, H.; Timmer, M.; van Cleef, P.; van Bergen En Henegouwen, P.; Best, M. G.; Wurdinger, T. D.; Tops, B. B.; Leenders, W. P., Identification of a novel MET mutation in high-grade glioma resulting in an auto-active intracellular protein. *Acta Neuropathol* **2015**.

41. van Horssen, R.; Willemse, M.; Haeger, A.; Attanasio, F.; Guneri, T.; Schwab, A.; Stock, C. M.; Buccione, R.; Fransen, J. A.; Wieringa, B., Intracellular NAD(H) levels control motility and invasion of glioma cells. *Cellular and molecular life sciences : CMLS* **2013,** *70* (12), 2175-90.

42. Krieger, E.; Koraimann, G.; Vriend, G., Increasing the precision of comparative models with YASARA NOVA--a self-parameterizing force field. *Proteins* **2002,** *47* (3), 393-402.

43. Vriend, G., WHAT IF: a molecular modeling and drug design program. *Journal of molecular graphics* **1990,** *8* (1), 52-6, 29.

44. Esmaeili, M.; Hamans, B. C.; Navis, A. C.; van Horssen, R.; Bathen, T. F.; Gribbestad, I. S.; Leenders, W. P.; Heerschap, A., IDH1 R132H mutation generates a distinct phospholipid metabolite profile in glioma. *Cancer Res* **2014,** *74* (17), 4898-907.

CHAPTER 3

Differences in cellular metabolism of renal cell carcinoma cell lines translate into differential sensitivity to metabolic inhibitors

Sanne A.M. van Lith[1], Krissie Lenting[2], Niels Kramer[1], Luuk Swanenberg[1], Paul N. Span[3], Egbert Oosterwijk[4], William P.J. Leenders[2]

[1]Department of Pathology, Radboud Institute for Molecular Life Sciences, Radboudumc, Nijmegen, The Netherlands
[2]Department of Biochemistry, Radboud Institute for Molecular Life Sciences, Radboudumc, Nijmegen, The Netherlands
[3]Department of Radiation Oncology, Radiotherapy & Oncoimmunology laboratory, Radboudumc, Nijmegen, The Netherlands
[4]Department of Urology, Radboud Institute for Molecular Life Sciences, Radboudumc, Nijmegen, The Netherlands

ABSTRACT

In approximately 80% of clear cell renal cell carcinomas (ccRCCs) the *von Hippel-Lindau* (*VHL*) tumor suppressor gene is mutated or silenced, resulting in stabilization of hypoxia inducible transcription factors- (HIF) 1α and/or 2α. This results in gene expression profiles that stimulate use of glucose for aerobic glycolysis and lactate production, rather than for synthesis of citrate in the tricarboxylic acid cycle (TCA). To accommodate the demand of growing cells for citrate, a precursor of fatty acids and membranes, VHL-defective ccRCC cells feed the TCA cycle with glutamine, a process that is mediated primarily via HIF-2α. Additionally, sustained growth requires synthesis of nucleic acid precursors and NADPH in the pentose phosphate pathway (PPP). We hypothesize that altered metabolism in RCC may provide handles for (adjuvant) therapies with metabolic inhibitors.

We investigated the cellular metabolism of VHL-impaired ccRCC cell lines SKRC-17 and SKRC-7 with differential HIF-1α and HIF-2α activity by carbon source depletion studies, measurement of oxygen consumption rates, and RNA sequencing. Furthermore we exposed the cells to metabolic inhibitors epigallocatechin-3-gallate (EGCG) and 6-aminonicotinamide (6-AN), and determined the effect on proliferation and sensitivity to radiotherapy.

Both SKRC-7 and SKRC-17 cells could still proliferate, albeit slower, upon depletion of D-glucose. Only SKRC-17 cells were fully dependent on L-glutamine for cell proliferation, and this was accompanied by increased sensitivity to EGCG and 6-AN. Furthermore EGCG sensitized only SKRC-17 cells to ionizing radiation.

We show that SKRC-7 cells and SKRC-17 cells display marked differences in metabolism that translate into differential sensitivity to the metabolic inhibitors. These data show a potential role for EGCG as (adjuvant) therapy in ccRCC, however the mechanism of action should be unraveled further to select subgroups of ccRCC patients that could benefit from this therapy.

INTRODUCTION

Clear cell renal cell carcinoma (ccRCC) represents the most common subtype of RCC[1]. In approximately 80% of these cancers the *von Hippel-Lindau* (*VHL*) tumor suppressor gene is inactivated by mutations or gene silencing[2-3]. Under normoxic conditions pVHL forms a multi-protein complex with E3-ubiquitin ligase that targets prolyl-hydroxylated hypoxia-inducible factors HIF-1α and HIF-2α for ubiquitin mediated degradation[4]. Under hypoxia HIF1/2α cannot be hydroxylated, leading to stabilization and accumulation of these transcription factors. The same events occur under normoxic conditions if VHL function is compromised[5]. This results in ccRCC transcriptional profiles that are normally seen under hypoxia, including elevated expression levels of genes involved in angiogenesis, regulation of apoptosis and metabolism[2 6-7].

Activation of the HIF-1 pathway equips the cells with a specific set of enzymatic machineries that favor aerobic glycolysis over the mitochondrial tricarboxylic acid (TCA) cycle. Increased uptake of glucose and its phosphorylation to glucose-6-phosphate leads to an increased flux through the pentose phosphate pathway (PPP)[8]. The PPP provides the cell with NADPH, the most important form of reducing power in cells and an intermediate in lipid synthesis, and additionally produces ribose-5-phosphate (R5P), a precursor of nucleotides[8]. Since oxidative glucose metabolism is inhibited in RCC cells[9], they are reliant on alternative carbon sources for fatty acids and lipid synthesis. The glutamine-glutamate pathway is one of the important anaplerotic pathways in VHL-mutated cancers[10]. Increased dependency on pathways like the PPP and glutamine metabolism translates into increased sensitivity to metabolic inhibitors of enzymes in these pathways[8,11]. Furthermore, the metabolic phenotype of RCC is correlated to disease prognosis, both on transcriptome level, where low activity of TCA genes[12] in combination with high activity of PPP genes[13] correlates with poor survival, as on metabolome level, where high levels of metabolites related to the biosynthesis of glutathione correlates with poor survival[14].

The differential roles of HIF-1α and HIF-2α in ccRCC development and progression is receiving increasing interest. Both proteins are highly similar in structure, but HIF-1α expression is ubiquitous in hypoxic cells whereas HIF-2α expression is restricted to few organs among which the kidney[15]. In ccRCC differential expression of HIF-1α and HIF-2α may be observed as HIF-1α can be lost during progression to higher disease stages[16]. Whereas HIF-1α and HIF-2α share some target genes, they have differential effects on cell metabolism: HIF-1α stimulates glycolysis and restrains mitochondrial pyruvate consumption[17-19], while HIF-2α promotes reductive carboxylation of α-KG to isocitrate, rendering cells dependent on glutamine for proliferation[10].

Unraveling the metabolic pathways that cancer cells have adopted to facilitate malignant behavior is of high importance, since these may be appropriate targets for (adjuvant) therapy. Inhibition of tumor-specific metabolic pathways may impair cell growth or interfere with the capacity of cells to maintain redox potential, overriding the insensitivity of these cancers to

3

radiotherapy or chemotherapy. Here we investigated the metabolism of two ccRCC cell lines carrying endogenous non-sense mutations in *VHL*. These cells have differential HIF expression (SKRC-17 expresses HIF-2α and SKRC-7 expresses HIF-1α and HIF-2α)[20-21]. Furthermore, we investigated sensitivity of these cell lines to metabolic inhibitors epigallocatechin-3-gallate (EGCG, an inhibitor of glutamate dehydrogenase and other NADP$^+$-dependent enzymes) and 6 aminonicotinamide (6-AN, an inhibitor of the PPP-enzyme G6PD).

RESULTS

The metabolic phenotype of SKRC-7 and SKRC-17

Previous research has shown that in VHL-deficient RCC aerobic glycolysis is enhanced, and glucose oxidation in the TCA is mitigated. Glutaminolysis is an important salvage pathway to supply the TCA with α-KG and to maintain Acetyl-CoA and lipid production in VHL deficient cells, a prerequisite for membrane production during cell division[10,22]. First, we determined dependency of SKRC-7 and SKRC-17 on D-glucose and L-glutamine for cell proliferation. Deprivation of either D-glucose or L-glutamine restricted proliferation of SKRC-7 cells significantly with 44% or 33%, respectively (Figure 1A, left graph).
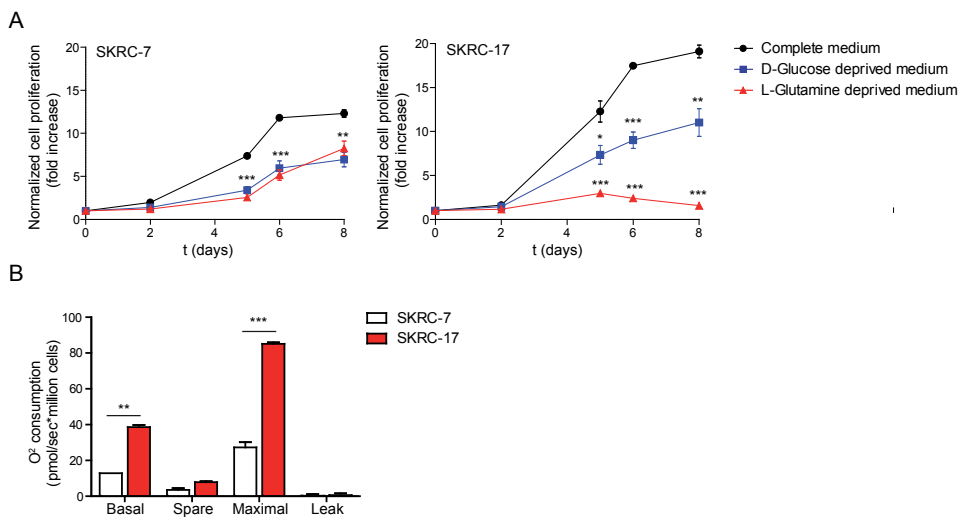

Figure 1. Cell proliferation in complete medium or medium without L-glutamine or D- glucose as determined with a SRB assay (A). Basal and maximal mitochondrial oxygen consumption in all cell types was measured with the Oroboros (B). * $p < 0.05$, ** $p < 0.01$, *** $p < 0.001$.

In SKRC-17, D-glucose deprivation also inhibited cell proliferation with 43%, while L-Glutamine deprivation completely inhibited growth of these cells (Figure 1A, right graph). Of note, the proliferation rate of SKRC-17 in glucose and glutamine proficient medium was higher than of SKRC-7 cells and this was accompanied by a 3-fold higher basal and maximal oxygen consumption by SKRC-17 cells (Figure 1B).

Effect of metabolic inhibitors on cell proliferation and radiosensitivity

The dependency on glutamine for mitochondrial anaplerosis is expected to make VHL-deficient RCC cells sensitive to inhibitors of glutamine processing enzymes[10]. Epigallo-catechin-3-gallate (EGCG), a polyphenol compound that is extracted from green tea, is an inhibitor of NADP+-dependent enzymes glucose-6-phosphate dehydrogenase (G6PDH; the rate limiting enzyme in the PPP)[23], and glutamate dehydrogenase (GLUD; converting glutamate to α-KG). SKRC-17 was more sensitive to EGCG with an IC50 concentration of 10.55 μM compared to 28.77 μM for SKRC-7. This was reflected in proliferation assays, where 10 μm EGCG significantly inhibited proliferation of SKRC-17 cells with 20%, but not that of SKRC-7 (Figure 2A). Strikingly, while lower concentrations of EGCG (5 μM) had no effect on proliferation rates of SKRC-17, it induced a 22% increase in cell proliferation of SKRC-7. Similar observations were made for 6-AN. IC50 concentrations of 18.02 μM were observed for SKRC-7 and 1.76 μM for SKRC-17. 6-AN significantly inhibited proliferation of SKRC-17 at both 1 μM and 10 μM with 18.4% and 87.4%, respectively, while 1 μM 6-AN induced cell proliferation of SKRC-7 with 22.1% (Figure 2B).
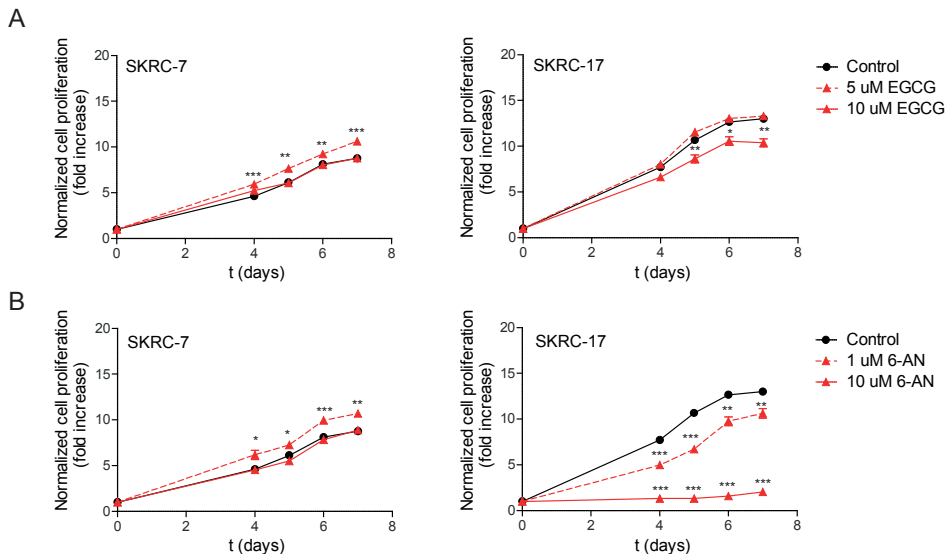

Figure 2. Effects on cell proliferation of EGCG (A) and 6-AN (B) as determined in SRB assays. * p < 0.05, ** p < 0.001, *** p < 0.001.

Inhibition of NADP+-dependent enzymes is expected to result in decreased cellular NADPH levels, and inhibition of glutamine metabolism is expected to impair glutathione (GSH) synthesis. Altogether this is expected to result in diminished reductive potential of the cells. To investigate this, we tested the effects of EGCG treatment on the capacity of cells to scavenge reactive oxygen species (ROS). In line with the proposed hypothesis, 24 hours of EGCG treatment reduced the capacity of SKRC-17 cells to protect against H_2O_2 (Figure 3A). In contrast, EGCG increased the capacity of SKRC-7 cells to neutralize ROS.
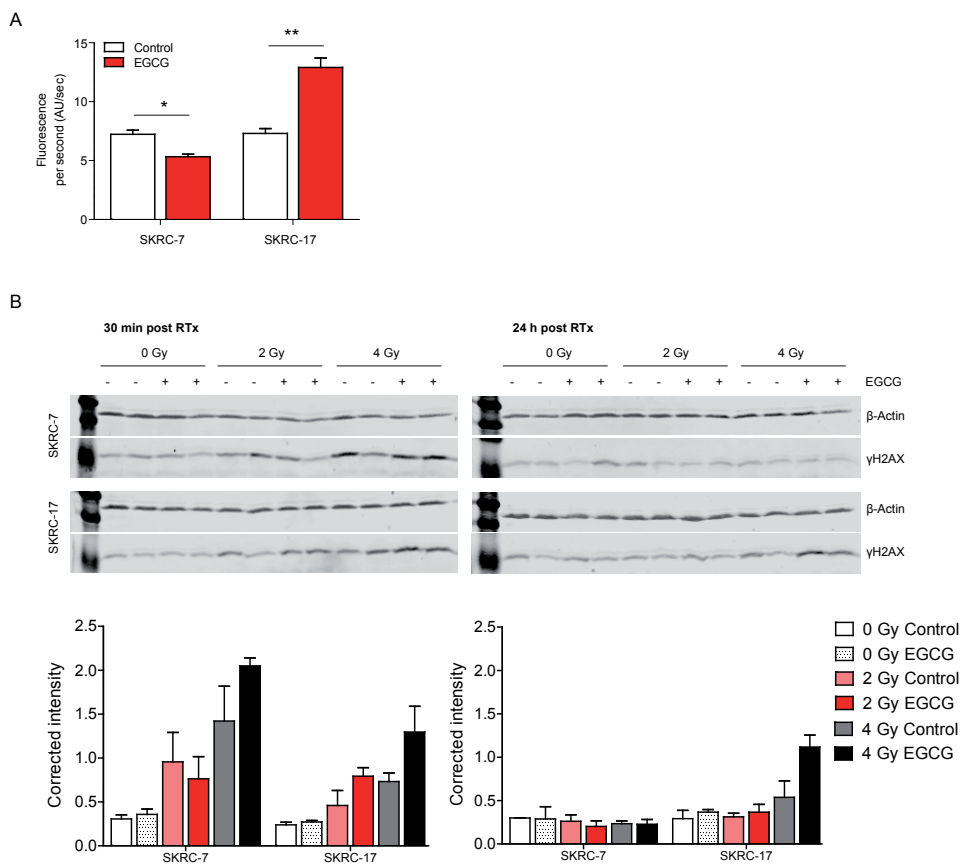
Figure 3. A) Effects of 10 μM EGCG on ROS-scavenging capacity of H_2O_2- treated SKRC7 an SKRC17 cells. ROS formation was determined by measuring CM-H_2DCFDA induced fluorescence. B) DNA double strand breaks induced 30 min (left) or 24 hrs (right) after irradiation with 0, 2 or 4 Gy in presence or absence of 10 μM EGCG as detected with western blot stained for γH2AX. Expression is corrected for β-actin expression. * p < 0.05, ** p < 0.01.

The decreased capacity of SKRC-17 cells to scavenge ROS after EGCG treatment implies increased sensitivity of these cells to radiation therapy (RTx). In line with this, EGCG treatment increased initial DNA damage (30 min after RTx) and residual DNA damage (24 hrs after RTx) in SKRC-17 cells upon irradiation with 2 and 4 Gy (Figure 3B). EGCG did not consistently alter initial irradiation-induced DNA damage in SKRC-7 cells. Residual DNA damage was absent in SKRC-7 cells, suggesting higher DNA damage repair capacity in this cell line than in SKRC-17 cells (Figure 3B).

Relation between metabolic phenotype and sensitivity to inhibitors with gene expression of metabolic pathways

To explore differences in gene expression that can explain the metabolic phenotype and the differential sensitivities of SKRC-7 and SKRC-17 cells to EGCG and 6-AN, we performed gene set enrichment analysis (GSEA, using the Kyoto Encyclopedia of Genes and Genomes) to identify possibly relevant metabolic pathways in both cell lines. Significantly enriched metabolic pathways are listed in Table 1. One of the top listings in pathways enriched in SKRC-17 compared to SKRC-7 was 'oxidative phosphorylation', corroborating our finding of high oxygen consumption in SKRC-17. Furthermore, in SKRC-17 the gene sets 'pentose phosphate pathway' and 'purine and pyrimidine metabolism' were significantly enriched compared to SKRC-7. In SKRC-7, 'glycolysis and gluconeogenesis' and 'pyruvate metabolism' pathways were most significantly enriched compared to SKRC-17.

3

Table 1. GSEA of pathways that are enriched in SKRC-7 compared to SKRC-17 and vice versa. GSEA was run on genes using KEGG pathways as a geneset. The enrichment score (ES), Normalized enrichment score (NES), Nominal P-value (NOM p-val) and False Discovery Rate q-value (FDR q-val), using http:// software.broadinstitute.org/gsea/index.jsp. An FDR value of 0.1 was chosen as a cutoff to identify significantly upregulated pathways.

Enriched in SKRC-17 compared to SKRC-7

Name of pathway	# genes in pathway	ES	NES	NOM p-val	FDR q-val
OXIDATIVE PHOSPHORYLATION	115	-0.379	-4.791.779	0.0	<0.0001
PURINE METABOLISM	155	-0.292	-41.392.727	0.0	<0.0001
N GLYCAN BIOSYNTHESIS	46	-0.513	-40.980.806	0.0	<0.0001
GLYCOSAMINOGLYCAN BIOSYNTHESIS HEPARAN SULFATE	26	-0.523	-32.705.708	0.0	<0.0001
PYRIMIDINE METABOLISM	96	-0.264	-3.078.896	0.0	<0.0001
SELENOAMINO ACID METABOLISM	26	-0.496	-29.956.176	0.0	<0.0001
AMINO SUGAR AND NUCLEOTIDE SUGAR METABOLISM	44	-0.385	-29.713.745	0.0	0.0001
ARGININE AND PROLINE METABOLISM	53	-0.262	-22.265.048	0.0018	0.0019
CYSTEINE AND METHIONINE METABOLISM	34	-0.286	-201.192	0.0059	0.0065
BIOSYNTHESIS OF UNSATURATED FATTY ACIDS	22	-0.339	-19.078.964	0.0061	0.0117
OTHER GLYCAN DEGRADATION	16	-0.383	-18.811.492	0.0079	0.0132
SPHINGOLIPID METABOLISM	40	-0.247	-18.714.112	0.0040	0.0140
HISTIDINE METABOLISM	28	-0.258	-16.304.612	0.0338	0.0425
PENTOSE PHOSPHATE PATHWAY	26	-0.245	-15.040.808	0.0562	0.0726
FATTY ACID METABOLISM	42	-0.193	-14.870.046	0.0730	0.0775
NITROGEN METABOLISM	23	-0.249	-14.447.575	0.0864	0.0929

Enriched in SKRC-7 compared to SKRC-17

Name of pathway	# genes in pathway	ES	NES	NOM p-val	FDR q-val
GLYCOLYSIS GLUCONEOGENESIS	61	0.330	2959917	0.0	<0.0001
ARACHIDONIC ACID METABOLISM	58	0.314	27.986.128	0.0	<0.0001
GLYCOSPHINGOLIPID BIOSYNTHESIS LACTO AND NEOLACTO SERIES	26	0.394	24.064.589	0.0	0.0012
BUTANOATE METABOLISM	34	0.352	24.026.713	0.0	0.0011
GLUTATHIONE METABOLISM	50	0.238	2018984	0.0020	0.0090
PYRUVATE METABOLISM	39	0.243	18042277	0.0100	0.0227
ONE CARBON POOL BY FOLATE	17	0.340	17.081.867	0.0163	0.0352
GLYCINE SERINE AND THREONINE METABOLISM	31	0.275	1808924	0.0164	0.0227
FRUCTOSE AND MANNOSE METABOLISM	34	0.237	16287769	0.0293	0.0494
NICOTINATE AND NICOTINAMIDE METABOLISM	22	0.283	15995301	0.0398	0.0552
STARCH AND SUCROSE METABOLISM	52	0.183	15702217	0.0482	0.0606
GALACTOSE METABOLISM	26	0.246	15214988	0.0624	0.0719
PHENYLALANINE METABOLISM	18	0.292	15213037	0.0647	0.0705

DISCUSSION

For patients with localized or locally advanced ccRCC, surgical resection followed by observation is the current standard of care[24], however up to 30% of these patients will develop metastases[25]. Patients with metastatic disease are candidate for surgical resection and local therapy after multidisciplinary review, or they are treated first-line with agents targeting the VEGF (e.g. sunitinib, bevacizumab, pazopanib, sorafenib) or mTOR (e.g. temsirolimus) pathways[24]. Though these systemic therapies can provide significantly increased progression free survival, most patients develop treatment resistance and therefore effects on long-term response or survival are rarely induced[26]. Both effective neo-adjuvant treatment options and treatment options for metastatic disease are therefore a major unmet clinical need. When considering RCC as a metabolic disease, characterized by enhanced glycolysis, decreased glucose oxidation and increased reductive metabolism of glutamine[9,17-19], this could provide alternative targets for therapy. In this work we analyzed the metabolism of two different RCC cell lines, SKRC-7 and SKRC-17, and we determined if altered metabolic pathways provide handles for (adjuvant) therapy with metabolic inhibitors.

Relative to SKRC-7 cells, SKRC-17 cells presented with increased cellular respiration levels and proliferation rates. Both cell types were equally sensitive to glucose deprivation while only SKRC-17 cells showed an absolute requirement for glutamine for their proliferation, consistent with the observation that HIF-2 induces lipid synthesis via reductive carboxylation of glutamine derived α-KG[10]. The glutamine dependency of SKRC-17 cells was accompanied by inhibition of proliferation upon treatment with EGCG. This could be explained by several mechanisms such as impaired lipid synthesis, NADPH and GSH synthesis and inhibition of gluthathione peroxidase activity (GPX)[27]. Decreased glutamine availability due to EGCG treatment can also impair de novo pyrimidine synthesis[28], which hypothetically causes growth inhibition and DNA replication stress in SKRC-17. This potentially explains the extreme sensitivity of SKRC-17 cells to 6-AN, inhibitor of PPP, which is the main supplier of R5P, a precursor for synthesis of purine and pyrimidine. In line with this observation, RNA sequencing revealed increased expression of the genes active in the PPP and purine and pyrimidine synthesis, possibly indicating sensitivity of these cells to inhibitors of these pathways.

In sharp contrast with the findings in SKRC-17, EGCG increased proliferation and reductive potential of SKRC-7. Since EGCG affects many cellular processes, such as cell surface receptor signalling, intracellular signalling, nuclear function, mitochondrial function and autophagy[29], it is difficult to identify the exact mechanism by which changes in proliferation are induced. EGCG is also known as an anti-oxidant and induces expression of anti-oxidant enzymes such as superoxide dismutase (SOD) and catalase[30]. Increased expression of the latter enzymes could protect the cells against oxidative insults such as ROS production induced by RTx or H_2O_2, as we have observed in SKRC-7 cells. GSEA analyses indicated increased expression of the gene set 'glycolysis gluconeogenesis' in SKRC-7 when compared to SKRC-17, so it is interesting

to determine sensitivity of these cells to glycolysis inhibitors such as 3-Bromopyruvic acid or 2-Deoxy-D-glucose.

The observation that EGCG sensitized SKRC-17 cells to radiotherapy, demonstrated by increased residual DNA damage upon EGCG treatment and ionizing radiation, emphasizes the usefulness of metabolic inhibition for a synthetic lethality approach with other treatment modalities. In view of the observation that a high-gluthatione cluster corresponds to a poor-survival subgroup[14], EGCG may provide an interesting personalized treatment option for these patients, and targeted sequencing of metabolic pathways[31] could be used as a stratification tool. The opposing effects of EGCG in SKRC-7 and SKRC-17 however show that it is essential to gain more information about tumor metabolism before an upregulated general pathway like glutaminolysis can be inhibited in a clinical setting.

CONCLUSIONS

RCC cell lines SKRC-7 and SKRC-17 display marked differences in metabolism that translate into differential sensitivity to the metabolic inhibitors EGCG and 6-AN. Furthermore these data show a potential role for EGCG as (adjuvant) therapy in ccRCC, however the mechanism of action should be investigated further to select the subtype of RCC that is sensitive to this therapy.

METHODS

Cell culture
Cell lines SKRC-7 and SKRC-17 carrying endogenous non-sense mutations in *VHL*[31-32] were cultured in RPMI 1640 medium (Lonza Group, Switzerland) supplemented with 10% fetal calf serum (FCS) (Gibco, Thermo Fisher Scientific, Waltham, MA, USA) and 40 µg/ml gentamycin (Centrafarm, Etten-Leur, The Netherlands).

Cell proliferation assays
To determine the sensitivity of cells to glutamine or glucose deprivation, cells were seeded at 1,000 cells per well in 96-wells plates (Nunc, Roskilde, Denmark) in standard medium. After one day medium was substituted for D-glucose depleted (0 g/L D-glucose/ 4 g/L L-glutamine), L-glutamine depleted (5 g/L D-glucose/ 0 g/L L-glutamine) or regular RPMI medium (5 g/L D-glucose/4 g/L L-glutamine), supplemented with 10% FCS and antibiotics. At different periods of culture, protein contents were measured with sulforhodamine blue (SRB) assays[33] as a measure of cell proliferation.

Epigallocatechin-3-gallate (EGCG) and 6-aminonicotinamide (6-AN) were purchased from Sigma (Saint Louis, MO) and dissolved in DMSO. First the IC50 was determined for both inhibitors. 1,000 cells were seeded per well in 96-wells plates (Nunc, Roskilde, Denmark) and various concentrations of inhibitors in medium were added one day after seeding. After 3 days, protein contents were measured with SRB assays as a measure of cell proliferation. Secondly the effect of two concentrations of both compounds on cell proliferation was investigated. Inhibitors were added one day after seeding 1,000 cells per well in 96-wells plates (Nunc, Roskilde, Denmark), and protein content was determined at day 4, 5, 6 and 7. Two independent experiments were performed with internal quadruplicates, and statistical significance was determined with an unpaired Student's T test.

Cellular and mitochondrial respiration

Cells were grown to 80% confluency in culture flasks. Cells were harvested and $1.5*10^6$ cells were resuspended in culture medium and transferred to the temperature-controlled (37°C) chamber of an Oxygraph-2k equipped with Datlab recording and analysis software (Oroboros Instruments, Innsbruck, Austria). The basal respiration was recorded after which mitochondrial respiration was inhibited with 2.5 µM oligomycin (an inhibitor of complex V of the electron transport chain). Then, maximal respiration rate was measured after sequential addition of 0.5 µM trifluoromethoxy carbonylcyanide phenylhydrazone (FCCP, mitochondrial uncoupler). Subsequently 0.5 µM Rotenone (an inhibitor of complex I) and 2.5 µM complex III inhibitor Antimycin A were added to completely shut down the electron transport chain. The remaining oxygen consumption is due to non-mitochondrial respiration. Two independent experiments were performed. P-values were calculated with an unpaired Student's T test.

Quantification of ROS levels

Intracellular reactive oxygen species (ROS) levels were measured using the CM-H2DCFDA probe (Molecular probes, Eugene, OR, USA). Cells were seeded at 10,000 cells per well in black clear-bottom 96 well plates. The next day medium was replaced with medium containing 10 µM EGCG or DMSO solvent. Two days after seeding, cells were incubated with 1 µM CM-H2DCFDA in assay buffer (132 mM NaCl, 4.2 mM KCL, 1 mM $CaCl_2$, 1 mM $MgCl_2$, 5.5 mM D-glucose and 10 mM HEPES, pH 7.4) for 10 minutes at 37°C. After washing twice with warm assay buffer, 100 µM H_2O_2 in assay buffer was added to all wells, and fluorescence intensity (Ex/Em ~492-495/~517-527) was measured for 12 minutes with 12 seconds intervals on the Clariostar (BMG Labtech, Ortenberg, Germany). The experiments were performed with an internal triplicate and significance was determined with an unpaired Student's T test.

Detection of double strand DNA breaks

Cells were seeded in 6 well plates at 200,000 cells per well, treated with EGCG or DMSO control and irradiated with 2 or 4 Gy (IR, 3.1 Gy/min; XRAD 320 ix; Precision XRT; N. Brandford, CT,

USA). At 30 min and 24 hrs after irradiation, cytosolic extracts were prepared in RIPA buffer (Cell Signaling, Danvers, MA, USA). Protein concentrations were determined using the BCA kit (Thermo Fisher Scientific, Waltham, MA USA) and 25 μg of total protein was subjected to SDS-PAGE and electroblotting. Western blots were blocked with Odyssey blocking buffer and incubated with rabbit-anti-γH2AX (1:2000, Ser139; #9718, Cell Signaling, Danvers, MA, USA) and mouse-anti-β-Actin (1:1000; Santa Cruz, Dallas, TX, USA). Primary antibodies were detected with goat-anti-rabbit Alexa680 and goat-anti-rabbit Alexa800 (both 1:10.000, Invitrogen, Waltham, MA, USA) diluted in blocking buffer.

Blots were analyzed on the Odyssey scanner (LI-COR biotechnology, Lincoln, NE, USA). Signals were normalized to those for housekeeping protein β-actin. All analyses were performed in duplicate (biological replicas). Statistical significance was determined with an unpaired Student's T-test.

## Whole RNA next generation sequencing

RNA was isolated from 80% confluent SKRC-7 and SKRC-17 cells using TRIzol reagent (Life Technologies, ThermoFisher Scientific, Waltham, MA, USA) according to the manufacturers' instructions. RNA (RIN scores > 8) was subjected to whole transcriptome sequencing at the genomics core facility of the Netherlands Cancer Institute according to standard protocols. RNA was sequenced on an Illumina Hiseq (paired end sequencing protocol), yielding 30-50 million reads per sample. Data were analyzed using the 'Tuxedo' protocol; reads were mapped against the RefSeq human genome GRCh37.55 (hg19) with TopHat and final transcript assembly was done with the Cufflinks package [34]. Data were normalized with Cuffquant. Gene counts were extracted from BAM files with FeatureCount, and these were transformed to transcript per million mapped reads (TPM) to obtain relative expression values[35]. Gene Set Enrichment Analysis (GSEA) was run based on genes sorted on the ratio of their TPMs between SKRC-7 and SKRC-17. The Kyoto Encyclopedia of Genes and Genomes (KEGG) pathways were used as gene set and the analysis was run with a false discovery rate (FDR) of 0.1 and in the classic mode (http://software.broadinstitute.org/gsea/index.jsp)

REFERENCES

1. Patard, J. J.; Leray, E.; Rioux-Leclercq, N.; Cindolo, L.; Ficarra, V.; Zisman, A.; De La Taille, A.; Tostain, J.; Artibani, W.; Abbou, C. C.; Lobel, B.; Guille, F.; Chopin, D. K.; Mulders, P. F.; Wood, C. G.; Swanson, D. A.; Figlin, R. A.; Belldegrun, A. S.; Pantuck, A. J., Prognostic value of histologic subtypes in renal cell carcinoma: a multicenter experience. *Journal of clinical oncology : official journal of the American Society of Clinical Oncology* **2005,** *23* (12), 2763-71.

2. Baldewijns, M. M.; van Vlodrop, I. J.; Vermeulen, P. B.; Soetekouw, P. M.; van Engeland, M.; de Bruine, A. P., VHL and HIF signalling in renal cell carcinogenesis. *The Journal of pathology* **2010,** *221* (2), 125-38.

3. Kim, W. Y.; Kaelin, W. G., Role of VHL gene mutation in human cancer. *Journal of clinical oncology : official journal of the American Society of Clinical Oncology* **2004,** *22* (24), 4991-5004.

4. Kaelin, W. G., Jr., The von Hippel-Lindau tumor suppressor protein and clear cell renal carcinoma. *Clinical cancer research : an official journal of the American Association for Cancer Research* **2007,** *13* (2 Pt 2), 680s-684s.

5. Kim, W.; Kaelin, W. G., Jr., The von Hippel-Lindau tumor suppressor protein: new insights into oxygen sensing and cancer. *Current opinion in genetics & development* **2003,** *13* (1), 55-60.

6. Majmundar, A. J.; Wong, W. J.; Simon, M. C., Hypoxia-inducible factors and the response to hypoxic stress. *Molecular cell* **2010,** *40* (2), 294-309.

7. Semenza, G. L., HIF-1 mediates metabolic responses to intratumoral hypoxia and oncogenic mutations. *The Journal of clinical investigation* **2013,** *123* (9), 3664-71.

8. Lucarelli, G.; Galleggiante, V.; Rutigliano, M.; Sanguedolce, F.; Cagiano, S.; Bufo, P.; Lastilla, G.; Maiorano, E.; Ribatti, D.; Giglio, A.; Serino, G.; Vavallo, A.; Bettocchi, C.; Selvaggi, F. P.; Battaglia, M.; Ditonno, P., Metabolomic profile of glycolysis and the pentose phosphate pathway identifies the central role of glucose-6-phosphate dehydrogenase in clear cell-renal cell carcinoma. *Oncotarget* **2015,** *6* (15), 13371-86.

9. Metallo, C. M.; Gameiro, P. A.; Bell, E. L.; Mattaini, K. R.; Yang, J.; Hiller, K.; Jewell, C. M.; Johnson, Z. R.; Irvine, D. J.; Guarente, L.; Kelleher, J. K.; Vander Heiden, M. G.; Iliopoulos, O.; Stephanopoulos, G., Reductive glutamine metabolism by IDH1 mediates lipogenesis under hypoxia. *Nature* **2011,** *481* (7381), 380-4.

10. Gameiro, P. A.; Yang, J.; Metelo, A. M.; Perez-Carro, R.; Baker, R.; Wang, Z.; Arreola, A.; Rathmell, W. K.; Olumi, A.; Lopez-Larrubia, P.; Stephanopoulos, G.; Iliopoulos, O., In vivo HIF-mediated reductive carboxylation is regulated by citrate levels and sensitizes VHL-deficient cells to glutamine deprivation. *Cell metabolism* **2013,** *17* (3), 372-85.

11. Abu Aboud, O.; Habib, S. L.; Trott, J.; Stewart, B.; Liang, S.; Chaudhari, A. J.; Sutcliffe, J.; Weiss, R. H., Glutamine Addiction in Kidney Cancer Suppresses Oxidative Stress and Can Be Exploited for Real-Time Imaging. *Cancer Res* **2017,** *77* (23), 6746-6758.

12. Ricketts, C. J.; De Cubas, A. A.; Fan, H.; Smith, C. C.; Lang, M.; Reznik, E.; Bowlby, R.; Gibb, E. A.; Akbani, R.; Beroukhim, R.; Bottaro, D. P.; Choueiri, T. K.; Gibbs, R. A.; Godwin, A. K.; Haake, S.; Hakimi, A. A.; Henske, E. P.; Hsieh, J. J.; Ho, T. H.; Kanchi, R. S.; Krishnan, B.; Kwiatkowski, D. J.; Lui, W.; Merino, M. J.; Mills, G. B.; Myers, J.; Nickerson, M. L.; Reuter, V. E.; Schmidt, L. S.; Shelley, C. S.; Shen, H.; Shuch, B.; Signoretti, S.; Srinivasan, R.; Tamboli, P.; Thomas, G.; Vincent, B. G.; Vocke, C. D.; Wheeler, D. A.; Yang, L.; Kim, W. Y.; Robertson, A. G.; Cancer Genome Atlas Research, N.; Spellman, P. T.; Rathmell, W. K.; Linehan, W. M., The Cancer Genome Atlas Comprehensive Molecular Characterization of Renal Cell Carcinoma. *Cell Rep* **2018,** *23* (12), 3698.

13. Cancer Genome Atlas Research, N., Comprehensive molecular characterization of clear cell renal cell carcinoma. *Nature* **2013,** *499* (7456), 43-9.

14. Hakimi, A. A.; Reznik, E.; Lee, C. H.; Creighton, C. J.; Brannon, A. R.; Luna, A.; Aksoy, B. A.; Liu, E. M.; Shen, R.; Lee, W.; Chen, Y.; Stirdivant, S. M.; Russo, P.; Chen, Y. B.; Tickoo, S. K.; Reuter, V. E.; Cheng,

E. H.; Sander, C.; Hsieh, J. J., An Integrated Metabolic Atlas of Clear Cell Renal Cell Carcinoma. *Cancer Cell* **2016,** *29* (1), 104-116.

15. Wiesener, M. S.; Jurgensen, J. S.; Rosenberger, C.; Scholze, C. K.; Horstrup, J. H.; Warnecke, C.; Mandriota, S.; Bechmann, I.; Frei, U. A.; Pugh, C. W.; Ratcliffe, P. J.; Bachmann, S.; Maxwell, P. H.; Eckardt, K. U., Widespread hypoxia-inducible expression of HIF-2alpha in distinct cell populations of different organs. *FASEB J.* **2003,** *17* (2), 271-3.

16. Shen, C.; Beroukhim, R.; Schumacher, S. E.; Zhou, J.; Chang, M.; Signoretti, S.; Kaelin, W. G., Jr., Genetic and functional studies implicate HIF1alpha as a 14q kidney cancer suppressor gene. *Cancer discovery* **2011,** *1* (3), 222-35.

17. Hu, C. J.; Wang, L. Y.; Chodosh, L. A.; Keith, B.; Simon, M. C., Differential roles of hypoxia-inducible factor 1alpha (HIF-1alpha) and HIF-2alpha in hypoxic gene regulation. *Molecular and cellular biology* **2003,** *23* (24), 9361-74.

18. Kim, J. W.; Tchernyshyov, I.; Semenza, G. L.; Dang, C. V., HIF-1-mediated expression of pyruvate dehydrogenase kinase: a metabolic switch required for cellular adaptation to hypoxia. *Cell metabolism* **2006,** *3* (3), 177-85.

19. Papandreou, I.; Cairns, R. A.; Fontana, L.; Lim, A. L.; Denko, N. C., HIF-1 mediates adaptation to hypoxia by actively downregulating mitochondrial oxygen consumption. *Cell metabolism* **2006,** *3* (3), 187-97.

20. Grabmaier, K.; MC, A. d. W.; Verhaegh, G. W.; Schalken, J. A.; Oosterwijk, E., Strict regulation of CAIX(G250/MN) by HIF-1alpha in clear cell renal cell carcinoma. *Oncogene* **2004,** *23* (33), 5624-31.

21. Sjolund, J.; Johansson, M.; Manna, S.; Norin, C.; Pietras, A.; Beckman, S.; Nilsson, E.; Ljungberg, B.; Axelson, H., Suppression of renal cell carcinoma growth by inhibition of Notch signaling in vitro and in vivo. *The Journal of clinical investigation* **2008,** *118* (1), 217-28.

22. Metallo, C. M.; Gameiro, P. A.; Bell, E. L.; Mattaini, K. R.; Yang, J.; Hiller, K.; Jewell, C. M.; Johnson, Z. R.; Irvine, D. J.; Guarente, L.; Kelleher, J. K.; Vander Heiden, M. G.; Iliopoulos, O.; Stephanopoulos, G., Reductive glutamine metabolism by IDH1 mediates lipogenesis under hypoxia. *Nature* **2012,** *481* (7381), 380-4.

23. Shin, E. S.; Park, J.; Shin, J. M.; Cho, D.; Cho, S. Y.; Shin, D. W.; Ham, M.; Kim, J. B.; Lee, T. R., Catechin gallates are NADP+-competitive inhibitors of glucose-6-phosphate dehydrogenase and other enzymes that employ NADP+ as a coenzyme. *Bioorg. Med. Chem.* **2008,** *16* (7), 3580-6.

24. Escudier, B.; Porta, C.; Schmidinger, M.; Rioux-Leclercq, N.; Bex, A.; Khoo, V.; Gruenvald, V.; Horwich, A.; Committee, E. G., Renal cell carcinoma: ESMO Clinical Practice Guidelines for diagnosis, treatment and follow-up. *Ann Oncol* **2016,** *27* (suppl 5), v58-v68.

25. Herout, R.; Graff, J.; Borkowetz, A.; Zastrow, S.; Leike, S.; Koch, R.; Draeger, D. L.; Protzel, C.; Hakenberg, O. W.; Wirth, M. P.; Froehner, M., Surgical resection of locally recurrent renal cell carcinoma after nephrectomy: Oncological outcome and predictors of survival. *Urol Oncol* **2018,** *36* (1), 11 e1-11 e6.

26. Rini, B. I.; Atkins, M. B., Resistance to targeted therapy in renal-cell carcinoma. *Lancet Oncol* **2009,** *10* (10), 992-1000.

27. Miess, H.; Dankworth, B.; Gouw, A. M.; Rosenfeldt, M.; Schmitz, W.; Jiang, M.; Saunders, B.; Howell, M.; Downward, J.; Felsher, D. W.; Peck, B.; Schulze, A., The glutathione redox system is essential to prevent ferroptosis caused by impaired lipid metabolism in clear cell renal cell carcinoma. *Oncogene* **2018**.

28. Okazaki, A.; Gameiro, P. A.; Christodoulou, D.; Laviollette, L.; Schneider, M.; Chaves, F.; Stemmer-Rachamimov, A.; Yazinski, S. A.; Lee, R.; Stephanopoulos, G.; Zou, L.; Iliopoulos, O., Glutaminase and poly(ADP-ribose) polymerase inhibitors suppress pyrimidine synthesis and VHL-deficient renal cancers. *The Journal of clinical investigation* **2017,** *127* (5), 1631-1645.

29. Lambert, J. D.; Elias, R. J., The antioxidant and pro-oxidant activities of green tea polyphenols: a role in cancer prevention. *Arch. Biochem. Biophys.* **2010,** *501* (1), 65-72.

30. Kim, H. S.; Quon, M. J.; Kim, J. A., New insights into the mechanisms of polyphenols beyond antioxidant properties; lessons from the green tea polyphenol, epigallocatechin 3-gallate. *Redox Biol* **2014,** *2*, 187-95.

31. de Bitter, T.; van de Water, C.; van den Heuvel, C.; Zeelen, C.; Eijkelenboom, A.; Tops, B.; Oosterwijk, E.; Kolev, D.; Mulders, P.; Ter Laan, M.; van Lith, S.; Leenders, W., Profiling of the metabolic transcriptome via single molecule molecular inversion probes. *Scientific reports* **2017,** *7* (1), 11402.

32. Ebert, T.; Bander, N. H.; Finstad, C. L.; Ramsawak, R. D.; Old, L. J., Establishment and characterization of human renal cancer and normal kidney cell lines. *Cancer Res* **1990,** *50* (17), 5531-6.

33. Skehan, P.; Storeng, R.; Scudiero, D.; Monks, A.; McMahon, J.; Vistica, D.; Warren, J. T.; Bokesch, H.; Kenney, S.; Boyd, M. R., New colorimetric cytotoxicity assay for anticancer-drug screening. *Journal of the National Cancer Institute* **1990,** *82* (13), 1107-12.

34. Trapnell, C.; Roberts, A.; Goff, L.; Pertea, G.; Kim, D.; Kelley, D. R.; Pimentel, H.; Salzberg, S. L.; Rinn, J. L.; Pachter, L., Differential gene and transcript expression analysis of RNA-seq experiments with TopHat and Cufflinks. *Nat Protoc* **2012,** *7* (3), 562-78.

35. Botman, D.; Tigchelaar, W.; Van Noorden, C. J., Determination of phosphate-activated glutaminase activity and its kinetics in mouse tissues using metabolic mapping (quantitative enzyme histochemistry). *J. Histochem. Cytochem.* **2014,** *62* (11), 813-26.

3
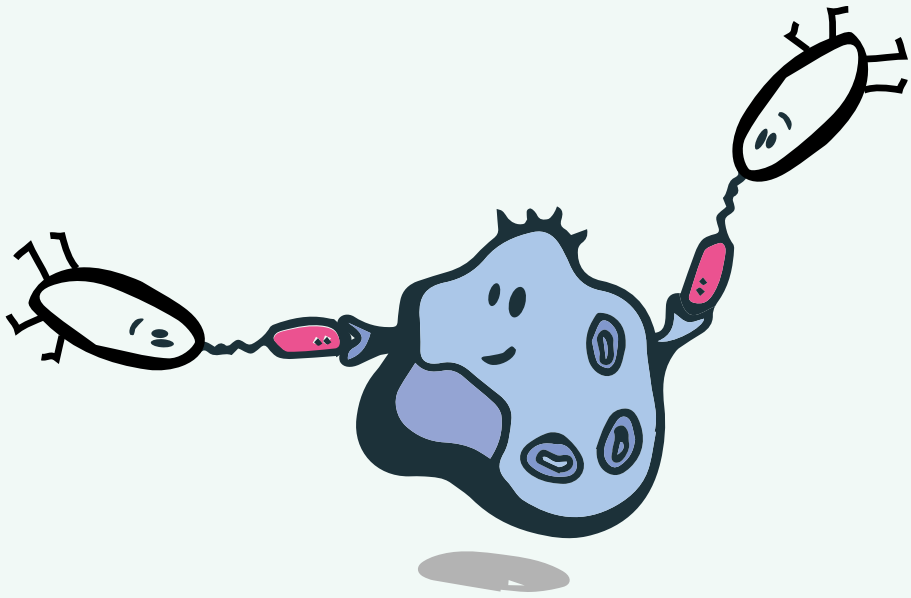
CHAPTER 4

In vivo phage display screening for tumor vascular targets in glioblastoma identifies a llama VHH against dynactin-1-p150[Glued]

Sanne A.M. van Lith[1*], Ilse Roodink[1,5*], Joost J.C. Verhoeff[2], Petri I Mäkinen[3], Jari P. Lappalainen[3], Seppo Ylä-Herttuala[3,4], Jos Raats[5], Erwin van Wijk[6], Ronald Roepman[7], Stef J. Letteboer[7], Kiek Verrijp[1] and William P.J. Leenders[1]

*Authors contributed equally

[1]Department of Pathology, Radboud Institute for Molecular Life Sciences, Radboudumc, Nijmegen, The Netherlands
[2]Department of Radiotherapy, AMC, Amsterdam, The Netherlands
[3]Department of Biotechnology and Molecular Medicine, University of Eastern Finland, Kuopio, Finland
[4]Science Service Center and Gene Therapy Unit, Kuopio University Hospital, Kuopio, Finland.
[5]Modiquest BV, LSP Oss, The Netherlands
[6]Department of Otorhinolaryngology, Radboudumc, Nijmegen, The Netherlands
[7]Department of Genetics, Radboudumc, Nijmegen,The Netherlands

ABSTRACT

Diffuse gliomas are primary brain cancers that are characterised by infiltrative growth. Whereas high-grade glioma characteristically presents with perinecrotic neovascularisation, large tumor areas thrive on pre-existent vasculature as well. Clinical studies have revealed that pharmacological inhibition of the angiogenic process does not improve survival of glioblastoma patients. Direct targeting of tumor vessels may however still be an interesting therapeutic approach as it allows pinching off the blood supply to tumor cells. Such tumor vessel targeting requires the identification of tumor-specific vascular targeting agents (TVTAs).

Here we describe a novel TVTA, C-C7, which we identified via *in vivo* biopanning of a llama VHH phage display library in an orthotopic mouse model of diffuse glioma. We show that C-C7 recognizes a subpopulation of tumor blood vessels in glioma xenografts and clinical glioma samples. Additionally, C-C7 recognizes macrophages and activated endothelial cells in atherosclerotic lesions. By using C-C7 as bait in yeast-2-hybrid screens we identified dynactin-1-p150^{Glued} as its binding partner. The interaction was confirmed by co-immunostainings with C-C7 and a commercial anti-dynactin-1-p150^{Glued} antibody, and via co-immunoprecipitation/western blot studies. Normal brain vessels do not express dynactin-1-p150^{Glued} and its expression is reduced under anti-VEGF therapy, suggesting that dynactin-1-p150^{Glued} is a marker for activated endothelial cells.

In conclusion, we show that *in vivo* phage display combined with Y2H screenings provides a powerful approach to identify tumor-targeting VHHs and their binding partners. Using this combination of methods we identify dynactin-1-p150^{Glued} as a novel targetable protein on activated endothelial cells and macrophages.

INTRODUCTION

In order to grow and disseminate, tumors depend on an adequate blood supply[1-2]. Based on the assumption that tumors arrange their own blood supply via induction of angiogenesis, in the last decade angiogenesis inhibitors (e.g. the anti-VEGF-A antibody bevacizumab or VEGFR2-specific tyrosine kinase inhibitors) have been widely implemented in clinical practice for a number of tumor types[3-4]. Effects of anti-angiogenesis (mostly in combination with chemotherapy) are however mostly transient[5-6] and cancer patients who undergo anti-angiogenic treatment mostly experience recurrences, one possible cause being that tumors adopt an invasive phenotype to accommodate their metabolic needs[7-10]. Resistance to anti-angiogenic treatment may also be related to heterogeneity of the tumor vasculature. Vessel formation in cancer is a multistep process and consequently cancers contain neovessels in different stages of development[11-12]. Because endothelial cells in matured vessels are less dependent on VEGF-VEGFR2 signalling, these are also more refractory to VEGF inhibition[13].

Vessel heterogeneity is especially prominent in glioblastoma, a highly malignant brain tumor of glial origin[14]. One hallmark of glioblastoma is the presence of large areas of diffuse infiltrative growth in which tumor cells thrive on pre-existent vessels (co-option) without the need for angiogenesis[15-16]. Another characteristic of glioblastoma is focal angiogenesis in the vicinity of areas of necrosis, and this has been rationale for preclinical and clinical testing of anti-VEGF therapy for recurrent and primary diagnosed glioblastoma. Such studies have shown effective inhibition of angiogenesis, however without preventing tumor progression in areas of diffuse infiltrative growth[17-19]. This growth pattern thus provides tumors with a route of escape from anti-angiogenic therapies[5,20-21] and recent clinical trials confirmed a lack of prolonged survival of glioblastoma patients upon treatment with bevacizumab[22-23].

An alternative approach to deprive cancers from blood is direct anti-vascular therapy that aims at tumor-specific thrombosis and infarction. Such an approach requires that tumor vascular targeting agents (TVTAs) are developed with high enough specificity for tumor vasculature. Available TVTAs (e.g. RGD peptides or cilengitide, targeting endothelial $\alpha v \beta 3$ integrin[24-25], the L19 single chain antibody that targets the ED-B fragment of fibronectin[26], anti-V-CAM antibodies[27], anti-plexinD1 antibodies[28]) are directed against newly formed vessels and do not target tumor vessels in more matured stages of development.

Biopanning of peptide or single chain-antibody phage display libraries is a powerful technique that allows identification and isolation of tumor endothelium binding partners[29-32]. VHHs (*Variable Heavy* chain domains of *Heavy* chain antibodies or Nanobodies®) are recombinant antibodies, cloned from cameloid IgG2 and IgG3 heavy chain-only antibodies (V-H) and consist of a single polypeptide chain, making this class of antibodies suitable for display on phages without significant loss of affinity[33-34]. Their small size (15-18 kDa) and stability make VHHs to an attractive class of diagnostic and therapeutic compounds[35]. VHH against epidermal

growth factor receptor (EGFR) or carcinoembryonic antigen (CEA) have already successfully been used for *in vivo* diagnosis and therapy[36-38].

In a search for novel relevant VHH-based TVTAs we performed *in vivo* biopannings with a VHH phage display library[29]. As a tumor model we utilized mice carrying orthotopic E98 human glioma xenografts that characteristically display both angiogenesis-dependent growth and diffuse infiltrative growth[18,39]. We identified a novel VHH, C-C7, that targets a subpopulation of tumor blood vessels. Using C-C7 as a bait protein in yeast-2-hybrid screens we identified dynactin-1-p150[Glued] as its binding partner.

RESULTS

In vivo selection of tumor vessel binding phages in cerebral E98 xenografts

A VHH-displaying phage library[28] was intravenously injected in mice carrying intracerebral E98 xenografts and irrelevant phages were removed from the circulation by cardiac perfusion. We chose to use mice carrying orthotopic E98 xenografts because these tumors display both areas of angiogenesis and diffuse infiltrative growth[39]. Similarly to our previous work using different tumor xenograft models and other phage libraries[29], anti-M13 immunostainings demonstrated already a tumor-specific vessel localization of phages after the first round of biopanning (Figure 1, compare the anti-M13 immunostaining in panel A to the endothelial cell CD34 staining in panel B). After collection of tumor areas from brain sections by laser
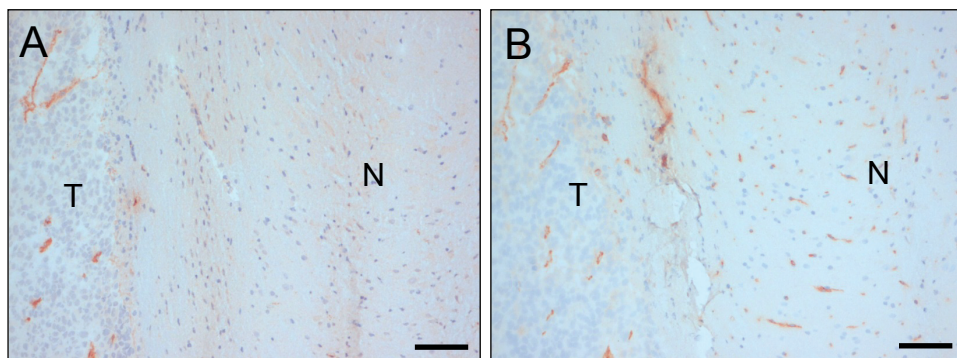

Figure 1. *In vivo* biopanning of a Llama phage library in an animal model of orthotopic glioma. Anti-M13-p8 (A) and anti-CD34 (B) immunostainings of sections of E98 xenografts in mouse brain after intravenous injection of 10^{12} phages of the VHH-phage display library, and cardiac perfusion. Note that phages are associated with tumor vasculature, but to a lesser extent with blood vessels in normal brain. N = normal, T = tumor. Bars correspond to 100 μm.

capture dissection microscopy and subsequent trypsin treatment, a total of 453 colony-forming phages was rescued of which 192 clones were randomly picked and analysed for full length VHH expression and diversity. Dot blot analysis revealed that 95% of clones expressed VHH and restriction enzyme finger print analysis resulted in five different restriction patterns (not shown). As there is some chance of VHH clones with similar restriction patterns being different on the nucleotide level, we arbitrarily chose to analyze from each group the 30% of clones with highest VHH expression levels.

Immunohistochemistry

Immunohistochemical stainings were performed on sections of intracerebral E98 xenografts to select for VHHs that specifically recognize tumor vessels. Because interpretation of staining of delicate capillaries requires optimal morphology, we chose to perform immunostainings on sections of FFPE-tissue blocks instead of cryosections, and accepted that potentially interesting VHH (recognizing conformational epitopes that are disrupted during formalin fixation) could be lost during analyses. Positive staining of blood vessels was observed with 27 of the 39 analyzed VHH of which 10 were not tumor-specific. The remaining 17 VHHs stained subsets of tumor vessels. Of these, VHH C-C7 showed most prominent staining of tumor vasculature in E98 xenografts and was analyzed in more detail. C-C7 stained both small and medium-sized tumor vessels in the diffuse infiltrative component of E98 xenografts[39-40] (Figure 2A). Interestingly, not all tumor associated vessels were recognized (compare the C-C7 staining pattern with the anti-CD34 staining of the serial sections in the inset in Figure 2A). VHH C-C7 did not stain normal vasculature in mouse brain (Figure 2B). The observation that C-C7 stained only a subpopulation of tumor vessels prompted us to further characterize C-C7 by immunohistochemistry in other mouse tumor models. VHH C-C7 showed delicate staining of the vasculature in colorectal cancer xenografts (Figure 3). Interestingly, blood vessels in angiogenic brain metastases of the human melanoma cell line Mel57-VEGF$_{165}$[41] were homogeneously positive (see representative example in Figure 2C) while staining was absent in Mel57-VEGF$_{165}$ tumors after treatment with the VEGFR2 inhibitor vandetanib[42] (Figure 2D). This suggests that C-C7 recognizes VEGF-activated endothelial cells.
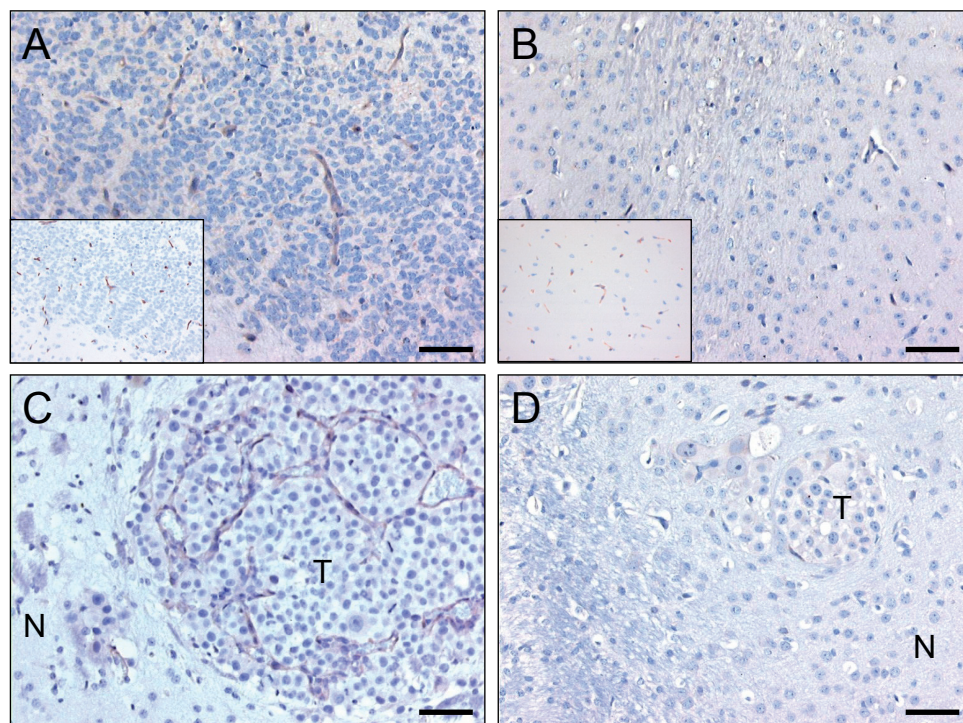
Figure 2. C-C7 recognizes tumor vessels in glioma xenografts and brain metastasis. Immunohistochemical analysis of VHH C-C7 in a diffuse-invasive part of cerebral E98 xenografts (A), normal mouse brain parenchyma (B), a representative brain metastasis of Mel57-VEGF$_{165}$ melanoma (C) and a Mel57-VEGF-A xenograft after treatment with the VEGFR2 inhibitor vandetanib[42] (D). C-C7 recognizes subsets of tumor vessels in cerebral E98 lesions, while normal mouse brain vessels are negative. Insets in A and B show CD34 immunostainings of serial sections. Note that inhibition of VEGFR2 activity in panel D results in loss of C-C7 reactivity. N = normal, T = tumor. Bars correspond to 50 μm.

To investigate whether VHH C-C7 might have clinical relevance, we performed immunostainings on 9 clinical glioblastoma samples as well as normal human brain tissue. Subpopulations of tumor vessels in most glioma tissues stained positive for C-C7 (see representative examples in Figure 4A-E) while C-C7 did not stain vasculature in normal human brain (inset in Figure 4A). In this set only one grade II glioma did not show any immunoreactivity towards C-C7 (Figure 4D). Of interest, paired glioma samples collected before and after avastin treatment[21], showed that vascular expression of the C-C7 ligand was absent after anti-angiogenic treatment (compare Figure 4E and F).
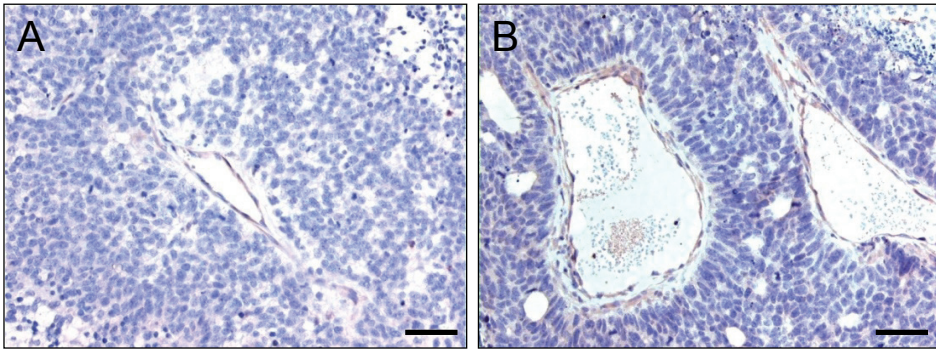
Figure 3. C-C7 recognizes tumor vessels in colon carcinoma xenografts. Immunohistochemical analysis shows that C-C7 recognizes vasculature in subcutaneous colorectal cancer xenografts C26 (A) and C38 (B). Bars correspond to 50 μm.
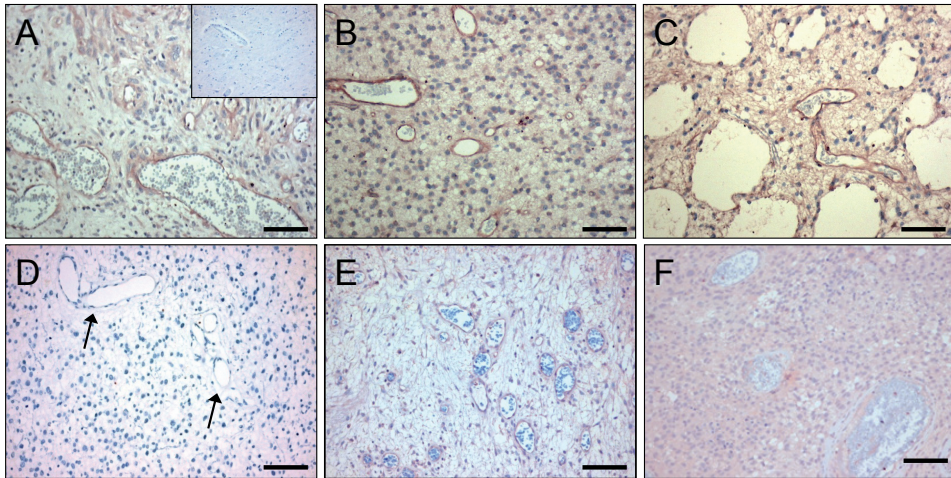
4

Figure 4. C-C7 recognizes tumor vessels in human glioblastoma multiforme. Subsets of vessels in human glioma are strongly positive for C-C7 (A-C,E). Panels E and F represent a paired primary and recurrent tumor from a patient before (E) and after (F) treatment with bevacizumab and temozolomide. Note the absence of C-C7 reactivity on vasculature a low grade glioma (D) (arrow). The inset in panel A illustrates absence of C-C7 reactivity in the vasculature of normal brain. Bars in A-C correspond to 50 μm, in panels D-F 100 μm.

Vessel activation is not exclusive for cancers but also occurs in a number of other pathologies, e.g. atherosclerosis. Also in atherosclerotic lesions obtained from human carotid artery we observed CC7 immunostaining of endothelial cells, but also prominent staining of macrophages (compare C-C7 stainings in Figure 5A,D to CD68 stainings in Figure 5B,E and the CD31 staining in Figure 5C). Staining with anti-dynactin-1-p150Glued (Figure 5F, see later for identification of dynactin-1-p150Glued as the C-C7 target) showed clear colocalization with C-C7 (compare D and F).
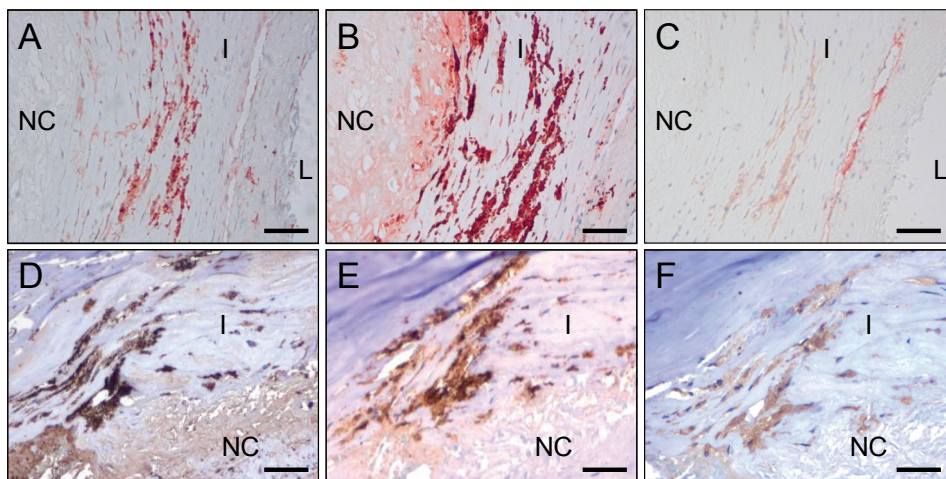
Figure 5. C-C7 recognizes blood vessels and macrophages in human atherosclerosis. Immunostainings on areas of surgical samples of atherosclerotic lesions from carotid arteries, immunostained with CC7 (A,D) the macrophage marker CD68 (B,E) and the endothelial marker CD31 (C) and anti-dynactin-1 (F, the anti-dynactin-1 antibody was implemented in this staining based on identification of dynactin-1-p150^{Glued} as a binding partner of C-C7). A-C and D-F represent serial sections from two different leisons. Note the similarity in staining profiles for C-C7 and dynactin-1-p150^{Glued} (D and F, respectively). Tissues in A-C were stained with AEC, tissues in D-F with DAB. NC = nectrotic core, I = intima, L = lumen. Bars correspond to 100 µM in panels A-C and to 50 µm in panels D-F.

To further investigate whether macrophage staining could be reproduced, we stained *in vitro* differentiated mouse HoxB8 macrophages with C-C7 and anti-dynactin-1-p150^{Glued}. Both antibodies showed similar staining profiles. Control VHH A9 did not stain these cells (Figure 6).
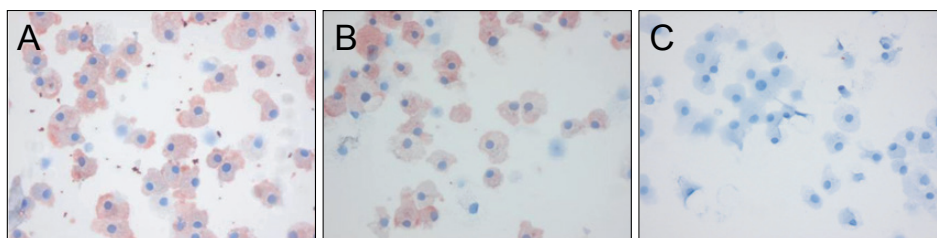

Figure 6. C-C7 recognizes dynactin-1 epitopes on macrophages. Immunostainings with C-C7 (A), anti-dynactin-1-p150^{Glued} antibody (B) and an irrelevant control VHH A9 (C) on differentiated HoxB8 mouse macrophages. Note the similarity in staining profiles of C-C7 and dynactin-1 stainings.

C-C7 can be used for targeting of cancer and atherosclerosis

C-C7 was isolated from an *in vivo* biopanning experiment after intravenous injection, suggesting that it recognizes epitopes that are accessible to circulating VHHs. To confirm the ability of C-C7 to target tumor vasculature, we injected monoclonal C-C7-phages in mice carrying orthotopic E98 xenografts, using the *in vivo* biopanning protocol which was used for its selection. C-C7-phages accumulated in subsets of vessels in E98 xenografts, but not in normal brain blood vessels (compare the phage localization in Figure 7A and C with the anti-CD34 staining of serial sections in Figure 7B and D). Control phages did not show specific tumor vessel localization, although some aspecific extravasation from leaky vessels was detected (data not shown). Similar experiments in LDLR$^{-/-}$ ApoB$^{100/100}$ mice carrying atherosclerotic lesions showed prominent homing of C-C7-phages to luminal endothelium, intraplaque neovasculature and macrophages (Figure 7E). C-C7-phages colocalized with dynactin-1-p150^{Glued} as shown by immunostainings (compare panels 7E and 7F).

C-C7 recognizes the carboxyterminal domain of dynactin-1-p150^{Glued}

Since endothelial proteins are greatly underrepresented in tumor extracts, we argued that a proteomic approach to identify the C-C7 ligand would be unlikely to succeed. Therefore we decided to use VHH C-C7 as bait protein in a Y2H screen against a large yeast expression library, using histidine (HIS3), adenine and β-galactosidase (LacZ) as reporter genes[43]. Three independent clones were identified from these screens which represented the carboxyterminal part of the p150^{Glued} subunit of dynactin-1. Clones C-C7-INT1 and C-C7-INT3 were composed of the carboxyterminal 432 amino acids of p150^{Glued} (aa 808-1240) and included 150 nucleotides of the 3′-untranslated region, while clone C-C7-INT2 spanned aa 890-1238 of the p150^{Glued} sequence (Figure 8A). A comparison of bovine dynactin-1-p150^{Glued} with the human homologue revealed 96% sequence identity in this region (not shown).

To confirm the interaction between C-C7 and human dynactin-1-p150^{Glued}, the region encompassing aa 816-1278 (human numbering) was RT-PCR-cloned from human glioblastoma tissue and transiently expressed in COS-1 cells. Confocal microscopy of transfected cells, co-stained with VHH C-C7 (visualized using FITC) and anti-dynactin-1 (visualized using TRITC) showed that both antibodies co-localized to cytoplasmic vesicular structures (Figure 8B). Non-transfected cells did not stain with both antibodies (see Figure 8C).
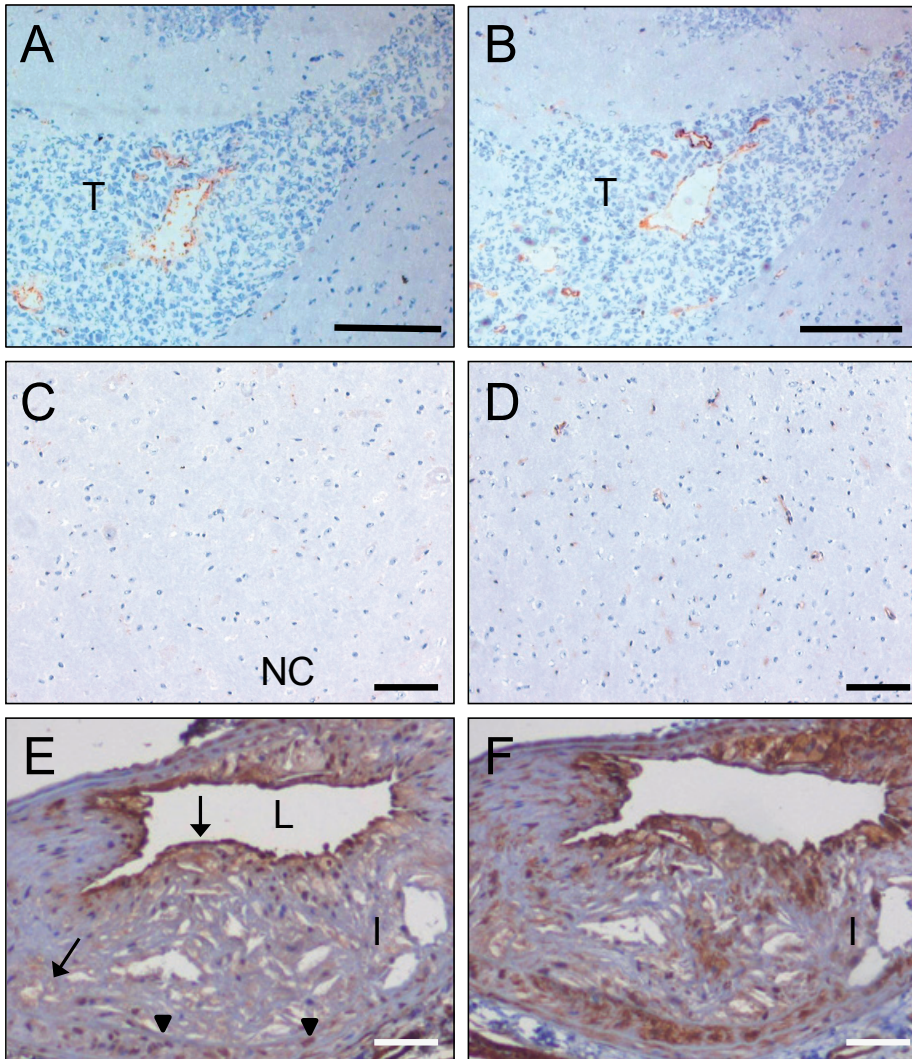
Figure 7. *In vivo* targeting of glioma xenografts and atherosclerotic lesions by C-C7-displaying M13 phages. Monoclonal C-C7 phages were injected intravenously in mice carrying orthotopic E98 xenografts and phage distribution was analyzed by M13-p8 immunostaining after cardiac perfusion (A). A serial section was stained with CD34 to highlight vasculature (B). Phages displaying C-C7 home to a subpopulation of tumor vessels in E98 xenografts. Phages do not accumulate in normal vasculature in non-affected brain parts, as illustrated by M13-p8 (C) and CD31 (D) immunostainings. E) M13-p8 immunostaining of atherosclerotic lesions of LDLR^{-/-} ApoB[100/100] mice after an *in vivo* biodistribution experiment. Note that C-C7-phages home to luminal endothelium, intraplaque neovasculature (arrows) and macrophages (arrowheads). The M13-p8 immunostaining colocalizes with anti-Dynactin-1 immunostaining (F). T= tumor, I = intima, L = lumen. Bars in panels A,B correspond to 100 µm, in panels C-F: 50 µm
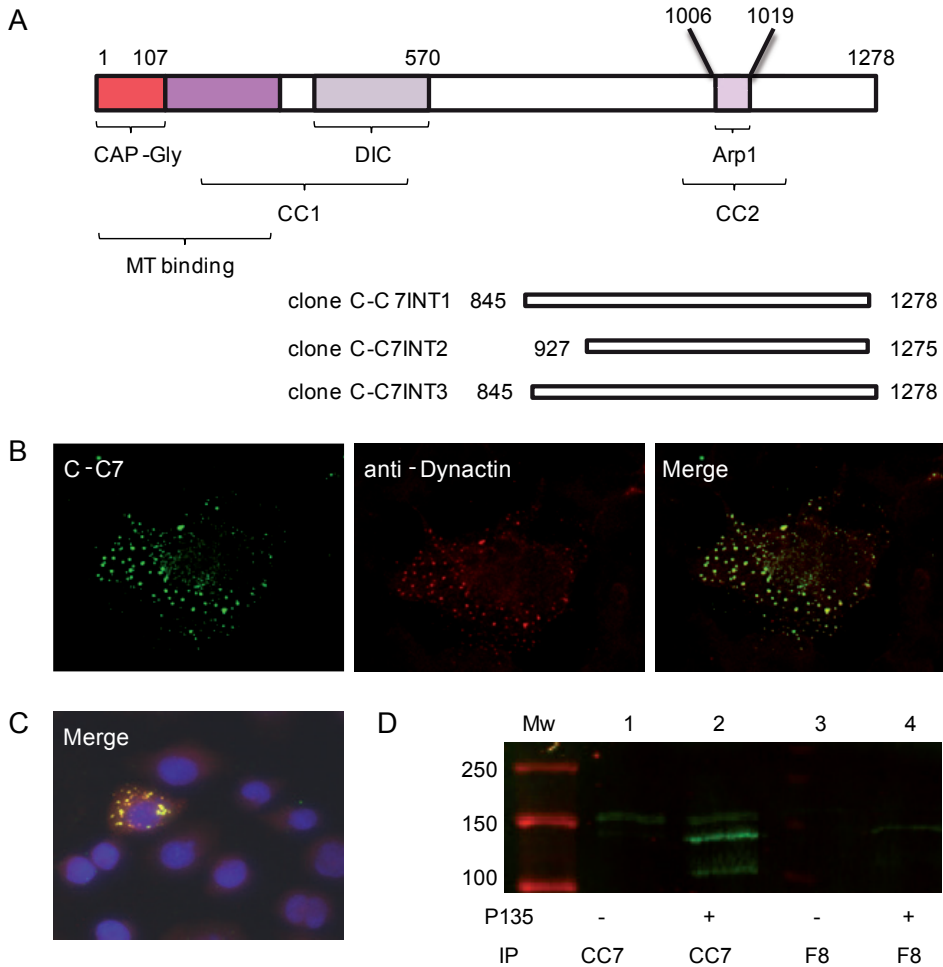
Figure 8. Dynactin-1-p150^{Glued} is identified as a C-C7 binding partner by a yeast-2-hybrid screen. Structural domains of dynactin-1-p150^{Glued} and p150 domains identified by yeast-2-hybrid screens as C-C7 interactants (A). The aminoterminal domain contains a CAP-Gly domain and a coiled-coil domain which are responsible for microtubule (MT) binding and dynein binding (DIC = dynein intermediate chain). A second coiled-coil domain (CC2), encompassing a binding site for Arp1, is present in the carboxyterminal part of the protein and mediates binding to membrane components. Confocal microscopy showed colocalization of C-C7 (green) and commercial anti-dynactin-1-p150^{Glued} (red) in COS-1 cells, transfected with the recombinant carboxyterminal domain of dynactin-1-p150^{Glued} (B). Non-transfected cells did not stain with both antibodies (C, see negative DAPI-stained cells surrounding one transfected cell in this panel). C-C7 immunoprecipitates from extracts from CHO-s cells transfected with recombinant p135^{Glued} were analyzed on western blot using commercial anti-dynactin-1-p150^{Glued} as indicated (D). Note that p135 is readily precipitated by C-C7 (lane 2) but not by an irrelevant VHH F8 (lane 4).

C-C7 specifically precipitates p150 ^{Glued} and recombinant p135 ^{Glued}

Because colocalization of C-C7 with commercial antibodies as shown in figure 8B and 8C formally does not exclude indirect interactions with other proteins than p150 ^{Glued} in the same vesicular structures, we wanted to further validate binding via immunoprecipitation. Under the conditions of cell lysis used in our experiments, the majority of carboxyterminal p150 ^{Glued} 816-1278 protein ended up in the pellet fraction (data not shown). As this problem did not occur with the P135-isoform of P150 ^{Glued44} we performed immunoprecipitation on extracts of P135-overexpressing CHO-s cells. P135 differs from p150 only in the N-terminal region, and hence contains the binding sites for both C-C7 and the commercial antibody. Furthermore, this variant can be readily distinguished from endogenous p150 ^{Glued} based on molecular weight. Figure 8D shows effective precipitation of p135 by C-C7 but not by irrelevant VHH F8. Also, small amounts of endogenous p150 ^{Glued} were precipitated. In summary, these results confirm binding of C-C7 to p150 ^{Glued} and indicate that it is not an artefact of the Y2H screen.

To further validate that p150 ^{Glued} is expressed in tumor vasculature we performed immunostainings on clinical glioma samples with a commercially available rabbit anti-dynactin-1-p150 ^{Glued} antibody. In all tumors examined this antibody gave a similar staining profile as VHH C-C7 (see figure 9A and B respectively, note that these figures contain serial sections of the tissues presented in the C-C7 stainings in Figure 4E and 4F). Normal brain vasculature did not stain with anti-dynactin although positivity could be found on neurons, consistent with literature data[44] (Figure 9C).
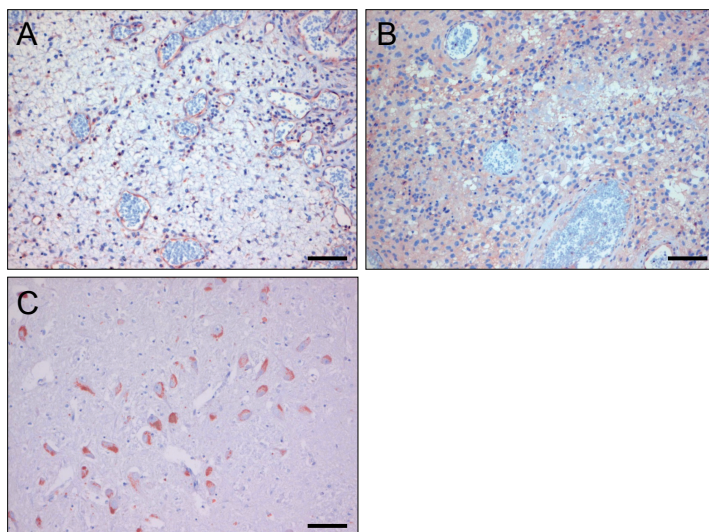

Figure 9. Immunostaining with anti-dynactin-1 of human glioblastoma before (A) and after bevacizumab treatment (B). Note the similarity with C-C7 immunostainings in Figure 3E and F. Panel C shows an anti-dynactin staining of normal brain, showing positive neurons, confirming literature data. Bars correspond to 100 μm.

DISCUSSION

In human tumors the vasculature is in general highly heterogeneous with glioblastomas as a prime example[45-46]. The diffuse infiltrative growth of human gliomas and the relatively undisturbed blood-brain barrier in these areas contribute to their poor response to surgery and radio- and chemotherapy[14,47]. Gliomas do not adequately respond to anti-angiogenic therapies either[16,21-23,48] which is likely a consequence of angiogenesis-independent progression of diffusely infiltrating tumor cells. Therefore, a strategy of tumor-vessel targeting aiming at the induction of tumor infarctions is worth investigating. To this end (combinations of) targeting agents that specifically and selectively recognize tumor vasculature are needed.

Here we employed *in vivo* biopanning of a VHH phage display library in the E98 orthotopic mouse model of diffuse glioma[19,39]. This approach resulted in the isolation of a set of VHH of which 44% specifically recognized tumor blood vessels, indicating tumor-specific enrichment already during one round of biopanning.. Presumably during the *in vivo* selection procedure, phages that bind to the surplus of common epitopes on quiescent endothelial cells in the circulation are competitively depleted, enriching for tumor-vessel specific binders in the tumor tissue. *In vivo* biopanning of phage display libraries therefore appears to be a relatively quick and efficient method to identify tumor targeting VHH.

In this study we concentrated on VHH C-C7 because it proved to be the most suitable for immunostainings on formalin-fixed tissues. In line with the complexity of neovascularization and the resulting molecular heterogeneity of tumor blood vessels, we found that C-C7 stained only a subpopulation of blood vessels in glioma xenografts and human glioma, but also neovasculature and macrophages in atherosclerotic plaques. Interestingly, C-C7 stained VEGF-A- activated endothelial cells in cerebral Mel57-VEGF-A xenografts, but not endothelial cells in blood vessels in these xenografts after treatment with the VEGFR2 inhibitor vandetanib[49]. In line, cerebral metastases of Mel57 xenografts that do not express VEGF-A and grow entirely via vessel co-option[41] also did not show vascular staining with C-C7 (not shown). This suggests that VEGF activation of endothelial cells is involved in expression of the C-C7 ligand, and this was corroborated in staining of paired surgical samples of a human glioblastoma before and after bevacizumab treatment. Of note, these data predict that tumor-vascular targeting with C-C7-like TVTAs should not be combined with anti-angiogenesis, as this would reduce the 'activation-status' of the vasculature and reduce targeting potential. Whatever the molecular underpinnings of C-C7 ligand expression, the approach of *in vivo* biopanning with VHH-phage display libraries may yield proper candidates for further development of anti-vascular therapies, e.g. by generating VHH fused to truncated tissue factor, inducing tumor-vessel specific thrombosis[27,50-51]. A similar approach has been employed using phage libraries displaying peptides[52].

Using yeast-2-hybrid screens we identified dynactin-1-p150[Glued] as the binding partner of C-C7 and we verified this interaction via co-immunostainings with VHH C-C7 and commercial anti-dynactin-1 antibodies on tumor tissues, on atherosclerotic plaque tissues and dynactin-1-

4

p150[Glued] transfected cells. Further validation came from immunoprecipitations of recombinantly expressed domains of dynactin-1-p150[Glued].

Dynactin-1-p150[Glued] is involved in vesicular trafficking along microtubules, mitotic spindle assembly, cell migration and nuclear envelope breakdown during mitosis[53-55]. Co-immunostaining of COS-1 cells transiently overexpressing the carboxyterminal part of p150[Glued], with VHH C-C7 and a commercial anti-p150[Glued] antibody showed a vesicular pattern, in agreement with a previous study on a dynactin-p150[Glued] mutant that is defective in microtubule binding[56].

Since our biopanning protocol was designed to identify tumor-vessel associated proteins that are targetable via intravenous injection, the binding of VHH C-C7 to the alleged intracellular protein p150[Glued] was unexpected. Which mechanisms are involved in extracellular presentation of dynactin-1-p150[Glued] making it accessible to intravenously administered phages, is unclear. However, a number of proteins have been shown to use non-conventional ways of trafficking in the cell[57]. Extracellular presentation of otherwise cytoplasmic or even nuclear proteins in a tumor context has been described before, examples being transglutaminase, fatty acid binding protein 3, and GRP78, although also for these targets the molecular basis for their extracellular localization is still enigmatic[52,58-61]. A possible mechanism explaining extracellular presentation of p150[Glued] involves exocytosis of dynactin-decorated vesicles via multivesicular endosomes[62-63]. After exocytosis of these vesicles, fusion with activated endothelial cells may lead to extracellular p150[Glued] presentation. This resembles the horizontal transmission of tumor targets via exosomes that has been proposed as an explanation for endothelial expression of tumor-derived EGFRvIII[64-66]. Of note, we also observed high expression of dynactin-1-p150[Glued] in macrophages in atherosclerotic lesions. Based on our immunohistochemical analyses we conclude that dynactin-1-p150[Glued] is not expressed at high levels in tumor cells. The actual source of dynactin-1-150[Glued] may therefore be activated macrophages/ microglial cells. These issues are currently under investigation.

In conclusion, *in vivo* biopanning of phage VHH-display libraries in animal models of cancer in combination with Y2H technology represents a powerful platform to identify novel TVTAs and their binding ligands. We identified C-C7 as a targeting VHH against dynactin-1-p150[Glued] in a glioma xenograft model and in a model of atherosclerosis. It remains to be seen whether this VHH can be used for therapeutic anti-vascular targeting purposes.

METHODS

Tumor models

All animal experiments were approved by the Animal Experiment Committee of the RadboudUMC. Orthotopic E98 glioma xenografts were established in 6-8 week old Balb/c nude mice by intracerebral injections of E98 tumor cell suspensions as described previously[18]. In this model mice characteristically start to display weight loss and neurological symptoms due to tumor growth 3-4 weeks after tumor implantation. When tumor-related symptoms were apparent, mice were used for *in vivo* biopanning.

In vivo biopanning

Hundred µl of phosphate buffered saline (PBS) containing 10^{12} phages of a VHH-displaying phage library (cloned from lymphocytes of non-immunized Llama glama in phagemid pHENIX-8xHis-Vsv[28]) was injected in the tail vein of nude mice, carrying cerebral E98 tumors (n=2). Phages were allowed to circulate for 15 minutes. Mice were subsequently put under deep anaesthesia with a mixture of isoflurane/N_2O and chests were opened. Cardiac perfusion was performed with 10 ml sterile 0.9% NaCl solution to remove unbound phages from the circulation. Brains were removed and snap frozen in liquid nitrogen. Sections of 4 µm were stained with anti-M13 p8 antibody (Abcam Limited, Cambridge, UK) to assess phage distribution. Using a laser dissection microscope (Leica AS LMD, Wetzlar, Germany) tumor areas were dissected from 10 µm brain sections. Phages were eluted from these sections by incubation with trypsin (10 mg/ml in PBS) for 30 min at room temperature. Following infection in 10 ml of log-phase E. coli TG1 culture, bacteria were seeded on 2xTY plates containing 100 mg/L ampicillin and 2% glucose. After overnight incubation, individual clones were picked and analyzed via colony-PCR for the presence of full-length VHH insert using flanking primers M13rev (5`-TCA CAC AGG AAA CAG CTA TGA-3`) and Fedseq3 (5`-GTA ACG ATC TAA AGT TTT GTC G-3`). Subsequently, PCR products were digested with the 4-cutter restriction enzyme BstNI (New England Biolabs, Ipswich, MA, USA) to analyze the diversity of the phage population. Small scale production of soluble VHH by independent clones was induced in log-phase TG1 cells by culturing at 30°C in 2xTY medium, containing 100 mg/L ampicillin and 1 mmol/L isopropylthiogalactoside (IPTG, Serva, Heidelberg, Germany). Expression of VHHs was verified by dot blot analysis of medium using anti-Vsv antibodies, as previously described[28]. Based on combined data of full length PCR, BstNI restriction digestion and dot blot analysis, expression of selected individual VHH was induced in 50 ml log-phase TG1 cells with 1 mM IPTG for 3 hours at 30°C. VHH were isolated from the periplasm by osmotic lysis and purified by Ni-NTA sepharose (IBA Life Sciences, Gottingen, Germany) as described previously [28].

Immunohistochemistry

VHHs were tested in immunohistochemical stainings on 4 μm sections of formalin-fixed paraffin-embedded (FFPE) tissues and tumor xenografts of different origin (intracerebral E98 xenografts; brain metastases of Mel57-VEGF$_{165}$ melanoma after treatment with vandetanib or controls[49], subcutaneous Mel57-VEGF$_{165}$ xenografts and subcutaneous xenografts of the colon carcinoma cell lines C26 and C38[67]). Human gliomas, classified by an experienced neuropathologist as grade II (n=2) and grade IV (n=7) gliomas, as well as normal brain tissue (n=2) were retrieved from the archives of the departments of Pathology of RadboudUMC and of the Academic Medical Center. GBM patients provided written informed consent, and the study was conducted in accordance with the Declaration of Helsinki and was approved by the Academic Medical Center Institutional Review Board and the Dutch Central Committee on Research investigating Human Subjects (ISRCTN23008679). Use of the other archival tissues was in accordance with institutional guide lines.

Following deparaffinization, endogenous peroxidase activity was blocked by incubation with 3% H_2O_2. Antigen retrieval was performed by boiling in 10 mmol/L citrate buffer (pH 6.0). Sections were pre-incubated with normal goat serum to block non-specific binding sites, followed by overnight incubation with 3 μM VHH in PBS/2%BSA at 4^{0}C. Detection was performed by sequential incubations with rabbit anti-Vsv-G antibody (for mouse tissues, Sigma-Aldrich Chemie B.V., Zwijndrecht, The Netherlands,) or anti-Vsv-G P5D4 (for human tissues), biotinylated anti-rabbit antibody (Vector, Burlingame, CA) and avidin-biotin peroxidase complex (Vector). Peroxidase was visualized with 3-amino-9-ethylcarbazole (AEC, ScyTek, Utah, USA) with haematoxylin as counterstain. Tumor vessels in mouse xenograft tissues were visualized in serial sections with rat-anti-mouse CD34 antibody (Hycult, Uden, The Netherlands). Rabbit antibodies against dynactin-1-p150[Glued] were from Abcam (Cambridge, UK).

C-C7 in atherosclerosis

Carotid artery atherosclerotic tissue from patients at risk for ischemic stroke was obtained from routine surgical procedures at the department of Vascular Surgery of RadboudUMC (kindly provided by Dr. J. Pol). Directly after surgery tissues were processed to FFPE blocks. Four μm sections were deparrafinized and pretreated as described, and incubated with 3 μM C-C7 in normal antibody diluent (Immunologic, Duiven, The Netherlands). Then slides were incubated with anti-VSV-G P5D4, PolyHRP-anti-Ms/Rt/Rb (Immunologic, Duiven, The Netherlands), and peroxidase was visualized with bright 3'3Diaminobenzidine (DAB) (Immunologic, Duiven, The Netherlands).

Furthermore, specificity of C-C7 was assessed by staining on mouse macrophages, obtained by differentiating ER-HoxB8 myeloid precursor cells by 25 ng/ml GM-CSF on 8-well Lab-Tek Chamber Slide™ System (Nunc, Roskilde, Denmark)[68]. Cells were fixed with 2% paraformaldehyde for 10 min, and pre-incubated with normal goat serum. Then cells were

incubated with 3 µM C-C7 or rabbit-anti-Dynactin-1-P150[Glued] in PBS/2%BSA. Detection was performed as described above in immunohistochemistry.

In another set of experiments hypercholesterolemic (low-density lipoprotein receptor (LDLR)[-/-] apolipoprotein B (ApoB) [100/100] mice[69] were subjected to high-cholesterol diet (TD 88137, Harlan Laboratories, Indianapolis, IN, USA) for 8 weeks after which a peri-adventitial collar was placed around a carotid artery. Hundred µl PBS containing 10^{12} M13-phages displaying VHH C-C7 or helper phages as control, was injected via the tail vein and allowed to circulate for 15 minutes after which a cardiac perfusion with 10 ml PBS was performed. Lesions from the carotid artery were harvested and processed to FFPE blocks, sections of which were stained with anti-M13 p8 or with anti-dynactin-pGlued[150] antibody.

Y2H screens

All cloning steps were performed using the Gateway System (Invitrogen, Carlsbad, CA). The cDNA encoding VHH C-C7 (without pelB leader) was flanked by attB sites via PCR and cloned in vector pDONR201 before transfer into destination vector pBD-GAL4-CAM/DEST, generating a C-C7 fusion protein with the GAL4 DNA binding domain. After sequence-verification this vector was transfected into yeast strain PJ69 (A-mating type) using standard protocols[43]. Generation of a randomly primed bovine retina cDNA library in pAD-GAL4, transfected in PJ69 (α-mating type, 2×10^6 clones) has been previously described[43]. The yeast strain containing pBD-GAL4-C-C7 was mated with this library and diploid cells in which C-C7-prey interactions led to functional GAL4 transcription factor, were selected based on histidine and adenine prototrophy and transactivation of ß-galactosidase activity. Production of ß-galactosidase by activation of the LacZ reporter gene was detected by a filter-lift assay[43]. From positive yeast clones, pAD-GAL4 library expression plasmids were rescued and amplified in E. coli. Plasmids were sequenced using flanking forward and reverse primers. Sequences were blasted (http://www.ncbi.nlm.nih.gov/blast/Blast.cgi) and aligned with multalin software (http://bioinfo.genotoul.fr/multalin/ multalin.html). All sequenced clones contained intact reading frames in fusion with the GAL4-activation domain.

Verification of the C-C7-dynactin-1 interaction

The carboxyterminal part of dynactin-1-p150[Glued] was RT-PCR-cloned from human glioblastoma cDNA using primers attB1-dyn 2532 (5'-AAA AAG CAG GCT TCA CCA TGG CAG CTG CTG CTG CC-3', sense) and attB2-dyn 3837 (AGA AAG CTG GGT GTT AGG AGA TGA GGC GAC TGT G-3', antisense). AttB1 and attB2 sites were extended in a second PCR and products were cloned via pDONR201 in p3xflg-CMV (Invitrogen, Carlsbad, CA, USA) to generate p3xflg-CMV-dyn 2532-3837. Plasmids were transfected into COS1 cells in 8-well glass slides (Lab-Tek Chamber Slide™ System, Nunc, Roskilde, Denmark). Forty-eight hours later, cells were fixed with ice-cold acetone and incubated with VHH C-C7 for 1 hr, followed by sequential incubations with mouse anti-Vsv and goat-anti-mouse FITC (Invitrogen, Carlsbad, CA, USA). After washing, slides

were stained with rabbit-anti-dynactin-1 which was detected with donkey-anti-rabbit TRITC (Invitrogen, Carlsbad, CA, USA). Images were processed on a Leica Discovery Fluorescence Microscope and a Leica confocal microscope.

Immunoprecipitation studies

In another set of experiments, the p135 variant of dynactin[44] was obtained via RT-PCR from glioblastoma RNA using primers P135fw-ClaI (5'-CATCGATACCATGATGAGACAGGCACC-3') and P135rev-NotI (5' CAGCGGCCGCTTAGGAGATGAGGCGACTG-3') and digested and cloned in ClaI-NotI digested pIRESneo (Clontech, Mountain View, CA). Suspension cultures of Chinese Hamster Ovary cells (CHO-s) in SFM4CHO medium with L-glutamin (ThermoFisher, Landsmeer, The Netherlands) were transfected with pIRES-Dynactin-p135 using the Amaxa Nucleofactor kit according to the manufacturer's instructions (Lonza, Cologne, Germany). Cells were harvested 48 hours later and lysates prepared in lysis buffer [50 mM Tris-HCl, pH 7.4, 1% Triton-X100, 150 mM NaCl and protease inhibitors (Complete™ protease inhibitor cocktail, Roche, Mannheim, Germany)] with untransfected CHO-s cells serving as control. Lysates were clarified at 13,000 g for 10 min at 4^0C. Dynactin-p135 expression was verified on western blot using rabbit-anti-Dynactin (AbCam Cambridge, UK).

For immunoprecipitations, periplasmic extracts of His-tagged C-C7 or irrelevant control VHH F8 were diluted five times in IPP_{500} (50 mM phosphate buffer pH 8.0, 500 mM NaCl) and incubated with Ni-NTA sepharose for 2 hours at 4°C. After washing three times with IPP_{500} and three times with IPP_{150} (50 mM phosphate buffer, pH 8.0, 150 mM NaCl) beads with immobilized C-C7 were incubated with cleared cell lysates for 2 hours at RT. Beads were washed two times with IPP_{150} incubated with 5 mM imidazole in IPP_{150} for 10 min at RT, boiled for 5 minutes in reducing sample buffer and loaded on a 7% SDS-PAGE gel for Western blot analysis with rabbit anti-Dynactin and goat anti-rabbit $IRDye_{800}$ (LI-COR, Lincoln, NE, USA) using the Odyssey infrared imaging system (LI-COR, Lincoln, NE, USA).

REFERENCES

1. Folkman, J., Angiogenesis in cancer, vascular, rheumatoid and other disease. *Nat Med* **1995,** *1* (1), 27-31.

2. Krishna Priya, S.; Nagare, R. P.; Sneha, V. S.; Sidhanth, C.; Bindhya, S.; Manasa, P.; Ganesan, T. S., Tumour angiogenesis - origin of blood vessels. *Int J Cancer* **2016**.

3. Hurwitz, H.; Fehrenbacher, L.; Novotny, W.; Cartwright, T.; Hainsworth, J.; Heim, W.; Berlin, J.; Baron, A.; Griffing, S.; Holmgren, E.; Ferrara, N.; Fyfe, G.; Rogers, B.; Ross, R.; Kabbinavar, F., Bevacizumab plus irinotecan, fluorouracil, and leucovorin for metastatic colorectal cancer. *N Engl J Med* **2004,** *350* (23), 2335-42.

4. Tirumani, S. H.; Fairchild, A.; Krajewski, K. M.; Nishino, M.; Howard, S. A.; Baheti, A. D.; Rosenthal, M. H.; Jagannathan, J. P.; Shinagare, A. B.; Ramaiya, N. H., Anti-VEGF molecular targeted therapies in common solid malignancies: comprehensive update for radiologists. *Radiographics* **2015,** *35* (2), 455-74.

5. Kerbel, R. S., Tumor angiogenesis. *N Engl J Med* **2008,** *358* (19), 2039-49.

6. Roodink, I.; Leenders, W. P., Targeted therapies of cancer: angiogenesis inhibition seems not enough. *Cancer Lett* **2010,** *299* (1), 1-10.

7. Ebos, J. M.; Lee, C. R.; Cruz-Munoz, W.; Bjarnason, G. A.; Christensen, J. G.; Kerbel, R. S., Accelerated metastasis after short-term treatment with a potent inhibitor of tumor angiogenesis. *Cancer Cell* **2009,** *15* (3), 232-9.

8. Paez-Ribes, M.; Allen, E.; Hudock, J.; Takeda, T.; Okuyama, H.; Vinals, F.; Inoue, M.; Bergers, G.; Hanahan, D.; Casanovas, O., Antiangiogenic therapy elicits malignant progression of tumors to increased local invasion and distant metastasis. *Cancer Cell* **2009,** *15* (3), 220-31.

9. Kats-Ugurlu, G.; Oosterwijk, E.; Muselaers, S.; Oosterwijk-Wakka, J.; Hulsbergen-van de Kaa, C.; de Weijert, M.; van Krieken, H.; Desar, I.; van Herpen, C.; Maass, C.; de Waal, R.; Mulders, P.; Leenders, W., Neoadjuvant sorafenib treatment of clear cell renal cell carcinoma and release of circulating tumor fragments. *Neoplasia* **2014,** *16* (3), 221-8.

10. Verhoeff, J. J.; van Tellingen, O.; Claes, A.; Stalpers, L. J.; van Linde, M. E.; Richel, D. J.; Leenders, W. P.; van Furth, W. R., Concerns about anti-angiogenic treatment in patients with glioblastoma multiforme. *BMC Cancer* **2009,** *9*, 444.

11. Jin, Y.; Kaluza, D.; Jakobsson, L., VEGF, Notch and TGFbeta/BMPs in regulation of sprouting angiogenesis and vascular patterning. *Biochem Soc Trans* **2014,** *42* (6), 1576-83.

12. Augustin, H. G.; Koh, G. Y.; Thurston, G.; Alitalo, K., Control of vascular morphogenesis and homeostasis through the angiopoietin-Tie system. *Nat Rev Mol Cell Biol* **2009,** *10* (3), 165-77.

13. Bergers, G.; Song, S.; Meyer-Morse, N.; Bergsland, E.; Hanahan, D., Benefits of targeting both pericytes and endothelial cells in the tumor vasculature with kinase inhibitors. *J Clin Invest* **2003,** *111* (9), 1287-95.

14. Wesseling, P.; Ruiter, D. J.; Burger, P. C., Angiogenesis in brain tumors; pathobiological and clinical aspects. *J Neurooncol* **1997,** *32* (3), 253-65.

15. Claes, A.; Idema, A. J.; Wesseling, P., Diffuse glioma growth: a guerilla war. *Acta Neuropathol* **2007,** *114* (5), 443-58.

16. Claes, A.; Wesseling, P.; Jeuken, J.; Maass, C.; Heerschap, A.; Leenders, W. P., Antiangiogenic compounds interfere with chemotherapy of brain tumors due to vessel normalization. *Mol Cancer Ther* **2008,** *7* (1), 71-8.

17. Norden, A. D.; Drappatz, J.; Wen, P. Y., Antiangiogenic therapy in malignant gliomas. *Curr Opin Oncol* **2008,** *20* (6), 652-61.

18. Navis, A. C.; Bourgonje, A.; Wesseling, P.; Wright, A.; Hendriks, W.; Verrijp, K.; van der Laak, J. A.; Heerschap, A.; Leenders, W. P., Effects of dual targeting of tumor cells and stroma in human

4

glioblastoma xenografts with a tyrosine kinase inhibitor against c-MET and VEGFR2. *PloS one* **2013,** *8* (3), e58262.

19. Navis, A. C.; Hamans, B. C.; Claes, A.; Heerschap, A.; Jeuken, J. W. M.; Wesseling, P.; Leenders, W. P. J., Effects of targeting the VEGF and PDGF pathways in diffuse orthotopic glioma models. *Journal of Pathology* **2011,** *223* (5), 626-634.

20. Narayana, A.; Kelly, P.; Golfinos, J.; Parker, E.; Johnson, G.; Knopp, E.; Zagzag, D.; Fischer, I.; Raza, S.; Medabalmi, P.; Eagan, P.; Gruber, M. L., Antiangiogenic therapy using bevacizumab in recurrent high-grade glioma: impact on local control and patient survival. *J Neurosurg* **2009,** *110* (1), 173-80.

21. Verhoeff, J. J.; van Tellingen, O.; Claes, A.; Stalpers, L. J.; van Linde, M. E.; Richel, D. J.; Leenders, W. P.; van Furth, W. R., Concerns about anti-angiogenic treatment in patients with glioblastoma multiforme. *BMC Cancer* **2009,** *9* (1), 444.

22. Gilbert, M. R.; Dignam, J. J.; Armstrong, T. S.; Wefel, J. S.; Blumenthal, D. T.; Vogelbaum, M. A.; Colman, H.; Chakravarti, A.; Pugh, S.; Won, M.; Jeraj, R.; Brown, P. D.; Jaeckle, K. A.; Schiff, D.; Stieber, V. W.; Brachman, D. G.; Werner-Wasik, M.; Tremont-Lukats, I. W.; Sulman, E. P.; Aldape, K. D.; Curran, W. J., Jr.; Mehta, M. P., A randomized trial of bevacizumab for newly diagnosed glioblastoma. *N Engl J Med* **2014,** *370* (8), 699-708.

23. Chinot, O. L.; Wick, W.; Mason, W.; Henriksson, R.; Saran, F.; Nishikawa, R.; Carpentier, A. F.; Hoang-Xuan, K.; Kavan, P.; Cernea, D.; Brandes, A. A.; Hilton, M.; Abrey, L.; Cloughesy, T., Bevacizumab plus radiotherapy-temozolomide for newly diagnosed glioblastoma. *N Engl J Med* **2014,** *370* (8), 709-22.

24. Holig, P.; Bach, M.; Volkel, T.; Nahde, T.; Hoffmann, S.; Muller, R.; Kontermann, R. E., Novel RGD lipopeptides for the targeting of liposomes to integrin-expressing endothelial and melanoma cells. *Protein Eng Des Sel.* **2004,** *17* (5), 433-41.

25. Tabatabai, G.; Tonn, J. C.; Stupp, R.; Weller, M., The role of integrins in glioma biology and anti-glioma therapies. *Curr Pharm Des* **2011,** *17* (23), 2402-10.

26. Palumbo, A.; Hauler, F.; Dziunycz, P.; Schwager, K.; Soltermann, A.; Pretto, F.; Alonso, C.; Hofbauer, G. F.; Boyle, R. W.; Neri, D., A chemically modified antibody mediates complete eradication of tumours by selective disruption of tumour blood vessels. *Br J Cancer* **2011,** *104* (7), 1106-15.

27. Dienst, A.; Grunow, A.; Unruh, M.; Rabausch, B.; Nor, J. E.; Fries, J. W.; Gottstein, C., Specific occlusion of murine and human tumor vasculature by VCAM-1-targeted recombinant fusion proteins. *J Natl Cancer Inst* **2005,** *97* (10), 733-47.

28. Roodink, I.; Raats, J.; van der Zwaag, B.; Verrijp, K.; Kusters, B.; van Bokhoven, H.; Linkels, M.; de Waal, R. M.; Leenders, W. P., Plexin D1 expression is induced on tumor vasculature and tumor cells: a novel target for diagnosis and therapy? *Cancer Res.* **2005,** *65* (18), 8317-23.

29. Roodink, I.; Franssen, M.; Zuidscherwoude, M.; Verrijp, K.; van der Donk, T.; Raats, J.; Leenders, W. P., Isolation of targeting VHH against co-opted tumor vasculature. *Lab Invest* **2009,** *90* (1), 61-7.

30. Kolonin, M. G.; Sun, J.; Do, K. A.; Vidal, C. I.; Ji, Y.; Baggerly, K. A.; Pasqualini, R.; Arap, W., Synchronous selection of homing peptides for multiple tissues by in vivo phage display. *Faseb J.* **2006,** *20* (7), 979-81. Epub 2006 Mar 31.

31. Rajotte, D.; Arap, W.; Hagedorn, M.; Koivunen, E.; Pasqualini, R.; Ruoslahti, E., Molecular heterogeneity of the vascular endothelium revealed by *In vivo* phage display. *J Clin Invest.* **1998,** *102* (2), 430-7.

32. Valadon, P.; Garnett, J. D.; Testa, J. E.; Bauerle, M.; Oh, P.; Schnitzer, J. E., Screening phage display libraries for organ-specific vascular immunotargeting *In vivo. Proc Natl Acad Sci U S A.* **2006,** *103* (2), 407-12. Epub 2005 Dec 29.

33. Hoogenboom, H. R., Selecting and screening recombinant antibody libraries. *Nat Biotechnol.* **2005,** *23* (9), 1105-16.

34. Rahbarizadeh, F.; Ahmadvand, D.; Sharifzadeh, Z., VHH; an old concept and new vehicle for immunotargeting. *Immunol Invest* **2011,** *40* (3), 299-338.

35. Unciti-Broceta, J. D.; Del Castillo, T.; Soriano, M.; Magez, S.; Garcia-Salcedo, J. A., Novel therapy based on camelid VHH. *Ther Deliv* **2013**, *4* (10), 1321-36.

36. Huang, L.; Gainkam, L. O.; Caveliers, V.; Vanhove, C.; Keyaerts, M.; De Baetselier, P.; Bossuyt, A.; Revets, H.; Lahoutte, T., SPECT imaging with 99mTc-labeled EGFR-specific VHH for in vivo monitoring of EGFR expression. *Mol Imaging Biol* **2008,** *10* (3), 167-75.

37. Cortez-Retamozo, V.; Backmann, N.; Senter, P. D.; Wernery, U.; De Baetselier, P.; Muyldermans, S.; Revets, H., Efficient cancer therapy with a VHH-based conjugate. *Cancer Res* **2004,** *64* (8), 2853-7.

38. van Driel, P. B.; van der Vorst, J. R.; Verbeek, F. P.; Oliveira, S.; Snoeks, T. J.; Keereweer, S.; Chan, B.; Boonstra, M. C.; Frangioni, J. V.; van Bergen en Henegouwen, P. M.; Vahrmeijer, A. L.; Lowik, C. W., Intraoperative fluorescence delineation of head and neck cancer with a fluorescent anti-epidermal growth factor receptor VHH. *Int J Cancer* **2014,** *134* (11), 2663-73.

39. Claes, A.; Schuuring, J.; Boots-Sprenger, S.; Hendriks-Cornelissen, S.; Dekkers, M.; van der Kogel, A. J.; Leenders, W. P.; Wesseling, P.; Jeuken, J. W., Phenotypic and genotypic characterization of orthotopic human glioma models and its relevance for the study of anti-glioma therapy. *Brain Pathol* **2008,** *18* (3), 423-33.

40. Navis, A. C.; Hamans, B. C.; Claes, A.; Heerschap, A.; Jeuken, J. W.; Wesseling, P.; Leenders, W. P., Effects of targeting the VEGF and PDGF pathways in diffuse orthotopic glioma models. *J Pathol* **2011,** *223* (5), 626-34.

41. Kusters, B.; de Waal, R. M.; Wesseling, P.; Verrijp, K.; Maass, C.; Heerschap, A.; Barentsz, J. O.; Sweep, F.; Ruiter, D. J.; Leenders, W. P., Differential effects of vascular endothelial growth factor A isoforms in a mouse brain metastasis model of human melanoma. *Cancer Res* **2003,** *63* (17), 5408-13.

42. Leenders, W.; Kusters, B.; Verrijp, K.; Maass, C.; Wesseling, P.; Heerschap, A.; Ruiter, D.; Ryan, A.; de Waal, R., Antiangiogenic therapy of cerebral melanoma metastases results in sustained tumor progression via vessel co-option. *Clinical Cancer Research* **2004,** *10* (18), 6222-6230.

43. Roepman, R.; Schick, D.; Ferreira, P. A., Isolation of retinal proteins that interact with retinitis pigmentosa GTPase regulator by interaction trap screen in yeast. *Methods Enzymol* **2000,** *316*, 688-704.

44. Tokito, M. K.; Howland, D. S.; Lee, V. M.; Holzbaur, E. L., Functionally distinct isoforms of dynactin are expressed in human neurons. *Mol Biol Cell* **1996,** *7* (8), 1167-80.

45. Roodink, I.; van der Laak, J.; Kusters, B.; Wesseling, P.; Verrijp, K.; de Waal, R.; Leenders, W., Development of the tumor vascular bed in response to hypoxia-induced VEGF-A differs from that in tumors with constitutive VEGF-A expression. *Int J Cancer.* **2006,** *119* (9), 2054-62.

46. Leenders, W.; Kusters, B.; De Waal, R., Vessel co-option: How tumors obtain blood supply in the absence of sprouting angiogenesis. *Endothelium* **2002,** *9*, 83-87.

47. Kleihues, P.; Louis, D. N.; Scheithauer, B. W.; Rorke, L. B.; Reifenberger, G.; Burger, P. C.; Cavenee, W. K., The WHO classification of tumors of the nervous system. *J Neuropathol Exp Neurol.* **2002,** *61* (3), 215-25; discussion 226-9.

48. van Kempen, L. C., Leenders, W. P., Tumours can adapt to anti-angiogenic therapy depending on the stromal context: lessons from endothelial cell biology. *Eur J Cell Biol* **2006,** *85* (2), 61-8.

49. Leenders, W. P.; Kusters, B.; Verrijp, K.; Maass, C.; Wesseling, P.; Heerschap, A.; Ruiter, D.; Ryan, A.; de Waal, R., Antiangiogenic therapy of cerebral melanoma metastases results in sustained tumor progression via vessel co-option. *Clin Cancer Res* **2004,** *10* (18 Pt 1), 6222-30.

50. Lv, S.; Ye, M.; Wang, X.; Li, Z.; Chen, X.; Dou, X.; Dai, Y.; Zeng, F.; Luo, L.; Wang, C.; Li, K.; Luo, X.; Yan, J.; Li, X., A recombined fusion protein SP5.2/tTF induce thrombosis in tumor blood vessel. *Neoplasma* **2015,** *62* (4), 531-40.

51. Hu, P.; Yan, J.; Sharifi, J.; Bai, T.; Khawli, L. A.; Epstein, A. L., Comparison of three different targeted tissue factor fusion proteins for inducing tumor vessel thrombosis. *Cancer Res.* **2003,** *63* (16), 5046-53.

52. Hyvonen, M.; Enback, J.; Huhtala, T.; Lammi, J.; Sihto, H.; Weisell, J.; Joensuu, H.; Rosenthal-Aizman, K.; El-Andaloussi, S.; Langel, U.; Narvanen, A.; Bergers, G.; Laakkonen, P., Novel target for peptide-based imaging and treatment of brain tumors. *Mol Cancer Ther* **2014,** *13* (4), 996-1007.

53. Schroer, T. A., Dynactin. *Annu Rev Cell Dev Biol* **2004,** *20,* 759-79.

4

54. Vaughan, K. T., Microtubule plus ends, motors, and traffic of Golgi membranes. *Biochim Biophys Acta* **2005,** *1744* (3), 316-24.

55. Li, H.; Liu, X. S.; Yang, X.; Song, B.; Wang, Y.; Liu, X., Polo-like kinase 1 phosphorylation of p150Glued facilitates nuclear envelope breakdown during prophase. *Proc Natl Acad Sci U S A* **2010,** *107* (33), 14633-8.

56. Dixit, R.; Levy, J. R.; Tokito, M.; Ligon, L. A.; Holzbaur, E. L., Regulation of dynactin through the differential expression of p150Glued isoforms. *J Biol Chem* **2008,** *283* (48), 33611-9.

57. Butler, G. S.; Overall, C. M., Proteomic identification of multitasking proteins in unexpected locations complicates drug targeting. *Nat Rev Drug Discov* **2009,** *8* (12), 935-48.

58. Roesli, C.; Borgia, B.; Schliemann, C.; Gunthert, M.; Wunderli-Allenspach, H.; Giavazzi, R.; Neri, D., Comparative analysis of the membrane proteome of closely related metastatic and nonmetastatic tumor cells. *Cancer Res* **2009,** *69* (13), 5406-14.

59. Zemskov, E. A.; Janiak, A.; Hang, J.; Waghray, A.; Belkin, A. M., The role of tissue transglutaminase in cell-matrix interactions. *Front Biosci* **2006,** *11*, 1057-76.

60. Jakobsen, C. G.; Rasmussen, N.; Laenkholm, A. V.; Ditzel, H. J., Phage display derived human monoclonal antibodies isolated by binding to the surface of live primary breast cancer cells recognize GRP78. *Cancer Res* **2007,** *67* (19), 9507-17.

61. Gonzalez-Gronow, M.; Selim, M. A.; Papalas, J.; Pizzo, S. V., GRP78: a multifunctional receptor on the cell surface. *Antioxid Redox Signal* **2009,** *11* (9), 2299-306.

62. Lo Cicero, A.; Stahl, P. D.; Raposo, G., Extracellular vesicles shuffling intercellular messages: for good or for bad. *Curr Opin Cell Biol* **2015,** *35*, 69-77.

63. Rak, J.; Guha, A., Extracellular vesicles--vehicles that spread cancer genes. *Bioessays* **2012,** *34* (6), 489-97.

64. Deregibus, M. C.; Cantaluppi, V.; Calogero, R.; Lo Iacono, M.; Tetta, C.; Biancone, L.; Bruno, S.; Bussolati, B.; Camussi, G., Endothelial progenitor cell derived microvesicles activate an angiogenic program in endothelial cells by a horizontal transfer of mRNA. *Blood* **2007,** *110* (7), 2440-8.

65. Skog, J.; Wurdinger, T.; van Rijn, S.; Meijer, D. H.; Gainche, L.; Sena-Esteves, M.; Curry, W. T., Jr.; Carter, B. S.; Krichevsky, A. M.; Breakefield, X. O., Glioblastoma microvesicles transport RNA and proteins that promote tumour growth and provide diagnostic biomarkers. *Nat Cell Biol* **2008,** *10* (12), 1470-6.

66. D'Asti, E.; Garnier, D.; Lee, T. H.; Montermini, L.; Meehan, B.; Rak, J., Oncogenic extracellular vesicles in brain tumor progression. *Frontiers in physiology* **2012,** *3*, 294.

67. van Laarhoven, H. W.; Bussink, J.; Lok, J.; Punt, C. J.; Heerschap, A.; van Der Kogel, A. J., Effects of nicotinamide and carbogen in different murine colon carcinomas: immunohistochemical analysis of vascular architecture and microenvironmental parameters. *Int J Radiat Oncol Biol Phys.* **2004,** *60* (1), 310-21.

68. Rosas, M.; Osorio, F.; Robinson, M. J.; Davies, L. C.; Dierkes, N.; Jones, S. A.; Reis e Sousa, C.; Taylor, P. R., Hoxb8 conditionally immortalised macrophage lines model inflammatory monocytic cells with important similarity to dendritic cells. *Eur J Immunol* **2011,** *41* (2), 356-65.

69. Theelen, T. L.; Lappalainen, J. P.; Sluimer, J. C.; Gurzeler, E.; Cleutjens, J. P.; Gijbels, M. J.; Biessen, E. A.; Daemen, M. J.; Alitalo, K.; Yla-Herttuala, S., Angiopoietin-2 blocking antibodies reduce early atherosclerotic plaque development in mice. *Atherosclerosis* **2015,** *241* (2), 297-304.

4
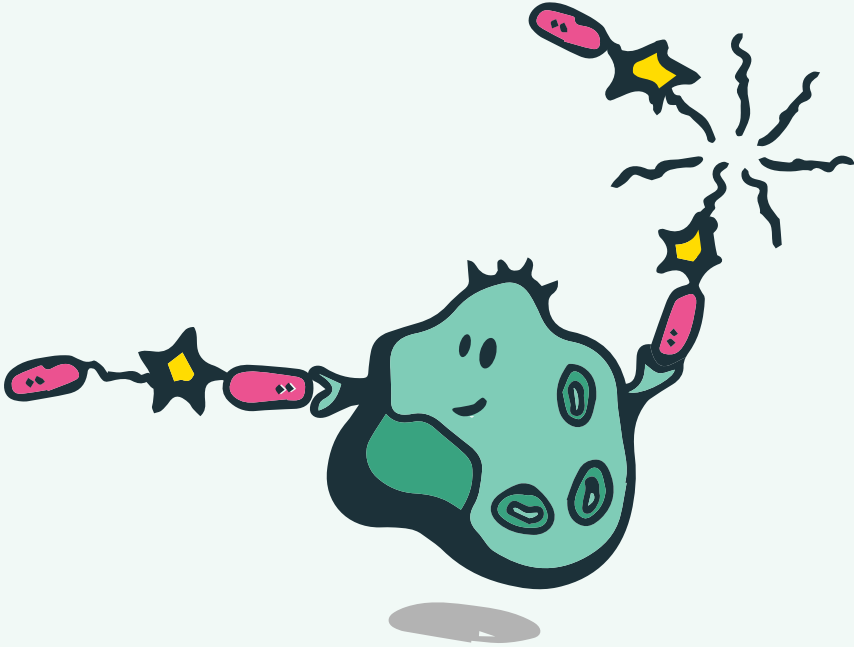
CHAPTER 5

Legomedicine - A versatile chemo-enzymatic approach for the preparation of targeted dual-labeled llama antibody-nanoparticle conjugates.

Sanne A.M. van Lith[1*], Sander M.J. van Duijnhoven[1*], Anna C. Navis[1], Edward Dolk[2], Jos W.H. Wennink[3], C.F. van Nostrum[3], Jan C.M. van Hest[4], William P.J. Leenders[1]

*Authors contributed equally

[1]Department of Pathology, Radboud Institute for Molecular Life Sciences, Radboudumc, Nijmegen, The Netherlands
[2]QVQ, Utrecht university, Utrecht, The Netherlands
[3]Department of Pharmaceutics, Utrecht University, Utrecht, The Netherlands
[4]Department of Bio-organic Chemistry, Eindhoven University of Technology, Eindhoven, The Netherlands

ABSTRACT

Conjugation of llama single domain antibody fragments (Variable Heavy chain domains of Heavy chain antibodies, VHHs) to diagnostic or therapeutic nanoparticles, peptides, proteins or drugs offers many opportunities for optimized targeted cancer treatment. Currently, mostly nonspecific conjugation strategies or genetic fusions are used that may compromise VHH functionality.

In this paper we present a versatile modular approach for bioorthogonal VHH modification and conjugation. First, sortase A mediated transPEGylation is used for introduction of a chemical click moiety. The resulting clickable VHHs are then used for conjugation to other groups employing the Cu^+-independent strain-promoted alkyne-azide cycloadition (SPAAC) reaction. Using this approach, tail-to-tail bispecific VHHs and VHH-targeted nanoparticles are generated without affecting VHH functionality. Furthermore, this approach allows the bioconjugation of multiple moieties to VHHs for simple and convenient production of VHH-based theranostics.

INTRODUCTION

The challenge in cancer therapy is to specifically deliver therapeutic agents to tumor cells with minimal delivery to and effects on healthy tissues. Targeted delivery of drugs with antibody drug conjugates (ADCs) has received a lot of attention in the last decades. Also, nanoparticles have been used for drug delivery. Liposomes can carry hydrophilic drugs in the lumen[1,2] while micelles are suited for carrying hydrophobic drugs[3]. Liposomes and micelles however distribute relatively randomly in the body after intravenous injection[1] and introduction of tumor specificity in these nanoparticles could greatly increase local delivery and efficacy of cancer therapeutics[4-6].

A number of therapeutic antibodies with relative tumor specificity are now applied clinically (e.g. trastuzumab and cetuximab against HER2 and EGFR)[7,8]. Effects of treatments with these targeted drugs are often limited because of recurrences of drug-resistant tumors[9-12]. The challenge should therefore be to develop a multispecific tumor-targeting nanoparticle platform that can deliver cytotoxic payload to all cancer cells in a tumor, resulting in specific and acute death of all cells in a tumor.

Conventional protein conjugation strategies mostly use relatively nonspecific methods, e.g. N-hydroxysuccinimide (NHS) chemistry utilizing ε-NH_2 groups from lysines. Depending on number and distribution of lysines in the active binding domain of the targeting agent, these conjugation protocols may compromise functionality. This specifically applies to single domain antibody fragments (VHHs, Nanobodies®) due to their small size. VHHs are recombinant antigen-binding domains that are derived from cameloid heavy chain-only antibodies and receive increasing interest as therapeutic or diagnostic compounds[13,14]. VHHs typically have a molecular weight of 15-20 kDa and may bind target antigens with pM to nM affinity, similar to conventional antibodies. The ease of genetic engineering and handling of VHHs, combined with a number of other advantages such as high water solubility, low production cost, small size, low immunogenicity in humans and high thermo- and pH stability[15] makes this class of antibodies a highly interesting alternative to conventional antibodies.

A number of VHHs with high specificity and affinity against tumor targets (e.g. EGFR, HER2, MET) have been developed[16-18]. Approaches to conjugate VHHs without compromising functionality include the site specific introduction of a carboxyterminal cysteine allowing maleimide chemistry[19] and introduction of a carboxyterminal five amino acid sequence (LPXTG) allowing sortase A transpeptidation[20].

Here we present a versatile modular approach for bioorthogonal VHH conjugations, using sortase A mediated transPEGylation to introduce a carboxyterminal click moiety, and subsequent Cu+-independent strain-promoted alkyne-azide cycloadition (SPAAC) for conjugation of a functional group that may be connected to another VHH and/or polymeric micelles. Furthermore, introduction of a cysteine before the LPXTG tag allows maleimide chemistry to introduce a second diagnostic or therapeutic compound. This method allows

the production of highly uniform VHH-based conjugates that can consist of multiple modular moieties, examples being labeled bispecific VHHs, bivalent VHHs and VHH-targeted nanoparticles. Because all chemistry occurs at the carboxyterminus, this method does not affect VHH functionality. Furthermore, concomitant with conjugation, carboxy-terminal tags that allow purification of the VHHs after bacterial expression are removed, a prerequisite for future clinical applications.

RESULTS AND DISCUSSION

VHHs were successfully expressed and purified as VHH-C-LPETG-8xHis-Vsv or VHH-LPETG-8xHis-Vsv fusion proteins with yields of 5-10 mg/L *E.coli* culture (see Figure 1A for a representative Coomassie Brilliant Blue (CBB) stained SDS-PAGE gel of 7D12-C-LPETG-8xHis-Vsv (referred to as 7D12), the anti-EGFR VHH that was used as a prototype in this study). Since the 8xHis-Vsv tags are substituted by compounds of interest during the sortase A reaction, loss of these tags was compensated for by introducing a cysteine residue directly upstream of the LPETG-8xHis-Vsv sequence, allowing maleimide-based labelling with alternative tags for detection. Liquid chromatography mass spectrometry (LC-MS) indicated the correct mass for expressed 7D12 and it showed that the free thiol group of this cysteine was oxidized, presumably by glutathione based on its molecular weight of 307 Da (Figure 1B). After a mild TCEP reduction, the thiol was available for conjugation (Figure 1C). The reaction of the 7D12 protein with fluorescein-5-maleimide was efficient, resulting in a pure preparation of 7D12[Fluo] (Figure 2A+B, lanes 1). LC-MS confirmed the conjugation of one fluorescein residue per VHH in 7D12[Fluo] (Figure 2C), demonstrating that the two native framework cysteine residues that are involved in an intramolecular disulfide bridge[21] were not reactive towards fluorescein-5-maleimide under the used conditions. This was further confirmed in additional experiments that showed absence of maleimide reaction with multiple VHHs lacking the C terminal cysteine (Figure 3).
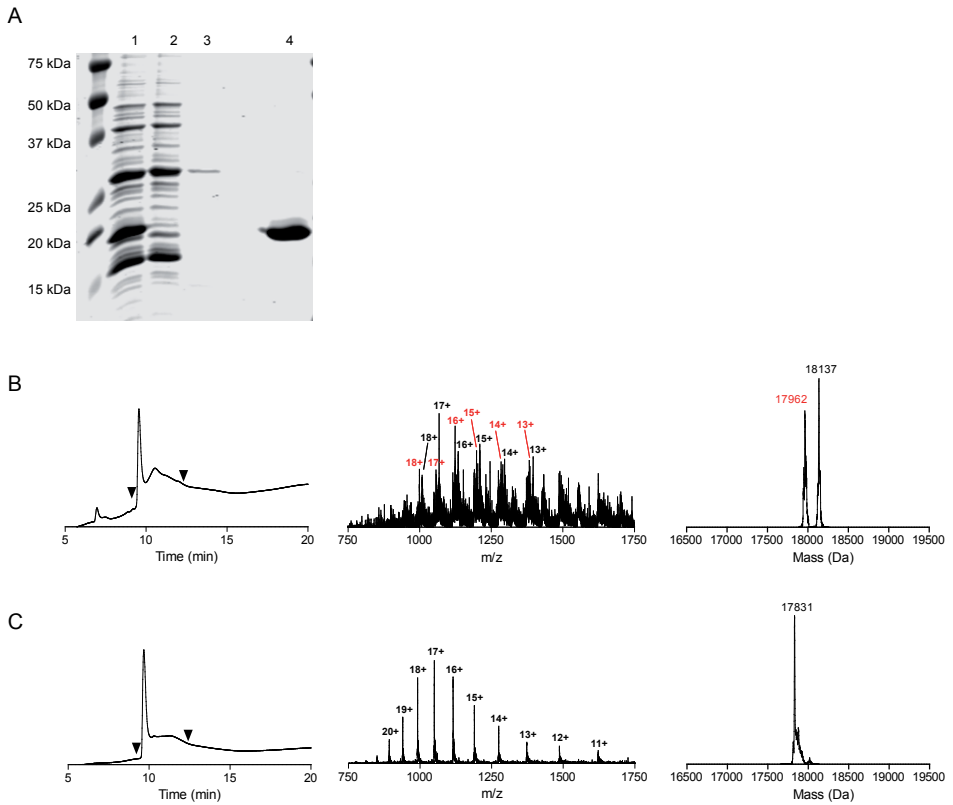
Figure 1. A) CBB stained SDS-PAGE gel of samples obtained during 7D12 production. 1 = bacterial lysate, 2 = flow-through Ni-NTA purification, 3 = pre-eluate Ni-NTA purification, 4 = eluate post Ni-NTA purification and dialysis. B) LC-MS characterization of 7D12 (with an expected mass of 17837 Da, observed 17962 and 18137 Da) before TCEP reduction. C) LC-MS characterization of 7D12 after 20 min incubation with 20 mM TCEP. A pure product of 17831 Da was detected, suggesting that the thiol before TCEP reduction was oxidized by small molecules, among which presumably glutathione. The left graphs show the ultraviolet absorbance chromatograms (at 215 nm) and the middle and right graphs show the total mass spectra and deconvoluted spectra of the UV-peaks bracketed by the arrowheads, respectively.
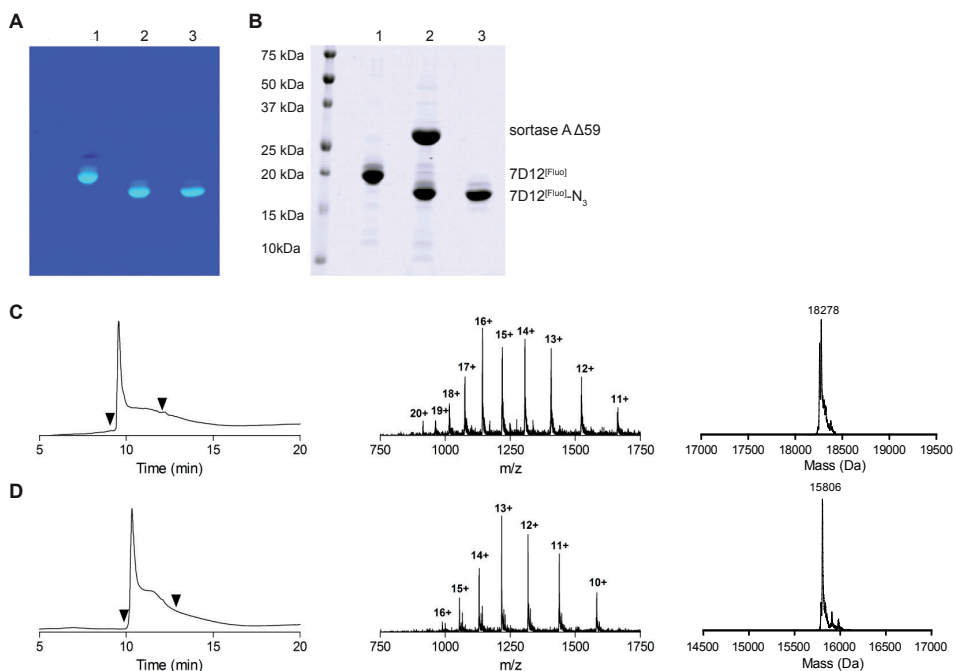
Figure 2. A) Fluorescent image and B) CBB staining of an SDS-PAGE gel of samples obtained during the procedure of sortagging. 1 = 7D12[Fluo], 2 = 7D12[Fluo]/sortase A/H_2N-PEG_3-N_3 reaction mixture after overnight reaction, 3 = purified 7D12[Fluo]-N_3. Note the molecular shift between lanes 1 and 2, 3 that is a result of removal of the G-8xHis-Vsv tag and simultaneous addition of the small PEG_3-N_3 group. C) LC-MS characterization of 7D12[Fluo] (expected 18265 Da, observed 18278 Da) D) LC-MS characterization of 7D12[Fluo]-N_3 (expected 15790 Da, observed 15806 Da). The left graphs show the ultraviolet absorbance chromatograms (at 215 nm) and the middle and right graphs show the total mass spectra and the deconvoluted spectra of the UV-peaks bracketed by the arrowheads, respectively.
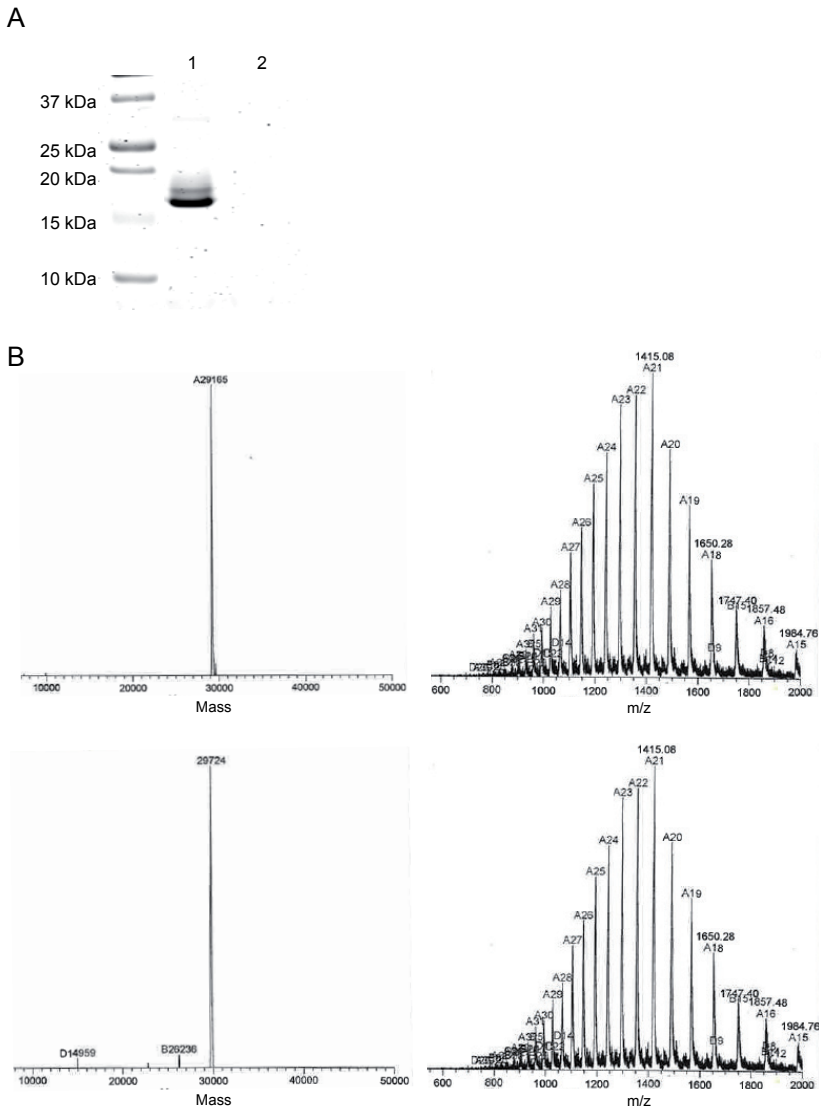
Figure 3. Only the C-terminally introduced thiol in VHHs is avalaible for maleimide chemistry. A) Western blot stained with Avidin Alexa680. 1 = A12-C-LPETG-8xHis-Vsv after incubation with biotin-maleimide. 2 = the same amount of A12-LPETG-8xHis-Vsv as a control, incubated under the same conditions. Note absence of maleimide labelling of A12, indicating that the 2 cysteines involved in an intramolecular disulphide bond are not available for this reaction B) Deconvoluted spectra (left) and total mass spectra (right) showing incorporation of fluorescein-5-maleimide only in bihead $^N7D12^C$-$[G_4S]_{10}$-$^N4E4^C$ with a c-terminal cysteine. Upper graphs depict $^N7D12^C$-$[G_4S]_{10}$-$^N4E4^C$-Flag-6xHis incubated with fluorescein-5-maleimide (expected 29164.89 Da, observed 29165 Da), lower graphs depict $^N7D12^C$-$[G_4S]_{10}$-$^N4E4^C$-C-Flag-6xHis incubated with fluorescein-5-maleimide (expected 29713.4 Da, observed 29724 Da).

The LPETG-8xHis-Vsv tag in 7D12[Fluo] allows sortase A mediated transpeptidation which releases the G-8xHis-Vsv tag in exchange for an H_2N-GGG-containing peptide (the prototypical substrate of sortase A). This allows rapid and easy purification of the reaction product to homogeneity, because the G-8xHis-Vsv cleavage product and the 6xHis-tagged sortase A enzyme can be removed from the reaction mixture by Ni-bead depletion. Because a wide variety of chemically modified monodisperse PEG compounds is nowadays available, sortase A mediated conjugation of such compounds to the carboxyterminus is a highly attractive approach.

Using H_2N-PEG_x-X as a nucleophile for sortase A mediated PEGylation, a range of VHH–PEG_x-X constructs can be generated in which X represents a drug or a reactive group. In this work we used the combination of H_2N-PEG_3-N_3 and H_2N-PEG_3-DBCO in the SPAAC reaction[22]. In an attempt to improve the reaction with H_2N-PEG_x-X we tested recently described mutants of sortase A with optimized LPETG cleavage activity[23], and compared them to the variants with a N-terminal deletion of either 25 or 59 amino acids (supporting information, Figure S1 + S2). These optimizations were performed using the anti-PlexinD1 VHH A12[24]. Sortase A Δ59 was ultimately selected as most optimal since despite increased LPETG cleavage rates, the low affinity of the mutant sortases for H_2N-GGG or H_2N-PEGx-X resulted in high levels of hydrolysis at the threonine. Furthermore, we found that the sortase A Δ25 variant, that contains an N-terminal 6xHis-tag, experienced unexplained proteolysis just downstream of the His-tag during the sortase A reaction (supporting information and Figure S2D). Since this precluded complete removal of sortase A activity, we discarded this variant.

Further experimentation using different molar ratios of H_2N-PEG_x-X or H_2N-GGG revealed that H_2N-PEG_x-X was incorporated less efficiently than H_2N-GGG, requiring a 200-fold molar excess of H_2N-PEG_x-X over VHH-(C)-LPETG-8xHis-Vsv as compared to a 25-fold excess of H_2N-GGG (under conditions of 4 hrs reaction at 30°C with sortase A Δ59). Lower concentrations of both nucleophiles in the reaction resulted in formation of VHH-LPET-OH hydrolysis products, as observed with LC-MS (supporting information, Figure S3A). These results were in line with those of Parthasarathy et al, who showed that conjugation of H_2N-PEG_x to EGFP in a ratio of 1:1 by sortase A Δ59 was highly inefficient[25]. Yet, the use of H_2N-PEG_x-X nucleophiles instead of triglycine-containing substrates would have an important advantage: conjugation of H_2N-PEG_x-X yields VHH-(C)-LPETG-PEG_x-X in a one-way reaction, unlike conjugation of H_2N-GGG-X that reconstitutes a sortase A substrate site in the VHH-(C)LPET-GGG-X reaction product. Indeed we could show that VHH-LPET-PEG_x-X is not a substrate for sortase A, in contrast to VHH-LPETGGG-peptide (Figure 4).
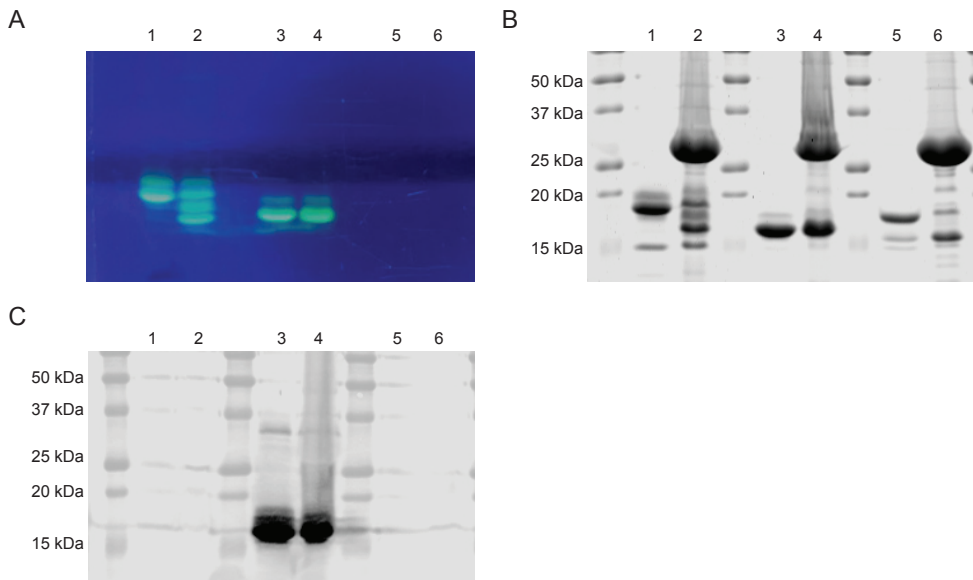
Figure 4. Conjugation of H_2N-PEG$_3$-X does not reconstitute the sortase A recognition site. 7D12[Fluo], 7D12[Fluo]–PEG$_3$-N$_3$-DBCO-biotin or 7D12-LPETGGG-peptide were incubated with sortase A without nucleophile to investigate which are sortase A substrates. Panel A= fluorescent image of SDS-PAGE gel, panel B= CBB stained gel of panel A, panel C= western blot of a similar gel as in A,B, stained with avidin-AlexaFluor680. 1 = 7D12[Fluo], 2 = 7D12[Fluo] after incubation with sortase A, 3 = 7D12[Fluo]-N$_3$-DBCO-biotin, 4 = 7D12[Fluo]-N$_3$-DBCO-biotin after incubation with sortase A, 5 = 7D12-LPETGGG-peptide, 6 = 7D12-LPETGGG-peptide after incubation with sortase A. Note that incubation of 7D12-LPETGGG-peptide with sortase A leads to formation of the smaller hydrolyzed product 7D12-LPET, whereas 7D12[Fluo]-LPET-PEG$_3$-N$_3$-DBCO-biotin remains intact as can be seen in panel C.

Using the optimized conditions, 7D12[Fluo] was conjugated to H_2N-PEG$_3$-N$_3$ with sortase A Δ59 to yield 7D12[Fluo]-N$_3$ (Figure 2A+B). After removal of sortase A Δ59, G-8xHis-Vsv and unreacted 7D12[Fluo] by Ni-NTA depletion, 7D12[Fluo]-N$_3$ was obtained in a 66% yield with a >95% purity based on LC-MS (Figure 2D). Similar results were obtained when H_2N-PEG$_3$-DBCO was used in the reaction with sortase A Δ59 (Figure 5A+B). Furthermore, the methodology has been successfully tested and validated for three more VHHs in our lab (supporting information, Figure S4) demonstrating the versatility of this approach.
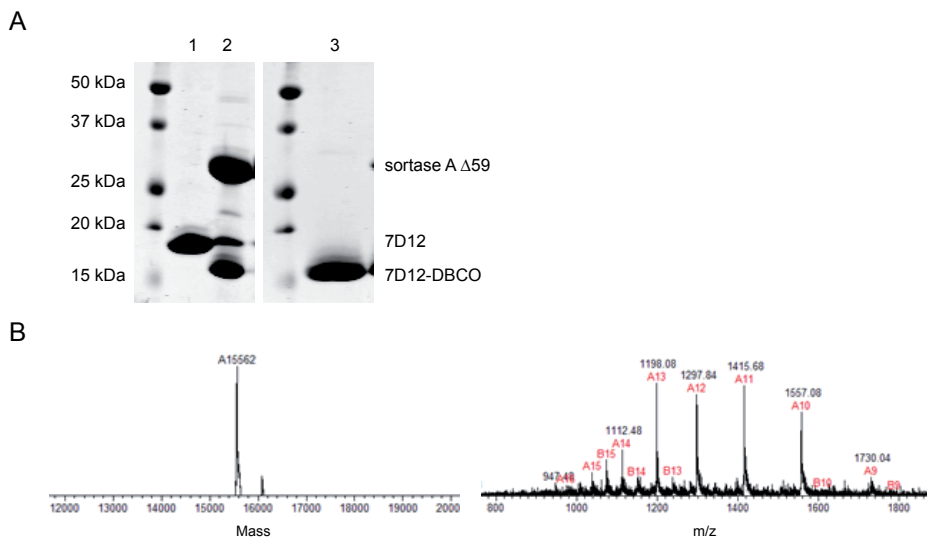
Figure 5. A) CBB stained SDS-PAGE gel of samples obtained during the sortagging procedure. 1 = 7D12, 2 = 7D12/sortase A/H_2N-PEG$_3$-DBCO reaction mixture, 3 = purified 7D12-DBCO. B) LC-MS characterization of 7D12-DBCO showing the deconvoluted spectrum (left) and total mass spectrum (right) (expected 15565 Da, observed 15562 Da).

Bispecific or bivalent antibody conjugates are valuable compounds for targeted cancer therapy[26,27]. Current approaches to make bispecific or bivalent VHHs often involve genetic fusion of VHH open reading frames, allowing production only in head-to-tail fusion format. It has already been shown that the affinity of the second VHH in such bispecific constructs may be dramatically affected by the presence of the first VHH[28]. Sortase A technology allows the generation of tail-to-tail dimers, leaving antigen binding sites of the individual composing VHHs intact[20] (Figure 6 and 7A). We tested the validity of this hypothesis by using sortase A Δ59 in combination with H_2N-PEG$_3$-X linkers to generate 7D12[Fluo]-N$_3$ and 4E4-DBCO, 4E4 being a low-affinity Transferrin receptor (TfR)-binding VHH (unpublished results) that is used here as a control. After the click reaction (see Figure 7B+C for analysis of the reaction products), heterodimer ^{N}7D12$^{C[Fluo]}$-^{C}4E4^N could be readily purified from residual monomers by size exclusion chromatography, resulting in >90% pure product of 36 kDa (Figure 7D). In parallel, we generated conventional head-to-tail bispecific VHHs, with 7D12 and 4E4 separated by a [G$_4$S]$_{10}$ linker or a [G$_4$S]$_{20}$ linker and a C-terminal C-Flag-6xHis (compounds ^{N}7D12^C-[G$_4$S]$_n$-^{N}4E4^C and ^{N}4E4^C-[G$_4$S]$_n$-^{N}7D12^C, Figure 6 and 7A). *E.coli* expression of these bispecific VHHs was successful as shown with SDS-PAGE analysis (Figure 7E+F). Yields were 2-4 mg/L E.coli culture. The bispecifics were labeled on the C-terminal cysteine with fluorescein-5-maleimide as described for monomeric VHHs, and the correct mass was confirmed with LC-MS (data not shown).
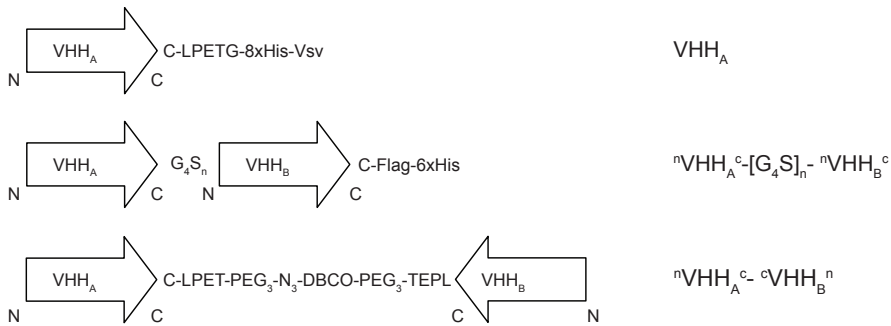
Figure 6. Schematic representation of the monomeric VHH, head-to-tail bispecific VHH and tail-to-tail bispecific VHH and their nomenclature in this report.

Importantly, in this context both the head-to-tail and the tail-to-tail bispecific VHHs contain only one fluorescein molecule, allowing quantitative comparison of the EGFR-binding capacity of these formats with $7D12^{[Fluo]}$. Constructs were tested in flow cytometry analyses using the high EGFR expressing squamous carcinoma cell line A431 (Figure 7G). Compounds $^{N}7D12^{C}$-$[G_4S]_n$-$^{N}4E4^{C[Fluo]}$ with both G_4S linker lengths and $^{N}7D12^{C[Fluo]}$-$^{C}4E4^{N}$ were equally effective as $7D12^{[Fluo]}$ in binding to A431 cells. In contrast, binding to EGFR was reduced with a factor 10 for compounds $^{N}4E4^{C}$-$[G_4S]_n$-$^{N}7D12^{C[Fluo]}$ with both G_4S linker lengths, confirming that, at least for VHH 7D12, epitope binding is hindered by the presence of a VHH at the amino-terminus. Thus, bispecific VHHs generated via tail-to-tail click fusion are more robust than head-to-tail bispecific VHHs.

5

Figure 7. A) Schematic overview of bispecific tail-to-tail (Structure 1) or head-to-tail (Structure 2) VHH constructs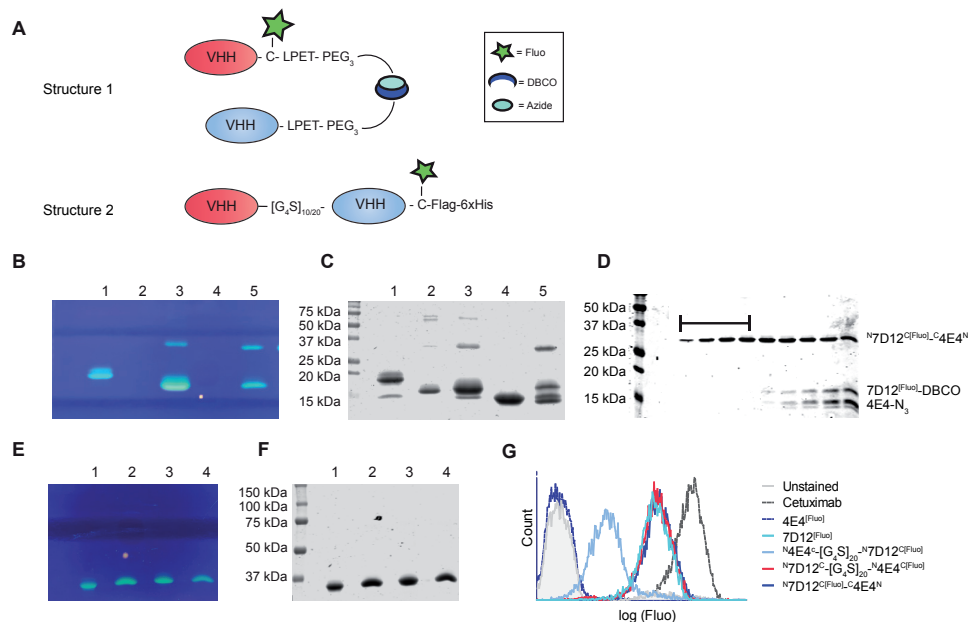. In panels B and C SDS-PAGE is shown (fluorescence signal and CBB staining, respectively) depicting the products of the sortase A reaction to produce bispecific ^{N}7D12$^{C[Fluo]}$-^{C}4E4^N. 1 = 7D12$^{[Fluo]}$, 2 = 4E4, 3 = 7D12$^{[Fluo]}$-DBCO, 4 = 4E4 –N$_3$, 5 = ^{N}7D12$^{C[Fluo]}$-^{C}4E4^N before sephadex G75 purification. D) CBB stained SDS-PAGE gel showing subsequent flow-through fractions from the sephadex G75 packed column that is used to separate bihead ^{N}7D12$^{C[Fluo]}$-^{C}4E4^N from monomeric 7D12$^{[Fluo]}$-DBCO and 4E4-N$_3$. The bracketed lanes contain >95% pure ^{N}7D12$^{C[Fluo]}$-^{C}4E4^N and are pooled and used for experiments. In panels E and F the expression of bispecific head-to-tail VHHs is depicted with E) fluorescence signal and F) CBB staining of an SDS-PAGE gel. 1 = ^{N}7D12^C-[G$_4$S]$_{10}$-^{N}4E4$^{C[Fluo]}$, 2 = ^{N}4E4^C-[G$_4$S]$_{10}$-^{N}7D12$^{C[Fluo]}$, 3 = ^{N}7D12^C-[G$_4$S]$_{20}$-^{N}4E4$^{C[Fluo]}$, 4 = ^{N}4E4^C-[G$_4$S]$_{20}$-^{N}7D12$^{C[Fluo]}$. F) Flow cytometry histogram derived from A431 cells incubated with the various bispecific constructs and controls.

PEGylation is an important modification of nanoparticles that is applied to increase half life in the circulation by avoiding rapid clearance by spleen, liver and kidney[29]. PEGylation of VHHs, accomplished by clicking DBCO-PEG to VHH-N$_3$ indeed results in better *in vivo* characteristics[30]. Sortase A mediated conjugation of H$_2$N-PEG$_x$ yields the interesting option to decorate PEGylated nanoparticles with functionally active VHHs. To test this hypothesis we applied click chemistry to conjugate 7D12$^{[Fluo]}$-N$_3$ to benzoyl-poly(ε-caprolactone)-methoxypoly(ethyleneglycol) (ben-PCL$_7$-mPEG$_{2000}$) diblock-based micelles, equipped with a small percentage of DBCO groups. Ben-PCL$_7$-mPEG$_{2000}$ diblock-based micelles are biocompatible and biodegradable, and can be used as carrier of hydrophobic drugs that can be incorporated in the micellar core[31]. The decoration of micelles with VHHs may increase affinity of the nanoparticles to targets by an avidity effect. Also, this approach allows the generation of multispecific drug-loaded targeting nanoparticles by simply decorating these with different tumor-targeting VHHs.

¹H-NMR spectra showed that synthesis of intermediate products (data not shown) and end products ben-PCL₇-mPEG₂₀₀₀ and ben-PCL₇-mPEG₂₀₀₀-DBCO (Figure 8A+B) was successful. Micelles were prepared by film-hydration of a mixture of 90% ben-PCL₇-mPEG₂₀₀₀ diblock polymers and 10% ben-PCL₇-mPEG₂₀₀₀-DBCO, resulting in micelles that contain a calculated 20-30 DBCO click groups per particle. Dynamic light scattering (DLS) experiments of the resulting micelles revealed a mean particle size of 28±2 nm and a polydispersity index (PDI) of 0.32±0.02.
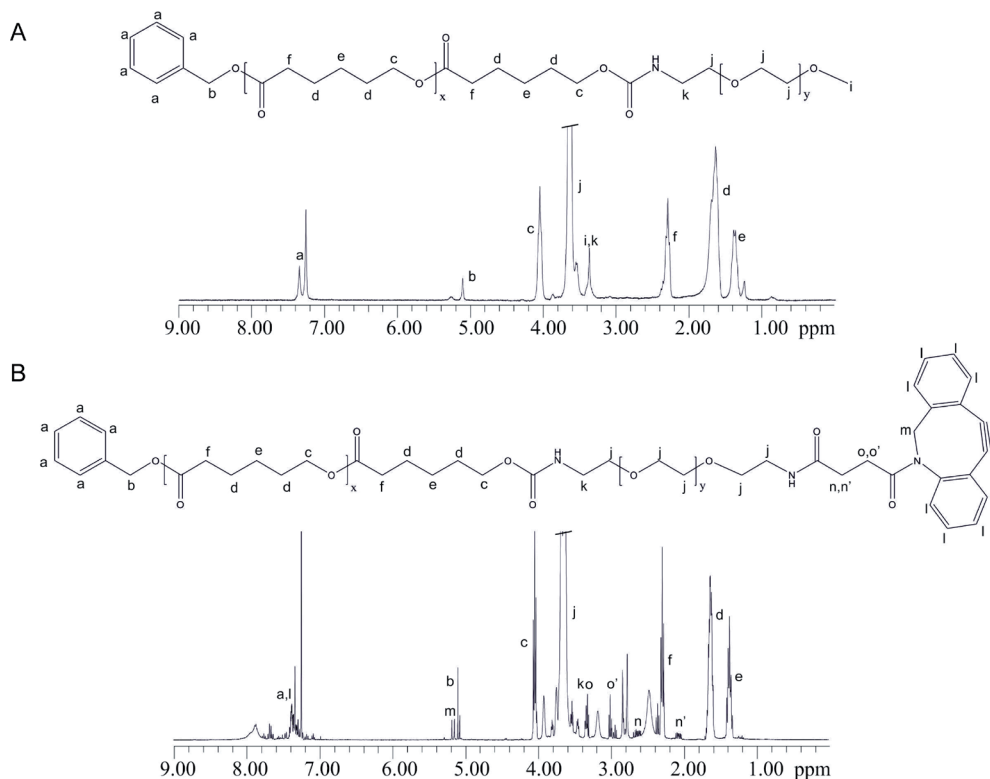

Figure 8. Chemical structures and corresponding ¹H-NMR-spectra of A) Ben-PCL₇-mPEG₂₀₀₀ and B) Ben-PCL₇-PEG₂₀₀₀-DBCO measured in CDCl₃.

DBCO-micelles were decorated with 7D12 via a click chemistry reaction with 7D12$^{[Fluo]}$-N$_3$ in a 2:1 DBCO:N$_3$ ratio, to minimize amounts of residual unconjugated 7D12$^{[Fluo]}$-N$_3$ after the click reaction. To confirm that during handling and experimentation micelles remained intact, we included the hydrophobic photosensitizer Meta-tetra(hydroxyphenyl)chlorin (mTHPC) during micel formation, equipping the micelles with a fluorescent signal that is readily distinguishable from 7D12-associated fluorescein (Figure 9A). SDS-PAGE of the 7D12 conjugated micelles revealed a shift of ~3 kDa as compared to the starting material 7D12$^{[Fluo]}$-N$_3$, indicating successful conjugation of 7D12$^{[Fluo]}$-N$_3$ to the DBCO-block-copolymer with a conjugation yield of >85% (Figure 9B,C). Again this conjugation method was verified for other available VHHs in our lab (supporting information, Figure S5A+B), showing its versatility.

We next tested whether 7D12 on the decorated micelles had retained EGFR affinity by performing flow cytometry after incubation with EGFR-positive A431 squamous cell carcinoma or EGFR-negative E98 glioma cells[32], using 7D12$^{[Fluo]}$ as reference. 7D12$^{[Fluo]}$-micelles showed efficient binding to A431 cells but negligible binding to E98 cells (Figure 9D). Importantly, binding of 7D12$^{[Fluo]}$-micelles led to 70% higher cell-associated fluorescein-fluorescence than binding of monomeric 7D12$^{[Fluo]}$. This may reflect the loading of individual micelles with multiple fluorescein-labeled 7D12 moieties or may be due to cooperative binding and an avidity effect. Increased binding of 7D12$^{[Fluo]}$-micelles to A431 cells was confirmed with fluorescence microscopy, using the fluorescein signal as readout (Figure 9E, green signal in panel 2, compare to 7D12$^{[Fluo]}$ in panel 1). The increase in fluorescein signal was accompanied by an increased association of mTHPC fluorescence in 7D12$^{[Fluo]}$-micelles as compared to non-decorated micelles (Figure 9D, right graph and Figure 9E, cyan signal). There was no difference in binding of 7D12$^{[Fluo]}$-micelles and non-decorated micelles to E98 cells, suggesting that 7D12$^{[Fluo]}$-micelles bound as intact particles to A431 cells in an EGFR-dependent manner. It must however be noted that there was also some non-specific association of mTHPC with both A431 cells and E98 cells. Whether this reflects non-specific binding of micelles or of free mTHPC that is released from micelles is difficult to discriminate.

These results indicate that the multivalency induced by coupling multiple VHHs to a micelle, increased uptake of these particles and their payload in target positive cells. Although we restricted ourselves in this study to micelles, this conjugation approach is predicted to work with many other types of protein- or PEG-based nanoparticles (e.g. liposomes, polymersomes) once a controlled percentage of the building blocks is equipped with a chemical click group. Interestingly, this procedure will also allow the controlled synthesis of multi-specific targeting nanoparticles, e.g. by preparing nanoparticles with a defined number of non-compatible clickable agents such as DBCO and tetrazine moieties, allowing simultaneous conjugation of VHH-PEG$_3$-N$_3$ and VHH-PEG$_x$-TCO (trans-cyclooctene). Whereas the free thiol group in VHH-C-LPET-PEG$_x$-X may be used for maleimide-based conjugation of hydrophilic drugs, micelles may be used to simultaneously carry hydrophobic drugs, making this to a versatile approach.
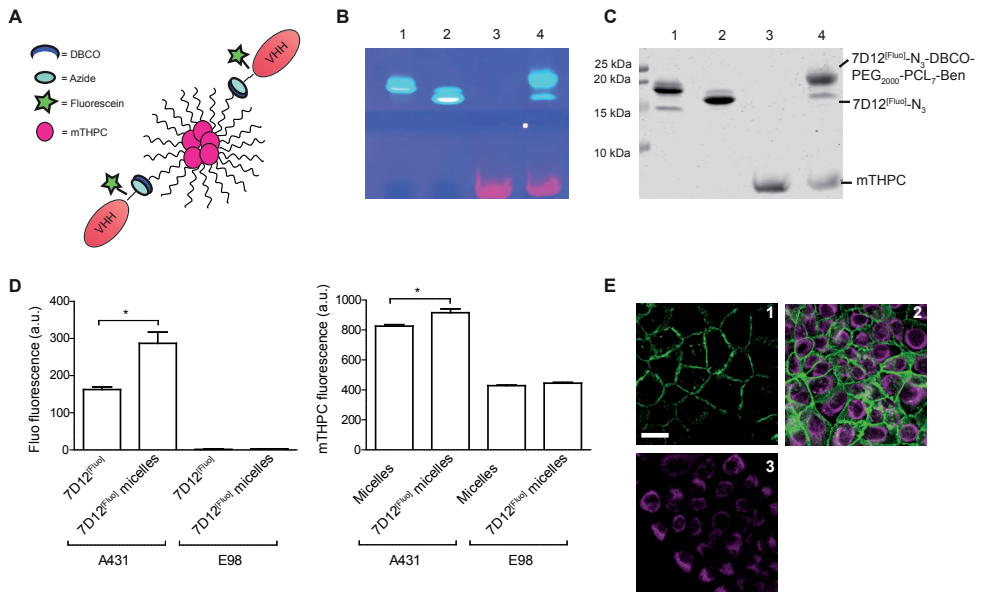
Figure 9. A) Cartoon of VHH[Fluo]-decorated mTHPC loaded micelles. B) Fluorescein visualization and C) CBB staining of the SDS-PAGE analysis of SPAAC reaction between 7D12[Fluo]-N$_3$ and DBCO-micelles. 1 = 7D12[Fluo], 2 = 7D12[Fluo]-N$_3$, 3 = 10% DBCO-micelles with 5% mTHPC and 4 = 10% DBCO-micelles with 5% mTHPC and 5% 7D12[Fluo]. D) Median values of fluorescence intensity as measured in flow cytometry. Left bargraph = fluorescein total signal on A431 (EGFR[+]) and E98 (EGFR [-]) cells after incubation with 7D12[Fluo] as a positive control and 7D12[Fluo]-micelles. Right bargraph = mTHPC total signal on both A431 and E98 cells after incubation with targeted or non-targeted micelles. * indicates significance with p<0.05. E) Fluorescence microscopy of A431 cells immediately after incubation with 1 = 7D12[Fluo], 2 = 7D12[Fluo]-micelles and 3 = non-targeted micelles. Cyan depicts mTHPC, incorporated in the micelles, green depicts fluorescein. The scale bar depicts 20 µM.

CONCLUSION

Conjugations of VHHs to diagnostic or therapeutic compounds should involve the VHH's carboxy-terminus, distant from the antigen binding site, in order to retain full VHH functionality. Here, a bioorthogonal site-specific conjugation approach is presented based on sortase A and click chemistry, combined with cysteine-maleimide conjugation. This approach allows the preparation of molecularly defined targeted nanoparticles, preserving targeting potential and concomitantly removing unwanted tags from VHHs, a prerequisite for potential clinical applications. The potential to perform controlled dual labelling of proteins without loss of protein function is an important next step to the preparation of optimized theranostics.

METHODS

VHH production and purification

VHH 4E4 is a low affinity VHH (Kd~500 nM) directed against transferrin receptor (TfR) and was used as an inert VHH in this study. VHH 7D12 against EGFR has been described in detail before[17,33]. The VHH coding sequences were cloned in frame behind the pelB leader sequence in modified pHEN-IX vectors in which the sortase A recognition sequence LPETG, either or not preceded by a cysteine, was inserted just upstream of the 8xHis-Vsv tags, resulting in pHENIX-VHH-LPETG-8xHis-Vsv and pHENIX-VHH-C-LPETG-8xHis-Vsv. Plasmids were transformed in *E. coli* strain ER2566 for standard protein expression. Cells were grown in 2xTY medium containing 3.5% (w/v) glycerol and 50 μg/ml ampicillin at 37ºC. At an OD_{600} between 0.6 and 0.8, recombinant protein expression was induced with 1.0 mM isopropyl β-D-thiogalactoside (IPTG, Serva, Heidelberg, Germany) at 30ºC for 2.5 hrs. Cells were harvested by centrifugation at 2830 g for 20 min at 4ºC and the periplasmic protein fraction was isolated via osmotic lysis. Cells were resuspended in ice cold TES buffer (200 mM Tris pH 8.0, 0.5 mM EDTA, 20% w/v sucrose, protease inhibitors (Complete cocktail, Roche, Basel, Switzerland)) and incubated for 20 min on ice, followed by centrifugation (4424 g , 20 min, 4ºC). After collection of the supernatant the bacterial pellet was resuspended in TES buffer containing 15 mM $MgSO_4$ and incubated on ice for 20 min. After centrifuging, both supernatants were pooled and incubated with Ni-NTA sepharose (IBA, Goettingen, Germany), pre-equilibrated with 50 mM phosphate pH 7.4, 500 mM NaCl, for 1 hr at 4ºC. After washing of the beads with 50 mM phosphate pH 7.4, 500 mM NaCl and 10 mM imidazole, 8xHis-tagged proteins were eluted with 500 mM imidazole in 50 mM phosphate pH 7.4 and 500 mM NaCl. The eluate was dialyzed against 50 mM TRIS pH 7.5 and 150 mM NaCl in a 3.5 kDa dialysis membrane (Spectrum labs, Los Angeles, CA, USA). VHHs were analyzed by SDS-PAGE under reducing conditions (coomassie brilliant blue (CBB) staining), followed by analysis on the Odyssey CLx infrared imaging system (LI-COR, Lincoln, NE, USA)) and liquid chromatography and mass spectrometry (LC-MS, Shimadzu HPLC and Thermo Finnigan LCQ Fleet) on a C4 column. Protein concentrations were determined by absorbance at 280 nm using a Nanodrop spectrophotometer (Thermo Fisher Scientific, Waltham, MA, USA).

Generation and production of in tandem VHH dimers

In tandem bispecific [N]7D12[C]-[N]4E4[C] and the converse orientation [N]4E4[C]-[N]7D12[C] VHHs connected by $[G_4S]_{10}$ of $[G_4S]_{20}$ linkers and one C-terminal cysteine and Flag-8xHis-tags were synthesized as described before[32]. In short, reading frames encoding 7D12 and 4E4 were PCR amplified with primer sets that allowed fusion of the two VHHs, separated by $[G_4S]_{10}$ or $[G_4S]_{20}$ linkers. The N-terminal VHH was amplified with M13rev and primer (Rev10GS agtaGGATCCGCCACCTCCACTGCCACCGCCACCtgaggagaccgtgacctgggtccc) annealing to the VTVSS sequence of the VHH thereby introducing the linker including

a BamHI site. The C-terminal VHH was amplified with M13 and a primer (Forw10GS tcttGGATCCGGCGGGGGAGGTAGTGGGGGTGGGGGCTCAgaggtgcagctggtggagtctggg) annealing to EVQLV of the VHH introducing the rest of the linker and also including a BamHI site. The resulting fragments were respectively cut with SfiI/BamHI and BamHI/Eco91I and subsequently ligated into the vector (SffiI/Eco91I) in a three point ligation. Plasmids were validated by Sanger sequencing, and proteins expressed in *E.*coli strain TG1 and purified as described above. VHHs were analyzed by SDS-PAGE under reducing conditions.

Sortase A production and purification

Plasmid pGBMCS-SortA (Addgene, Cambridge, MA, USA, plasmid #21931), encoding sortase A with a deletion of amino acids 1-59 and an N-terminal Gb1 domain was transformed into *E. coli* ER2566 and protein expression induced using standard conditions as used for VHHs. After harvesting cells by centrifugation and resuspension in 50 mM TRIS pH 8.0, 150 mM NaCl and Cocktail protease inhibitor (Roche), cells were lysed by sonication at 4°C using a Bandalin Sonopuls HD2070 sonicator. The bacterial extracts were cleared by centrifugation and the 6xHis-tagged sortase A Δ59 was purified with Ni-NTA sepharose as described for VHHs. The purified sortase A Δ59 was dialyzed in a 3.5 kDa membrane against 50 mM TRIS pH 7.5 and 150 mM NaCl. The protein was analyzed by SDS-PAGE under reducing conditions (CBB staining) and LC-MS. Protein concentration was determined by absorbance at 280 nm using a Nanodrop spectrophotometer.

Fluorescein-5-maleimide conjugation

Monomeric VHH-C-LPETG-8xHis-Vsv and in-tandem bispecific $^{N}VHH_a^{C}$-$[G_4S]_n$-$^{N}VHH_b^{C}$-C-Flag-6xHis (typically ~50-250 μM) were incubated for 15 min at RT with 20 mM tris(2-carboxyethyl) phosphine (TCEP, Thermo Fisher Scientific, Waltham, MA, USA) to reduce the free thiol group. TCEP was removed by filtration over a 10 kDa MWCO centrifugal unit (Amicon, Millipore, Billerica, MS, USA) employing 5 washing cycles with 20 mM phosphate pH 7.0, 150 mM NaCl, and 5 mM EDTA. Fluorescein-5-maleimide (Thermo Fisher Scientific, Waltham, MA, USA) from a 10 mM stock in dimethylformamide was reacted with the reduced VHH construct in a 3:1 molar ratio, shielded from light and at RT for 2 hrs to yield VHH[Fluo] or $^{N}VHH_A^{C}$-$[G_4S]_{10/20}$$^{N}VHH_B^{C[Fluo]}$. Excess fluorescein-5-maleimide was removed by filtration in a 10 kDa MWCO centrifugal unit employing 4 washing cycles with 50 mM Tris pH 7.5 and 150 mM NaCl. Reaction products were analyzed by SDS-PAGE under reducing conditions and/or LC-MS. Fluorescein signal was visualized on a Chromato-vue TM-20 Transilluminator (UVP) after which the gel was stained with CBB. Protein concentration was determined by ultraviolet absorbance at 494 nm ($\varepsilon_{494,7D12-FLUO}$ = 70.000 M^{-1}cm^{-1}) using a Nanodrop spectrophotometer.

5

Sortase A mediated conjugation of click moieties

To produce clickable fluorescent VHHs, 50 µM VHH[Fluo] was incubated overnight at RT in the dark with 50 µM sortase A Δ59 and 4.0 mM H_2N-PEG_3-N_3 or H_2N-PEG_3-DBCO (Jena Biosciences, Jena, Germany) in 50 mM Tris pH 7.5, 150 mM NaCl supplemented with 10 mM $CaCl_2$. This reaction induces the covalent linkage of PEG linkers via the amine group to the threonine in the LPETG tag, releasing G-8xHis-Vsv. Sortase A Δ59, the cleaved G-8xHis-Vsv tag from the reacted VHH, and residual intact VHH were removed by adsorption to Ni-NTA sepharose, pre-equilibrated with 50 mM phosphate pH 7.4 and 500 mM NaCl, for 1 hr at 4°C. Then the excess of unreacted PEG linkers was removed by filtration in a 10 kDa MWCO centrifugal unit. The reaction product was washed three times with 50 mM phosphate pH 7.4 and 500 mM NaCl, and two times with 50 mM phosphate pH 7.4 and 500 mM NaCl containing 20% w/v glycerol. The protein constructs were analyzed by SDS-PAGE under reducing conditions and LC-MS, and protein concentration was determined by ultraviolet absorbance at 494 nm.

To check if LPET-PEG-X is a substrate for sortase A, 20 µM 7D12[Fluo], 20 µM 7D12[Fluo]-N_3-DBCO-biotin and 7D12-GGG-peptide were incubated with 50 µM sortase A Δ59 for 4 hours at 30°C. Reaction products were analyzed on a CBB stained SDS-PAGE gel and a western blot stained with 1:10.000 Avidin-Alexa680 (Invitrogen).

Generation of VHH dimers via C-to-C conjugation

Tail to tail coupled bispecific VHHs were produced by incubating 4E4-N_3 with 7D12[Fluo]-DBCO in a 1:1 molar ratio o/n at RT. Bispecific ^{N}7D12$^{C[Fluo]-C}$4E4^N was separated from single VHHs by separation on a G75 Sephadex (Pharmacia fine chemicals, Uppsala, Sweden) column. Fractions were analyzed on a SDS-PAGE gel under reducing conditions (CBB staining).

Synthesis of diblock copolymers

Ben-PCL7-PEG2000-methoxy: The amphiphilic diblock copolymer consisting of the hydrophobic poly-ε-caprolactone (PCL) and the hydrophilic methoxy-polyethylene glycol (mPEG) were synthesized using a method described by Wennink et al. (submitted for publication). Briefly, Ben-PCL-OH macromers were prepared using benzyl alcohol as the initiator in the Tin(II) ethylhexanoate $(Sn(Oct)_2)$ catalyzed ring opening polymerization of ε-caprolactone (CL) (Figure 10A). The monomer to initiator ratio was chosen such that the average degree of polymerization was 7 CL units. The hydroxyl end groups of ben-PCL_7-OH were subsequently reacted with p-nitrophenyl chloroformate to form p-nitrophenyl carbonate substituted polymers (PNC) (Figure 10B). The diblock copolymers were obtained by reacting ben-PCL_7-PNC and mPEG2000-NH_2 at 1:1 ratio in toluene at RT (Figure 10C). Average molecular weights of the polymers were determined by NMR.

Ben-PCL7-PEG2000-DBCO: NH_2-PEG2000-NH-Boc (1.00 g, 0.5 mmol)(Layson Bio, Arab, AL, USA) was added to a solution of ben-PCL_7-PNC (0.707 g, 0.5 mmol) in 20 mL dry toluene. This mixture was stirred for 1 hr at RT under nitrogen atmosphere (Figure 10D). The mixture

was washed at least 6 times with diethyl ether to remove p-nitrophenol. The product was dried in a vacuum oven and obtained as a white powder (yield: 97%). Subsequently, 0.2 g of the powder was dissolved in 20 ml of DCM and the Boc group was removed by bubbling HCL gas through the solution for 15 min (Figure 10E). The product, ben-PCL_7-PEG_{2000}-NH_2 (0.187 g, 0.063 mmol), was purified by precipitation in diethyl ether and subsequently dissolved in 20 ml of dry DCM. To produce clickable copolymers, dibenzocyclooctyne (DBCO)-NHS (0.025 g, 0.063 mmol)(Jena Biosciences, Jena, Germany) was added to this ben-PCL_7-PEG_{2000}-NH_2 solution, and the reaction mixture was stirred for 24 hrs at RT under a nitrogen atmosphere (Figure 10F). The mixture was carefully washed with diethyl ether to remove unreacted DBCO-NHS. The product was dried in a vacuum oven and obtained as a white powder (yield: 61%).

^{1}H (300MHz) NMR spectra were recorded using a Gemini NMR spectrometer (Varian Associates Inc. NMR instruments, Palo Alto, CA). Polymers were dissolved in $CDCl_3$ at a concentration of 0.015 g.ml^{-1}.
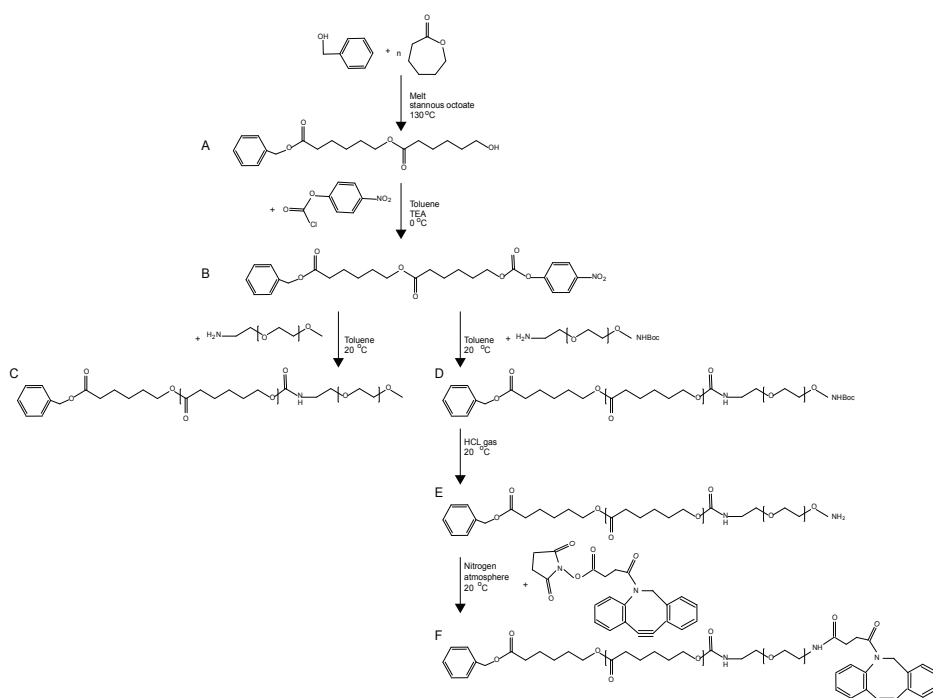
Figure 10. Synthesis routes for ben-PCL_7-$mPEG_{2000}$ and ben-PCL_7-$mPEG_{2000}$-DBCO. Synthesis of both molecules starts with A) ring opening polymerization of ε-caprolactone with benzyl alcohol which affords ben-PCL_7-OH and B) activation of the hydroxyl end group with p-nitrophenylchloroformate. Then for synthesis of amphiphilic ben-PCL_7-$mPEG_{2000}$, C) $mPEG_{2000}$-NH_2 is coupled to the activated ben-PCL_7-PNC. For synthesis of clickable ben-PCL_7-$mPEG_{2000}$-DBCO D) NH_2-PEG_{2000}-NHBoc is coupled to the activated ben-PCL_7-PNC, E) the Boc protection group is removed with HCl gas, and F) NHS-DBCO is conjugated to ben-PCL_7-$mPEG_{2000}$-NH_2.

Dynamic light scattering

The size and the size distribution of empty particles were measured by dynamic light scattering (DLS) using a Malvern CGS-3 multiangle goniometer (Malvern ltd., Malvern), consisting of a HeNe laser source (λ=632.8nm, 22mW output power), temperature controller (Julabo water bath) and a digital correlator ALV-5000/EPP. Time correlation functions were analyzed using the ALV-60X0 Software V.3.X provided by Malvern, to obtain the Z-average hydrodynamic diameter of the particles (Zave) and the particle size distribution (polydispersity index, PDI). The samples were analyzed at 25°C.

7D12 functionalized mTHPC loaded micelle preparation

Micelles were formed by film-hydration. To prepare micelles with 10% functional groups on the surface, ben-PCL_7-PEG_{2000} and ben-PCL_7-PEG_{2000}-DBCO were dissolved in dichloromethane (DCM, Sigma Aldrich, Saint Louis, MS, USA) and mixed in a 9:1 weight ratio in a 5 ml glass vial (VWR, Radnor, PA, USA). To this mixture, the hydrophobic photosensitizer mTHPC (*meta*-tetra(hydroxyphenyl) chlorine, Biolitec AG, Jena, Germany) in tetrahydrofuran (THF, Sigma Aldrich, Saint Louis, MS, USA) was added at a 5% *w/w* mTHPC/polymer ratio. DCM and THF were evaporated under vacuum. The obtained polymer film was hydrated to a 20 mg/ml solution in PBS for 2 hrs at RT, gently heated to 60°C, and filtered through a 0.22 µm filter. To obtain micelles with 5% surface coverage with VHH 7D12[Fluo], the DBCO-micelles were reacted with 7D12[Fluo]-N_3 in a 2:1 molar DBCO:N_3 ratio. To ensure efficient click reaction kinetics, we kept the N_3 and DBCO concentration >100 µM. Reactions were allowed to proceed overnight in the dark at 4°C with continuous shaking at 450 rpm. The final product was analyzed by SDS-PAGE under reducing conditions (Fluorescein signal and CBB staining). Non-targeted mTHPC-ben-PCL_7-PEG_{2000} micelles were prepared according to the same procedure, but without incubation with 7D12[Fluo]-N_3.

Cell culture

The EGFR-overexpressing squamous carcinoma cell line A431 and the EGFR-negative glioma cell line E98[34] were cultured in DMEM (Lonza, Basel, Switzerland) supplemented with 10% fetal calf serum (FCS, Gibco, Thermo Fisher Scientific, Waltham, MA USA) and 40 µg/ml gentamycin (Centrafarm, Etten-Leur, The Netherlands). Cells were incubated at 37°C in 5% CO_2 in a humidified atmosphere.

Flow cytometry and confocal fluorescence microscopy analysis

Cells were dissociated from culture flasks with 10 mM EDTA, counted and transferred to V-bottom shaped 96-well microplates (BD Biosciences, Franklin Lakes, NJ, USA) at $5x10^5$ cells/well. All subsequent steps were done on ice and all washing steps were executed by centrifugation of the plates at 1,500xg for 2 min. Cells were washed twice with PBS and aspecific binding sites were blocked by preincubating cells for 10 min with PBA (PBS, 0.5%BSA, 2%

FCS). Subsequently cells were incubated with 1 μM fluorescein-labeled VHHs in PBA for 20 min, washed and resuspended in PBA and analysed using the CyAn ADP analyzer (Beckman Coulter, Fullerton, CA, USA).

To analyse uptake of VHH-micelles with flow cytometry, cells were grown to 80% confluency in 8 well chambered glass slides (NUNC, Thermo Fisher Scientific, Waltham, MA, USA) and incubated with 20 μM (= 0.6 mg/ml) targeted or non-targeted mTHPC-micelles or equimolar VHH concentrations at 37°C for 30 min. Cells were washed twice with warm DMEM and dissociated with trypsin at 37°C. Then cells were taken up in PBA and analyzed using the CyAn flow cytometer. mTHPC was quantified with parameter FL-8, fluorescein was quantified with parameter FL-1. To visualize binding and uptake with confocal microscopy A431 and E98 cells were grown in 8 wells Lab-Tek borosilicate coverglass chambers (Nunc, ThermoFisher Scientific, Waltham, MA, USA), and incubated with the micelles and controls as described for flow cytometry. After washing, cells were kept in phenol red free DMEM supplemented with 20 mM HEPES, and imaged on a TCS SP8 microscope (Leica Microsystems, Mannheim, Germany) equipped with a HC PL APO C5 40x/0.85 dry objective. During imaging, cells were maintained at 37°C. The UV405 laser was used for excitation, and emission was collected between 500 and 600 nm for fluorescein and 630 and 730 nm for mTHPC.

5

SUPPORTING INFORMATION –
COMPARISON OF SORTASE A VARIANTS AND APPLICABILITY TO OTHER VHHS

Results: efficiency of $H_2N-PEG_3-N_3$ conjugation by sortase A variants

Various variants of *S.Aureus* wild-type sortase A have been generated, with either an N-terminal deletion of 25 amino acids (sortase A Δ25)[1] or 59 amino acids (sortase A Δ59)[2,3]. The molecular weight is different, but the enzymatic activity is stated to be identical[4]. Furthermore, sortase A mutants have been developed which show faster LPETG cleavage rates but have lower affinity for H_2N-GGG[5].

It has been shown that H_2N-PEG_x-X is substrate for sortase A Δ59, but it is not clear how the sortase A mutants behave in this respect. Therefore we tested the following variants for their capability to use $H_2N-PEG_3-N_3$ as a substrate: N-terminal 6xHis-tagged sortase A Δ25[1], C-terminal 6xHis-tagged sortase A Δ59 with an N-terminal Gb1 domain to enhance solubility of the protein[6], tri-mutant sortase A (P94S/D160N/D165A), tetra-mutant sortase A (P94S/D160N/D165A/K196T) and penta-mutant sortase A (P94R/D160N/D165A/K190E/K196T). Sortase A variants were expressed and purity and correct mass was confirmed with CBB stained SDS-PAGE gels and LC-MS (Figure S1A+B).

	Calculated mass (Da)	Observed mass (Da)
Sortase A Δ25	21947	21948
Sortase A Δ59	24352	24353
tri-mutant sortase A	17810	17809.8
tetra-mutant sortase A	17783	17783
penta-mutant sortase A	17853.1	17852.5
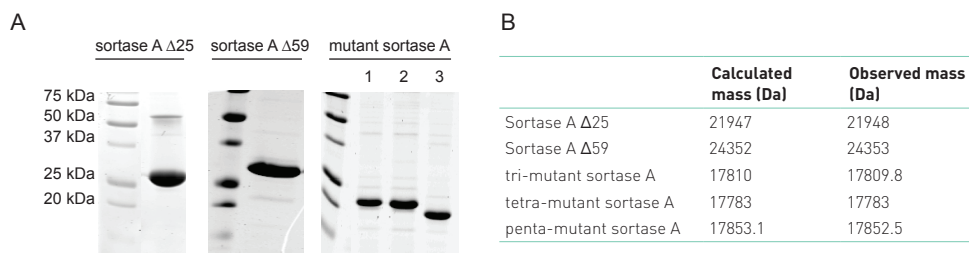
Figure S1. A) CBB stained SDS-PAGE gels showing expression and purity of the sortase A variants, 1 = tri-mutant sortase A, 2 = tetra-mutant sortase A, 3 = penta-mutant sortase A. B) Size of the various sortase A variants as verified with LC-MS.

Subsequently, they were tested for their capacity to conjugate VHH-LPETG-8xHis-Vsv to $H_2N-PEG_3-N_3$ at a molar ratio of 1:500. For penta-mutant sortase A, complete hydrolysis of the acyl intermediate was observed within 15 minutes, but there was no incorporation of $H_2N-PEG_3-N_3$ (data not shown). The tetra,- and tri-mutant showed efficient incorporation of $H_2N-PEG_3-N_3$ at these concentrations (Figure S2A). Further optimalization showed that at a sortase A:VHH-LPETG-8xHis-Vsv ratio of 1:5, <50% and >90% conversion to hydrolyzed VHH-LPET was observed after reacting for 4 hours for tri-mutant and tetra-mutant sortase A, respectively (Figure S2B). Furthermore >90% and ~50% incorporation of $H_2N-PEG_3-N_3$ was observed at a

100-fold molar excess of $H_2N-PEG_3-N_3$ over VHH-LPETG-8xHis-Vsv (Figure S2C). Results of these experiments and further optimization resulted in best efficiencies with sortase A:VHH-LPETG-8xHis-Vsv:$H_2N-PEG_3-N_3$ ratios of 1:2:400 and 1:4:2,000 for tri-mutant and tetra-mutant sortase A, respectively.

The N-terminally 6xHis-tagged sortase A Δ25 efficiently incorporated $H_2N-PEG_3-N_3$, however, during the reaction, hydrolysis of sortase A Δ25 at the N-terminus was observed (Figure S2D). The final reaction mixture therefore contained non-6xHis-tagged sortase A Δ25 that could not be removed with Ni-NTA beads. This variant was therefore excluded from further work.
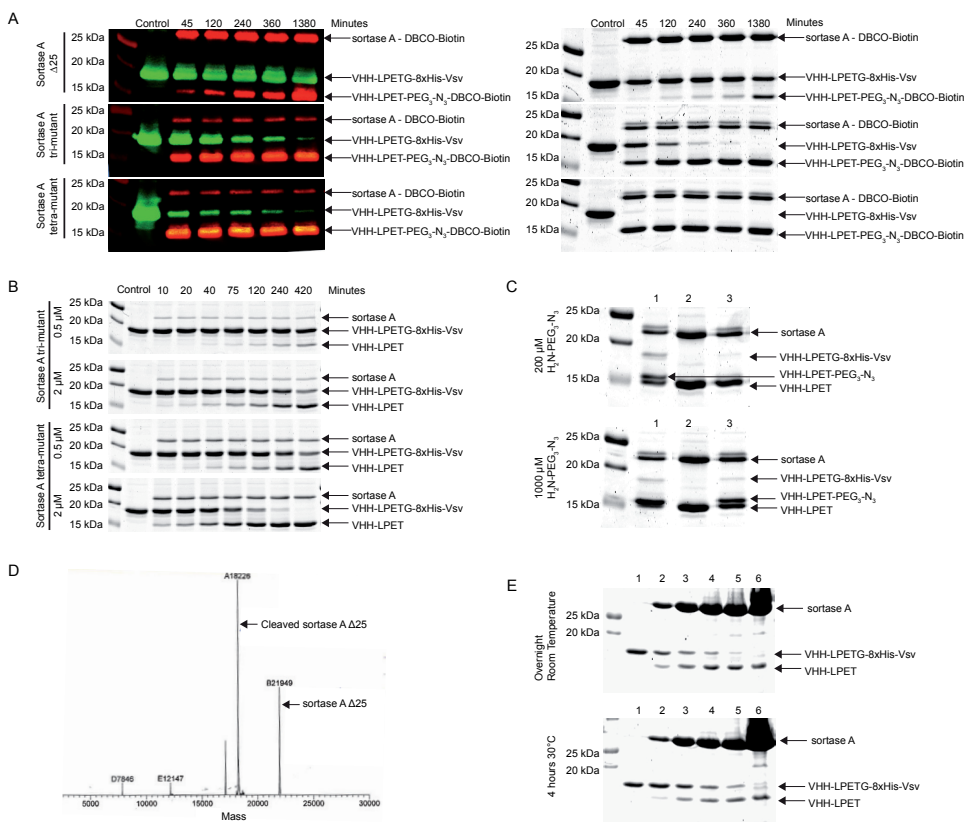
Figure S2. A) Western blot (left) and CBB stained SDS-PAGE gel (right) showing time-dependent cleavage of VHH-LPETG-8xHis-Vsv and subsequent incorporation of $H_2N-PEG_3-N_3$ by different sortase A mutants, followed by chemical clicking with DBCO-biotin. The control represents intact VHH-LPETG-8xHis-Vsv and the other lanes contain the reaction mixture of 10 μM VHH-LPETG-8xHis-Vsv with 5 μM sortase A and 5 mM $H_2N-PEG_3-N_3$ at various incubation times. On the western blot the VHH-LPETG-8xHis-Vsv is stained in green with anti-Vsv and anti-mouse DyeLight800. VHH-LPET-PEG$_3$-N$_3$-DBCO-Biotin is stained in red with Streptavidin Alexa680 conjugate. Since during sample heating the sortase A protein reacts with DBCO-

biotin as well, this product is also visible as a red band on the blot . B) CBB stained SDS-PAGE gel showing the rate of hydrolysis of the acyl intermediate formed when incubating 10 µM VHH-LPETG-8xHis-Vsv with 0.5 and 2 µM tri-, and tetra-mutant sortase A. C) CBB stained SDS-PAGE gel showing either hydrolysis or incorporation of 200 µM or 1000 µM H_2N-PEG_3-N_3 when incubating 10 µM VHH-LPETG-8xHis-Vsv with 5 µM tri,- or 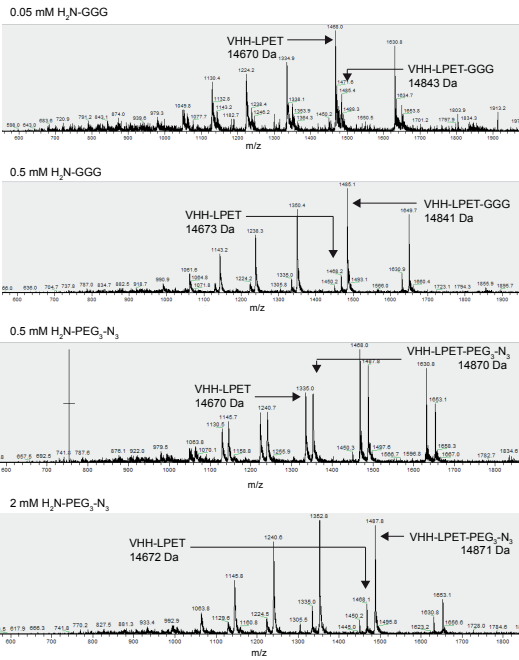tetra-mutant sortase A. 1 = tri-mutant sortase A reaction mixture, 2 = control reaction mixture without NH_2-PEG_3-N_3, 3 = tetra-mutant sortase A reaction mixture. D) LC-MS deconvoluted spectrum showing the intact sortase A Δ25, and the 18226 Da product resulting from cleavage of the N-terminal domain. E) CBB stained SDS-PAGE gel showing the rate of hydrolysis of the acyl intermediate formed when incubating 20 µM VHH-LPETG-8xHis-Vsv with increasing concentrations of sortase A Δ59 for either overnight at room temperature or 4 hours at 30°C. Lane 1 = intact VHH-LPETG-8xHis-Vsv, lane 2 to 6 represent ratios of sortase A Δ59:VHH-LPETG-8xHis-Vsv of 1:20, 1:4, 1:2, 1:1 and 2.5:1, respectively.

For sortase A Δ59, the optimal sortase A:VHH-LPETG-8xHis-Vsv ratio was 2.5:1 when reacting for 4 hours at 30°C (Figure S2E). Incorporation of H_2N-PEG_3-N_3 was found to be >90% complete when adding an 100-fold molar excess over VHH-LPETG-8xHis-Vsv (Figure S3A). From these experiments we deduced a sortase A:VHH-LPETG-8xHis-Vsv:H_2N-PEG_3-N_3 ratio of 2.5:1:200. When using these conditions in an overnight reaction at room temperature however, we still observed uncleaved VHH-LPETG-8xHis-Vsv, so we increased the VHH concentration and found that a sortase A:VHH-LPETG-8xHis-Vsv:H_2N-PEG_3-N_3 ratio of 1:1:80 led to complete probe incorporation.

Results: comparison of H_2N-GGG to H_2N-PEG_3-N_3 incorporation

Incorporation of H_2N-PEG_3-N_3 by tri-mutant sortase A and sortase A Δ59 was compared to incorporation of H_2N-GGG, the classical substrate of the enzyme. For sortase A Δ59 >90% incorporation was observed at a 25-fold molar excess of H_2N-GGG over VHH-LPETG-8xHis-Vsv, and at a 100-fold molar excess for H_2N-PEG_3-N_3 (Figure S3A). H_2N-GGG incorporation by tri-mutant sortase A is 10x more efficient than H_2N-PEG_3-N_3 incorporation, since complete incorporation of H_2N-GGG was already observed at a 20-fold molar excess of H_2N-GGG over VHH-LPETG-8xHis-Vsv compared to a 200-fold molar excess of H_2N-PEG_3-N_3 (Figure S3B).

A

0.05 mM H$_2$N-GGG

VHH-LPET
14670 Da

VHH-LPET-GGG
14843 Da

m/z

0.5 mM H$_2$N-GGG

VHH-LPET
14673 Da

VHH-LPET-GGG
14841 Da

m/z

0.5 mM H$_2$N-PEG$_3$-N$_3$

VHH-LPET
14670 Da

VHH-LPET-PEG$_3$-N$_3$
14870 Da

m/z

2 mM H$_2$N-PEG$_3$-N$_3$

VHH-LPET
14672 Da

VHH-LPET-PEG$_3$-N$_3$
14871 Da

m/z

B

0.2 mM H$_2$N-GGG

VHH-LPET-GGG

Mass

m/z

2 mM H$_2$N-GGG

VHH-LPET-GGG

Mass

m/z

0.2 mM H$_2$N-PEG$_3$-N$_3$

VHH-LPET

VHH-LPET-PEG$_3$-N$_3$

Mass

m/z

2 mM H$_2$N-PEG$_3$-N$_3$

VHH-LPET-PEG$_3$-N$_3$

VHH-LPET

Mass

m/z

5

Figure S3. A) LC-MS analysis showing total mass spectra of the total reaction mixture of 20 µM VHH-LPETG-8xHis-Vsv, 100 µM sortase A Δ59 and either 0.05 mM H2N-GGG, 0.5 mM H_2N-GGG, 0.5 mM H_2N-PEG$_3$-N$_3$ or 2 mM H_2N-PEG$_3$-N$_3$ after 4 hours at 30°C. B) LC-MS analysis showing deconvoluted (left) and total mass (right) spectra of the total reaction mixture of 20 µM VHH-LPETG-8xHis-Vsv, 10 µM tri-mutant sortase A and either 0.2 mM or 2 mM of H_2N-GGG or H_2N-PEG$_3$-N$_3$ after 4 hours at 30°C.

Results: applicability of sortase A conjugations to other VHHs

Sortase A as a method to produce clickable VHHs can also be applied to other VHHs, as is shown by successful production of A9-N$_3$, A9-DBCO, CC7-N$_3$[7] and CC7-DBCO (Figure S4A+B+C+D, respectively). The azide functionalized A9 and CC7 could also be conjugated successfully to ben-PCL$_7$-mPEG$_{2000}$-DBCO polymers as observed on CBB stained SDS-PAGE gels (Figure S5A+B). Furthermore [N]CC7[C]-[C]CC7[N] dimers could be produced with the 2 clickable VHHs, as was verified with LC-MS (Figure S5C), and this product was stable over 50 hours at 37°C (Figure S5D).

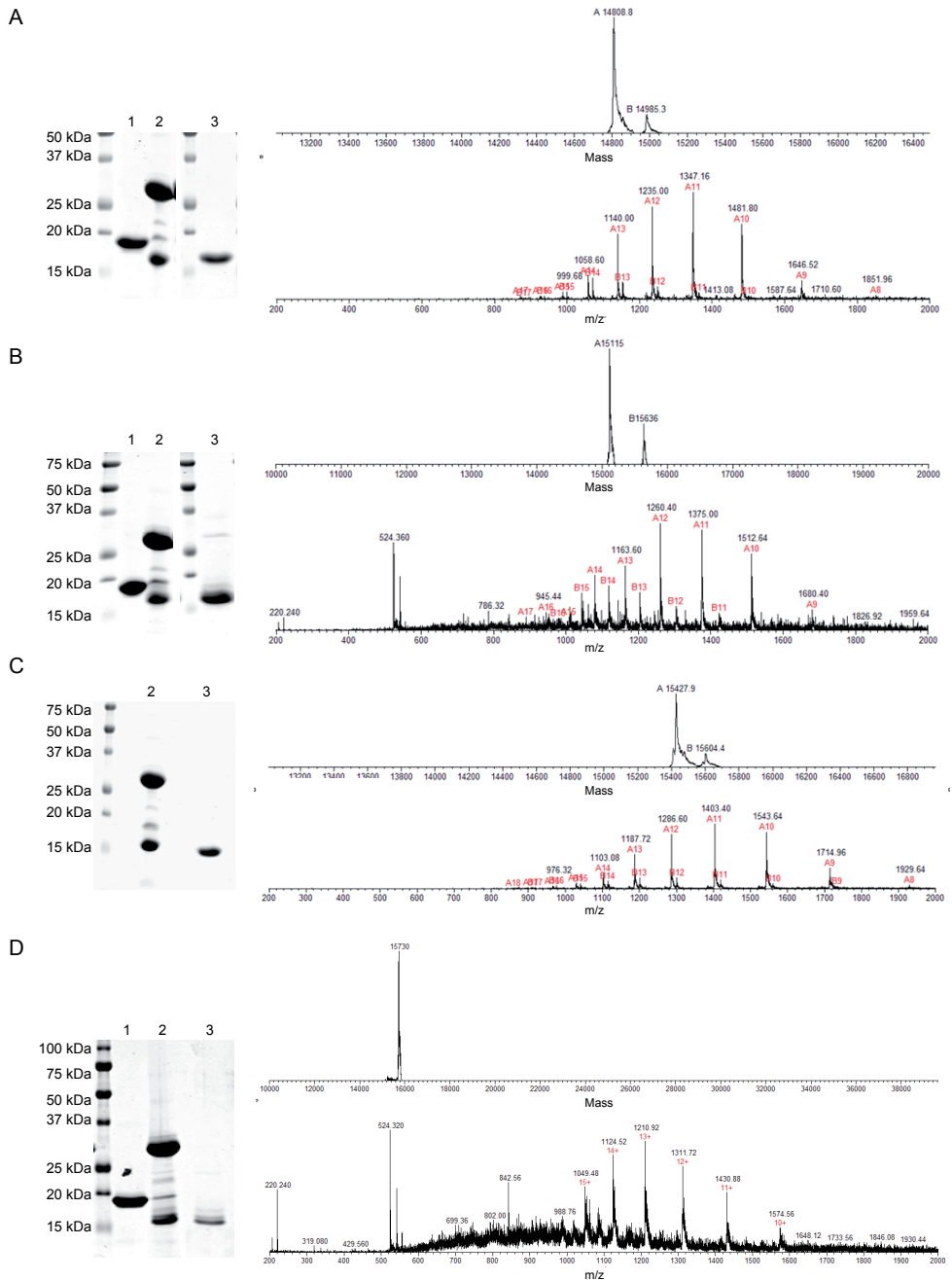**Figure S4.** CBB stained SDS-PAGE gels (1 = unconjugated VHH-LPETG-8xHis-Vsv, 2 = sortase A reaction mixture, 3 = purified VHH-DBCO or VHH-N$_3$) and LC-MS deconvoluted (upper) and total mass (lower) spectra showing successful conjugation of (A) A9-N$_3$ (expected 14809.5 Da, observed 14808.8 Da and a small fraction of unknown composition of 14985.3 Da), (B) A9-DBCO (expected 15114.9 Da, observed 15115

Da and a small fraction of unknown composition of 15636 Da), (C) CC7-N$_3$ (expected 15425.1 Da, observed 15427.9 Da and a small fraction of unknown composition of 15604.4 Da), (D) CC7-DBCO (expected 15730.5 Da, observed 15730 Da).
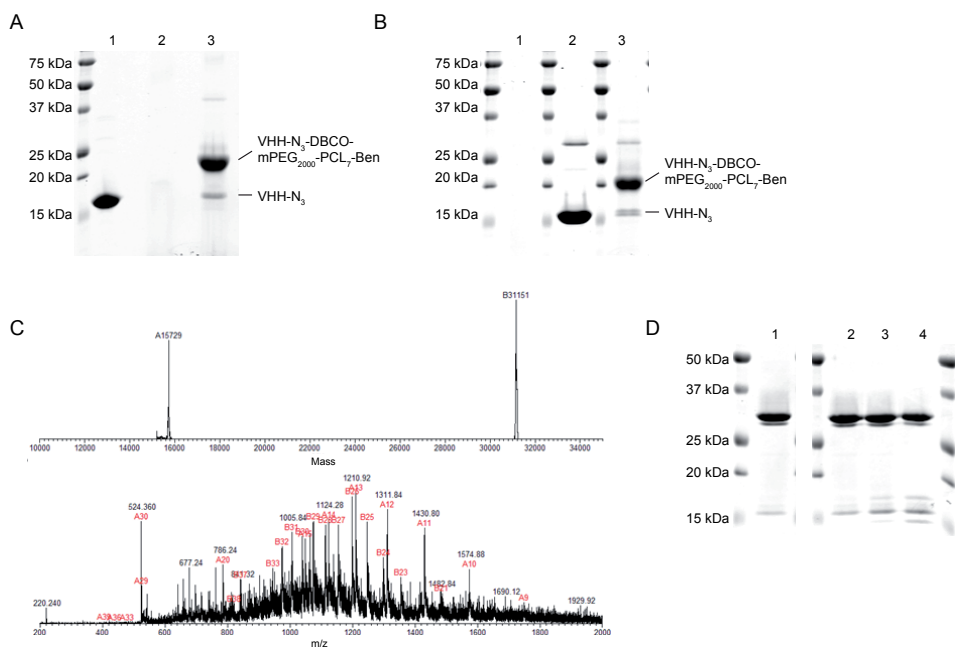
Figure S5. A) CBB stained SDS-PAGE gel showing the SPAAC reaction between A9-N$_3$ and DBCO micelles. 1 = A9-N$_3$, 2 = 10% DBCO micelles, 3 = 10% DBCO micelles and 10% A9-N$_3$. B) CBB stained SDS-PAGE gel showing the SPAAC reaction between CC7-N$_3$ and DBCO micelles. 1 = 10% DBCO micelles, 2 = CC7-N$_3$, 3 = 10% DBCO micelles and 10% CC7-N$_3$. C) LC-MS analysis showing deconvoluted (upper) and total mass spectrum (lower) of ^{N}CC7^{C} -^{C}CC7^{N} before sephadex purification (expected 31151 Da, observed 31151 Da and 15729 Da (excess of CC7-DBCO)). D) CBB stained SDS-PAGE analysis showing the stability of ^{N}CC7^{C} -^{C}CC7^{N}. 1, 2, 3, 4 = ^{N}CC7^{C}-^{C}CC7^{N} after 0, 4, 20 and 50 hours incubation at 37°C, respectively.

Methods: efficiency of H$_2$N-PEG-N$_3$ conjugation by sortase A Δ25 and sortase A mutants

pQE30-SortA (sortase A Δ25) and pQE29-penta-mutant sortase A, pQE29-tetra-mutant sortase A or pQE29-penta-mutant sortase A were transformed into E.Coli ER2566 and protein was produced and purified as described for pGBMCS-SortA (sortase A Δ59). Purity of the protein was assessed by CBB stained SDS-PAGE gel under reducing conditions and LC-MS. Concentration was determined by absorbance at 280 nm using a Nanodrop spectrophotometer.

To check the capacity of the tri,- tetra,- and penta,- mutant sortase A and sortase A Δ25 to incorporate H$_2$N-PEG$_3$-N$_3$, 10 µM VHH-LPETG-8xHis-Vsv was incubated with 5 µM of the sortase A variants and 5 mM H$_2$N-PEG$_2$-N$_3$ in presence of 10 mM CaCl$_2$ in 50 mM TRIS-HCL pH 7.5, NaCl 500 mM. Samples of the reaction mixture were taken after various incubation times, and excess H$_2$N-PEG$_3$-N$_3$ was removed by filtration over a 10 kDa MWCO centrifugal unit employing 4 washing cycles with PBS. EDTA was added to a final concentration of 20 mM, to inactivate sortase A. Then VHHs were incubated with a 500 fold molar excess DBCO-biotin (Sigma) for 2 hours at 30°C, and these samples were run on a 15% SDS-PAGE gel under reducing conditions, after which they were blotted onto nitrocellulose. The blot was blocked with LI-COR blocking buffer and incubated with 1:20,000 Streptavidin AlexaFluor680 (Invitrogen) and 1:2,000 mouse-anti-Vsv and goat-anti-mouse IgG Dylight800 (Thermo). Signal was visualized on the Odyssey CLx infrared imaging system.

The effect of sortase A enzyme concentrations was determined by incubating 10 uM VHH-LPETG-8xHis-Vsv with 2 or 0.5 µM tri-mutant or tetra-mutant sortase A for 7 hours at RT. Again samples were taken after various incubation times, and the presence of hydrolyzed acyl intermediate was analyzed on CBB stained 15% SDS-PAGE gels under reducing conditions. The effect of H$_2$N-PEG$_3$-N$_3$ was determined by incubating 10 µM VHH-LPETG-8xHis-Vsv with 5 µM sortase and either 200 µM of 1000 µM H$_2$N-PEG$_3$-N$_3$ for 4 hours at 30°C. Reaction products were analyzed on CBB stained SDS-PAGE gel.

For sortase A Δ59 the optimal sortase A:VHH ratio was determined by incubating 20 µM VHH-LPETG-8xHis-Vsv with increasing concentrations of sortase A Δ59 for 4 hours at 30°C or overnight at room temperature. Reaction products were analyzed on CBB stained SDS-PAGE gel.

Methods: comparison of H$_2$N-GGG to H$_2$N-PEG$_3$-N$_3$ incorporation

To compare efficiency of H$_2$N-GGG versus H$_2$N-PEG$_3$-N$_3$ incorporation by sortase A Δ59, 20 µM VHH-LPETG-8xHis-Vsv was incubated with 100 µM sortase A Δ59 and either 0.05 mM or 0.5 mM of H$_2$N-GGG or 0.5 mM or 2 mM of H$_2$N-PEG$_2$-N$_3$ in presence of 10 mM CaCl2 in 50 mM TRIS-HCL pH 7.5, NaCl 500 mM for 4 hours at 30°C. Similar experiments were performed for tri-mutant sortase A by incubating 20 µM VHH-LPETG-8xHis-Vsv with 10 µM tri-mutant sortase A and either 0.2 mM or 2 mM of H$_2$N-GGG or H$_2$N-PEG$_3$-N$_3$ for 4 hours at 30°C. Whole reaction mixtures were analyzed using LC-MS.

5

Methods: applicability of sortase A conjugations to other VHHs

VHHs CC7[7] and A9 (non-published) were expressed and purified as described for 7D12 and 4E4. Conjugation of SPAAC click probes was done by incubating 50 µM VHH-LPETG-8xHis-Vsv with 50 µM sortase A Δ59 and 4 mM H_2N-PEG$_3$-X in presence of 10 mM CaCl2 in 50 mM Tris-HCL pH 7.5 and 150 mM NaCl overnight at RT. VHH-N_3 was conjugated to DBCO micelles and VHH-DBCO as described for 7D12 in the main text.

REFERENCES

1. Barenholz, Y. C., Doxil(R) - The first FDA-approved nano-drug: Lessons learned. *J Control Release* **2012,** *160* (2), 117-34.

2. Dawidczyk, C. M.; Kim, C.; Park, J. H.; Russell, L. M.; Lee, K. H.; Pomper, M. G.; Searson, P. C., State-of-the-art in design rules for drug delivery platforms: lessons learned from FDA-approved nanomedicines. *J Control Release* **2014,** *187*, 133-44.

3. Gou, M.; Zheng, X.; Men, K.; Zhang, J.; Wang, B.; Lv, L.; Wang, X.; Zhao, Y.; Luo, F.; Chen, L.; Zhao, X.; Wei, Y.; Qian, Z., Self-assembled hydrophobic honokiol loaded MPEG-PCL diblock copolymer micelles. *Pharmaceutical research* **2009,** *26* (9), 2164-73.

4. Molavi, O.; Xiong, X. B.; Douglas, D.; Kneteman, N.; Nagata, S.; Pastan, I.; Chu, Q.; Lavasanifar, A.; Lai, R., Anti-CD30 antibody conjugated liposomal doxorubicin with significantly improved therapeutic efficacy against anaplastic large cell lymphoma. *Biomaterials* **2013,** *34* (34), 8718-25.

5. Arachchige, M. C.; Reshetnyak, Y. K.; Andreev, O. A., Advanced targeted nanomedicine. *J Biotechnol* **2015,** *202*, 88-97.

6. Fan, M.; Liang, X.; Yang, D.; Pan, X.; Li, Z.; Wang, H.; Shi, B., Epidermal growth factor receptor-targeted peptide conjugated phospholipid micelles for doxorubicin delivery. *J Drug Target* **2015**, 1-9.

7. Stemmler, H. J.; Kahlert, S.; Siekiera, W.; Untch, M.; Heinrich, B.; Heinemann, V., Prolonged survival of patients receiving trastuzumab beyond disease progression for HER2 overexpressing metastatic breast cancer (MBC). *Onkologie* **2005,** *28* (11), 582-6.

8. Grigorean, V. T.; Ciuhu, A. N.; Rahnea Nita, G.; Strambu, V.; Straja, D. N.; Popescu, M.; Sandu, A. M.; Rahnea Nita, R. A., Efficacy of cetuximab in metastatic colon cancer - case report. *Chirurgia (Bucur)* **2014,** *109* (3), 383-9.

9. Monteiro Ide, P.; Madureira, P.; de Vasconscelos, A.; Pozza, D. H.; de Mello, R. A., Targeting HER family in HER2-positive metastatic breast cancer: potential biomarkers and novel targeted therapies. *Pharmacogenomics* **2015,** *16* (3), 257-71.

10. Xie, C.; Jin, J.; Bao, X.; Zhan, W. H.; Han, T. Y.; Gan, M.; Zhang, C.; Wang, J., Inhibition of mitochondrial glutaminase activity reverses acquired erlotinib resistance in non-small cell lung cancer. *Oncotarget* **2015**.

11. Soucheray, M.; Capelletti, M.; Pulido, I.; Kuang, Y.; Paweletz, C. P.; Becker, J. H.; Kikuchi, E.; Xu, C.; Patel, T. B.; Al-Shahrour, F.; Carretero, J.; Wong, K. K.; Janne, P. A.; Shapiro, G. I.; Shimamura, T., Intratumoral Heterogeneity in EGFR-Mutant NSCLC Results in Divergent Resistance Mechanisms in Response to EGFR Tyrosine Kinase Inhibition. *Cancer Res* **2015,** *75* (20), 4372-83.

12. Lee, Y.; Wang, Y.; James, M.; Jeong, J. H.; You, M., Inhibition of IGF1R signaling abrogates resistance to afatinib (BIBW2992) in EGFR T790M mutant lung cancer cells. *Molecular carcinogenesis* **2015**.

13. Kijanka, M.; Dorresteijn, B.; Oliveira, S.; van Bergen en Henegouwen, P. M., Nanobody-based cancer therapy of solid tumors. *Nanomedicine (Lond)* **2015,** *10* (1), 161-74.

14. Chakravarty, R.; Goel, S.; Cai, W., Nanobody: the "magic bullet" for molecular imaging? *Theranostics* **2014,** *4* (4), 386-98.

15. Harmsen, M. M.; De Haard, H. J., Properties, production, and applications of camelid single-domain antibody fragments. *Appl. Microbiol. Biotechnol.* **2007,** *77* (1), 13-22.

16. Moghimi, S. M.; Rahbarizadeh, F.; Ahmadvand, D.; Parhamifar, L., Heavy Chain Only Antibodies: A New Paradigm in Personalized HER2+ Breast Cancer Therapy. *Bioimpacts* **2013**, *3* (1), 1-4.

17. Roovers, R. C.; Laeremans, T.; Huang, L.; De Taeye, S.; Verkleij, A. J.; Revets, H.; de Haard, H. J.; van Bergen en Henegouwen, P. M., Efficient inhibition of EGFR signaling and of tumour growth by antagonistic anti-EFGR Nanobodies. *Cancer immunology, immunotherapy : CII* **2007,** *56* (3), 303-317.

18. Heukers, R.; Altintas, I.; Raghoenath, S.; De Zan, E.; Pepermans, R.; Roovers, R. C.; Haselberg, R.; Hennink, W. E.; Schiffelers, R. M.; Kok, R. J.; van Bergen en Henegouwen, P. M., Targeting hepatocyte

growth factor receptor (Met) positive tumor cells using internalizing nanobody-decorated albumin nanoparticles. *Biomaterials* **2014,** *35* (1), 601-10.

19. Massa, S.; Xavier, C.; De Vos, J.; Caveliers, V.; Lahoutte, T.; Muyldermans, S.; Devoogdt, N., Site-specific labeling of cysteine-tagged camelid single-domain antibody-fragments for use in molecular imaging. *Bioconjug Chem* **2014,** *25* (5), 979-88.

20. Witte, M.D.; Cragnolini, J.J.; Dougan, S. K.; Yoder, N.C.; Popp, M. W.; Ploegh H., Preparation of unnatural N-to-N and C-to-C protein fusions. *Proc. Natl. Acd. Sci. U.S.A* **2012,** *109* (30), 11993-8

21. Rahbarizadeh, F.; Ahmadvand, D.; Sharifzadeh, Z., Nanobody; an old concept and new vehicle for immunotargeting. *Immunol Invest* **2011,** *40* (3), 299-338.

22. Debets, M. F.; van Berkel, S. S.; Schoffelen, S.; Rutjes, F. P.; van Hest, J. C.; van Delft, F. L., Aza-dibenzocyclooctynes for fast and efficient enzyme PEGylation via copper-free (3+2) cycloaddition. *Chem Commun (Camb)* **2010,** *46* (1), 97-9.

23. Chen, I.; Dorr, B. M.; Liu, D. R., A general strategy for the evolution of bond-forming enzymes using yeast display. *Proc. Natl. Acad. Sci. U.S.A.* **2011,** *108* (28), 11399-404

24. Roodink, I.; Raats, J.; van der Zwaag, B.; Verrijp, K;, Kusters, B.; van Bokhoven, H.; Linkels, M.; de Waal, R. M.; Leenders, W. P., Plexin D1 expression is induced on tumor vasculature and tumor cells: a novel target for diagnosis and therapy? *Cancer Res.* **2005,** *65* (18), 8317-23.

25.   Parthasarathy, R.; Subramanian, S.; Boder, E. T., Sortase A as a novel molecular "stapler" for sequence-specific protein conjugation. *Bioconjugate Chem.* **2007,** *18* (2), 469-76.

26. Baeuerle, P. A.; Reinhardt, C., Bispecific T-cell engaging antibodies for cancer therapy. *Cancer Res* **2009,** *69* (12), 4941-4.

27. Kontermann, R. E.; Brinkmann, U., Bispecific antibodies. *Drug Discov Today* **2015,** *20* (7), 838-47.

28. Els Conrath, K.; Lauwereys, M.; Wyns, L.; Muyldermans, S., Camel single-domain antibodies as modular building units in bispecific and bivalent antibody constructs. *J. Biol. Chem.* **2001,** *276* (10), 7346-50.

29. Veronese, F. M.; Mero, A., The impact of PEGylation on biological therapies. *BioDrugs : clinical immunotherapeutics, biopharmaceuticals and gene therapy* **2008,** *22* (5), 315-29.

30. Rashidian, M.; Wang, L.; Edens, J. G.; Jacobsen, J. T.; Hossain, I.; Wang, Q.; Victora, G. D.; Vasdev, N.; Ploegh, H.; Liang, S. H., Enzyme-Mediated Modification of Single-Domain Antibodies for Imaging Modalities with Different Characteristics. *Angew. Chem., Int. Ed. Engl.* **2016,** *55* (2), 528-33.

31. Hofman, J. W.; Carstens, M. G.; van Zeeland, F.; Helwig, C.; Flesch, F. M.; Hennink, W. E.; van Nostrum, C. F., Photocytotoxicity of mTHPC (temoporfin) loaded polymeric micelles mediated by lipase catalyzed degradation. *Pharm. Res.* **2008,** *25* (9), 2065-73.

32. Navis, A. C.; van Lith, S. A.; van Duijnhoven, S. M.; de Pooter, M.; Yetkin-Arik, B.; Wesseling, P.; Hendriks, W. J.; Venselaar, H.; Timmer, M.; van Cleef, P.; van Bergen En Henegouwen, P.; Best, M. G.; Wurdinger, T. D.; Tops, B. B.; Leenders, W. P., Identification of a novel MET mutation in high-grade glioma resulting in an auto-active intracellular protein. *Acta Neuropathol* **2015,** *130* (1), 131-44.

33. Roovers, R. C.; Vosjan, M. J.; Laeremans, T.; el Khoulati, R.; de Bruin, R. C.; Ferguson, K. M.; Verkleij, A. J.; van Dongen, G. A.; van Bergen en Henegouwen, P. M., A biparatopic anti-EGFR nanobody efficiently inhibits solid tumour growth. *Int J Cancer* **2011,** *129* (8), 2013-24.

34. Claes, A.; Schuuring, J.; Boots-Sprenger, S.; Hendriks-Cornelissen, S.; Dekkers, M.; van der Kogel, A. J.; Leenders, W. P.; Wesseling, P.; Jeuken, J. W., Phenotypic and genotypic characterization of orthotopic human glioma models and its relevance for the study of anti-glioma therapy. *Brain Pathol* **2008,** *18* (3), 423-33

REFERENCES SUPPORTING INFORMATION

1. Ton-That, H.; Liu, G.; Mazmanian, S. K.; Faull, K. F.; Schneewind, O., Purification and characterization of sortase, the transpeptidase that cleaves surface proteins of Staphylococcus aureus at the LPXTG motif. *Proc. Natl. Acad. Sci. U.S.A. 1999, 96* (22), 12424-9.

2. Ton-That, H.; Mazmanian, S. K.; Alksne, L.; Schneewind, O., Anchoring of surface proteins to the cell wall of Staphylococcus aureus. Cysteine 184 and histidine 120 of sortase form a thiolate-imidazolium ion pair for catalysis. *J. Biol. Chem.* **2002**, *277* (9), 7447-52.

3. Parthasarathy, R.; Subramanian, S.; Boder, E. T., Sortase A as a novel molecular "stapler" for sequence-specific protein conjugation. *Bioconjugugate Chem.* **2007**,*18* (2), 469-76.

4. Ilangovan, U.; Ton-That, H.; Iwahara, J.; Schneewind, O.; Clubb, R. T., Structure of sortase, the transpeptidase that anchors proteins to the cell wall of Staphylococcus aureus. *Proc. Natl. Acad. Sci. U.S.A.* **2009,** *98* (11), 6056-61.

5. Chen, I.; Dorr, B. M.; Liu, D. R., A general strategy for the evolution of bond-forming enzymes using yeast display. *Proc. Natl. Acad. Sci. U.S.A.* **2011,** *108* (28), 11399-404.

6. Kobashigawa, Y.; Kumeta, H.; Ogura, K.; Inagaki, F., Attachment of an NMR-invisible solubility enhancement tag using a sortase-mediated protein ligation method. *J. Biomol. NMR* **2009,** *43* (3), 145-50.

7. van Lith, S. A.; Roodink, I.; Verhoeff, J. J.; Makinen, P. I.; Lappalainen, J. P.; Yla-Herttuala, S.; Raats, J.; van Wijk, E.; Roepman, R.; Letteboer, S. J., In vivo phage display screening for tumor vascular targets in glioblastoma identifies a llama nanobody against dynactin-1-p150Glued. *Oncotarget* **2016,** *7* (44), 71594-7160

5
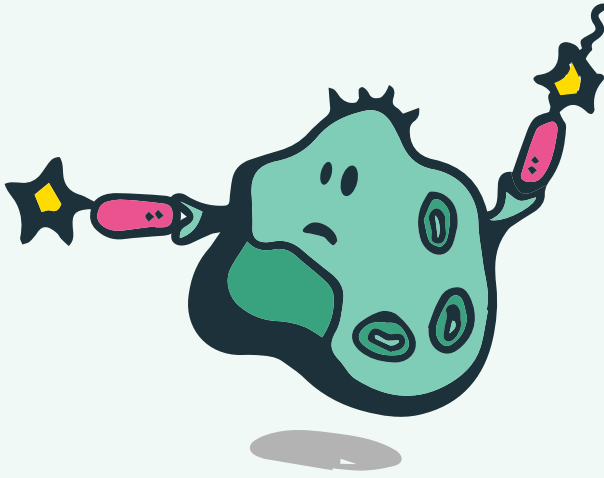
CHAPTER 6

A conjugate of an anti-Epidermal Growth Factor Receptor (EGFR) VHH and a cell-penetrating peptide drives receptor internalization and blocks EGFR activation

Sanne A.M. van Lith[1*], Dirk van den Brand[2,3], Rike Wallbrecher[2], Sander M.J. van Duijnhoven[1], Roland Brock[2], William P.J. Leenders[1,2]

*Authors contributed equally

[1]Department of Pathology, Radboud Institute for Molecular Life Sciences, Radboudumc, Nijmegen, The Netherlands
[2]Department of Biochemistry, Radboud Institute for Molecular Life Sciences, Radboudumc, Nijmegen, The Netherlands
[3]Department of Gynaecology, Radboud Institute for Molecular Life Sciences, Radboudumc, Nijmegen, The Netherlands

ABSTRACT

Overexpression of (mutated) receptor tyrosine kinases is a characteristic of many aggressive tumors and induction of receptor uptake has long been recognized as a therapeutic modality. A conjugate of a synthetically produced cell penetrating peptide (CPP), corresponding to amino acids 38-59 of human lactoferrin, and the recombinant llama single-domain antibody (VHH) 7D12 that binds the human epidermal growth factor receptor (EGFR), was generated via sortase A-mediated transpeptidation. The conjugate blocks EGF-mediated EGFR activation with higher efficacy than both modalities alone, a phenomenon that is caused by both effective receptor blockade and internalization. Thus, the VHH-cell penetrating peptide (VHH-CPP) conjugate shows a combination of activities that implements a highly powerful new design principle to block receptor activation by its clearance from the cell surface.

INTRODUCTION

The last decade has been characterized by enormous efforts to personalize the treatment of cancer patients via specific targeting of cancer cells, thereby reducing the adverse effects of chemotherapies that affect all proliferating cells in the body[1]. An important prototypic tumor target is the epidermal growth factor receptor (EGFR), a receptor tyrosine kinase which regulates many cellular processes such as proliferation, survival, cell motility and differentiation[2]. Deregulation of EGFR signaling caused by amplifications, activating point mutations, and truncations occurs in a wide range of tumor types, and it correlates with shortened disease-free and overall survival[3-5]. EGFR-targeting monoclonal antibodies (e.g. panitumumab, cetuximab) have become part of routine cancer treatment[6-7]. These monoclonal antibodies mainly act by blocking ligand binding and receptor dimerization[8], and by promoting internalization of EGFR and its degradation[9].

However, tumors acquire resistance to these agents via multiple mechanisms[10-12]. Also, because of their large size antibodies can only poorly penetrate tumors after extravasation. Thus, there is dire need to add new therapeutic modalities with novel molecular characteristics to the repertoire.

Single variable domains of heavy chain llama antibodies (VHHs) are an interesting alternative for standard antibodies. VHHs are characterized by high stability, small size and low immunogenicity while affinity for its target antigens can be as high as that of conventional antibodies[13-14]. VHH 7D12, which binds to domain III of the EGFR molecule, competes for binding of EGF and of the therapeutic antibody cetuximab[15]. However, because of their monovalency these molecules are poorly active in cross-linking receptors and inducing internalization[16]. Cell penetrating peptides (CPPs) have become a broadly utilized tool to drive cellular uptake of molecules that otherwise do not enter cells[17], such as oligonucleotides, nanoparticles, peptides and proteins[18-22]. A peptide corresponding to amino acids 38-59 of the human milk protein lactoferrin acts as an effective CPP[23-24]. This peptide (referred to as hLF) is of specific interest as it is expected to be non-immunogenic because of its human origin and also because it contains relatively little cationic residues which limits toxicity.

So far, the rationale for the use of CPPs has been restricted to the intracellular delivery of cargo. Here, we hypothesized that combination with a CPP would endow the VHH with new effector functionalities and that combining the receptor targeting capacity of the VHH with the internalization-inducing capacity of the CPP should accelerate clearance rate of the receptor from the cell surface.

Conventional methods to conjugate CPPs to proteins are faced with several challenges. Expression of CPP-fusion proteins is frequently compromised by poor expression of the polycationic peptide stretches. Our attempts to produce a functional VHH-hLF conjugate in E. coli was also ineffective (data not shown). For standard protein conjugations using side chain functionalities, maintenance of the chemical and biological properties of both

conjugate constituents strongly depends on the number and distribution of reactive groups. Intein-mediated protein ligation has been used to site-specifically introduce handles for click chemistry but this is a laborious method[25]. Alternatively, coupling can be performed by sortase A-mediated transpeptidation[26-29].

Herein, we used the enzyme sortase A for site-specific conjugation of 7D12 and the anti-cMet VHH G2[30], to GGG-hLF[Fluo] (Figure 1). The hLF peptide was synthesized with a C-terminal fluorescein label to enable detection of cell binding and trafficking. VHH G2 was included as a control since c-MET expression in A431 squamous carcinoma cells, used in this study, is much lower than EGFR expression (http://www.proteinatlas.org/.)

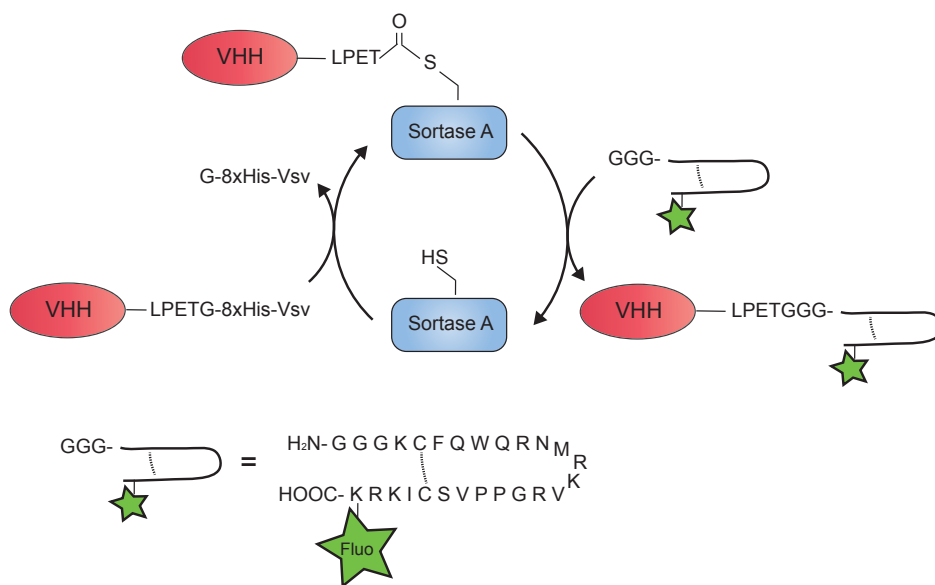**Figure 1.** Scheme of site-specific conjugation of a VHH equipped with a C-terminal LPETG amino acid tag to GGG-hLF[39-58] with sortase A. The used sortase A variant carried a carboxyterminal 6xHis-tag to allow a rapid and simple purification of the conjugate via Ni-bead adsorption of the byproducts. By placing the LPETG sortase A recognition sequence before the 8xHis-Vsv tags, these tags were removed during the reaction.

RESULTS AND DISCUSSION

Sortase A and VHH 7D12-LPETG-8xHis-Vsv or VHH G2-LPETG-8xHis-Vsv were expressed in E.Coli[29]. After purification of VHHs and sortase A from bacterial lysates, the GGG-hLF[Fluo] was coupled to the VHH via sortase-mediated transpeptidation and the VHH-LPETGGG-hLF[Fluo] (referred to as VHH-hLF[Fluo], Figure 2) conjugates were purified. For 7D12 and G2, coupling efficiencies were 89% and 91% respectively (Figure 3A). The masses observed for 7D12-hLF[Fluo] (18410 Da) and G2-hLF[Fluo] (18988 Da) corresponded well to the calculated molecular weights of 18415.5 Da and 18993.3 Da (Figure 3B).

For the non-conjugated VHHs, a cysteine residue was introduced just before the LPETG sequence, resulting in VHH-C-LPETG-8xHis-Vsv. The free thiol was used for labeling with maleimide fluorescein, resulting in 7D12-C[Fluo]-LPETG-8xHis-Vsv and G2-C[Fluo]-LPETG-8xHis-Vsv (referred to as VHH-C[Fluo], Figure 2), enabling monitoring of cell association and uptake for the VHHs. Successful and efficient conjugation was validated using LC-MS (Figure 3C). Of importance, all VHHs and conjugates carried exactly one fluorescein per VHH molecule, allowing reliable comparison of cell-associated fluorescence in functional studies.

6
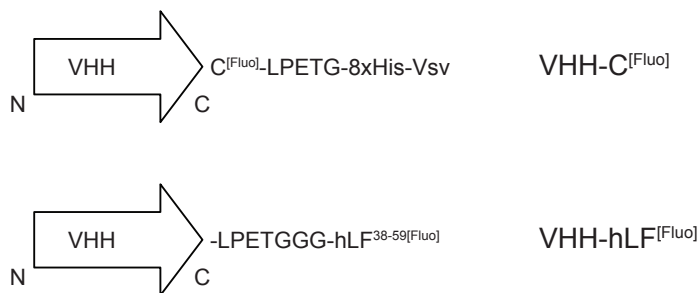
Figure 2. Schematic representation of the VHHs and the nomenclature used herein.
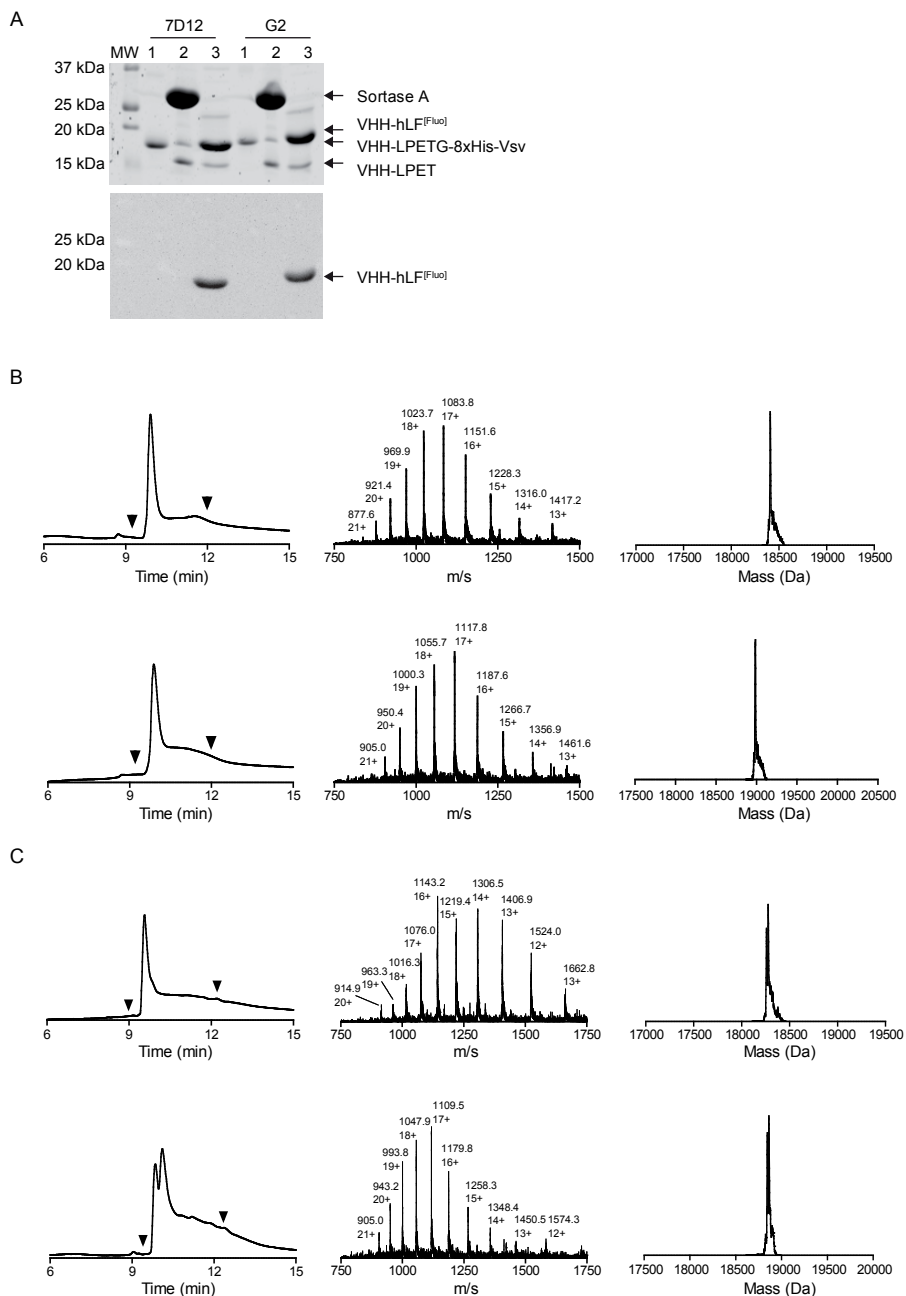
Figure 3. Analytical characterization of the conjugates. A) Coomassie brilliant blue stained SDS-PAGE gel of the reaction products and controls (1 = input VHH-LPETG-8xHis-Vsv, 2 = sortase A cleaved VHH-LPET, 3 = purified VHH-hLF[Fluo]). Upper picture shows absorption at 680 nm and lower picture shows fluorescein signal using UV excitation. LC-MS characterization of B) 7D12-hLF[Fluo] (upper, observed 18410

Da, calculated 18415.5 Da) and G2-hLF[Fluo] (lower, observed 18988 Da, calculated 18993.3 Da) and C) 7D12-C[Fluo] (upper, observed 18262.0 Da, calculated 18265.0 Da) and G2-C[Fluo] (lower, observed 18845.2 Da, calculated 18842.9 Da). The left graphs show the UV absorbance spectrum, the middle graphs the total mass spectrum of the UV-peak bracketed by arrowheads and the right graphs the deconvoluted mass spectrum.

Next, we assessed the functional consequences of the combination of moieties in the conjugates. Cellular binding, uptake and subcellular distribution of 7D12-hLF[Fluo] and G2-hLF[Fluo] were investigated in A431 cells using confocal laser scanning microscopy (Figure 4). Unconjugated GGG-hLF[Fluo] showed a punctate intracellular staining, indicating endocytic uptake, as typically observed for this CPP at concentrations below 10 µM[23] (Figure 4). 7D12-C[Fluo] showed intense membrane staining. In comparison to the free CPP, 7D12-hLF[Fluo] showed a much stronger cell-associated fluorescence than observed for GGG-hLF[Fluo] alone, but the distribution of the conjugate was much more endocytotic.

GGG-hLF[Fluo]   7D12-C[Fluo]   7D12-hLF[Fluo]

G2-C{Fluo}   G2-hLF[Fluo]

Figure 4. Cell binding and uptake of the constructs. A431 cells were incubated with 2 µM of the constructs for 30 min, washed and imaged by confocal laser scanning microscopy. The scale bar denotes 20 µm.

Cell-associated fluorescence of the conjugate was consistently lower than that of the free VHH. To check whether this was the result of loss of fluorescein fluorescence due to acidic pH in endosomes, chloroquin was added after construct incubation to inhibit endosomal acidification[31]. No increase in fluorescence was observed (data not shown). The dissociation constant derived from binding under non-internalizing conditions was 11.9 ± 1.2 nM for 7D12 alone and 25.5 ± 2.5 nM for the conjugate (Figure 5).
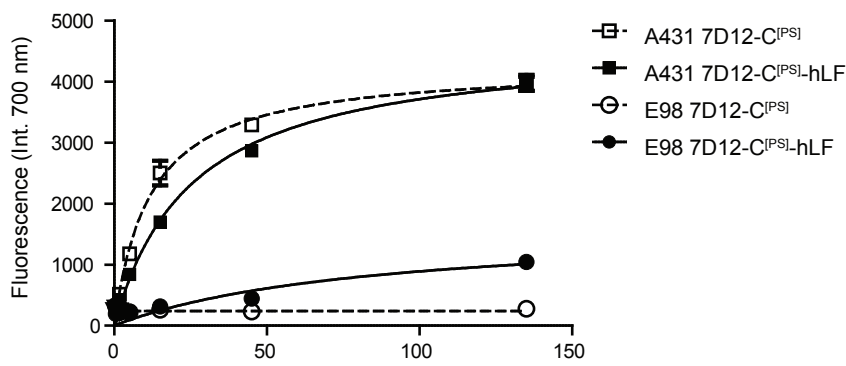
Figure 5. Cell binding of the constructs. Binding of various concentrations of 7D12-C[PS]- and 7D12-C[PS]-hLF to the cells was measured in cell ELISAs under non-internalizing conditions using PS fluorescence at 700 nm as readout. Note that in this experiment IRDye700DX with molecular weight similar to Fluorescein, was conjugated to the free thiol.

In agreement with low expression levels of c-Met in A431 cells, G2-C[Fluo] showed no cell-associated fluorescence (Figure 4). Conjugation of GGG-hLF[Fluo] to G2 induced some uptake, in line with the activity of hLF as a CPP but uptake of G2-hLF[Fluo] was much lower than of 7D12-hLF[Fluo] indicating that the interaction with the EGFR is crucial for efficient internalization. To further test EGFR specificity, identical assays were performed with cells of the EGFR-negative high-grade astrocytoma cell line E98, and no uptake was seen in these cells except, again, for little uptake of GGG-hLF[Fluo] (Figure 6). These experiments also show that affinity of 7D12 is not determined by the carboxyterminal 8xHis-Vsv tag. This is to be expected since target recognition of VHHs is mainly determined by the complementary determining regions (CDRs), which are located distant from the carboxy-terminal tags. Indeed the crystallized complex of 7D12 with EGFR showed that CDR1 and CDR3 contact domain III of EGFR[32].

GGG-hLF[Fluo]   7D12-C[Fluo]   7D12-hLF[Fluo]
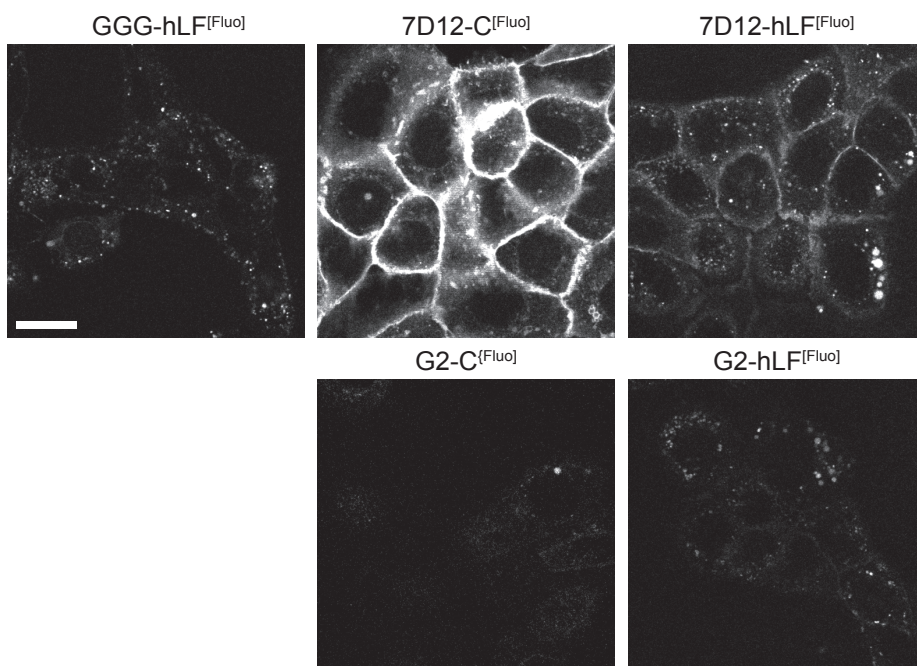
G2-C[Fluo]   G2-hLF[Fluo]

6
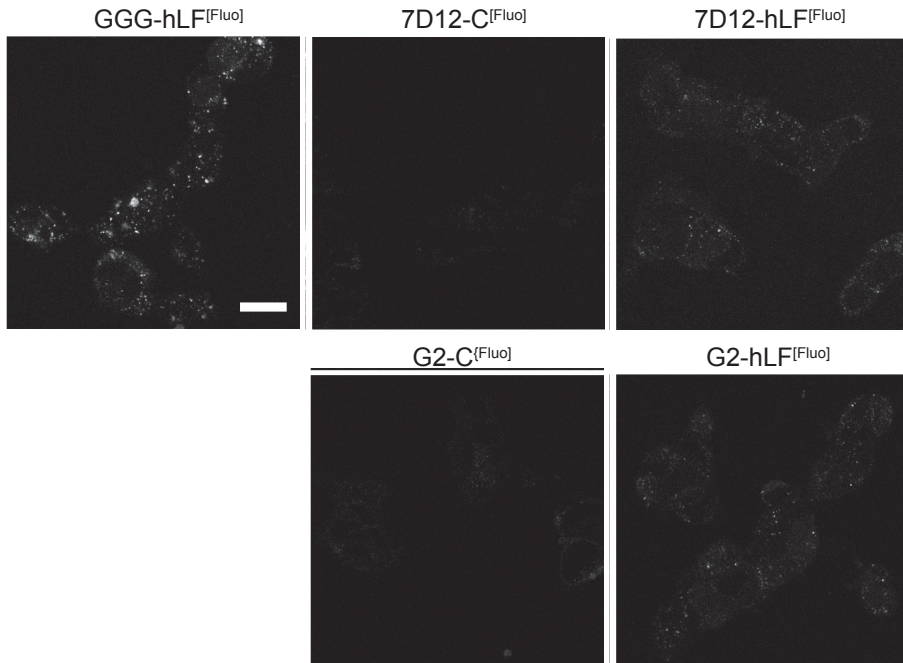
Figure 6. Cell binding and uptake of the constructs. E98 cells were incubated with 2 μM of the constructs for 30 min, washed and imaged by confocal laser scanning microscopy. The scale bar denotes 20 μm.

Next, we tested our hypothesis that 7D12-hLF[Fluo] induces EGFR internalization. Under normal physiological conditions, internalization of growth factor receptors is a consequence of receptor activation. However, internalization can also be induced in the absence of activation through crosslinking by antibodies or other binding moieties[33-36]. A431 cells were incubated with the various constructs in presence of LysoTracker Red, and immunostained for early endosome marker EEA-1 and EGFR. Colocalization of EGFR and early endosomes/lysosomes was increased in cells incubated with 7D12-hLF[Fluo] compared to control cells and cells incubated with 7D12-C[Fluo], which indicates that 7D12-hLF[Fluo] induces endosomal uptake of EGFR (Figure 7A+B).
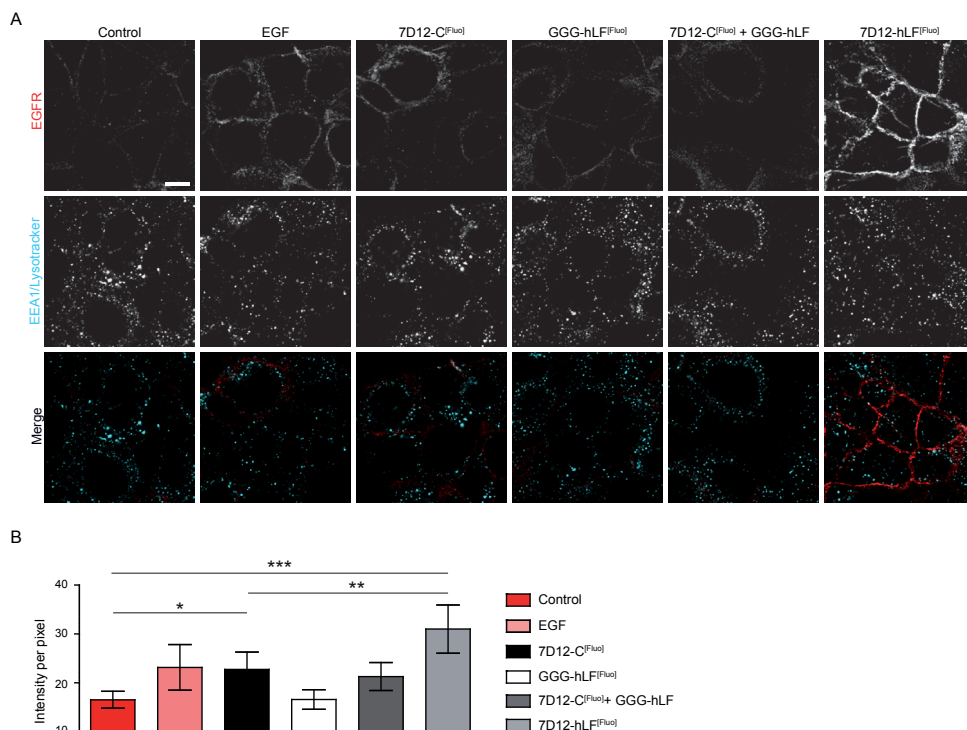
Figure 7. EGFR internalization after incubation with the constructs. A431 cells were incubated with 2 µM of the various contructs for 30 minutes or left untreated (control) in presence of LysoTracker Red DND99. Subsequently they were fixed, immunostained with anti-EGFR and anti-EEA-1 and imaged (A) Scale bar denotes 10 µM. The intensity per pixel of EEA-1/LysoTracker positive EGFR vesicles was quantified (B). * indicates significance for $p<0.05$, ** for $p<0.01$ and *** for $p<0.001$.

Besides induction of uptake, conjugation to hLF could also exert its effect by increased blockade of EGF binding as compared to 7D12. To address this point, A431 cells were incubated with conjugates and subsequently with EGF-biotin and streptavidin-Alexa594. Only 7D12-hLF[Fluo] caused near-complete inhibition of EGF binding (Figure 8). Since a major part of the conjugate was still membrane bound we conclude that the conjugate blocks the EGF binding site, or drives the receptor into a conformation that is incompatible with ligand binding. 7D12-C[Fluo] showed only a minor decrease in EGF binding and internalization compared to controls, and GGG-hLF[Fluo] did not inhibit EGF binding. To further investigate the separate effects on affinity and induction of target internalization, these experiments should be performed with other VHHs that bind non-internalizing target proteins.

A

B

Figure 8. Inhibition of EGF binding and internalization by the constructs. A431 cells were incubated with 2 μM of the various contstructs for 30 min or left untreated (control), after which they were incubated with EGF-biotin and streptavidin-Alexa594 and imaged (A). The scale bar denotes 10 μm. Total fluorescence of EGF (both internalized and membrane bound) was measured in regions of interest drawn in the corresponding brightfield images (B). ** indicates significance for $p < 0.01$ and *** for $p < 0.001$.

As the most critical aspect in relation to activity, we tested whether the constructs also inhibited receptor activation by EGF. To this end we incubated A431 cells with 7D12-C[Fluo] or 7D12-hLF[Fluo], using again the G2 variants as controls, followed by a 5-minute EGF activation. After fixation of cells immunofluorescent staining of EGFR and phosphorylated EGFR (pEGFR) was performed (Figure 9). 7D12-hLF[Fluo], but not hLF[Fluo] or 7D12-C[Fluo] significantly inhibited EGF-induced phosphorylation of EGFR. Incubation with constructs without EGF activation did not stimulate

EGFR phosphorylation, and as expected, G2 constructs did not interfere with EGFR activation by EGF (Figures 10 and 11). These results were confirmed on western blot (Figure 12). The lack of inhibition of EGF-induced EGFR activation by 7D12 is not in accordance with findings of Roovers et al.[37], who described a dose-dependent inhibition of EGF-induced phosphorylation by 7D12. The discrepancy between these results may be due to the experimental set up, as A431 cells express higher levels of EGFR than the HER14 cells that were used in the Roovers study. Also the difference in concentrations of EGF (16.6 nM as compared to 8 nM in the Roovers study), may have affected the results.
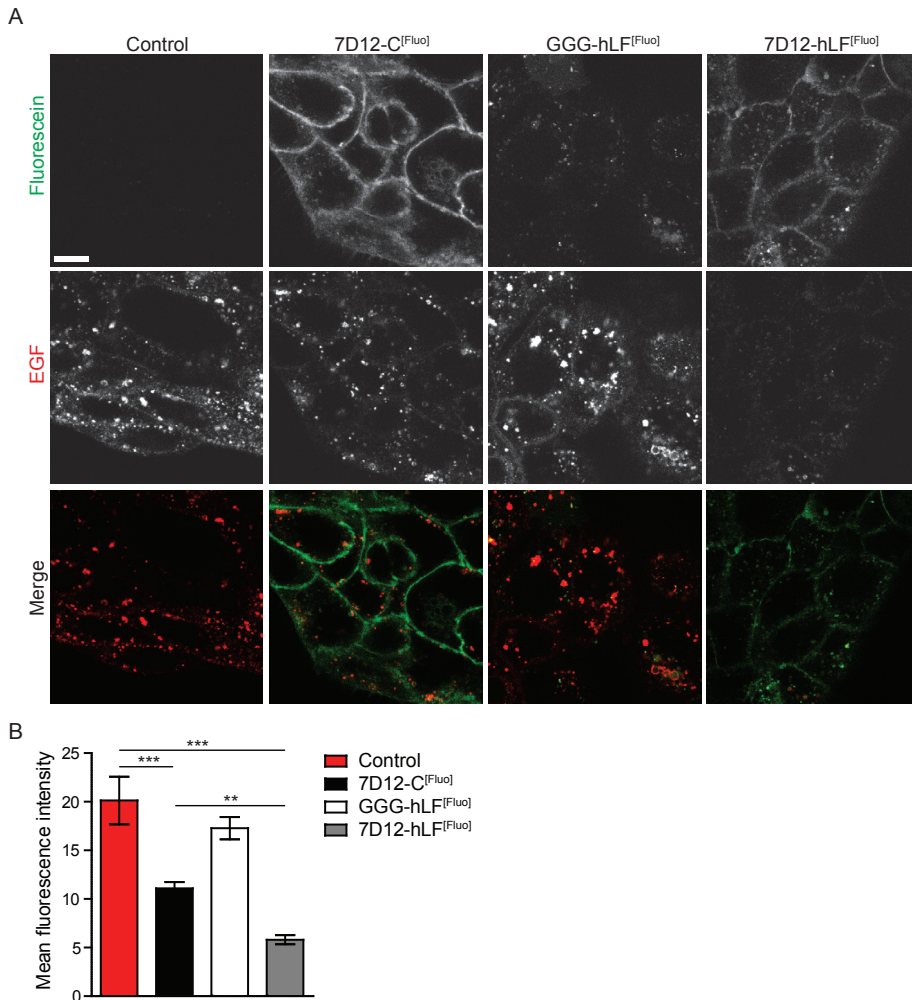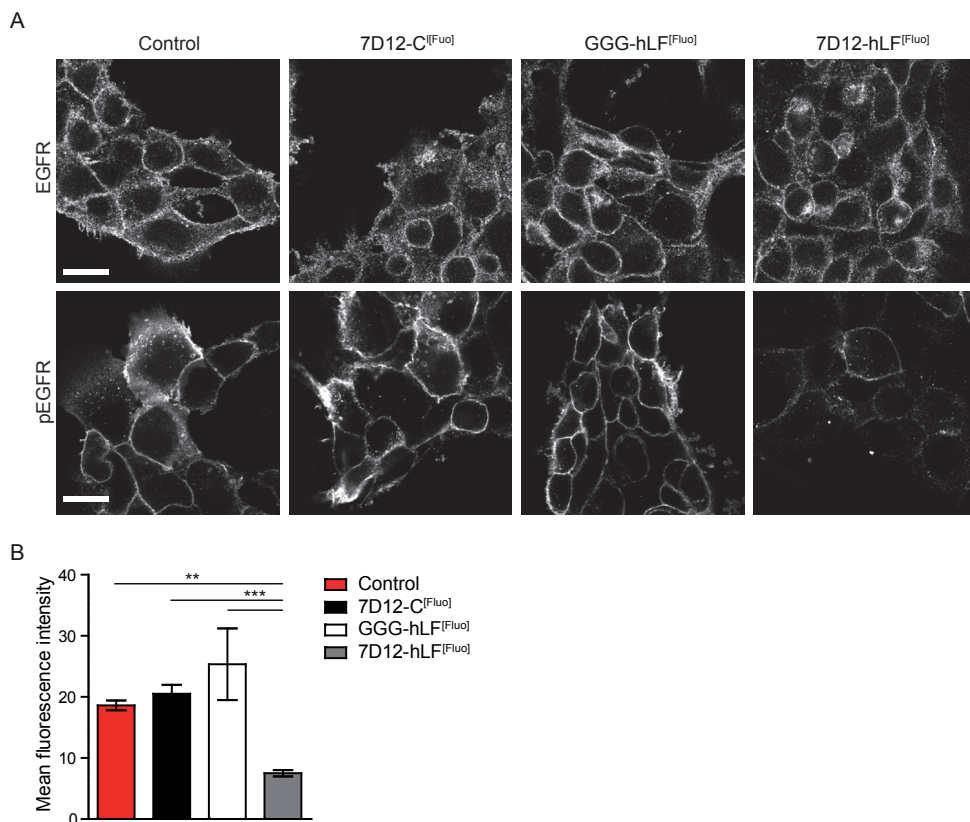

Figure 9. Inhibition of EGF induced EGFR phosphorylation by the constructs. A431 cells were incubated with 2 μM of the various constructs for 30 min or left untreated (control). After serum starvation, cells were activated with EGF and fixed. Then cells were immunostained with anti-EGFR or anti-pEGFR (A). Scale bar denotes 20 μm. Fluorescence intensities per pixel of the pEGFR signals were quantified (B). ** indicates significance for $p < 0.01$, ** for $p < 0.001$.
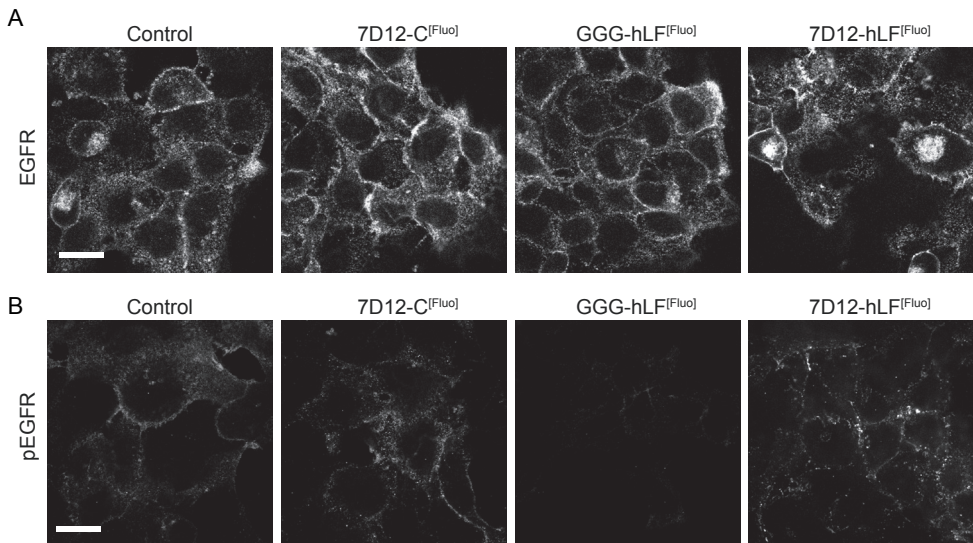
Figure 10. The constructs alone do not activate EGFR. A431 cells were incubated with 2 µM of the various constructs for 30 min or left untreated (control). After serum starvation ad fixation, cells were immunostained with anti-EGFR (A) or anti-pEGFR (B). Scale bar denotes 20 µm.

6
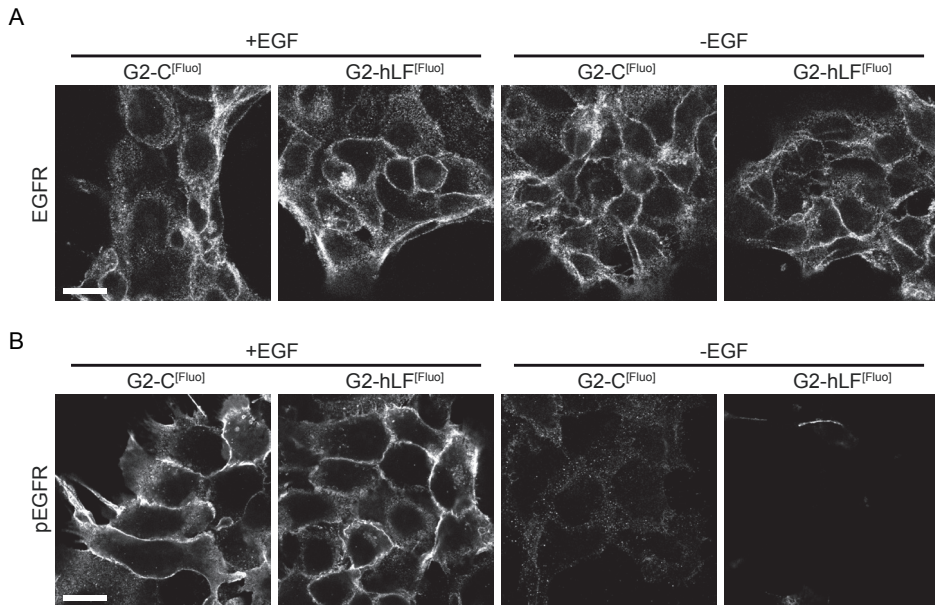
Figure 11. G2-constructs do not interfere with EGFR activation. A431 cells were incubated with 2 µM of the various constructs for 30 min or left untreated (control). After serum starvation, cells were activated with EGF. The samples were immunostained with anti-EGFR (A) or anti-pEGFR (B). Scale bar denotes 20 µm.

A
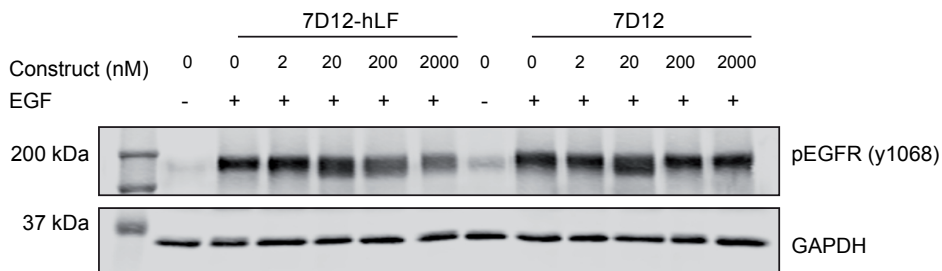
B
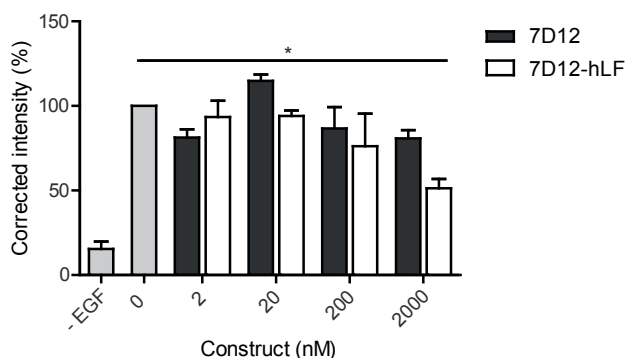
Figure 12. 7D12-LPETGGG-hLF[38-59] inhibits EGF induced EGFR activation. A431 cells were incubated for 30 min with either 7D12 or 7D12-hLF. After serum starvation cells were activated with EGF. Control cells were not incubated with constructs or EGF. Cytosolic extracts of the cells were immunoblotted (A) and normalized pEGFR levels were determined (B). * indicates significance for $p<0.05$.

In summary, we show that sortase A-mediated conjugation of synthetic CPPs to the anti-EGFR VHH 7D12 prevents EGF binding and EGFR activation with higher efficacy than 7D12 alone. Such protocols can be easily implemented for conjugation of other VHHs and overcome problems associated with the recombinant expression of CPP fusion proteins. This opens the way for further modifications of VHHs to produce VHH drug conjugates or conjugates for *in vivo* imaging.

METHODS

Cell culture

Human epidermoid carcinoma A431 cells, carrying an amplification of the EGFR gene[38], and EGFR negative high grade astrocytoma cells E98[39-40], were cultured in DMEM (Lonza, Basel, Switzerland) supplemented with 10% fetal calf serum (FCS) (Gibco, Thermo Fisher Scientific, Waltham, MA, USA) and 40 µg/ml gentamycin (Centrafarm, Etten-Leur, The Netherlands). Cells were incubated at 37°C in 5% CO_2 in a humidified atmosphere unless stated otherwise. The bacterial strain used for VHH expression was E.Coli ER2566, and the plasmids encoding VHH-7D12 and VHH-G2 were a kind gift from Paul van Bergen en Henegouwen (University of Utrecht, the Netherlands).

Peptide modification

The GGG-hLF[Fluo] was purchased from EMC microcollections (Tübingen, Germany). An additional lysine residue was introduced at the C-terminus to which carboxyfluorescein was coupled. The peptide was dissolved in 50 mM HEPES buffer pH 8.0 to ensure disulfide bridge formation[24]. The concentration of the peptide was determined by measuring the absorbance of fluorescein at 492 nm assuming an extinction coefficient of 75 000 $M^{-1}cm^{-1}$.

Sortase A expression

Plasmid pGBMCS-SortA (Addgene, Cambridge, MA, USA) was transformed into E. coli ER2566. A single, antibiotic-resistant clone was picked and grown over night at 37°C at 200 rpm in 2xTY medium containing 1% glucose w/v and 50 µg/mL ampicillin (Thermo Fisher Scientific, Waltham, MA, USA). The overnight culture was diluted 1/100 in 2xTY supplemented with 50 µg/mL ampicillin and incubated at 37°C at 200 rpm. At OD_{600} ≥ 0.6, the protein expression was induced with 1.0 mM isopropyl β-D-thiogalactoside (IPTG, Serva, Heidelberg, Germany) at 30°C for 3 hrs. Cells were harvested by centrifugation at 3500 rpm for 20 min at 4°C. The cell pellet was then resuspended in 50 mM Tris-HCl, pH 7.5 and 150 mM NaCl and lysed by sonication at 4°C. The sonicated lysate was centrifuged at 6000 rpm for 15 min at 4°C. The supernatant was incubated with Ni-NTA Agarose beads (IBA, Goettingen, Germany) pre-equilibrated with 50 mM phosphate pH 7.4, and 500 mM NaCl for 1 hr at 4°C. The beads were washed with 50 mM phosphate buffer pH 7.4, 500 mM NaCl, and 10 mM imidazole (Sigma Aldrich, Saint Louis, MO, USA) and the protein was eluted with 50 mM phosphate buffer pH 7.4, 500 mM NaCl, and 500 mM imidazole. Imidazole was removed by dialysis in a 3.5 kDa membrane against 50 mM Tris-HCL pH 7.5, and 150 mM NaCl, and the protein was subsequently concentrated in a 10 kDa MWCO centrifugal unit (Amicon, Millipore, Billerica, MS, USA). The protein was analyzed by SDS-PAGE under reducing conditions and liquid chromatography-mass spectrometry (LC-MS, Shimadzu HPLC and Thermo Finnigan LCQ Fleet) on a C4 column. Protein concentration

was determined by ultraviolet absorbance at 280 nm using a Nanodrop spectrophotometer (Thermo Fisher Scientific, Waltham, MA, USA).

VHH expression

The cDNA encoding the sequences of VHHs 7D12 and G2 (see results Supporting information) were PCR cloned from vectors Pur8100-7D12 and Pur8100-G2 into vector pHENIX as SfiI/NotI fragment. The pHENIX vector contains a carboxy-terminal sequence encoding the amino-acids (C)LPETG with an optional cysteine for maleimide chemistry and the 8xHis and Vsv tag. ER2566 E.Coli cells were transformed with these plasmids and single, antibiotic-resistant clones were picked for both VHHs and grown over night at 37°C at 200 rpm in 2xTY medium containing 1 % glucose w/v and 50 µg/mL ampicillin. The overnight culture was diluted 1/100 in 2xTY supplemented with 50 µg/ml ampicillin and incubated at 37°C at 200 rpm. At $OD_{600} \geq 0.6$, VHH expression was induced with 1.0 mM IPTG for 2.5 hrs at 30°C at 200 rpm. The periplasmic fraction was obtained by harvesting the cells through centrifugation (4000 rpm, 15 min, 4°C) and resuspending the pellet in ice-cold TES (200 mM Tris-HCL pH 8.0, 0.5 mM EDTA, 500 mM sucrose). After 20 min incubation on ice, the suspension was centrifuged (5000 rpm, 20 min, 4°C) and the supernatant containing the VHHs was collected. The pellet was resuspended in ice-cold TES with $MgSO_4$, left on ice for 15 min and spun down (5000 rpm, 20 min, 4°C) after which the supernatant was collected. The 8xHis-tagged VHHs were purified using Ni-NTA sepharose beads as described above for sortase A. After dialysis against 50 mM Tris-HCL pH 7.5, 150 mM NaCl VHH purity was analyzed by SDS page gel electrophoresis under reducing conditions, and VHH concentration was measured by ultraviolet absorbance at 494 nm ($\varepsilon_{494,FITC}$ = 70.000 $M^{-1}cm^{-1}$), using a Nanodrop spectrophotometer.

VHH maleimide-fluorescein labeling

VHH-C (typically ~50-250 µM) was incubated with 20 mM TCEP (Thermo Fisher Scientific, Waltham, MA, USA) for 15 min at room temperature. TCEP was removed by centrifuge filtration in a 10 kDa MWCO centrifugal unit employing 5 cycles against 20 mM phosphate pH 7.0, 150 mM NaCl, and 5 mM EDTA. Fluorescein-5-maleimide (Thermo Fisher Scientific, Waltham, MA, USA, from a 10 mM stock in dimethylformamide) was reacted with VHH-C in a 3:1 molar ratio in a thermoshaker at 450 rpm in the dark at room temperature for 2 hrs. Excess fluorescein-5-maleimide was removed by centrifuge filtration in a 10 kDa MWCO centrifugal unit employing 4 cycles against 50 mM Tris-HCL pH 7.5, and 150 mM NaCl. The protein was analyzed by SDS-PAGE gel electrophoresis under reducing conditions and LC-MS. Protein concentration was determined by ultraviolet absorbance at 494 nm using the nanodrop.

VHH hLF conjugation

VHH and GGG-hLF[Fluo] were conjugated using sortase A (figure 1). Sortase A (50 µM final concentration) and GGG-hLF[Fluo] (50 µM final concentration) were added to 7D12 (20 µM final

concentration) in sortase A buffer (50 mM Tris-HCL pH 7.5, 150 mM NaCl, 10 mM CaCl$_2$). The solution was incubated at 30°C at in a thermoshaker at 450 rpm for 5 hrs in the dark. Subsequently the reaction mixture was incubated with Ni-NTA sepharose beads to remove the 6xHis-tagged Sortase A, G-8xHis-Vsv and intact 7D12. Excess GGG-hLF[Fluo] was removed by washing the reaction mixture multiple times in a 10 kDa MWCO centrifugal filter unit employing 6 cycles against 20 mM phosphate, 500 mM NaCl, 20% v/v glycerol, pH 7.5. The product size and purity was analyzed by SDS page gel electrophoresis under reducing conditions and LC-MS.

Determine the Kd with IRDye700DX labeled constructs

To determine the Kd of the constructs, IRDye700DX labeled conjugates were used since these can be visualized on the Odyssey scanner (LI-COR, Lincoln, NE, USA). To this end, TCEP reduction of the 7D12-C was performed as described above. Then maleimide-PEG$_4$-DBCO (Jena Bioscience, Jena, Germany, 10 mM stock in DMF) was allowed to react for 2 hrs at room temperature in a thermoshaker (450 rpm) with 7D12-C in a 3:1 molar ratio, yielding 7D12-C[DBCO]. Excess maleimide-PEG$_4$-DBCO was removed by filter centrifugation over an Amicon 10 kDa MWCO centrifugal unit employing 4 cycles against 50 mM Tris-HCL pH 7.5 and 150 mM NaCl. In parallel, IRDye700DX-NHS (LI-COR) was incubated with H$_2$N-PEG$_3$-N3 (Jena Bioscience, Jena, Germany) in a 3:1 molar ratio in 100 mM phosphate pH 8.6 and 150 mM NaCl for 7 hrs in a thermoshaker, yielding PS-N$_3$. 7D12-C[DBCO] incubated with PS-N$_3$ in a 1:2 molar ratio over night at RT yielding 7D12-C[PS]. This conjugate was purified from unconjugated PS-N$_3$ by centrifugation over an Amicon 10 kDa MWCO centrifugal unit employing 4 cycles against 50 mM Tris-HCL pH 7.5 and 150 mM NaCl. The protein was analyzed by SDS-PAGE gel electrophoresis and protein concentration was determined by ultraviolet absorbance at 689 nm using the nanodrop.

Affinity of the IRDye00DX labeled 7D12 constructs for EGFR was determined in cell binding assays. A431 cells (5,000 cells per well), E98 cells (8,000 per well) and SK-OV-3 cells (6,000 per well) were seeded in a black 96 clear-bottom wells plate (Falcon, Corning, New York, USA) and allowed to grow over night. Then cells were incubated with various concentrations of 7D12-C[PS] or 7D12-C[PS]-hLF for 1 hour at 4°C in DMEM supplemented with 10% FCS. Cells were washed twice with cold DMEM with 10% FCS and once with cold PBS. Then plates were scanned with the Odyssey scanner (LI-COR, Lincoln, NE, USA) using the 700 nm channel. Total fluorescence intensity was plotted against conjugate concentration, and Kd's were determined in Graphpad Prism 5.02.

Cellular uptake of the constructs

To analyze uptake of the VHH -hLF[Fluo] conjugates in cells, A431 cells were seeded at a density of 4x10^4 /well in 8-well chambered coverglasses (NUNC, Thermo Fisher Scientific, Waltham, MA, USA). The next day, cells were incubated with 2 µM of either 7D12-hLF[Fluo], G2-hLF[Fluo], GGG-hLF[Fluo], 7D12-C[Fluo], G2-C[Fluo], or the combination of 2 µM 7D12-C[Fluo] with 2 µM GGG-

hLF in 200 μL phenol red free RPMI 1640 (Thermo Fisher Scientific, Waltham, MA, USA) with 10% FCS and 20 mM HEPES for 30 min at 37°C, 5% CO_2. Subsequently, cells were washed twice with RPMI with 10% FCS, and uptake and binding of the fluorescein-labeled constructs were analyzed by confocal laser scanning microscopy. After confocal imaging fluorescein fluorescence was dequenched by replacing 100 μl medium with 100 μl phenol red free RPMI containing 170 μM chloroquine (Sigma-Aldrich Chemie BV, Zwijndrecht) to a final concentration of 65 μM. The samples were incubated for 30 minutes and subsequently imaged again with the confocal microscope. Confocal laser scanning microscopy was performed on a TCS SP5 microscope (Leica Microsystems, Mannheim, Germany) equipped with an HCX PL APO 63 × 1.2 water immersion lens. During imaging, cells were maintained at 37 °C. The 488 nm laser line was used for excitation and emission was collected between 500 and 550 nm.

Endocytosis of EGFR and the constructs

To analyze the influence of the constructs on colocalization of early endosomes and lysosomes and EGFR, A431 cells were incubated with the various constructs as described above in presence of a 1:1000 dilution of LysoTracker Red DND99 (Life Technologies, ThermoFisher Scientific, Waltham, MA USA). The positive control was activated with 100 ng/mL (16.6 nM) EGF (PromoCell, Heidelberg, Germany) in serum free RPMI for 20 min at 37°C. Then cells were fixed in 2% paraformaldehyde in 0.2 M phosphate buffer pH 7.5 for 10 min at RT and washed with PBS. After blocking the free aldehyde groups with 100 mM glycine in PBS for 20 min at RT and cell permeabilization with 0.5 % triton in PBS for 15 min at RT, cells were blocked with Normal Antibody Diluent (ImmunoLogic, Duiven, The Netherlands) for 20 min at RT. Then cells were incubated with mouse-anti-EEA-1 (1:250, 610456, BD Biosciences, Franklin Lakes, NJ, USA) and rabbit-anti-EGFR (1:50, D38B1, Cell Signaling Technology, Danvers, MA, USA) in Normal Antibody Diluent for 1 hr at RT. After washing with PBS the cells were incubated for 1 hr with goat-anti-rabbit AlexaFluor 647 and goat-anti-mouse AlexaFluor 594 conjugates (both Life technologies, Thermo Fisher Scientific, Waltham, MA, USA) for visualization of bound antibodies. The antibody staining was analyzed with TCS SP5 confocal laser scanning microscope (Leica Microsystems, Mannheim, Germany) equipped with an HCX PL APO 63 × 1.2 water immersion lens. The constructs were visualized as described above and stained EGFR was excited with the 633 nm laser line and emission was collected between 672 and 800 nm. In a sequential scan lysotracker red and stained EEA-1 were excited with 561 nm laser line and emission was collected between 584 and 628 nm.

Visualization of EGF

A431 cells were incubated with the constructs as described above. Then, cells were washed twice with HBS (10 mM HEPES, 135 mM NaCl, 5 mM KCl, 1 mM $MgCl_2$, 1.8 mM $CaCl_2$, pH 7.4), and incubated for 10 min with 50 nM EGF-biotin (kind gift from Donna Arndt-Jovin, Max Planck Institute for Biophysical Chemistry, Göttingen) in HBS with 20 mM glucose and 1% BSA at 4°C.

After washing the cells twice with HBS, cells were incubated with Streptavidin-Alexa Fluor 594 (1:120 Invitrogen Molecular probes, Carlsbad, CA, USA) in HBS with 20 mM glucose and 1% BSA at 4°C. Cells were washed twice with HBS and then imaged in HBS 20 mM glucose 1% BSA on the SP5 microscope at 37°C (see above).

EGFR activation by EGF after incubation with constructs

To analyze effects on EGFR activation using confocal microscopy, cells were incubated with the constructs as described above. Then cells were washed twice with RPMI without FCS and incubated with 200 µL RPMI without FCS for 1 hr at 37°C, 5 % CO_2, after which the cells were either activated or not with 100 ng/mL EGF (16.6 nM) for 5 min at 37°C, 5% CO_2. Then cells were fixed in 2% paraformaldehyde in 0.2 M phosphate buffer pH 7.5 for 10 min at RT and washed with PBS. After blocking the free aldehyde groups and cell permeabilization, cells were blocked with Normal Antibody Diluent for 20 min at RT. Then cells were incubated with rabbit-anti-phosphoEGFR Tyr1068 (1:800, D7A5, Cell Signaling Technology, Danvers, MA, USA) in Normal Antibody Diluent for 1 hr at RT. After washing with PBS the cells were incubated for 1 hr with goat-anti-rabbit AlexaFluor 647 conjugate for visualization of bound antibodies. The antibody staining was analyzed by confocal microscopy. The 633 nm laser line was used for excitation and emission was collected between 650 and 750 nm.

To analyze effects on EGFR activation using western blot, A431 cells were seeded into 24-wells plates (Cellstar, Greiner-Bio One, Essen, Germany) at 150,000 cells/well and grown over night. Then cells were incubated with 400 µl of either 7D12-LPETGGG-hLF[38-59][Fluo] or 7D12-LPETG-8xHis-Vsv in DMEM with 10% FCS for 30 min at 37°C, 5% CO_2. Cells were washed twice and incubated with 500 µl serum free DMEM for 1 hr at 37°C, 5% CO_2, after which they were activated with 500 µl 100 ng/ml EGF in serum free DMEM for 5 min at 37°C, 5% CO_2. Then cells were washed once with PBS and cytosolic extracts were made in RIPA buffer (Cell Signaling Technology, Danvers, MA, USA) according to manufacturer's protocol. 20 µg of total protein was subjected to SDS-PAGE electrophoresis and western blot. Blots were blocked in LI-COR blocking buffer in PBS (1:1) and incubated with rabbit-anti-phosphoEGFR (1:1,000) and mouse-anti-GAPDH (1:10,000, ab8245, Abcam, Cambridge, UK) for 1 hr at RT, and goat-anti-rabbitIRDye800 and goat –anti-mouseIRDye680 (both Invitrogen Molecular probes, Carlsbad, CA, USA) for 1 hr at RT. The experiment was repeated 3 times and the signals were visualized and quantified using the Odyssey system (LI-COR, Lincoln, NE, USA).

Image analysis

Fiji (pacific.mpi-cbg.de/wiki/index.php/Fiji)[41] was used for image analysis. For the quantification of the EGF and pEGFR fluorescence, regions of interest (ROIs) were drawn in the brightfield image to exclude regions without cells. The mean of the fluorescence signal inside these ROIs was measured. Three images per condition were recorded in each experiment.

Colocalization of stained EGFR with the early endosomal marker EEA-1 and LysoTracker Red DND99 was analyzed by first making a binary mask of the EEA-1/LysoTracker Red image. This image was devided by 255 and the Raw integrated density (sum of all pixels) was measured. Subsequently the image was multiplied with the EGFR image resulting in an image showing all EEA-1/LysoTracker vesicles that are EGFR-positive. The Raw integrated density of this image was measured and divided with the value obtained in the first measurement. This results in the average EGFR intensity in EEA-1/LysoTracker Red positive vescicles per positive pixel.

Statistics

All experiments were performed at least in duplicate. A one-way ANOVA with post hoc Bonferroni was performed in Graphpad prism to check for significance.

REFERENCES

1. Baudino, T. A., Targeted Cancer Therapy: The Next Generation of Cancer Treatment. *Current drug discovery technologies* **2015,** *12* (1), 3-20.

2. Holbro, T.; Hynes, N. E., ErbB receptors: directing key signaling networks throughout life. *Annu Rev Pharmacol Toxicol* **2004,** *44*, 195-217.

3. Gullick, W. J., Prevalence of aberrant expression of the epidermal growth factor receptor in human cancers. *British medical bulletin* **1991,** *47* (1), 87-98.

4. Salomon, D. S.; Brandt, R.; Ciardiello, F.; Normanno, N., Epidermal growth factor-related peptides and their receptors in human malignancies. *Critical reviews in oncology/hematology* **1995,** *19* (3), 183-232.

5. Normanno, N.; De Luca, A.; Bianco, C.; Strizzi, L.; Mancino, M.; Maiello, M. R.; Carotenuto, A.; De Feo, G.; Caponigro, F.; Salomon, D. S., Epidermal growth factor receptor (EGFR) signaling in cancer. *Gene* **2006,** *366* (1), 2-16.

6. Mendelsohn, J.; Baselga, J., The EGF receptor family as targets for cancer therapy. *Oncogene* **2000,** *19* (56), 6550-65.

7. Martinelli, E.; De Palma, R.; Orditura, M.; De Vita, F.; Ciardiello, F., Anti-epidermal growth factor receptor monoclonal antibodies in cancer therapy. *Clinical and experimental immunology* **2009,** *158* (1), 1-9.

8. Li, S.; Schmitz, K. R.; Jeffrey, P. D.; Wiltzius, J. J.; Kussie, P.; Ferguson, K. M., Structural basis for inhibition of the epidermal growth factor receptor by cetuximab. *Cancer Cell* **2005,** *7* (4), 301-11.

9. Sunada, H.; Magun, B. E.; Mendelsohn, J.; MacLeod, C. L., Monoclonal antibody against epidermal growth factor receptor is internalized without stimulating receptor phosphorylation. *Proc Natl Acad Sci U S A* **1986,** *83* (11), 3825-9.

10. Wheeler, D. L.; Huang, S.; Kruser, T. J.; Nechrebecki, M. M.; Armstrong, E. A.; Benavente, S.; Gondi, V.; Hsu, K. T.; Harari, P. M., Mechanisms of acquired resistance to cetuximab: role of HER (ErbB) family members. *Oncogene* **2008,** *27* (28), 3944-56.

11. Vlacich, G.; Coffey, R. J., Resistance to EGFR-targeted therapy: a family affair. *Cancer Cell* **2011,** *20* (4), 423-5.

12. Montagut, C.; Dalmases, A.; Bellosillo, B.; Crespo, M.; Pairet, S.; Iglesias, M.; Salido, M.; Gallen, M.; Marsters, S.; Tsai, S. P.; Minoche, A.; Seshagiri, S.; Serrano, S.; Himmelbauer, H.; Bellmunt, J.; Rovira, A.; Settleman, J.; Bosch, F.; Albanell, J., Identification of a mutation in the extracellular domain of the Epidermal Growth Factor Receptor conferring cetuximab resistance in colorectal cancer. *Nature medicine* **2012,** *18* (2), 221-3.

13. Harmsen, M. M.; De Haard, H. J., Properties, production, and applications of camelid single-domain antibody fragments. *Appl. Microbiol. Biotechnol.* **2007,** *77* (1), 13-22.

14. Muyldermans, S.; Baral, T. N.; Retamozzo, V. C.; De Baetselier, P.; De Genst, E.; Kinne, J.; Leonhardt, H.; Magez, S.; Nguyen, V. K.; Revets, H.; Rothbauer, U.; Stijlemans, B.; Tillib, S.; Wernery, U.; Wyns, L.; Hassanzadeh-Ghassabeh, G.; Saerens, D., Camelid immunoglobulins and nanobody technology. *Veterinary immunology and immunopathology* **2009,** *128* (1-3), 178-83.

15. Roovers, R. C.; Laeremans, T.; Huang, L.; De Taeye, S.; Verkleij, A. J.; Revets, H.; de Haard, H. J.; van Bergen en Henegouwen, P. M., Efficient inhibition of EGFR signaling and of tumour growth by antagonistic anti-EFGR Nanobodies. *Cancer immunology, immunotherapy : CII* **2007,** *56* (3), 303-317.

16. Heukers, R.; Vermeulen, J. F.; Fereidouni, F.; Bader, A. N.; Voortman, J.; Roovers, R. C.; Gerritsen, H. C.; van Bergen En Henegouwen, P. M., Endocytosis of EGFR requires its kinase activity and N-terminal transmembrane dimerization motif. *J. Cell Sci.* **2013,** *126* (Pt 21), 4900-12.

17. Milletti, F., Cell-penetrating peptides: classes, origin, and current landscape. *Drug Discov Today* **2012,** *17* (15-16), 850-60.

6

18. Schwarze, S. R.; Ho, A.; Vocero-Akbani, A.; Dowdy, S. F., In vivo protein transduction: delivery of a biologically active protein into the mouse. *Science* **1999,** *285* (5433), 1569-72.

19. Astriab-Fisher, A.; Sergueev, D.; Fisher, M.; Shaw, B. R.; Juliano, R. L., Conjugates of antisense oligonucleotides with the Tat and antennapedia cell-penetrating peptides: effects on cellular uptake, binding to target sequences, and biologic actions. *Pharm. Res.* **2002,** *19* (6), 744-54.

20. Wadia, J. S.; Dowdy, S. F., Protein transduction technology. *Curr. Opin. Biotechnol.* **2002,** *13* (1), 52-6.

21. Patel, L. N.; Zaro, J. L.; Shen, W. C., Cell penetrating peptides: intracellular pathways and pharmaceutical perspectives. *Pharm. Res.* **2007,** *24* (11), 1977-92.

22. Crombez, L.; Morris, M. C.; Dufort, S.; Aldrian-Herrada, G.; Nguyen, Q.; Mc Master, G.; Coll, J. L.; Heitz, F.; Divita, G., Targeting cyclin B1 through peptide-based delivery of siRNA prevents tumour growth. *Nucleic Acids Res.* **2009,** *37* (14), 4559-69.

23. Duchardt, F.; Ruttekolk, I. R.; Verdurmen, W. P.; Lortat-Jacob, H.; Burck, J.; Hufnagel, H.; Fischer, R.; van den Heuvel, M.; Lowik, D. W.; Vuister, G. W.; Ulrich, A.; de Waard, M.; Brock, R., A cell-penetrating peptide derived from human lactoferrin with conformation-dependent uptake efficiency. *J. Biol. Chem.* **2009,** *284* (52), 36099-108.

24. Wallbrecher, R.; Verdurmen, W. P.; Schmidt, S.; Bovee-Geurts, P. H.; Broecker, F.; Reinhardt, A.; van Kuppevelt, T. H.; Seeberger, P. H.; Brock, R., The stoichiometry of peptide-heparan sulfate binding as a determinant of uptake efficiency of cell-penetrating peptides. *Cellular and molecular life sciences : CMLS* **2014,** *71* (14), 2717-29.

25. Debets, M. F.; Leenders, W. P.; Verrijp, K.; Zonjee, M.; Meeuwissen, S. A.; Otte-Holler, I.; van Hest, J. C., Nanobody-functionalized polymersomes for tumor-vessel targeting. *Macromolecular bioscience* **2013,** *13* (7), 938-45.

26. Witte, M. D.; Cragnolini, J. J.; Dougan, S. K.; Yoder, N. C.; Popp, M. W.; Ploegh, H. L., Preparation of unnatural N-to-N and C-to-C protein fusions. *Proc Natl Acad Sci U S A* **2012,** *109* (30), 11993-8.

27. Alt, K.; Paterson, B. M.; Westein, E.; Rudd, S. E.; Poniger, S. S.; Jagdale, S.; Ardipradja, K.; Connell, T. U.; Krippner, G. Y.; Nair, A. K.; Wang, X.; Tochon-Danguy, H. J.; Donnelly, P. S.; Peter, K.; Hagemeyer, C. E., A Versatile Approach for the Site-Specific Modification of Recombinant Antibodies Using a Combination of Enzyme-Mediated Bioconjugation and Click Chemistry. *Angew. Chem. Int. Ed. Engl.* **2015**.

28. Mazmanian, S. K.; Liu, G.; Ton-That, H.; Schneewind, O., Staphylococcus aureus sortase, an enzyme that anchors surface proteins to the cell wall. *Science* **1999,** *285* (5428), 760-3.

29. van Lith, S. A.; van Duijnhoven, S. M.; Navis, A. C.; Leenders, W. P.; Dolk, E.; Wennink, J. W.; van Nostrum, C. F.; van Hest, J. C., Legomedicine-A Versatile Chemo-Enzymatic Approach for the Preparation of Targeted Dual-Labeled Llama Antibody-Nanoparticle Conjugates. *Bioconjug Chem* **2017,** *28* (2), 539-548.

30. Heukers, R.; Altintas, I.; Raghoenath, S.; De Zan, E.; Pepermans, R.; Roovers, R. C.; Haselberg, R.; Hennink, W. E.; Schiffelers, R. M.; Kok, R. J.; van Bergen en Henegouwen, P. M., Targeting hepatocyte growth factor receptor (Met) positive tumor cells using internalizing nanobody-decorated albumin nanoparticles. *Biomaterials* **2014,** *35* (1), 601-10.

31. Favretto, M. E.; Brock, R., Stereoselective uptake of cell-penetrating peptides is conserved in antisense oligonucleotide polyplexes. *Small* **2015,** *11* (12), 1414-7.

32. Schmitz, K. R.; Bagchi, A.; Roovers, R. C.; van Bergen en Henegouwen, P. M.; Ferguson, K. M., Structural evaluation of EGFR inhibition mechanisms for nanobodies/VHH domains. *Structure* **2013,** *21* (7), 1214-24.

33. Friedman, L. M.; Rinon, A.; Schechter, B.; Lyass, L.; Lavi, S.; Bacus, S. S.; Sela, M.; Yarden, Y., Synergistic down-regulation of receptor tyrosine kinases by combinations of mAbs: implications for cancer immunotherapy. *Proc Natl Acad Sci U S A* **2005,** *102* (6), 1915-20.

34. Spangler, J. B.; Neil, J. R.; Abramovitch, S.; Yarden, Y.; White, F. M.; Lauffenburger, D. A.; Wittrup, K. D., Combination antibody treatment down-regulates epidermal growth factor receptor by inhibiting endosomal recycling. *Proc Natl Acad Sci U S A* **2010,** *107* (30), 13252-7.

35. Boersma, Y. L.; Chao, G.; Steiner, D.; Wittrup, K. D.; Pluckthun, A., Bispecific designed ankyrin repeat proteins (DARPins) targeting epidermal growth factor receptor inhibit A431 cell proliferation and receptor recycling. *J. Biol. Chem.* **2011,** *286* (48), 41273-85.

36. Hackel, B. J.; Neil, J. R.; White, F. M.; Wittrup, K. D., Epidermal growth factor receptor downregulation by small heterodimeric binding proteins. *Protein engineering, design & selection : PEDS* **2012,** *25* (2), 47-57.

37. Roovers, R. C.; Vosjan, M. J.; Laeremans, T.; el Khoulati, R.; de Bruin, R. C.; Ferguson, K. M.; Verkleij, A. J.; van Dongen, G. A.; van Bergen en Henegouwen, P. M., A biparatopic anti-EGFR nanobody efficiently inhibits solid tumour growth. *International journal of cancer* **2011,** *129* (8), 2013-24.

38. Merlino, G. T.; Xu, Y. H.; Ishii, S.; Clark, A. J.; Semba, K.; Toyoshima, K.; Yamamoto, T.; Pastan, I., Amplification and enhanced expression of the epidermal growth factor receptor gene in A431 human carcinoma cells. *Science* **1984,** *224* (4647), 417-9.

39. Navis, A. C.; Bourgonje, A.; Wesseling, P.; Wright, A.; Hendriks, W.; Verrijp, K.; van der Laak, J. A.; Heerschap, A.; Leenders, W. P., Effects of dual targeting of tumor cells and stroma in human glioblastoma xenografts with a tyrosine kinase inhibitor against c-MET and VEGFR2. *PloS one* **2013,** *8* (3), e58262.

40. Claes, A.; Schuuring, J.; Boots-Sprenger, S.; Hendriks-Cornelissen, S.; Dekkers, M.; van der Kogel, A. J.; Leenders, W. P.; Wesseling, P.; Jeuken, J. W., Phenotypic and genotypic characterization of orthotopic human glioma models and its relevance for the study of anti-glioma therapy. *Brain Pathol* **2008,** *18* (3), 423-33.

41. Schindelin, J.; Arganda-Carreras, I.; Frise, E.; Kaynig, V.; Longair, M.; Pietzsch, T.; Preibisch, S.; Rueden, C.; Saalfeld, S.; Schmid, B.; Tinevez, J. Y.; White, D. J.; Hartenstein, V.; Eliceiri, K.; Tomancak, P.; Cardona, A., Fiji: an open-source platform for biological-image analysis. *Nature methods* **2012,** *9* (7), 676-82.

6
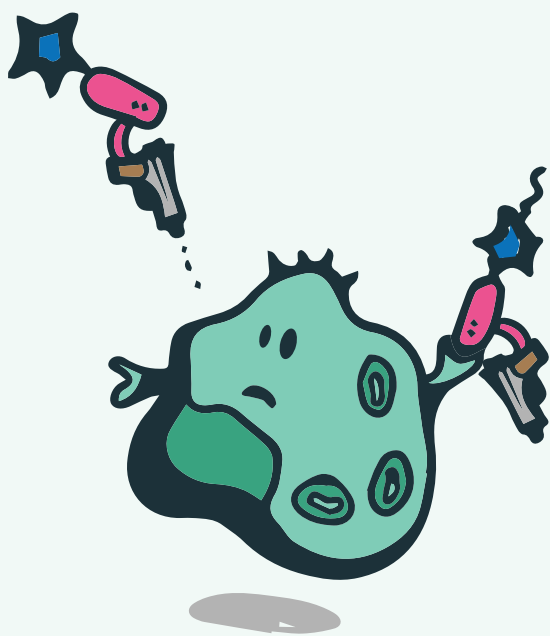
CHAPTER 7

The effect of subcellular localization on the efficiency of EGFR-targeted VHH photosensitizer conjugates.

Sanne A.M. van Lith[1], Dirk van den Brand[2,3], Rike Wallbrecher[2], Lina Wübbeke[1], Sander M.J. van Duijnhoven[1], Petri Mäkinen[4], Janneke S. Hoogstad-van Evert[3], Leon F. Massuger[3], Seppo Ylä-Herttuala[4], Roland Brock[2], William P.J. Leenders[1,2]

[1]Department of Pathology, Radboud Institute for Molecular Life Sciences, Radboudumc, Nijmegen, The Netherlands
[2]Department of Biochemistry, Radboud Institute for Molecular Life Sciences, Radboudumc, Nijmegen, The Netherlands
[3]Department of Gynaecology, Radboud Institute for Molecular Life Sciences, Radboudumc, Nijmegen, The Netherlands
[4]Department of Biotechnology and Molecular Medicine, University of Eastern Finland, Kuopio, Finland

ABSTRACT

Photodynamic therapy (PDT) is an emerging method to treat light-accessible cancers. To increase specificity and allow dose reduction, conjugates of photosensitizers (PS) with antibodies against tumor-associated antigens have been developed for photoimmunotherapy (PIT). However, so far it is unclear whether cellular internalization of these conjugates after binding affects PIT efficacy.

The use of low molecular weight llama single domain antibodies (VHHs, nanobodies) for PIT is preferred above full size antibodies because of better tumor penetration. Therefore, we functionalized the VHH 7D12, directed against the epidermal growth factor receptor (EGFR), with a PS (IRDye700DX). To assess the impact of cellular internalization on activity, the VHHs were additionally conjugated to a cell-penetrating peptide (VHH[PS]-CPP).

Here we show that upon illumination with near-infrared (NIR) light, both VHH[PS] and VHH[PS]-CPP conjugates specifically induce cell death of EGFR expressing cancer cell lines and of EGFR-expressing cells derived from surgically obtained ascites from patients with high-grade serous ovarian cancer. However, VHH[PS] conjugates were significantly more effective compared to internalizing VHH[PS]-CPP suggesting that cell surface association is required for optimal therapeutic activity.

INTRODUCTION

Photodynamic therapy (PDT) is a method to induce cell death through administration and activation of a photo-sensitizer (PS). When activating the PS with light of the appropriate wavelength, the PS is transferred from its ground state into an excited triplet state[1] that can return to the ground state via transmitting its energy to molecular oxygen, leading to the formation of reactive oxygen species (ROS). In general, these ROS are formed through type II photo-oxidative reactions that result in the formation of singlet oxygen, a highly toxic and short-lived radical that induces peroxidation and breakdown of lipids, proteins and nucleic acids[2].

For tumors that are amenable for local light application, PDT has a number of advantages as compared to other therapies. It is less invasive than surgery and, because of its local character, more selective than chemotherapy. Furthermore, the direct cell killing effects of PDT prevent development of resistance, as is seen with chemotherapy and most targeted therapies[3] and may also induce a vaccination effect because PDT-induced necrotic cell death challenges the immune system[4]. PDT has been tested in clinical trials for cancer of the bladder, skin, head and neck. Various PSs are now approved as PDT drugs[5].

There are, however, some issues with PDT that still need to be solved. Currently used PSs suffer from low water solubility and dark toxicity. To enhance solubility, significant efforts have been made in engineering drug delivery systems that allow tumor-specific targeting of PS[6-12]. Even though antibodies are highly potent targeting vehicles, antibody-PS conjugates for photoimmunotherapy (PIT)[13-14] have the disadvantage that antibodies have circulation times of weeks, increasing the risk of dark toxicity and phototoxicity in light-exposed skin[15]. To reduce circulation time, conjugates of PS with small-sized recombinant llama antibodies (VHHs) have been used to induce epidermal growth factor receptor (EGFR)-dependent cell death[14,16]. The small size of these delivery systems also allows faster tumor accumulation and better tissue penetration as compared to full-size antibodies, and improves the carrier-to-drug molecular weight ratio[17].

The half-life of singlet-oxygen in biological systems is <40 ns, restricting its toxic action radius to <20 nm[2]. Studies using photosensitizers with different physicochemical properties that behave differently with respect to cell uptake have shown that intracellular localization greatly influences the cellular response to light-induced activation. PSs that localize to the mitochondria or cytoplasm are described to induce apoptosis, while necrosis is induced when the plasma membrane is the site of action[18-19]. Furthermore, more efficient membrane binding and membrane photooxidation increases phototoxicity of the PS[20].

Next to relying on internalization of targeted receptors, internalization of VHHs can also be triggered by conjugation to cell-penetrating peptides (CPPs)[21], a class of peptides that mediate cellular uptake of molecules that otherwise do not enter the cell[22]. Conjugation of the anti-EGFR VHH 7D12 to the CPP hLF, derived from human lactoferrin[23], endows the VHH with the capacity to enter the cell[24].

To investigate how the efficacy of PIT is influenced by the subcelullar localization of the PS we used a site-selective bioconjugation protocol to functionalize the EGFR targeting VHH 7D12 [25-26] with the PS IRDye700DX. Using sortase A transpeptidation we conjugated hLF to VHH 7D12[PS], yielding 7D12[PS]-hLF. We then investigated the efficacy of both constructs on light induced cell death and show that the CPP-free non-internalizing variant is more active in inducing cell death.

RESULTS AND DISCUSSION

Preparation and characterization of 7D12-C[PS] conjugates

Targeted PDT of cancers requires high tumor selectivity and specificity, concomitant with a lack of dark toxicity. Approaches that improve tumor selectivity of the PS by conjugation to antibodies still have major drawbacks due to the long circulation half-lives of these conjugates, and poor penetration of these large constructs into poorly perfused tumor areas. To tackle these problems, smaller targeting moieties like VHHs are interesting alternative PS carriers. Here, the anti-EGFR VHH 7D12 was used as a clinically relevant model VHH to examine how subcellular localization of PSs affects PDT efficacy. It was published before that 7D12-IRdye700DX conjugates can be prepared successfully via NHS-based conjugation to lysines[14]. This approach however, carries a risk of overlabeling of lysines that are involved in antigen binding, resulting in reduced affinity. Also, this procedure yields a heterogeneous mixture of VHHs, containing a fraction of unlabeled VHHs that may act as competitor for the labeled ones. We therefore chose to perform a site-selective reaction at an introduced cysteine at the carboxyterminus (Figure 1A). Because IRDye700DX was not available as maleimide conjugate at the time of this study, we first coupled a dibenzocyclo-octyn (DBCO)-functionality to the VHH and an azide functionality to the PS.

This enabled us to use the highly specific and bio-orthogonal click reaction between azide and DBCO[27]. 7D12-C[DBCO]-LPETG-8xHis-Vsv (referred to as 7D12-C[DBCO]) and 7D12-C[PS]-LPETG-8xHis-Vsv (referred to as 7D12-C[PS]) were produced successfully as verified with SDS-PAGE electrophoresis (Figure 1B) and LC-MS (Figure 1C). LC-MS verified conjugation of only one maleimide-DBCO and PS molecule per VHH, as we have seen before for maleimide-fluorescein[28]. This method is generally applicable to all VHHs, as long as these do not carry unpaired cysteines in the CDR, and since all reactions occur distant from the VHHs' antigen binding site, this approach is predicted to retain VHH affinity.

By employing sortase-A-mediated ligation of GGG-hLF (Figure 1D), we successfully produced 7D12-C[PS]-LPETGGG-hLF (referred to as 7D12-C[PS]-hLF (Figure 1B, E). Because we did not have lasers compatible for detection of IRDye700DX–fluorescence with confocal microscopy, we also prepared fluorescein labeled variants 7D12-C[Fluo]-LPETG-8xHis-Vsv (7D12-C[Fluo]) and 7D12-LPETGGG-hLF[Fluo] (7D12-hLF[Fluo]).
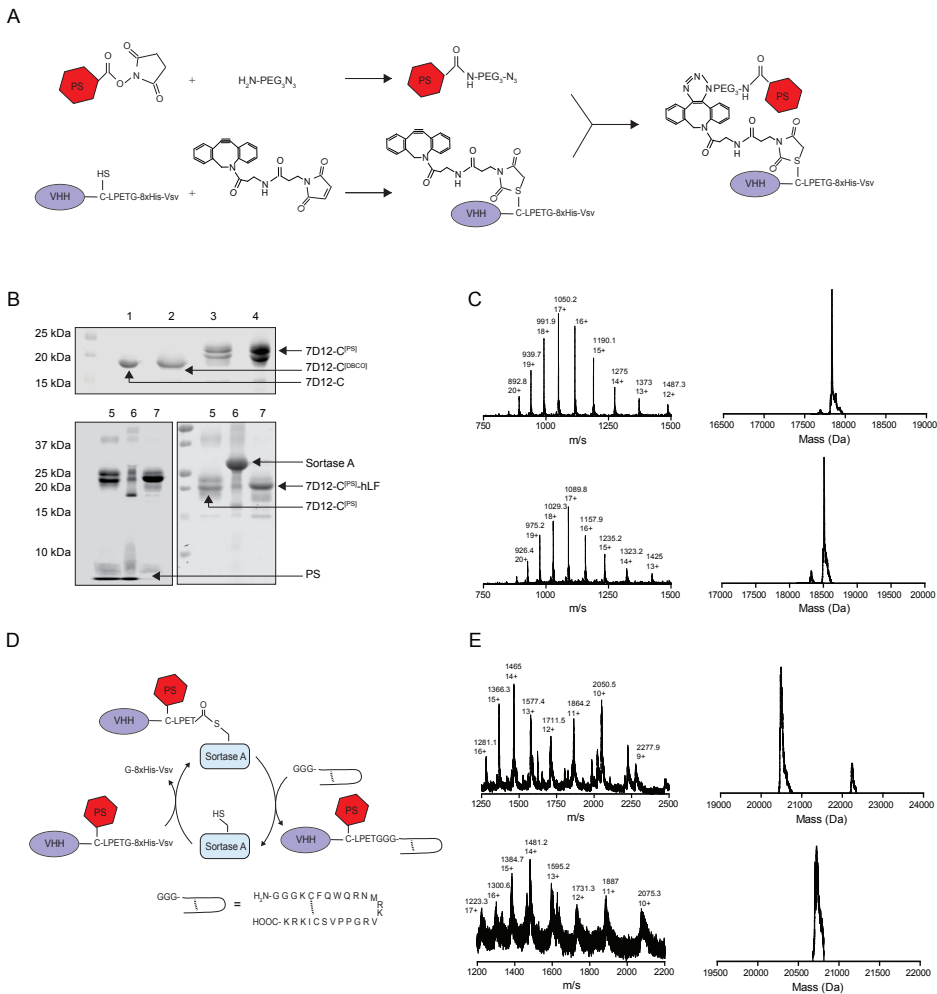
Figure 1. Analytical characterization of the conjugates. A) Scheme of bio-orthogonal conjugation of azide-functionalized PS to the DBCO-functionalized VHH. B) Upper panel: coomassie brilliant blue (CBB) stained SDS-PAGE gel of the reaction products after conjugation of the N_3-PEG_3-PS to 7D12-C[DBCO] (1: 7D12-C, 2: 7D12-C[DBCO], 3: 7D12-C[PS] before column purification, 4: 7D12-C[PS] after column purification). Lower panel: visualization of the SDS-page gel at 680 nm before coomassie (left) and of the coomassie-stained gel (right) with reaction products and controls of the sortase A conjugation to functionalize 7D12-C[PS] with GGG-hLF (5: 7D12-C[PS], 6: Sortase A /7D12-C[PS] after 5 hours incubation at 30°C, 7: the final product 7D12-C[PS]-hLF after Ni-NTA purification). C) LC-MS characterization of TCEP-reduced 7D12-C (upper, observed 17837 Da, calculated 17837.6 Da) and 7D12-C[DBCO] (lower, observed 18511 Da, calculated 18512.4 Da). The left graphs show the total mass spectra, the right graphs show the deconvoluted spectra. D) Scheme of site specific conjugation of VHH-C[PS] to GGG-hLF with sortase A. E) ESI-ToF characterization of 7D12-C[PS] (upper graphs, observed 20495 Da, calculated 20569.7 Da) and 7D12-C[PS]-hLF (lower graphs, observed 20724 Da, calculated 20720.2 Da). The left graphs show the total mass spectra, the right graphs show the deconvoluted spectra.

Cellular binding and uptake of 7D12 conjugates

Previous research has shown that hLF is taken up by endocytosis at concentrations below 10 µM[23], and that functionalization of 7D12 with hLF causes increased internalization of the VHH[24]. Here we confirmed these patterns of cellular uptake in A431 and SK-OV-3 cells (Figure 2A). Cells were incubated with the conjugates at a concentration of 2 µM at which little vesicular uptake of hLF alone was observed (Figure 2B). Vesicular uptake of 7D12-hLF[Fluo] was observed in A431 cells, whereas under the same conditions 7D12-C[Fluo] was predominantly associated with the plasma membrane. SK-OV-3 cells showed very weak membrane staining after incubation with 7D12-C[Fluo], but after incubation with 7D12-hLF[Fluo], intracellular vesicular staining was observed, which was more clearly visible after quenching extracellular fluorescence with trypan blue (Figure 2A). No binding to or uptake in E98 was observed for both 7D12 conjugates (Figure 2C). This latter finding further confirmed that cell association was primarily VHH and not hLF driven.

It is generally accepted that CPPs lack cell line selectivity, however such experiments are typically conducted al medium micromolar concentrations[29]. The dissociation constant of the binding of hLF to cell surface glycosaminoglycans is in the low micromolar range[30], while reported Kd values of 7D12 binding to cell-associated EGFR is in the order of 10-20 nM[14,17,26]. Cell ELISAs, performed at 4°C to study binding in the absence of internalization, confirmed high affinity binding of 7D12-C[PS] and 7D12-C[PS]-hLF to EGFR overexpressing A431 cells (Kd = 11.85 ± 1.203 and 25.53 ± 2.514 nM, respectively). At the low micromolar and subnanomolar concentrations that we employed in the uptake and PDT assays, respectively, binding of the different conjugates is therefore expected to be determined by the 7D12 moiety, rather than hLF. This finding has important implications for *in vivo* applications of CPP-based strategies. Except for those tissues that show a high propensity for CPP uptake[31], uptake of VHH-CPP conjugates is directed by presence of the EGFR. In this case, the CPP module is a modulator of subcellular trafficking rather than an unspecific driver of uptake.
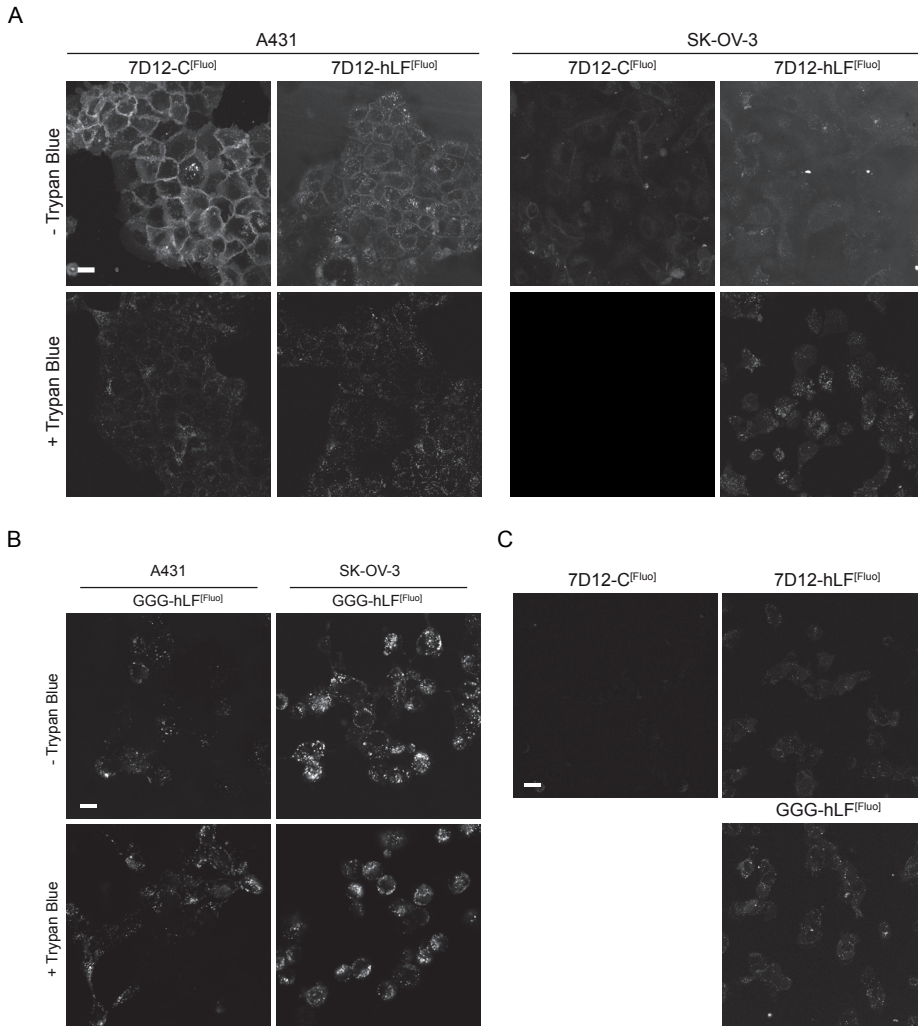
Figure 2. Cell binding and uptake of the constructs. A) A431 and SK-OV-3 cells were incubated with 2 μM of 7D12-C[Fluo] and 7D12-hLF[Fluo] and imaged by confocal laser scanning microscopy before and after quenching fluorescence from extracellular located fluorescein with trypan blue (TB). B) A431 and SK-OV-3 cells were incubated with 2 μM of GGG-hLF[Fluo] and imaged by confocal laser scanning microscopy before and after quenching fluorescence from extracellular located fluorescein with trypan blue (TB). C) E98 cells were incubated with 2 μM of 7D12-C[Fluo]-LPETG-His$_8$-Vsv, 7D12-C-LPETGGG-hLF[Fluo], and GGG-hLF[Fluo] and imaged by confocal laser scanning microscopy. The scale bars denote 10 μm.

hLF mediated uptake of 7D12 is initiated by clathrin mediated endocytosis

In previous work we showed that 7D12-hLF[Fluo] induces internalization of EGFR, which can be initiated by clathrin mediated endocytosis (CME) and/or clathrin independent endocytosis[32]. To investigate if the 7D12-hLF[Fluo] induced internalization of EGFR is clathrin-dependent we incubated A431 cells with the various CPP constructs in the presence of transferrin-Alexa633 (Figure 3). Both 7D12-hLF[Fluo] and hLF[Fluo] but not 7D12[Fluo] induced vesicular uptake as seen by enhanced transferrin staining that colocalized with the hLF-containing constructs.
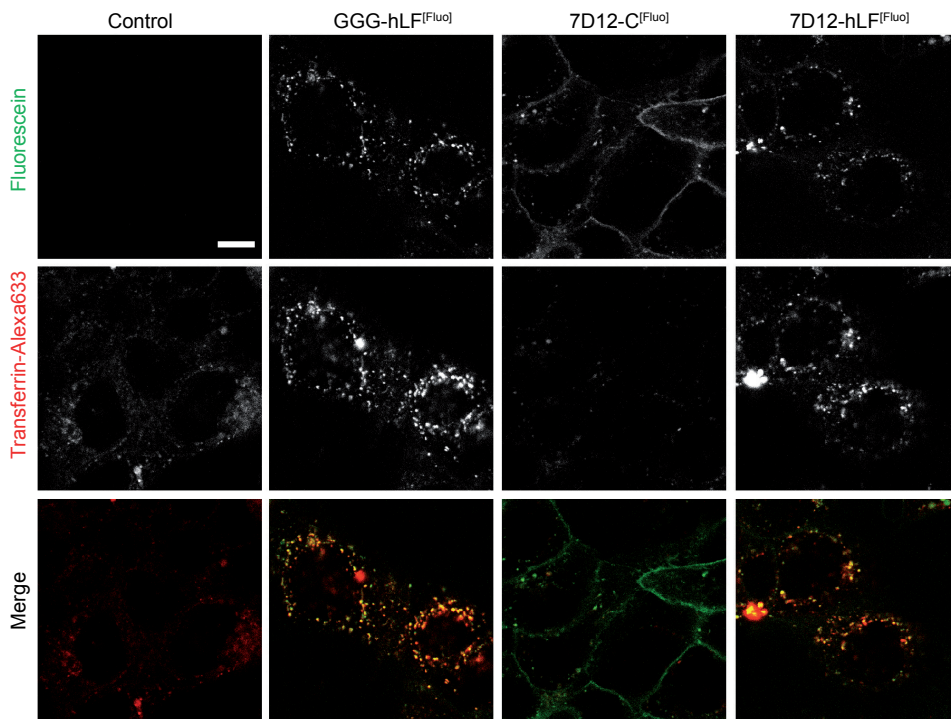
Figure 3. Induction of clathrin-dependent endocytosis by hLF conjugates. A431 cells were incubated for 30 min with 2 µM of the CPP constructs in presence of transferrin-Alexa633. The scale bar denotes 10 µm.

PIT efficacy of 7D12-C[PS] constructs in adherent cell cultures

Cell killing assays showed that 7D12-C[PS] conjugates were very potent and specific PDT agents, without inducing dark toxicity (Figure 4A). Incubation with PS alone, followed by illumination did not induce cell killing under the conditions used (Figure 4B). Although the 7D12-C[PS] conjugates that we produced via a two-step click reaction contain only one PS per VHH, these induced EGFR-specific cell death very efficiently, with an IC50 value for 7D12-C[PS] on A431 cells of 87.8 ± 4.3 pM after NIR light illumination with 60 J/cm^2. Interestingly, conjugates containing hLF were less effective with an IC50 of 234.1 ± 122.7 pM (p = 0.3556) (Figure 4C). In the intermediate EGFR expressing SK-OV-3 cells, similar differences were observed between 7D12-C[PS] (IC50 = 705.1 ± 164 pM) and the internalizing variant 7D12-C[PS]-hLF (IC50 = 2680 ± 323.5 pM) (p = 0.0055). Interestingly, in previous reports it was demonstrated that VHH-PS conjugates with higher affinity for EGFR had higher PIT efficacy and it was suggested that increased internalization due to higher affinity was responsible for increased photosensitivity[14]. Furthermore, internalizing antibody-PS conjugates were shown to be more effective in PIT than non-internalizing antibody-PS[33]. Our data however show that increased cell surface association is a more important determinant. Interestingly, no phototoxicity was induced in non-EGFR expressing E98 cells in line with the low cell binding capacity mediated by the CPP alone.

To further assess the selectivity of the 7D12-C[PS] conjugates, co-culture experiments with A431, E98 and SK-OV-3 were performed. These cell types were distinguished by pre-labeling them with different membrane associated dyes. Labeled and dead cells were visualized immediately, 2 h and 16 h after illumination. Only EGFR expressing cells were killed after PDT (Figure 4D). No cell death was observed in the controls (no PS-conjugates added). Parallel experiments with monocultures of the cells showed that cell death was induced immediately after illumination for the A431 cells, and after 2-16 h for the SK-OV-3 cells (Figure 5). The cell death of A431 immediately after PDT suggested that necrosis was induced. Neither A431 and SK-OV-3 cells were stained with Annexin-V (not shown), and they did not induce caspase-3 dependent apoptosis at 4 h after PDT, which further indicates that cells indeed died by necrosis (Figure 6). Unconjugated IRDye700DX did not lead to phototoxicity in all used cell types, in agreement with previous studies, and did not display dark toxicity. This makes it a suitable compound for targeted PDT[34].
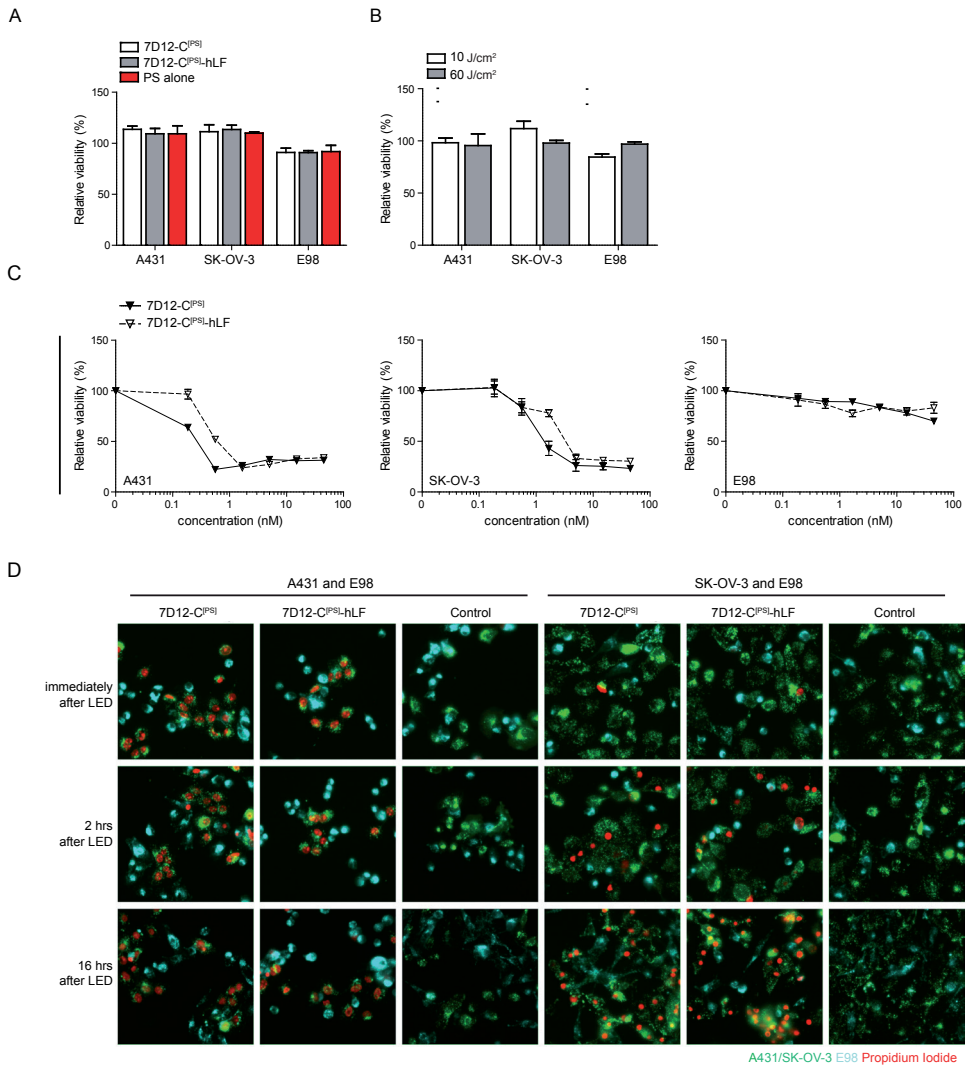
Figure 4. Phototoxicity induced by the constructs in adherent cells. A) Absence of dark toxicity of 7D12-C[PS] constructs and PS alone (45 nM) and B) absence of toxicity of non-targeted PS with illumination (45 nM for 10 J/cm² and 15 nM for 60 J/cm²). Results are shown as survival relative to untreated cells. C) The relative cell viability after incubation with various concentrations of 7D12-C[PS] constructs and illumination with a 60 J/cm² total light dose was also determined in SRB assays. D) Co-cultures fluorescently labeled with DiDyes were incubated with 15 nM 7D12-C[PS] constructs and illuminated with a 60 J/cm² total NIR light dose. Cells were imaged immediately, 2 and 16 hours after illumination. Controls were illuminated only.

A431 SK-OV-3 E98 Propidium Iodide
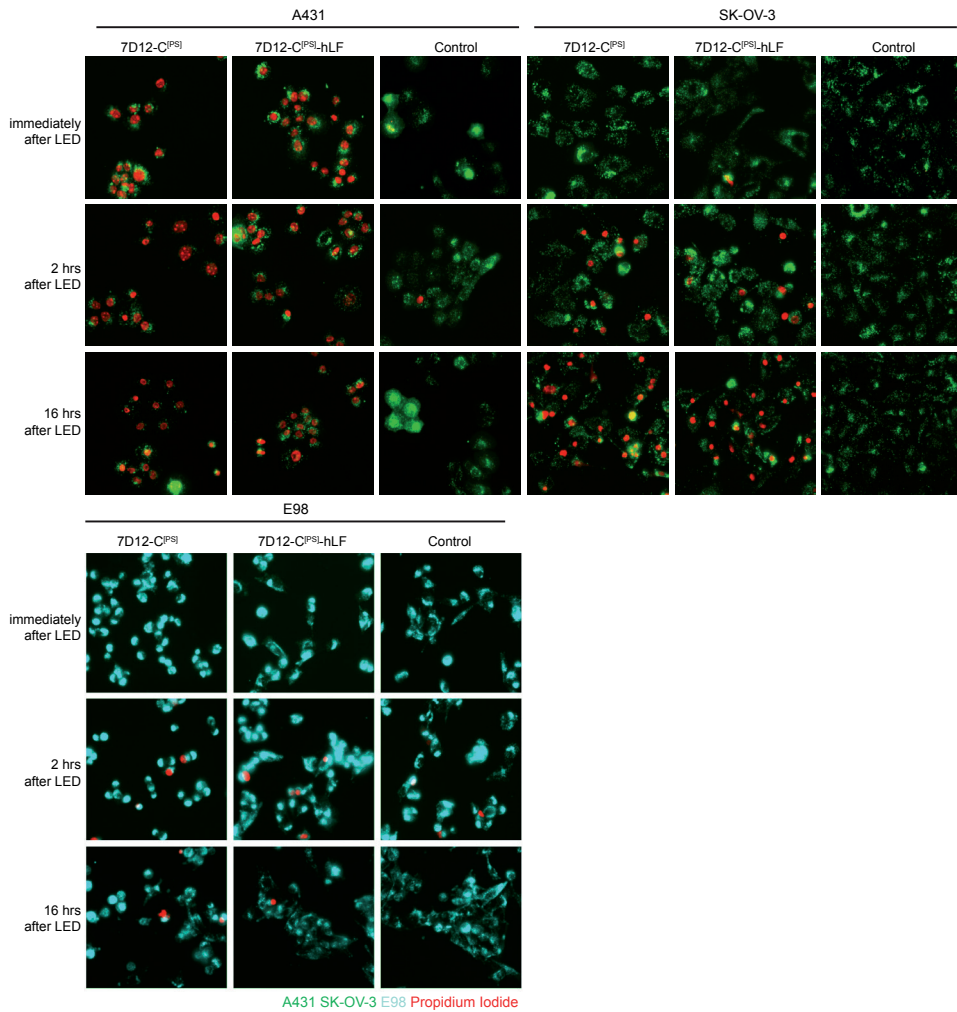
Figure 5. Specificity and timeframe of induced phototoxicity in adherent cells. Cell mono-cultures fluorescently labeled with DiDyes were incubated with 15 nM 7D12-C[PS] constructs and illuminated with a 60J/cm^2 total NIR light dose. Immediately, 2 h and 16 h after illumination they were imaged. Controls were illuminated only.
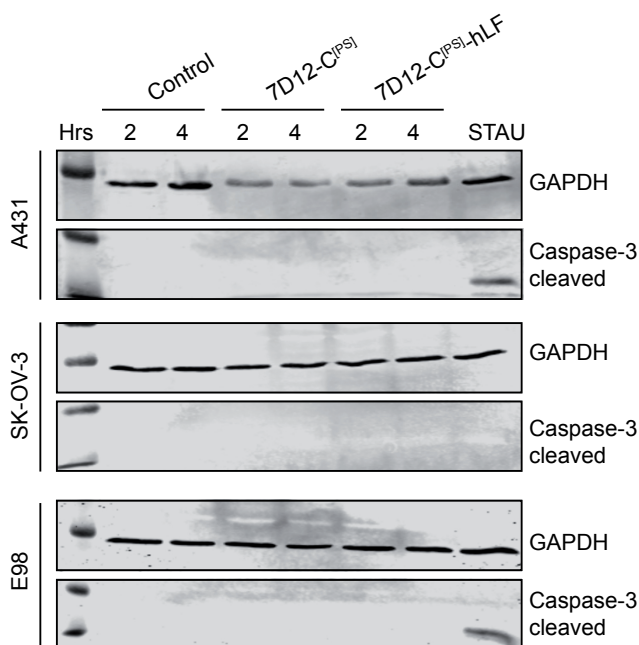
Figure 6. Expression of cleaved caspase-3 and GAPDH in A431, SK-OV-3 and E98 2 and 4 h after PDT with 15 nM 7D12-C[PS] constructs and a 60 J/cm² light dose.

Efficient PIT with ovarian carcinoma SK-OV-3 spheroids and EGFR positive cells in clinical ascites

To assess effectiveness of the conjugates in a cellular model with more resemblance to the *in vivo* tumor situation, conjugates were incubated with SK-OV-3 spheroids. PIT with SK-OV-3 spheroids showed efficient cell killing after incubation with 120 nM of the 7D12-C[PS] construct and a light dose of 60 J/cm², illustrated by the majority of cells with picnotic nuclei in the HE stained sections, and only a minority of cells in the centre that appeared viable (Figure 7A, enlargement in insert). In the 7D12-C[PS]-hLF treated cells, also dead cells with picnotic nuclei were observed but to a lesser extent. Control spheres showed only viable cells, indicating that the VHH conjugates can penetrate into the spheroid.

Finally, cells derived from clinical ascites from women with stage III or IV high-grade serous ovarian carcinoma (n=7) were incubated with 15 nM 7D12-C[PS] constructs and illuminated with 60 J/cm² NIR light. Phototoxicity was restricted to the EGFR-positive subpopulation of cells, as could be observed by costainings for dead cells (Propidium iodide) and EGFR (Cetuximab) (Figure 7B). The absence of costaining for dead cells and a population of cells positive for another tumor marker (EpCAM) indicated selectivity for EGFR (Figure 7C). SRB assays after
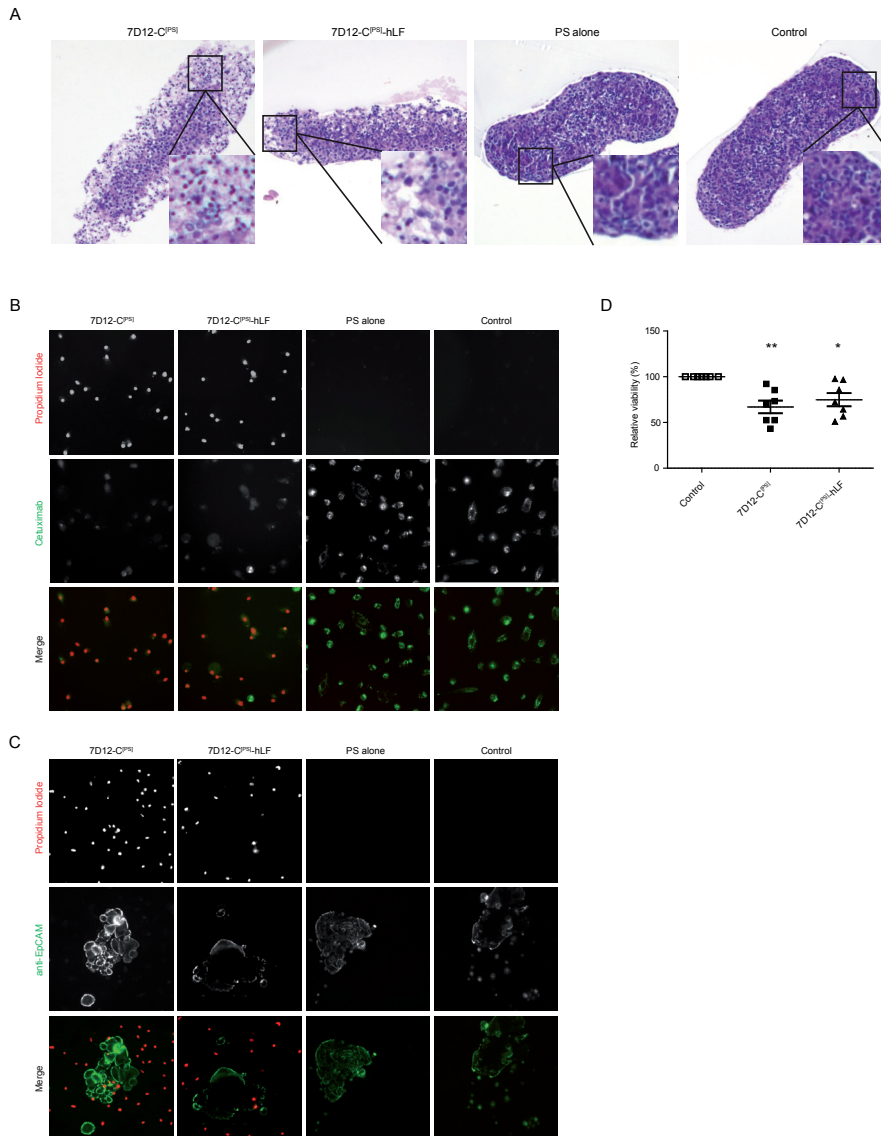
Figure 7. Phototoxicity induced by the constructs in ovarian carcinoma spheroids and clinical ascites. A) SK-OV-3 spheres were incubated with 15 nM of the 7D12-C[PS] constructs or controls and illuminated with a NIR light dose of 60 J/cm^2. Sections of agar embedded treated or control SK-OV-3 spheroids were stained with HE. Note that the outer layer of cells have picnotic nuclei, visualized more clearly in the enlarged insert. B+C) Cultured cells from clinical ascites were incubated with 15 nM of the various 7D12-C[PS] constructs and illuminated with a total NIR light dose of 60 J/cm^2. Dead cells and B) EGFR or C) EpCAM expressing cells in an ascites derived cell culture after PDT were imaged. Note the weaker signal of cetuximab in the dead 7D12-C[PS] treated samples compared to the live cells in the controls. D) The percentage of cell viability in multiple cultures was determined with SRB assays. * = p<0.05, ** = p<0.01.

incubation with 7D12-C[PS] constructs and illumination showed significant decreases in overall cell viability compared to controls (P<0.001 and P<0.03 for 7D12-C[PS] and 7D12-C[PS]-hLF, respectively (Figure 7D). The survival of about 60-70% of the cells is in agreement with the notion that ascites also contains numerous non-EGFR-expressing cells (as shown in Figure 7C) that are expected to survive the treatment.

With the use of optical fibers NIR light can be delivered to otherwise inaccessible tumors, as has been shown for peritoneal metastasis of ovarian cancer using Verteporfin[35]. In addition, peroperative fluorescent image-guided surgery is gaining momentum[36] and could be very well extended with compounds comparable to those described here.

CONCLUSION

Targeted PDT is a rapidly increasing field which promises to become of great importance for the treatment of light-accessible cancers. Targeted light-induced direct cancer cell death has great advantages as compared to currently applied targeted treatments which mostly delay progression of cancers, given these ample time to develop resistance. We here describe the construction of a highly defined VHH-PS via a controlled bioconjugation method that is easily applicable to other VHHs. Despite the fact that every VHH carries only one PS molecule, these constructs are highly selective and specific, requiring very low concentrations to induce efficient cell killing via necrosis. In 3D-spheroid models, efficient cell killing was observed, indicating that these low-weight constructs have good tissue penetrating properties. Furthermore we show that conjugation to a CPP decreases binding affinity, and endows the VHH-PS with an increased capacity to enter the cell via clathrin-mediated endocytosis. These changed properties decreased PDT efficacy, suggesting that association with the cell membrane is needed for optimal therapeutic activity.

METHODS

Cell culture

Human epidermoid carcinoma A431 cells, carrying an amplification of the EGFR gene[37], human high grade astrocytoma E98 cells without EGFR expression[38] and human ovarian adenocarcinoma SK-OV-3 cells with intermediate EGFR expression[39] were cultured in Dulbecco's Modified Eagle Medium (DMEM) (Lonza, Basel, Switzerland) supplemented with 10% fetal calf serum (FCS) (Gibco, Thermo Fisher Scientific, Waltham, MA, USA) and 40 µg/ml gentamycin (Centrafarm, Etten-Leur, The Netherlands). Cells were cultured at 37°C in 5% CO_2 in a humidified atmosphere.

Sortase A expression

E.coli ER2566 cells transformed with the plasmid pGBMCS-SortA, encoding His$_6$-tagged sortase A with an N-terminal deletion of 59 amino acids[40] (Addgene, Cambridge, MA, USA, plasmid #21931) were grown to log phase at 37°C, and protein expression was induced with 1.0 mM isopropyl β-D-thiogalactoside (IPTG, Serva, Heidelberg, Germany) at 30°C for 3 h. Cells were harvested, resuspended in ice-cold 50 mM Tris pH 8.0/300 mM NaCl containing a protease inhibitor cocktail (Roche, Basel, Switzerland) and lysed by sonication using a Bandelin Sonopuls HD2070 sonicator (Bandelin electronic GmbH & Co, Berlin, Germany). After centrifugation the supernatant was incubated with Ni-NTA sepharose (IBA, Goettingen, Germany) in 50 mM phosphate pH 7.4/500 mM NaCl for 1 h at 4°C. After washing, His$_6$-tagged sortase A was eluted from the beads with 500 mM imidazole. The eluate was dialyzed against 50 mM Tris pH 7.5/150 mM NaCl in a 3.5 kDa dialysis membrane (Spectrum Labs, Los Angeles, CA, USA). Protein purity was analyzed by SDS-PAGE gel electrophoresis under reducing conditions and mass spectrometry (LC-MS, Shimadzu HPLC and Thermo Finnigan LCQ Fleet) on a C4 column. Protein concentration was determined by absorbance at 280 nm using the Nanodrop spectrophotometer (LI-COR, Lincoln, NE, USA).

VHH expression

The cDNA encoding anti-EGFR VHH 7D12 (a gift from Paul van Bergen en Henegouwen, Utrecht University, The Netherlands) was recloned in vector pHENIX-C-LPETG-8xHis-Vsv, resulting in 7D12-C-LPETG-8xHis-Vsv (7D12-C), the cysteine providing a handle for maleimide conjugation, LPETG being a sortase A consensus recognition sequence and the His$_8$-Vsv tag allowing Ni-based purification and Vsv-based detection. 7D12-C expression was induced via standard methods in E.coli strain TG1. Cells were harvested by centrifugation at 2830 x g for 20 min at 4°C, resuspended in ice cold Tris/EDTA/Sucrose (TES) buffer (200 mM Tris pH 8.0/0.5 mM EDTA/20 % w/v sucrose/protease inhibitor cocktail) and incubated for 20 min on ice, followed by centrifugation (4424 x g, 20 min, 4°C). The supernatant was collected and the pellet was resuspended in TES buffer supplemented with 15 mM MgSO$_4$, and incubated on ice for 20 min. After centrifugation, both supernatants were pooled and protein was purified with Ni-NTA sepharose as described for sortase A.

IRDye700DX conjugation

All steps involving IRDye700DX were performed in the dark. 7D12-C was incubated with 20 mM tris(2-carboxyethyl)phosphine TCEP (Thermo Fisher Scientific, Waltham, MA, USA) for 15 min at room temperature to reduce the free thiol group of the cysteine. TCEP was removed in a 10 kDa MWCO centrifugal unit (Amicon, Millipore, Billerica, MS, USA) employing 5 washing cycles with 20 mM phosphate pH 7.0/150 mM NaCl/5 mM EDTA. Maleimide-PEG$_4$-DBCO (Jena Bioscience, Jena, Germany, 10 mM stock in DMF) was allowed to react for 2 h at room temperature in a thermoshaker at 450 rpm with 7D12-C in a 3:1 molar ratio, yielding 7D12-

C[DBCO]. Excess maleimide-PEG$_4$-DBCO was removed by filter centrifugation in a 10 kDa MWCO centrifugal unit employing 4 washing cycles with 50 mM Tris pH 7.5/150 mM NaCl. The protein conjugate was analyzed by LC-MS, and protein concentration was determined by ultraviolet absorbance at 309 nm using the Nanodrop spectrophotometer.

In parallel, IRDye700DX-NHS (LI-COR, Lincoln, NE, USA from now on referred to as PS-NHS) was incubated with H$_2$N-PEG$_3$-N$_3$ (Jena Bioscience, Jena, Germany) in a 3:1 molar ratio in 100 mM phosphate buffer pH 8.6/150 mM NaCl for 7 h at RT in a thermoshaker at 450 rpm, yielding PS-N$_3$. Subsequently 7D12-C[DBCO] was incubated with PS-N$_3$ in a 1:2 molar ratio o/n at RT in a thermoshaker at 450 rpm, yielding 7D12-C[PS]. This conjugate was purified from unconjugated PS-N$_3$ by centrifugation in a 10 kDa MWCO centrifugal unit employing 4 washing cycles with 50 mM Tris pH 7.5/150 mM NaCl. The protein was analyzed by SDS-PAGE gel electrophoresis under reducing conditions and with electrospray ionization time-of-flight mass spectrometry (ESI-ToF) on a JEOL AccuTOF-CS (JEOL, Tokio, Japan) . Protein concentration was determined by measuring absorbance at 689 nm (ε = 165000 M^{-1}cm^{-1}, assuming 1:1 complete labeling) using the Nanodrop spectrophotometer.

Functionalization of 7D12-C[PS] with hLF

GGG-hLF or GGG-hLF[Fluo] (synthesized by EMC microcollections, Tübingen, Germany) was dissolved in 50 mM HEPES pH 8.0 at 5-10 mM, to ensure intramolecular disulfide bridge formation that is required for CPP activity[30]. The carboxyfluorescein moiety was coupled to a C-terminal lysine residue. Subsequently sortase A (80 µM final concentration) and GGG-hLF (100 µM final concentration) were added to 7D12-C[PS] (20 µM final concentration) in 50 mM Tris pH 7.5/150 mM NaCl/10 mM CaCl$_2$. The sortase reaction was allowed to proceed for 5 h at 30°C in a thermoshaker at 450 rpm, after which the reaction mixture was incubated with pre-washed Ni-NTA sepharose beads to remove the 6xHis-tagged sortase A, G-8xHis-Vsv and unreacted 7D12-C[PS]. Excess GGG-hLF was removed from the Ni-NTA agarose supernatant by centrifuge filtration in a 10 KDa MWCO centrifugal unit employing 6 cycles against 20 mM phosphate pH 7.5/500 mM NaCl. Purity and concentration of the VHH conjugate was analyzed by SDS-PAGE gel electrophoresis and ESI-ToF. Protein concentrations were determined by measuring absorbance at 689 nm using the Nanodrop spectrophotometer.

Fluorescein labeled constructs for confocal microscopy applications

For confocal microscopy applications, 7D12 constructs directly labeled with fluorescein were produced. 7D12-C was reduced with 20 mM TCEP as described above. Then fluorescein-5-maleimide (Thermo Fisher Scientific, Waltham, MA, USA, 10 mM stock in DMF) was reacted with reduced 7D12-C in a 3:1 molar ratio in 20 mM phosphate pH 7.0/150 mM NaCl/5 mM EDTA for 2 h at RT in a thermoshaker at 450 rpm. Excess fluorescein-5-maleimide was removed by centrifuge filtration in a 10 kDa MWCO centrifugal unit employing 4 washing cycles with 50 mM Tris pH 7.5/150 mM NaCl. 7D12-hLF[Fluo] was prepared using sortase A as described above, using

50 μM sortase A, 50 μM GGG-hLF[Fluo] and 20 μM 7D12 in 50 mM Tris pH 7.5/150 mM NaCl/10 mM CaCl$_2$. The product was purified using Ni-NTA sepharose and filter centrifugation as described. Protein conjugates were analyzed by SDS PAGE gel electrophoresis under reducing conditions and LC-MS. Protein concentration was determined by measuring absorbance at 494 nm (ε = 75000 M^{-1}cm^{-1}, assuming 1:1 complete labeling) using the Nanodrop spectrophotometer.

Cell uptake assays with confocal microscopy

Cellular uptake of the different fluorescein-labeled 7D12 conjugates was examined with confocal microscopy on a TCS SP5 microscope (Leica Microsystems, Mannheim, Germany) equipped with an HCX PL APO 63 × 1.2 water immersion lens. During imaging, cells were maintained at 37°C. The 488 nm laser line of the argon laser was used for excitation and emission was collected between 500 and 550 nm. A431, E98 and SK-OV-3 cells (30,000, 50,000 and 30,000 cells per well, respectively) were plated in 8-well Lab-Tek borosilicate coverglass chambers (NUNC, Thermo Fisher Scientific, Waltham, MA, USA) and allowed to adhere and proliferate for 48 h. Then cells were incubated for 30 min at standard culture conditions in 200 μl phenol red-free RPMI/10% FCS, supplemented with 2 μM of 7D12-C[Fluo], 7D12-hLF[Fluo], or GGG-hLF[Fluo]. Subsequently, cells were washed twice with phenol red-free RPMI/10% FCS containing 20 mM HEPES and were imaged by confocal microscopy. Acidic pH in lysosomes reduces Fluorescein fluorescence. To investigate if this effect leads to an underestimation op 7D12-hLF[Fluo] uptake, we treated cells with 65 μM chloroquine, which increases the lysosomal pH and thereby enhances fluorescein fluorescence[41]. The samples were imaged once more, and to quench extracellular fluorescence, 0.4% trypan blue (Sigma Aldrich, Saint Louis, MO, USA) was added to the wells before imaging for a third time[42].

Study of cell uptake mechanism with confocal microscopy

To detect clathrin-dependent endocytosis, cells were co-incubated with the constructs as described above and 100 μg/ml transferrin-Alexa Fluor 633 (Life Technologies, Thermo Fisher Scientific, Waltham, MA, USA). After 30 min, the cells were washed and colocalization of transferrin and the constructs was detected by confocal microscopy. Fluorescein was excited with the argon laser at 488 nm and emission was detected between 500 and 550 nm. Alexa Fluor 633 was excited with the 633 nm helium-neon laser and detected between 650 and 715 nm.

In vitro PDT assays with adherent cell cultures

A431, E98 and SK-OV-3 cells were cultured in clear 96-well plates (Costar, Greiner-Bio One, Essen, Germany). At 80% confluency cells were incubated for 30 min with different concentrations of 7D12-C[PS], 7D12-C[PS]-hLF or equimolar concentrations of PS alone in DMEM/10% FCS. Controls were incubated with DMEM/10% FCS only. Cells were washed twice with warm DMEM/10% FCS. Immediately after washing, plates were illuminated with 100 mW/cm^2 for 600 s, reaching a total light dose of 60 J/cm^2, using a standardized light emitting

diode device (690 ± 10 nm) as described in[43]. To determine dark toxicity, cells were incubated with the highest used concentration of the conjugates without subsequent illumination. After overnight incubation a sulforhodamine-B-assays (SRB) assay was performed as described in[44] to determine total protein content. Results were expressed as cell viability relative to controls (untreated illuminated cells). Half maximal inhibitory concentration (IC50) of the various conjugates were determined in GraphPad Prism 5.02 (LaJolla, CA, USA).

To examine selectivity of PDT-induced cytotoxicity with the different conjugates, 5×10^5 cells were labeled with DiO (A431 and SK-OV-3) or DID (E98) dye (Life technologies, Thermo Fisher Scientific, Waltham, MA, USA) according to manufacturers protocol. Mixtures of A431, E98 and SK-OV-3 cells were plated and subjected to PDT as described above. Immediately, 2 h and 16 h after illumination cells were incubated with 1 μg/ml propidium iodide (Thermo Fisher Scientific, Waltham, MA, USA) in PBS for 15 min. Cells were visualized with the EVOS FL digital inverted fluorescence microscope (Thermo Fisher Scientific, Waltham, MA, USA) using the RFP LED light cube (Propidium Iodide), the GFP LED light cube (DiO labeled cells) and the Cy5 LED light cube (DiD labeled cells).

Mechanism of cell death

To check if apoptotic cell death was induced by 7D12-C[PS] conjugates, cells were treated with 15 nM 7D12-C[PS] conjugates and illuminated as described. Immediately, 2 h and 20 h after illumination cells were incubated with 1:250 Annexin-V-Alexa488 (Life Technologies, Thermo Fisher Scientific, Waltham, MA, USA) and 1 μg/ml propidium iodide in 10 mM HEPES pH 7.4/140 mM NaCl/2.5 mM $CaCl_2$ to stain apoptotic and dead cells, respectively. Stained cells were visualized with the EVOS. As a positive control, cells were treated with 2 μM staurosporin for 4 h at 37°C

Furthermore, extracts of treated cells 2 h and 4 h after illumination and of staurosporin treated control cells were made with RIPA buffer (#9806, Cell Signaling Technology, Danvers, MA, USA). 20 μg of total protein was run on an 8% SDS-PAGE gel, and electroblotted on a nitrocellulose membrane (GE healthcare, Little Chalfont, USA). Blots were stained with rabbit-anti-cleaved-Caspase-3 (Asp175) (1:1000, #9661, Cell Signaling Technology) and mouse-anti-GAPDH. Blots were visualized on the Odyssey scanner.

In vitro PDT assays with spheroids

Because 3D cell cultures better recapitulate clinical tumors than adherent 2D cell cultures, we grew SK-OV-3 cells as tumor spheroids. To this end, 96-well round bottom culture plates were coated with 100 μl/well 1% agarose (Sigma Aldrich, Saint Louis, MO, USA) in DMEM/F12 medium (Gibco, Thermo Fisher Scientific, Waltham, MA, USA). SK-OV-3 cells (30,000/well) were seeded in 100 μl DMEM/F12 medium containing 0.3% BSA. Three days after seeding, the spheres were incubated for 30 min or 1 h at 37°C in DMEM/10% FCS and 120 nM 7D12-C[PS], 7D12-C[PS]-hLF, PS alone or medium only. After washing with DMEM/10% FCS spheres were

illuminated with a 60 J/cm^2 total light dose. After overnight incubation at 37°C, spheres were fixed in Unifix (Klinipath, Duiven, The Netherlands) at RT, and embedded in agar. 4 µM sections were stained with hematoxylin and eosin.

Ex vivo PDT assays with clinical ascites samples

All experiments with patient materials were performed according to institutional guide lines. To examine whether PIT with our conjugates could be an option for treatment of ovarian cancer we tested our constructs on cells, freshly derived from malignant ascites of patients diagnosed with high-grade serous ovarian carcinoma. Ascites was filtered through a 70 µm cell strainer. Nucleated cells were isolated by centrifugation on Ficoll, according to the manufacturer's instructions (Sigma Aldrich, Saint Lois, MO, USA) and cultured in RPMI/10% FCS/40 ug/ml gentamycin. For PDT experiments, cells were seeded at 10,000 cells per well in a 96-well plate and grown until >50% confluency. After incubation with 15 nM of the 7D12-C[PS], 7D12-C[PS]-hLF or PS alone for 30 min, cells were illuminated with 60 J/cm^2 total light dose. The next day, cell viability was determined using the SRB assay. In parallel experiments, ascites-derived cells were incubated with 15 nM of the different 7D12-C[PS] conjugates, illuminated and incubated overnight. The next day, cells were incubated with either 1 µg/ml cetuximab for 20 min and goat-anti-human Alexa488 (1:200 Thermo Fisher Scientific, Waltham, MA, USA) for 20 min to verify EGFR expression, or mouse-anti-EpCAM (1:200 Abcam, Cambridge, UK, ab7504) and donkey-anti-mouse Alexa488 (1:200 Thermo Fisher Scientific, Waltham, MA, USA) to verify EpCAM expression, and with 1 µg/ml Propidium iodide (Thermo Fisher Scientific, Waltham, MA, USA) to visualize dead cells. Propidium iodide and bound antibodies were visualized using the EVOS microscope.

### Statistics

Experiments were performed at least in duplicate, and within experiments all measurements were done in triplicate. IC50 values were determined in Graphpad Prism and statistical significance was checked with a Student's T-test. To check for significance of other data a one-way ANOVA with post hoc Bonferroni was performed in Graphpad Prism; * = $p<0.05$, ** = $p<0.01$, *** = $p<0.001$.

REFERENCES

1.   Henderson, B. W.; Dougherty, T. J., How does photodynamic therapy work? *Photochem. Photobiol.* **1992,** *55* (1), 145-57.

2.   Moan, J.; Berg, K., The photodegradation of porphyrins in cells can be used to estimate the lifetime of singlet oxygen. *Photochem. Photobiol.* **1991,** *53* (4), 549-53.

3.   Holohan, C.; Van Schaeybroeck, S.; Longley, D. B.; Johnston, P. G., Cancer drug resistance: an evolving paradigm. *Nat Rev Cancer* **2013,** *13* (10), 714-726.

4.   Kono, H.; Rock, K. L., How dying cells alert the immune system to danger. *Nature reviews. Immunology* **2008,** *8* (4), 279-89.

5.   van Straten, D.; Mashayekhi, V.; de Bruijn, H. S.; Oliveira, S.; Robinson, D. J., Oncologic Photodynamic Therapy: Basic Principles, Current Clinical Status and Future Directions. *Cancers (Basel)* **2017,** *9* (2).

6.   Tian, J.; Ding, L.; Ju, H.; Yang, Y.; Li, X.; Shen, Z.; Zhu, Z.; Yu, J. S.; Yang, C. J., A multifunctional nanomicelle for real-time targeted imaging and precise near-infrared cancer therapy. *Angew. Chem. Int. Ed. Engl.* **2014,** *53* (36), 9544-9.

7.   Ding, H.; Sumer, B. D.; Kessinger, C. W.; Dong, Y.; Huang, G.; Boothman, D. A.; Gao, J., Nanoscopic micelle delivery improves the photophysical properties and efficacy of photodynamic therapy of protoporphyrin IX. *Journal of controlled release : official journal of the Controlled Release Society* **2011,** *151* (3), 271-7.

8.   Rijcken, C. J.; Hofman, J. W.; van Zeeland, F.; Hennink, W. E.; van Nostrum, C. F., Photosensitiser-loaded biodegradable polymeric micelles: preparation, characterisation and in vitro PDT efficacy. *Journal of controlled release : official journal of the Controlled Release Society* **2007,** *124* (3), 144-53.

9.   Battah, S.; Balaratnam, S.; Casas, A.; O'Neill, S.; Edwards, C.; Batlle, A.; Dobbin, P.; MacRobert, A. J., Macromolecular delivery of 5-aminolaevulinic acid for photodynamic therapy using dendrimer conjugates. *Mol Cancer Ther* **2007,** *6* (3), 876-85.

10. Master, A. M.; Rodriguez, M. E.; Kenney, M. E.; Oleinick, N. L.; Gupta, A. S., Delivery of the photosensitizer Pc 4 in PEG-PCL micelles for *in vitro* PDT studies. *J. Pharm. Sci.* **2010,** *99* (5), 2386-98.

11. Li, B.; Moriyama, E. H.; Li, F.; Jarvi, M. T.; Allen, C.; Wilson, B. C., Diblock copolymer micelles deliver hydrophobic protoporphyrin IX for photodynamic therapy. *Photochem. Photobiol.* **2007,** *83* (6), 1505-12.

12. Khdair, A.; Gerard, B.; Handa, H.; Mao, G.; Shekhar, M. P.; Panyam, J., Surfactant-polymer nanoparticles enhance the effectiveness of anticancer photodynamic therapy. *Molecular pharmaceutics* **2008,** *5* (5), 795-807.

13. Guillemard, V.; Saragovi, H. U., Taxane-antibody conjugates afford potent cytotoxicity, enhanced solubility, and tumor target selectivity. *Cancer Res* **2001,** *61* (2), 694-9.

14. Heukers, R.; van Bergen en Henegouwen, P. M.; Oliveira, S., Nanobody-photosensitizer conjugates for targeted photodynamic therapy. *Nanomedicine : nanotechnology, biology, and medicine* **2014,** *10* (7), 1441-51.

15. Mehraban, N.; Freeman, H. S., Developments in PDT Sensitizers for Increased Selectivity and Singlet Oxygen Production. *Materials (Basel)* **2015,** *8* (7), 4421-4456.

16. van Driel, P. B.; Boonstra, M. C.; Slooter, M. D.; Heukers, R.; Stammes, M. A.; Snoeks, T. J.; de Bruijn, H. S.; van Diest, P. J.; Vahrmeijer, A. L.; van Bergen En Henegouwen, P. M.; van de Velde, C. J.; Lowik, C. W.; Robinson, D. J.; Oliveira, S., EGFR targeted nanobody-photosensitizer conjugates for photodynamic therapy in a pre-clinical model of head and neck cancer. *Journal of controlled release : official journal of the Controlled Release Society* **2016**.

17. Oliveira, S.; van Dongen, G. A.; Stigter-van Walsum, M.; Roovers, R. C.; Stam, J. C.; Mali, W.; van Diest, P. J.; van Bergen en Henegouwen, P. M., Rapid visualization of human tumor xenografts through optical imaging with a near-infrared fluorescent anti-epidermal growth factor receptor nanobody. *Molecular imaging* **2012,** *11* (1), 33-46.

18. Kessel, D.; Reiners, J. J., Jr., Apoptosis and autophagy after mitochondrial or endoplasmic reticulum photodamage. *Photochem. Photobiol.* **2007,** *83* (5), 1024-8.

19. Hsieh, Y. J.; Wu, C. C.; Chang, C. J.; Yu, J. S., Subcellular localization of Photofrin determines the death phenotype of human epidermoid carcinoma A431 cells triggered by photodynamic therapy: when plasma membranes are the main targets. *J. Cell. Physiol.* **2003,** *194* (3), 363-75.

20. Pavani, C.; Uchoa, A. F.; Oliveira, C. S.; Iamamoto, Y.; Baptista, M. S., Effect of zinc insertion and hydrophobicity on the membrane interactions and PDT activity of porphyrin photosensitizers. *Photochemical & photobiological sciences : Official journal of the European Photochemistry Association and the European Society for Photobiology* **2009,** *8* (2), 233-40.

21. Li, H.; Tsui, T. Y.; Ma, W., Intracellular Delivery of Molecular Cargo Using Cell-Penetrating Peptides and the Combination Strategies. *International journal of molecular sciences* **2015,** *16* (8), 19518-36.

22. Milletti, F., Cell-penetrating peptides: classes, origin, and current landscape. *Drug Discov Today* **2012,** *17* (15-16), 850-60.

23. Duchardt, F.; Ruttekolk, I. R.; Verdurmen, W. P.; Lortat-Jacob, H.; Burck, J.; Hufnagel, H.; Fischer, R.; van den Heuvel, M.; Lowik, D. W.; Vuister, G. W.; Ulrich, A.; de Waard, M.; Brock, R., A cell-penetrating peptide derived from human lactoferrin with conformation-dependent uptake efficiency. *J. Biol. Chem.* **2009,** *284* (52), 36099-108.

24. van Lith, S. A. M.; van den Brand, D.; Wallbrecher, R.; van Duijnhoven, S. M. J.; Brock, R.; Leenders, W. P. J., A Conjugate of an Anti-Epidermal Growth Factor Receptor (EGFR) VHH and a Cell-Penetrating Peptide Drives Receptor Internalization and Blocks EGFR Activation. *Chembiochem* **2017,** *18* (24), 2390-2394.

25. Roovers, R. C.; Laeremans, T.; Huang, L.; De Taeye, S.; Verkleij, A. J.; Revets, H.; de Haard, H. J.; van Bergen en Henegouwen, P. M., Efficient inhibition of EGFR signaling and of tumour growth by antagonistic anti-EFGR Nanobodies. *Cancer immunology, immunotherapy : CII* **2007,** *56* (3), 303-317.

26. Roovers, R. C.; Vosjan, M. J.; Laeremans, T.; el Khoulati, R.; de Bruin, R. C.; Ferguson, K. M.; Verkleij, A. J.; van Dongen, G. A.; van Bergen en Henegouwen, P. M., A biparatopic anti-EGFR nanobody efficiently inhibits solid tumour growth. *International journal of cancer* **2011,** *129* (8), 2013-24.

27. Debets, M. F.; van Berkel, S. S.; Schoffelen, S.; Rutjes, F. P.; van Hest, J. C.; van Delft, F. L., Aza-dibenzocyclooctynes for fast and efficient enzyme PEGylation via copper-free (3+2) cycloaddition. *Chem Commun (Camb)* **2010,** *46* (1), 97-9.

28. van Lith, S. A.; van Duijnhoven, S. M.; Navis, A. C.; Leenders, W. P.; Dolk, E.; Wennink, J. W.; van Nostrum, C. F.; van Hest, J. C., Legomedicine-A Versatile Chemo-Enzymatic Approach for the Preparation of Targeted Dual-Labeled Llama Antibody-Nanoparticle Conjugates. *Bioconjug Chem* **2017,** *28* (2), 539-548.

29. Alves, I. D.; Bechara, C.; Walrant, A.; Zaltsman, Y.; Jiao, C. Y.; Sagan, S., Relationships between membrane binding, affinity and cell internalization efficacy of a cell-penetrating peptide: penetratin as a case study. *PloS one* **2011,** *6* (9), e24096.

30. Wallbrecher, R.; Verdurmen, W. P.; Schmidt, S.; Bovee-Geurts, P. H.; Broecker, F.; Reinhardt, A.; van Kuppevelt, T. H.; Seeberger, P. H.; Brock, R., The stoichiometry of peptide-heparan sulfate binding as a determinant of uptake efficiency of cell-penetrating peptides. *Cellular and molecular life sciences : CMLS* **2014,** *71* (14), 2717-29.

31. Sarko, D.; Beijer, B.; Garcia Boy, R.; Nothelfer, E. M.; Leotta, K.; Eisenhut, M.; Altmann, A.; Haberkorn, U.; Mier, W., The pharmacokinetics of cell-penetrating peptides. *Molecular pharmaceutics* **2010,** *7* (6), 2224-31.

32. Madshus, I. H.; Stang, E., Internalization and intracellular sorting of the EGF receptor: a model for understanding the mechanisms of receptor trafficking. *J. Cell Sci.* **2009,** *122* (Pt 19), 3433-9.

33. Carcenac, M.; Dorvillius, M.; Garambois, V.; Glaussel, F.; Larroque, C.; Langlois, R.; Hynes, N. E.; van Lier, J. E.; Pelegrin, A., Internalisation enhances photo-induced cytotoxicity of monoclonal antibody-phthalocyanine conjugates. *British journal of cancer* **2001,** *85* (11), 1787-93.

7

34. Mitsunaga, M.; Ogawa, M.; Kosaka, N.; Rosenblum, L. T.; Choyke, P. L.; Kobayashi, H., Cancer cell-selective in vivo near infrared photoimmunotherapy targeting specific membrane molecules. *Nature medicine* **2011,** *17* (12), 1685-91.

35. Zhong, W.; Celli, J. P.; Rizvi, I.; Mai, Z.; Spring, B. Q.; Yun, S. H.; Hasan, T., In vivo high-resolution fluorescence microendoscopy for ovarian cancer detection and treatment monitoring. *British journal of cancer* **2009,** *101* (12), 2015-22.

36. van Dam, G. M.; Themelis, G.; Crane, L. M.; Harlaar, N. J.; Pleijhuis, R. G.; Kelder, W.; Sarantopoulos, A.; de Jong, J. S.; Arts, H. J.; van der Zee, A. G.; Bart, J.; Low, P. S.; Ntziachristos, V., Intraoperative tumor-specific fluorescence imaging in ovarian cancer by folate receptor-alpha targeting: first in-human results. *Nature medicine* **2011,** *17* (10), 1315-9.

37. Merlino, G. T.; Xu, Y. H.; Ishii, S.; Clark, A. J.; Semba, K.; Toyoshima, K.; Yamamoto, T.; Pastan, I., Amplification and enhanced expression of the epidermal growth factor receptor gene in A431 human carcinoma cells. *Science* **1984,** *224* (4647), 417-9.

38. Navis, A. C.; Bourgonje, A.; Wesseling, P.; Wright, A.; Hendriks, W.; Verrijp, K.; van der Laak, J. A.; Heerschap, A.; Leenders, W. P., Effects of dual targeting of tumor cells and stroma in human glioblastoma xenografts with a tyrosine kinase inhibitor against c-MET and VEGFR2. *PloS one* **2013,** *8* (3), e58262.

39. Bijman, M. N.; van Berkel, M. P.; Kok, M.; Janmaat, M. L.; Boven, E., Inhibition of functional HER family members increases the sensitivity to docetaxel in human ovarian cancer cell lines. *Anti-cancer drugs* **2009,** *20* (6), 450-60.

40. Kobashigawa, Y.; Kumeta, H.; Ogura, K.; Inagaki, F., Attachment of an NMR-invisible solubility enhancement tag using a sortase-mediated protein ligation method. *J. Biomol. NMR* **2009,** *43* (3), 145-50.

41. Favretto, M. E.; Brock, R., Stereoselective uptake of cell-penetrating peptides is conserved in antisense oligonucleotide polyplexes. *Small* **2015,** *11* (12), 1414-7.

42. Loike, J. D.; Silverstein, S. C., A fluorescence quenching technique using trypan blue to differentiate between attached and ingested glutaraldehyde-fixed red blood cells in phagocytosing murine macrophages. *Journal of immunological methods* **1983,** *57* (1-3), 373-9.

43. de Boer, E.; Warram, J. M.; Hartmans, E.; Bremer, P. J.; Bijl, B.; Crane, L. M.; Nagengast, W. B.; Rosenthal, E. L.; van Dam, G. M., A standardized light-emitting diode device for photoimmunotherapy. *Journal of nuclear medicine : official publication, Society of Nuclear Medicine* **2014,** *55* (11), 1893-8.

44. Vichai, V.; Kirtikara, K., Sulforhodamine B colorimetric assay for cytotoxicity screening. *Nature protocols* **2006,** *1* (3), 1112-6.
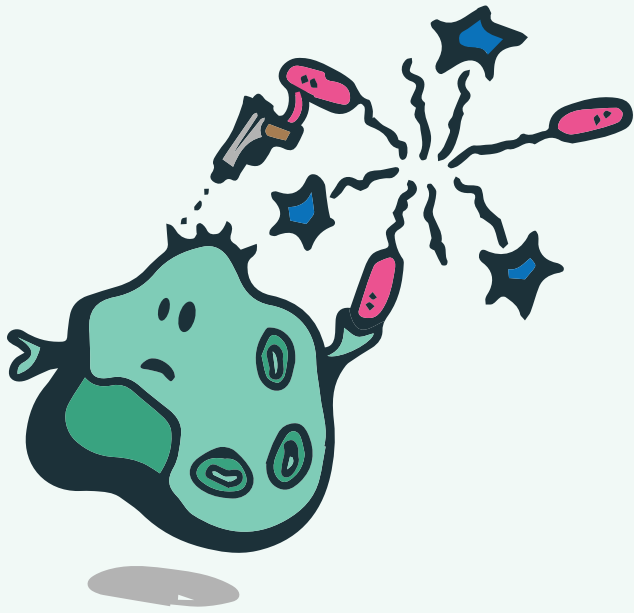
CHAPTER 8

Self-assembling VHH-elastin-like peptides for photodynamic nanomedicine.

Sanne A.M. van Lith[1*], Jan Pille[2,3*], Jan C.M. van Hest[2,3], William P.J. Leenders[1]

*Authors contributed equally

[1]Department of Pathology, Radboud Institute for Molecular Life Sciences, Radboudumc, Nijmegen, The Netherlands
[2]Institute for Molecules and Materials, Radboud University, Nijmegen, The Netherlands
[3]Bio-organic Chemistry Lab, Eindhoven University of Technology, Eindhoven, The Netherlands

ABSTRACT

Recombinant llama heavy-chain antibody fragments (VHHs) are promising tools in the field of targeted nanomedicine. 7D12, a VHH against the epidermal growth factor receptor (EGFR) that is overexpressed in various cancers, has been evaluated as an effective cancer-targeting VHH in multiple studies. The small size of VHHs (15-20 kDa) results in a low circulation half-life, which can be disadvantageous for certain applications. A solution to this problem is to attach VHHs to the surface of nanoparticles to increase the hydrodynamic radius of the conjugate. This approach simultaneously allows the incorporation of different VHHs and/or other targeting moieties and therapeutic components into one structure, creating multispecificity and versatility for therapy and diagnosis. Here, we present the construction of highly defined 7D12-containing nanoparticles by utilizing thermo-responsive diblock elastin-like peptides that reversibly self-assemble into micellar structures. The resulting particles have a hydrodynamic radius of 24.3 nm $\pm$ 0.9 nm and retain full EGFR-binding capacity. We present proof of concept of the usability of such particles by controlled incorporation of a photosensitizer and show that the resulting nanoparticles induce EGFR-specific light-induced cell killing. This approach is easily extended to the controlled incorporation of various functional modules, improving therapy and diagnosis with targeted nanomedicine

INTRODUCTION

The variable region of heavy-chain antibodies found in cameloids, called VHH, is of great interest to the field of nanomedicine[1-3]. VHHs are thermo- and pH-stable proteins that are well tolerated by the human immune system. Their affinity can equal or even supersede that of 'conventional' antibodies. In combination with cytotoxic agents, tumor-targeting VHHs can specifically recognize and kill cancer cells[4-5]. Although their small size of 15-20 kDa allows deeper tissue penetration than conventional antibodies, it also results in a low circulation half-life.

Nanoparticles decorated with VHHs have been developed to overcome the short blood-circulation time by increasing the hydrodynamic radius; the nanoparticle structure furthermore enables increased and more versatile drug loading[6-8]. Decoration with VHHs usually follows particle formation, and encapsulation or attachment of a desired payload is typically achieved during particle formation or via an additional coupling step. This procedure makes it difficult to precisely assess and reproducibly control the resulting VHH concentration on the particles' surface and the VHH-to-payload ratios. Controlling these parameters is essential to achieve maximum efficacy with minimal side effects. Thus, there is a clear need for optimally defined and controlled VHH-displaying nanoparticles.

Elastin-like peptides (ELPs) are biocompatible polypeptides that form amorphous coacervates in a temperature-dependent fashion[9-11]. They are composed of repeating pentameric units with the sequence glycine-X-glycine-valine-proline (GXGVP), where X can be any amino acid[11-12]. ELPs reversibly transform from a soluble, disordered state below the transition temperature to an assembled state consisting of type-II β-turns, type-I β-turns and β-strands above the transition temperature[13-16]. This behavior is thermodynamically driven: at the transition temperature, solvation of the protein backbone becomes entropically unfavorable. The conformational change and exposure of hydrophobic residues followed by assembly results in liberated water molecules, lowering the total energy of the system. Further increases in temperature enhance this effect. This so-called lower critical solution temperature (LCST) highly depends on the nature of the guest residue X, with hydrophilic residues raising the LCST and hydrophobic residues lowering it. ELP length, concentration and presence of salts also affect the LCST[17].

VHH-ELP fusion proteins have previously been synthesized with the aim to allow easy purification via temperature cycling, followed by VHH cleavage via introduced protease-sensitive tags[18]. ELP-based nanoparticles have been prepared out of amphiphilic block copolymers, either by employing ELP diblock polypeptides with different guest residues and hence different LCSTs[9-10,19], or by coupling ELPs with low LCST to hydrophilic polymers such as poly(ethylene glycol)[20]. Given the excellent bio-compatible properties of ELPs[21-22], we envisioned the possibility of integrating VHH-ELP expression systems with the nanoparticle-forming potential of ELPs.

Here we report the use of an ELP diblock polypeptide (ELP^DB) to create self-assembling theranostic VHH-nanoparticles. The ELP^DB was composed of a 'hydrophilic' and a 'hydrophobic'

block, terms that relate to the solvation state of the ELP block at physiological conditions. The hydrophilic block consisted of 60 pentamers with alanine or glycine guest residues in a ratio of 3 to 2. The hydrophobic block contained 60 pentamers with isoleucine as guest residues. We used the VHH 7D12 that targets the epidermal growth factor receptor (EGFR)[23-24]. Fc5, an unrelated VHH directed against the endothelial receptor Cdc50A, was used as control[25]. Well-defined composite nanoparticles were reproducibly made by combining 7D12-ELP^DB or Fc5-ELP^DB fusion proteins with ELP^DB as molecularly dissolved species at predetermined ratios, followed by heating the solution above the LCST of the hydrophobic block (Figure 1). The 7D12-decorated ELP micelles were able to selectively target tumor cells that (over) express EGFR. Upon incorporation of a third ELP^DB to which the photosensitizer IRDye700DX was conjugated, the composite nanoparticles could be used for highly effective and specific photoimmunotherapy (PIT).

= Hydrophobic ELP block
= Hydrophilic ELP block
= VHH
= Photosensitizer
= EGFR
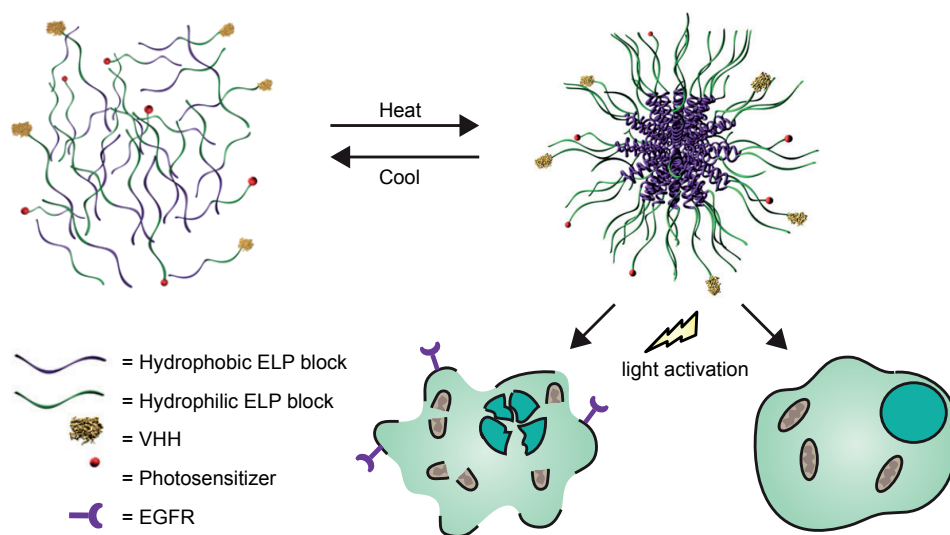
Figure 1. Schematic representation of photodynamic therapy with self-assembling recombinant Llama heavy-chain antibody fragments (VHHs). Amphiphilic diblock elastin-like polypeptides (ELP^DB) are mixed at low temperatures with ELP^DB functionalized with a photosensitizer and ELP^DB functionalized with a VHH directed against epidermal growth factor receptor (EGFR) at a known ratio. Upon heating to 37°C, components spontaneously assemble into supramolecular structures simultaneously displaying VHHs and photosensitizer. Only EGFR expressing cells die after incubation with particles and subsequent illumination.

RESULTS AND DISCUSSION

The VHH-ELP[DB]s were prepared by cloning cDNA sequences coding for 7D12 and Fc5 in frame with ELP[DB]. An intervening cysteine residue was introduced as a handle for maleimide-based modification. Fusion proteins were successfully expressed in BLR(DE3) *Escherichia coli* cells by auto-induction (Figure 2). The sequences were preceded by a pelB leader sequence to direct the protein to the periplasm of *E.coli*. The slightly oxidative milieu in the bacterial periplasm allowed the proper formation of internal disulfide bonds present in 7D12 and Fc5. The proteins were purified by inverse-transition cycling. ELP[DB] and VHH-ELP[DB] fusion proteins were obtained in > 95% purity with 20-50 mg/L yield (Table 1, Figure 2A). Molecular masses of the protein samples were measured via electrospray ionization time-of-flight spectrometry (ESI-ToF) and agreed well with the predicted masses (Table 1, Figure 2B). The N-terminal formyl methionine of ELP[DB] was cleaved off as expected[26]. For 7D12-ELP[DB] and Fc5-ELP[DB], complete removal of the pelB sequence was observed. For 7D12-ELP[DB], an additional peak was found. 7D12 contains an N-terminal glutamine, which is known to be converted in an autocatalytic or enzymatic step to pyroglutamate, resulting in the loss of ammonia, explaining the 18 Da difference[27]. Fc5-ELP[DB], which does not contain N-terminal glutamine, did not show this side product (Table 1).

Table 1. Overview of proteins used in this study.

Construct	Yield (mg/L)[1]	Theoretical mass (Da)[2]	Found mass (Da)[3]	Labelling efficiency (%)[4]
ELP[DB]	43	48198	48198	NA
7D12-ELP[DB]	33	63049	63031 & 63049	NA
Fc5-ELP[DB]	47	61903	61904	NA
Alexa[647]-ELP[DB]	NA	49037	49036	61 ± 2
PS-ELP[DB]	NA	49951	49951	Quantitative
7D12[FL]-ELP[DB]	NA	63475	63457 & 63475	89 ± 12
Fc5[FL]-ELP[DB]	NA	62330	62332	88 ± 3

[1]Yield specifies obtained product per liter of bacterial culture. [2]The theoretical mass was determined with ExPASy (http://www.expasy.org/) excluding the N-terminal methionine for ELP[DB] or the pelB sequence for 7D12-ELP[DB] and Fc5-ELP[DB] (see SI). [3]Mass found after deconvolution of mass spectrum. [4]Percentage of labeled protein.

8
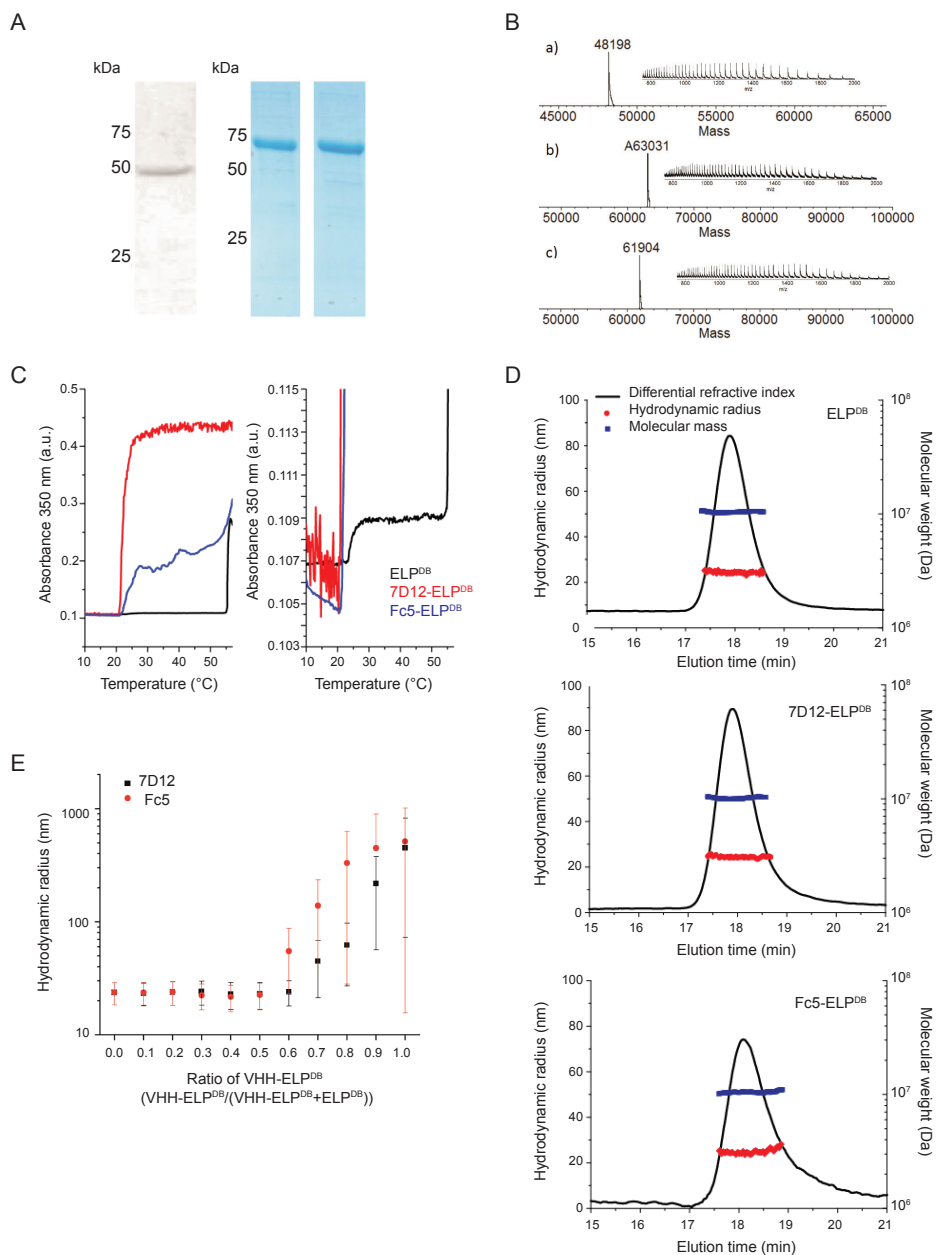
Figure 2. Characterization of expressed proteins and formed nanoparticles. A) SDS-PAGE of ELP^{DB} (silver-stained, absence of aromatic amino acids in the ELP prevents Coomassie Brilliant Blue (CBB) staining), 7D12-ELP^{DB} and Fc5-ELP^{DB} (stained with CBB). B) Mass spectra and deconvoluted masses of a) ELP^{DB}, b) 7D12-ELP^{DB} and c) Fc5-ELP^{DB}. C) Particle formation and aggregation of ELP^{DB} nanoparticles as determined by spectrometry. Left) A 10 μM solution of ELP^{DB}, 7D12-ELP^{DB} or Fc5-ELP^{DB} in PBS was gradually heated at 1°C/min. Right) Zoom-in showing the slight increase in turbidity at the first transition temperature around

25°C for ELP[DB] consistent with particle formation. The VHH-ELP[DB] constructs directly transition into bigger aggregates at a similar transition temperature as determined by DLS. D) Size-exclusion chromatography coupled to multi-angle light scattering of nanoparticles containing 100% ELP[DB], 10% 7D12-ELP[DB] or10% Fc5-ELP[DB]. E) Evaluation of nanoparticle stability as a function of the fraction of 7D12-ELP[DB] or Fc5-ELP[DB]. X-axis represents the ratio of VHH-ELP[DB] to ELP[DB] in the micelles.

Table 2. Results from SEC-MALS measurements of the different nanoparticle formulations.

Sample	R_h (nm)[1]	R_{rms} (nm)[2]	ρ[3]	Mass (kDa)[4]	Monomers per micelle[5]
ELP[DB]	24.0 ± 0.5	17.2 ± 0.1	0.72 ± 0.02	10300 ± 15	214
10% 7D12-ELP[DB]	24.6 ± 0.6	17.4 ± 0.1	0.71 ± 0.02	9958 ± 17	200
10 % Fc5-ELP[DB]	24.3 ± 0.6	19.8 ± 0.3	0.81 ± 0.02	10470 ± 16	211

[1]Hydrodynamic radius. [2]Radius of gyration. [3]Radius of gyration divided by the hydrodynamic radius. [4]Average molecular mass. [5]Monomers per micelle calculated with the weighted average molecular mass of ELP[DB] particles and monomers. See Figure 2D for SEC-MALS data.

ELP[DB] nanoparticles were stable between 25°C and 55°C (Figure 2C). For characterization, purified ELP[DB,] 10% 7D12-ELP[DB], 10% Fc5-ELP[DB] were heated to 37°C after which hydrodynamic radius, radius of gyration and molecular weight were determined by size-exclusion chromatography, followed by multi-angle light scattering (SEC-MALS) (Figure 2D). The hydrodynamic radius of particles with purified ELP[DB] was approximately 24 nm (Table 2). The ratio of radius of gyration to hydrodynamic radius, an indication of the morphology of particles, was close to the theoretical value of a homogeneous sphere (0.778)[28-29]. The mass distribution (with an average of 10.3 MDa) revealed that particles consisted of on average 214 monomers per micelle, in agreement with comparable ELP particles[11].

In order to determine the maximum possible functionalization degree of the nanoparticles with VHH, we proceeded by systematically mixing ELP[DB] with different percentages of 7D12-ELP[DB] or Fc5-ELP[DB]. We observed a transition point at 50% 7D12-ELP[DB] and 60% Fc5-ELP[DB], respectively. Above this ratio, uncontrolled aggregation resulted in micrometer-sized aggregates or coacervates (Figure 2E). The loss of particle stability can be explained by a geometrical model. Assuming a homogenous sphere with a radius of 24 nm, consisting of 214 monomers, each exposed monomer terminus occupies a surface of 33.8 nm[2], or a sphere with a radius of approximately 2 nm. Since the radius of VHHs is around 2-3 nm[30], it is highly plausible that steric hindrance at high VHH-ELP[DB] ratios occurs, leading to rearrangement and/or aggregation.

Incorporation of 10% VHH-ELP[DB] resulted in well-defined micelles with physicochemical characteristics similar to ELP[DB] micelles (Table 2, Figure 2D). This percentage should result in a display of approximately 20 VHH molecules per micelle.

Since the LCST of ELP[DB] is concentration dependent, we determined the critical micelle concentration (CMC) by dynamic light scattering (DLS) and found that the CMC is lower than 100 nM (Figure 3).

8

In order to mimic *in vivo* conditions we investigated the effect of the presence of human serum (HS) on the particle properties. ELP micelles in HS were shown to be stable for at least 2 h at 37°C, and furthermore could be reversibly assembled in a temperature-dependent manner (Figure 4).
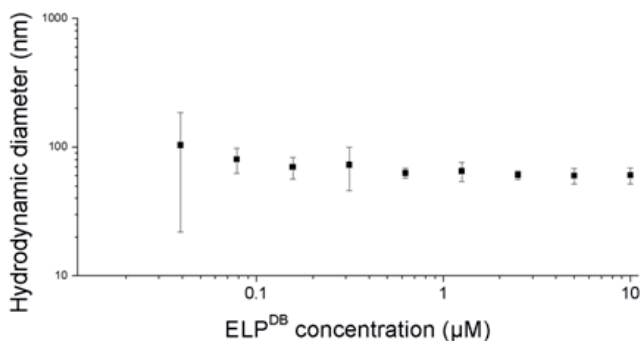
Figure 3. Concentration range of ELP^{DB} under assembling conditions with dynamic light scattering (DLS).
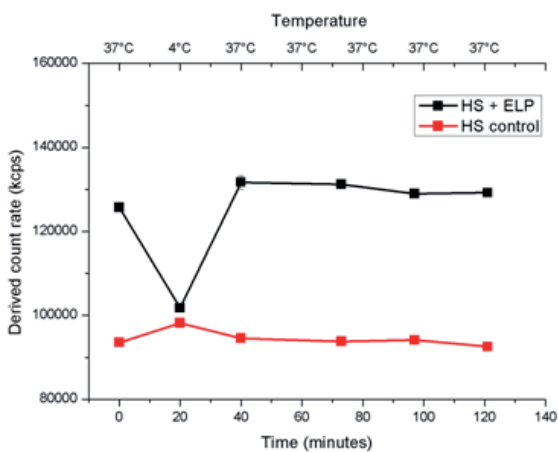
Figure 4. Stability of ELP^{DB} particles in human serum (HS). The temperature-dependent change in derived count rate shows the formation of larger species, which increases the total amount of light scattered, conform to the transition of ELP^{DB} monomers to micelles (data not shown) in the sample containing ELP^{DB}s (HS + ELP). As aggregation into precipitates was not observed with visual inspection, these data strongly indicate stable particles in the timeframe shown.
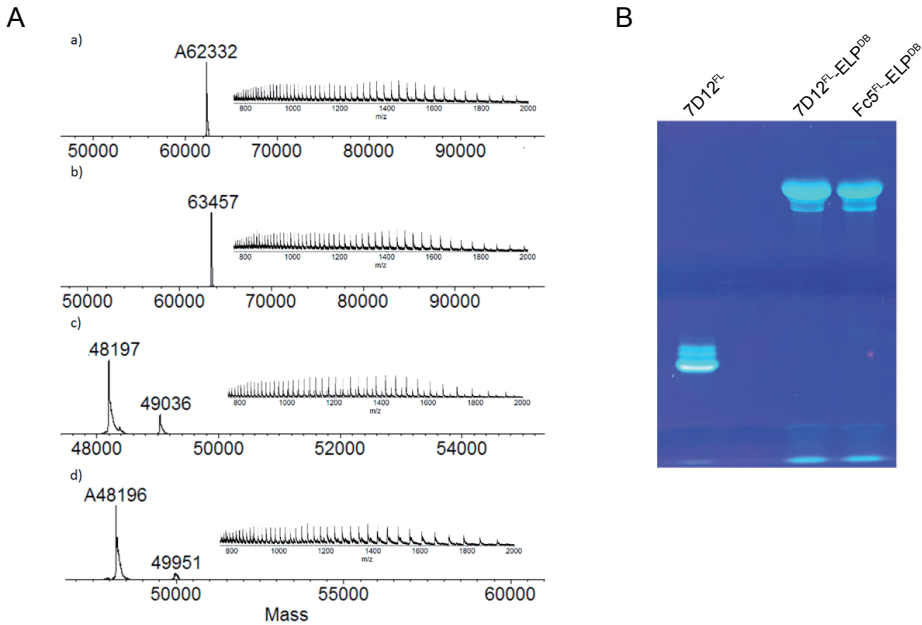
Figure 5. A) Obtained masses from a) Fc5FL-ELPDB, b) 7D12FL-ELPDB c) Alexa647-ELPDB and d) PS-ELPDB. B) SDS-PAGE of fluorescein-labeled 7D12 and VHH-ELPDB constructs by visualized by UV illumination.

To separately follow the fate of VHH-ELPDB and ELPDB after cellular uptake of composite micelles, we labeled VHH-ELPDB with fluorescein-5-maleimide (FL), yielding 7D12FL-ELPDB and Fc5FL-ELPDB (Figure 5A+B). ELPDB was labeled with Alexa647-N-hydroxysuccinimide (NHS) ester or IRDye700DX (PS) via NHS chemistry at the N-terminal amino group of ELPDB, yielding Alexa647-ELPDB and PS-ELPDB, respectively (Table 1, Figure 5A).

FL-fluorescence-based flow cytometry, performed at 4°C to prevent self-assembly into micelles and internalization, showed that monomeric 7D12FL-ELPDB, but not Fc5FL-ELPDB, effectively bound to EGFR-expressing A431 cells (Figure 6A), demonstrating that the 7D12 moiety had retained its EGFR affinity. 7D12FL-ELPDB binding was slightly less than the 7D12FL control, indicating that the fusion to ELPDB may induce some steric hindrance at low temperatures. No binding to the EGFR-negative E98 cell line was observed for either 7D12FL-ELPDB or Fc5FL-ELPDB. These experiments clearly illustrate that the specificity of 7D12 remains unchanged in the context of a fusion protein with ELPDB, and that ELPDB itself did not show aspecific binding to the cell lines tested.

We next prepared micelles by heating a mixture of ELPDB, Alexa647-ELPDB and VHHFL-ELPDB (85:5:10) to 37°C, and analyzed *in vitro* binding and uptake by measuring cell-associated FL fluorescence and Alexa647 fluorescence in flow cytometry experiments. 7D12FL-Alexa647-ELPDB micelles associated with A431 cells but not with EGFR-negative E98 cells (Figure 6B).

8

Incubation with composite 7D12[FL]-Alexa647-ELP[DB] micelles resulted in 44% higher cell-associated FL fluorescence relative to the situation in which equal concentrations of (monomeric) 7D12[FL] were used, indicating a multivalency and avidity effect of 7D12[FL] induced by particle formation. Of note, incubation of A431 with 7D12[FL]-Alexa647-ELP[DB] micelles also resulted in cell-associated Alexa647 fluorescence (Figure 6B), and fluorescence microscopy revealed membranous and intracellular colocalization of both Alexa647 and FL (Figure 6C), indicating that 7D12[FL] associated with the cells as part of intact micelles. Fc5[FL]-Alexa647-ELP[DB] micelles showed little background association with A431 cells. Altogether, these data show that composite 7D12[FL]-Alexa647-ELP[DB] micelles that target tumor cells in an EGFR-specific manner can be created.

Unfortunately, 7D12 binds to EGFR only in a cell context[31]. Since the VHH is internalized upon EGFR binding at 37 °C, it is difficult to quantitatively compare avidity effects of 7D12[FL] in micellar or monomeric form, because at 37°C results will always be biased by internalization effects. Future studies with other VHH-ELP constructs that can be used in cell-free systems may provide important answers on the subject of avidity.

In an effort to determine the CMC of the functionalized particles *in vitro*, we varied the concentration of all components, maintaining the same ratios. As shown in Figure 6D, 7D12-induced binding and uptake of Alexa647-ELP[DB] occurred at concentrations as low as 160 nM (VHH concentration of 16 nM), showing the presence of co-functionalized micelles and agreeing with results obtained by DLS. Using lower ELP[DB] concentrations for more accurate determination of the CMC was not feasible due to insufficient fluorophore signal to noise ratio. For a more accurate determination *in vitro* we used the photodynamic therapy assay as described below.

A

Fluorescein

Mean fluorescence (a.u.)

400
300
200
100
0

A431   E98

***

☐ 7D12FL
■ 7D12FL-ELPDB
■ Fc5FL-ELPDB

B

Fluorescein

Mean fluorescence (a.u.)

200
150
100
50
0
-50

A431   E98

**

Alexa647

Mean fluorescence (a.u.)

200
150
100
50
0
-50

A431   E98

***

☐ 7D12FL
■ 10% 7D12FL-ELPDB, 5% Alexa647-ELPDB, 85% ELPDB
■ 10% Fc5FL-ELPDB, 5% Alexa647-ELPDB, 85% ELPDB

C

7D12FL   10% 7D12FL-ELPDB, 5% Alexa647-ELPDB, 85% ELPDB   10% Fc5FL-ELPDB, 5% Alexa647-ELPDB, 85% ELPDB

Merge

Alexa647

Fluorescein

8

D

Fluorescein

Mean fluorescence (a.u.)

200
150
100
50
0

0   100   200   300   400   500
concentration VHH (nM)

Alexa647

Mean fluorescence (a.u.)

200
150
100
50
0

0   100   200   300   400   500
concentration VHH (nM)

▲ 7D12FL
● 10% 7D12FL-ELPDB, 5% Alexa647-ELPDB, 85% ELPDB
■ 10% Fc5FL-ELPDB, 5% Alexa647-ELPDB, 85% ELPDB

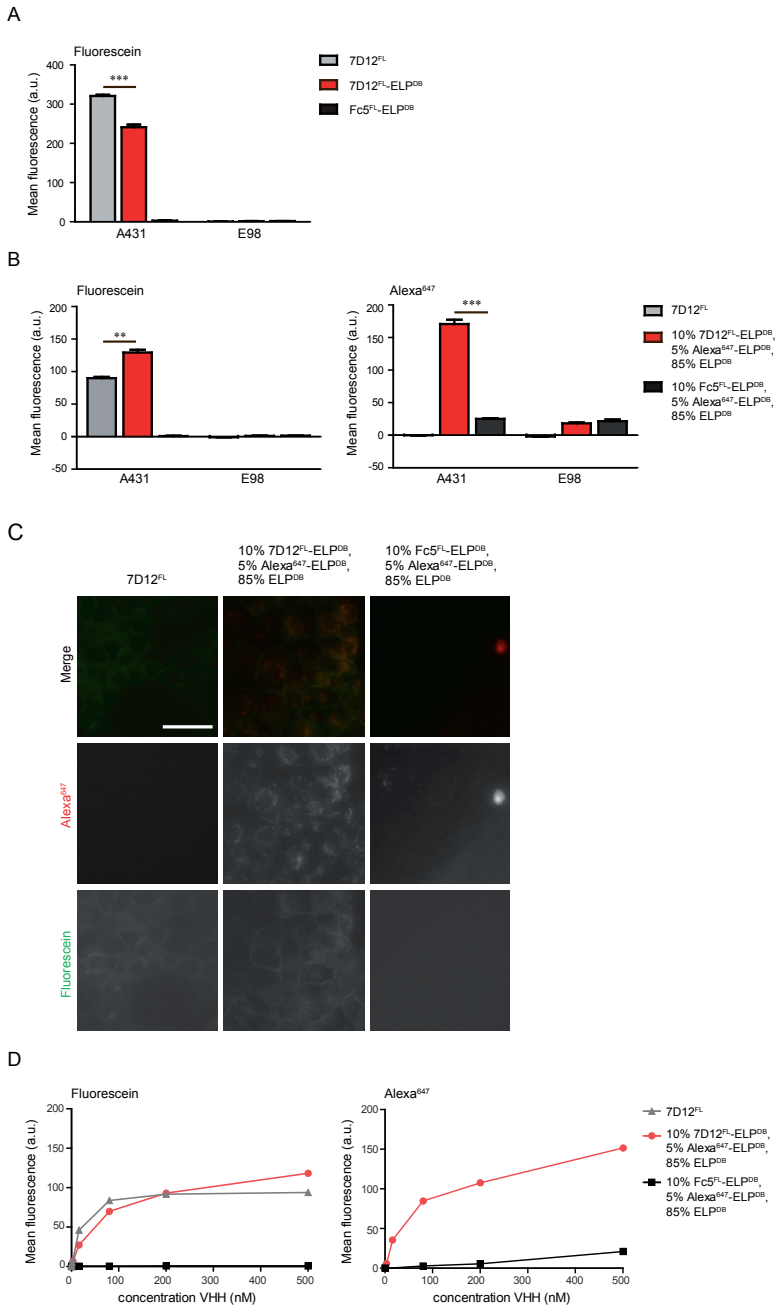**Figure 6.** Cellular binding and uptake of VHHFL-ELPDB monomers and micelles, respectively. A) Cell-associated FL fluorescence as determined with flow cytometry after cold (4°C) incubation with 1 µM 7D12FL, 7D12FL-ELPDB or Fc5FL-ELPDB monomers. B) Cell associated FL and Alexa647 fluorescence as determined with flow cytometry after warm (37 °C) incubation with 10 µM (refers to total ELPDB concentration) of

7D12^{FL}-Alexa647-ELP^{DB} micelles or Fc5^{FL}-Alexa647-ELP^{DB} micelles. Note that there is some unexplained non-specific background binding of Alexa- ELP^{DB} but not of VHH^{FL}-ELP^{DB} C) Microscopy of A431 cells visualizing cell-associated FL and Alexa647 fluorescence after incubation with VHH^{FL}-Alexa647-micelles. The scale bar denotes 50 µm. D) Cell-associated FL and Alexa647 fluorescence as determined with flow cytometry after warm (37 °C) incubation of A431 cells with a concentration range of 7D12^{FL}-Alexa647-ELP^{DB} micelles or Fc5^{FL}-Alexa647-ELP^{DB} micelles. * indicates significance with p<0.05, ** indicates significance with p<0.01, *** indicates significance with p<0.001.

To test whether EGFR-targeting ELP^{DB}-based micelles can be used in a therapeutic manner, we prepared 7D12^{FL}-ELP^{DB} micelles containing the photosensitizer IRDye700DX, conjugated to ELP^{DB} (PS-ELP^{DB}). Of note, the micelles with different compositions of VHH^{FL}-ELP^{DB} and PS-ELP^{DB} monomers, all have a hydrodynamic radius of 29-34 nm, as measured by DLS (Table 3).

Table 3. Hydrodynamic radius of different ELP^{DB} micelle compositions as measured by DLS (mean intensity).

Composition	Hydrodynamic radius (nm)
100 % PS - ELP^{DB}	30.7 $\pm$ 10.2
2 % 7D12^{FL} - ELP^{DB}, 98 % PS-ELP^{DB}	32.2 $\pm$ 10.0
2 % Fc5^{FL} - ELP^{DB}, 98 % PS-ELP^{DB}	29.3 $\pm$ 6.4
10 % 7D12^{FL} - ELP^{DB}, 10 % PS -ELP^{DB}	33.8 $\pm$ 13.5
10 % Fc5^{FL} - ELP^{DB}, 10 % PS -ELP^{DB}	33.4 $\pm$ 14.0
ELP^{DB}	30.5 $\pm$ 8.4

To achieve maximum drug loading while maintaining sufficient targeting capacity, we prepared micelles containing 2% VHH^{FL}-ELP^{DB} and 98% PS-ELP^{DB}. Cell-killing efficiency of these micelles was compared to cell killing by monomeric 7D12, directly conjugated with IRDye700DX (7D12^{PS}). A431 or E98 cells were incubated with 7D12^{FL}-PS-micelles or equimolar amounts of 7D12^{PS} prior to illumination. 7D12^{FL}-PS-ELP^{DB} micelles actively killed A431 cells in a light-dependent and 7D12-specific manner with an EC50 concentration of 82.7 pM compared to 121.5 pM for the 7D12^{PS} control. (Figure 7A). This indicates that micelles were formed already at a VHH concentration as low as 82.7 pM, corresponding to an ELP^{DB} concentration of 4.1 nM. No toxicity was observed towards E98 cells, proving that 7D12-mediated binding and/or uptake is necessary for toxicity. Control micelles composed of 2% Fc5^{FL}-ELP^{DB} and 98% PS-ELP^{DB} showed no light-dependent toxicity upon illumination of either A431 or E98 cells. Importantly, no dark toxicity of either particle was found (Figure 7B). The cell-killing efficiency of 7D12-ELP^{DB} particles pre-incubated in human serum at 37°C for up to 4 hours, was surprisingly increased compared to particles diluted in DMEM/10%FCS (Figure 7C), indicating that particles are stable and therapeutically active in 100% serum.
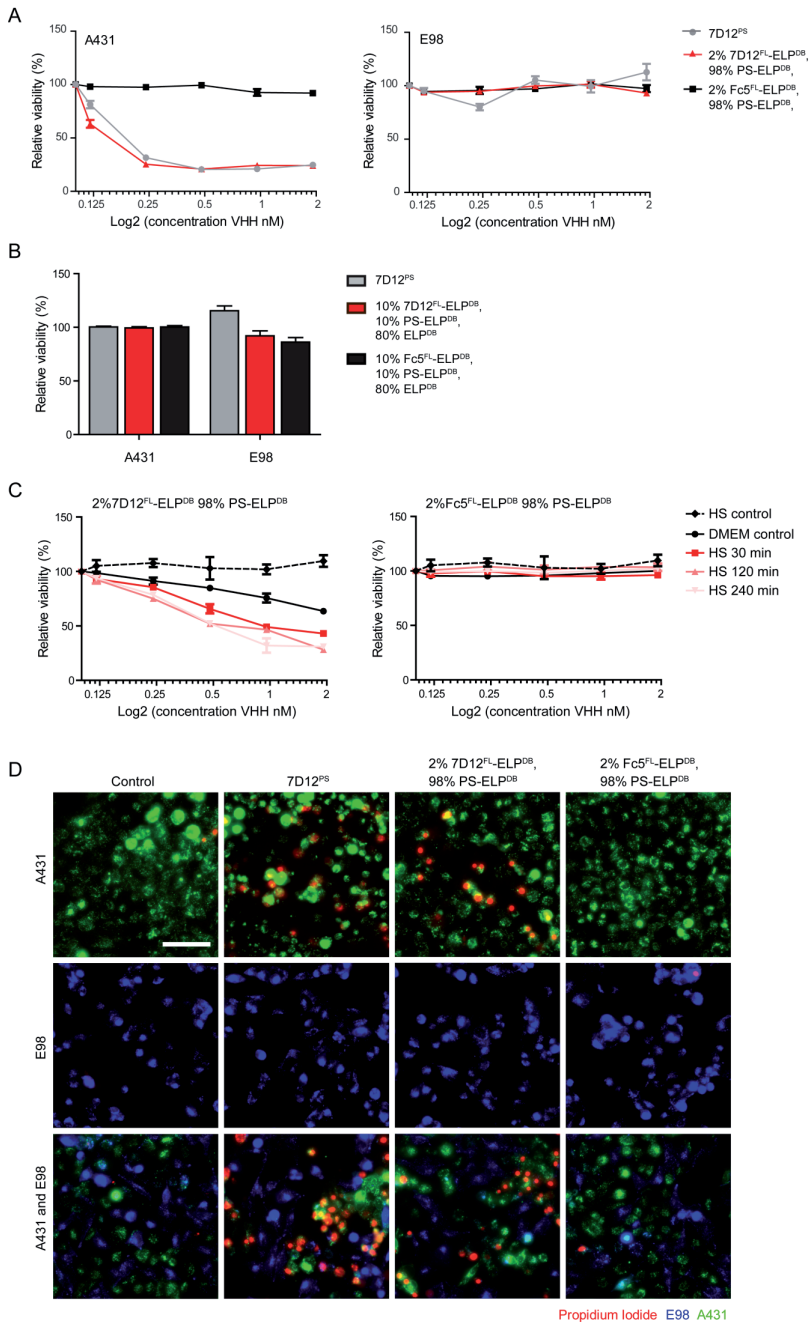
Figure 7. Phototoxicity induced by VHH^{FL}-PS-ELP^{DB} micelles in A431 and E98 cells. A) Relative cell viability after incubation and illumination with either 7D12^{FL}-PS-ELP^{DB} micelles, Fc5^{FL}-PS-ELP^{DB} micelles or 7D12^{PS} control. B) Relative cell viability after incubation without illumination with either 7D12^{FL}-PS-ELP^{DB} micelles or Fc5^{FL}-PS-ELP^{DB} micelles or 7D12^{PS} control. Note the absence of dark toxicity. C) Efficacy of PDT in

A431 cells after incubation of the VHH[FL]-PS-micelles in human serum (HS). The graphs depict the relative cell viability after incubation with either 7D12[FL]-PS-micelles or Fc5[FL]-PS-micelles that are pre-incubated for 30, 120 or 240 min in HS and subsequent illumination. HS only (HS control) and 7D12[FL]-PS-micelles or Fc5[FL]-PS-micelles directly diluted in DMEM (DMEM control) were taken as controls. D) Fluorescence microscopy of DiD labeled A431 (green) and DiO labeled E98 (blue) (co-)cultures that are incubated with propidium iodide (red) after incubation with 30 nM 7D12-ELP[DB] or Fc5-ELP[DB] based PS-ELP[DB] particles or equimolar VHH 7D12[PS] and illumination. The scale bar denotes 100 μm.

The cell-specificity of the particles was further confirmed by co-culturing DiO-labeled A431 (green) and DiD-labeled E98 (blue) cells and performing photo-immunotherapy as described above. By staining dead cells with propidium iodide, it was observed that only EGFR expressing A431 cells died (Figure 7D). Thus, targeted photoimmunotherapy with 7D12[FL]-PS-ELP[DB] micelles is highly specific for target-expressing cells without harming neighboring target-negative cells.

The used light dose of 60 J/cm^2 is physiologically relevant; clinical studies reported safe use of light doses up to 125 J/cm^2 in for example non-small cell carcinoma in the lung and cervical cancer[32]. Still, the penetration depth of near-infrared light is below 1 cm, and therefore this treatment will often have to be combined with surgery.

Assuming Poisson distribution, 2% VHH-ELP[DB] are sufficient to ensure that ~ 98% of all particles contain at least one targeting moiety. This leaves ample opportunities to combine several targeting groups in one particle and to further optimize their composition.

CONCLUSION

In conclusion, we have shown successful self-assembly of VHH-ELP[DB] conjugates into micelles that can be used for targeted photodynamic therapy *in vitro* and potentially *in vivo*. The 24 nm radii of these micelles are considered excellent for nanomedicine; large enough to avoid rapid clearance from the circulation, yet small enough to extravasate and penetrate the intercellular space of tumors. The system allows implementation of multiple VHHs to generate multi-targeted drug delivery nanoparticles. Spontaneous micelle formation required concentrations as low as 4.1 nM. Further efforts will focus on validating the *in vivo* stability and activity of ELP[DB] nanoparticles. Combining the system with therapeutic and diagnostic molecules may result in an interesting theranostic platform.

METHODS

Cloning and protein expression

The VHHs 7D12 and Fc5 were used in this study; 7D12 is directed against EGFR, and Fc5 targets the luminal brain endothelial cell protein Cdc50A[33]. 7D12 and Fc5 were expressed as fusion products with ELP[DB] and 7D12-C-LPETG-8xHis-Vsv, hereafter 7D12, was produced as a control for the *in vitro* studies. The gene sequences encoding for ELP[DB], pelB-Fc5-ELP[DB] and pelB-7D12-ELP[DB] were cloned into pET-24a(+) (Novagen) expression vectors[34], by recursive directional ligation, transformed into *E.coli* BLR(DE3) cells and grown on agar plates containing 30 µg/mL kanamycin overnight at 37°C. A single colony was grown overnight at 30°C, 250 rpm in LB medium containing 50 µg/mL kanamycin and 0.5% w/v D-glucose. The overnight culture was diluted to an OD_{600} of 0.1 in filter-sterilized AIM TB medium (Formedium) containing 6 g/L glycerol, 0.005% Antifoam 204 and 50 µg/mL kanamycin. Cells were grown at 300 rpm at 37 °C for 20 hours. For 7D12-ELP[DB] and Fc5-ELP[DB], the culture was shifted to 30 °C after 4 hours of growth.

The pHENIX-7D12-C-LPETG-HIS-VSV plasmid was transformed in E.coli strain ER2566. Cells were grown at 37°C in 2xTY medium containing 3.5% (w/v) glycerol and 50 µg/ml ampicillin till an OD_{600} of 0.6-0.8. Protein expression was induced with 1.0 mM isopropyl β-D-thiogalactoside (IPTG, Serva, Heidelberg, Germany) at 30°C for 2.5 hrs.

Protein extraction and purification

Cells were collected by centrifugation at 2000 g, 4°C for 30 minutes. For cytoplasmic extraction, 1 g of wet cell pellet was resuspended in 2 mL lysis buffer (50 mM Tris-HCl pH 8.0, 25 mM NaCl, 1 mM EDTA, 0.1 mM PMSF, cOmplete™ Protease Inhibitor Cocktail, 0.5 mg/mL lysozyme) and incubated for 4 h at 4°C. Lysis was followed by sonication on a Branson Sonifier 250 (power level 2-4, 12 cycles of 10 s sonication, 10 s breaks). Cell debris was collected by centrifugation at 15,000 g at 4°C for 15 min. Residual DNA was precipitated by adding 0.5% w/v poly(ethylene imine) and removed by centrifugation at 15,000 g at 4°C for 15 min. ELP[DB] was precipitated by adding a saturated solution of $(NH_4)_2SO_4$ up to 10-25 v/v%. Proteins were collected by centrifugation at 15,000 g at 4°C for 15 min. The pellet was resuspended in phosphate buffered saline and centrifuged to remove insoluble contaminants at 15,000 g at 4°C for 20 min. This cycle was repeated until sufficient purity was achieved, usually after 2-4 cycles. ELPs were resuspended in MilliQ, desalted on a HiPrep 26/10 (GE Healthcare Life Sciences) with an AKTA Explorer 10 (GE Healthcare Life Sciences) at 1 mL/min MilliQ. Residual salt concentration was below 0.001 mg/mL as determined by conductivity. The ELP solution was filter-sterilized with 0.22 µm PES syringe filters (Nalgene) and freeze-dried. Yield was determined by weighing and varied around 43 mg/L culture (Table 1).

For periplasmic extraction of 7D12, 7D12-ELP[DB] and Fc5-ELP[DB], 1 g of wet cell pellet was resuspended in 10 ml extraction buffer A (0.2 M TRIS pH 8.0, 0.5 mM EDTA, 20 w/v% sucrose, 0.1

8

mM PMSF, cOmplete™ protease inhibitor cocktail) and incubated for 30 min at 4°C. Cells were pelleted by centrifugation at 2000 g for 30 minutes at 4°C and the supernatant collected. The extraction was repeated with extraction buffer B (0.2 M TRIS pH 8.0, 15mM MgSO$_4$, cOmplete™ protease inhibitor cocktail). Both supernatants were pooled before further processing. ELPs were precipitated as described above. Yield was determined by integration of the absorbance at 280 nm after separation with a Bio-Sec 5 300 Å column on an Agilent Bio-Inert HPLC with a flow rate of 1 mL/min PBS (Table 1). Aliquots were flash-frozen in liquid nitrogen and stored at -80°C. 7D12 was purified using Ni-NTA sepharose (IBA, Goettingen, Germany) by incubating the extraction supernatant with pre-equilibrated Ni-NTA sepharose for 1 h at 4°C, and after washing, the proteins were eluted with 500 mM imidazole. The eluate was dialyzed against 50 mM Tris-HCl pH 7.5 and 150 mM NaCl.

Sodium dodecyl sulfate polyacrylamide gel electrophoresis (SDS-PAGE)

Proteins were run under reducing conditions on 12% SDS-PAGE gels. Gels were either silver-stained in the case of ELP[DB] or stained with coomassie brilliant blue (CBB) in the case of 7D12, 7D12-ELP[DB] and Fc5-ELP[DB]. Purity was calculated from integrated pixel intensity after scanning the gels with ImageJ (https://imagej.nih.gov/ij/).

Electrospray ionization – time of flight mass spectrometry (ESI-TOF)

Mass was determined by ESI-TOF on a JEOL AccuTOF. Freeze-dried samples were resuspended in MilliQ to a concentration of 10 µM, samples containing buffer were first desalted with MilliQ using Amicon Ultra-0.5 spin filter units (Millipore, 10 kDa MWCO). All samples were acidified with 0.1% formic acid upon injection. Deconvoluted spectra were obtained using MagTran 1.03 b2.

Size-exclusion chromatography followed by multi-angle light scattering (SEC-MALS)

For SEC-MALS, the samples were separated on a Bio-Sec 5 1000 Å column (Agilent) at 0.4 mL/min; the mobile phase was 0.1 M phosphate buffer pH 7.0 at 35 °C. 7D12-ELP[DB] and Fc5-ELP[DB] were reduced with a molar excess of TCEP to avoid dimer formation prior to injection for 20 minutes at 4°C. Samples were equilibrated at 35°C before injection of 20 µL. Light scattering data were collected on a DAWN HELEOS II MALS detector (Wyatt) and differential refractive index was measured on an Optilab T-rex refractometer (Wyatt). Dn/dc values were determined theoretically[35].

Alexa647-ELP[DB] and PS-ELP[DB]

Freeze-dried ELPs were resuspended in 50 mM NaHCO$_3$ pH 7.84. Alexa647-NHS ester and IRDye 700DX-NHS ester were resuspended in DMSO and added drop-wise to the protein solution. The molar ratio ELP[DB] to NHS ester was 1:1 in the case of Alexa 647 and 1:1.3 in the case of IRDye

700DX. The reaction was allowed to proceed for 4 hours at 21°C, 300 rpm. Unreacted dye was removed by dialysis against MilliQ using Amicon Ultra-0.5 spin filter units (Millipore, 10 kDa MWCO). The volume of the dialyzed protein samples was determined; efficiency of conjugation was determined by measuring dye concentration and weighing protein samples after freeze-drying. Concentrations of the dyes were determined at 650 nm (ε = 270,000 $cm^{-1}M^{-1}$) and at 689 nm (ε = 165,000 $cm^{-1}M^{-1}$) for Alexa647 and IRDye700 DX, respectively. Mass was determined by ESI TOF (Table 1).

7D12[FL] and 7D12[PS]

Fluorescein-5-maleimide and maleimide-PEG_4-DBCO (Jena Bioscience, Jena, Germany) were conjugated to 7D12. The free thiol of the C-terminal cysteine in 7D12 was reduced by incubation with 20 mM TCEP for 15 min at RT. TCEP was removed by dialysis to 20 mM phosphate buffer pH 7.0, 150 mM NaCl and 5 mM EDTA in a 10 kDa MWCO centrifugal unit (Amicon, Millipore, Billerica, MS, USA). The VHH was incubated with either maleimide-5-fluorescein or maleimide-PEG_4-DBCO in a 1:3 molar ratio for 2 hrs at RT. Excess of maleimide probes was removed by dialysis to 50 mM Tris-HCl pH 7.5 and 150 mM NaCl in a 10 kDa MWCO centrifugal filter unit. IRDye700DX-NHS ester (LI-COR, Lincoln, NE, USA) was incubated with H_2N-PEG_3-N_3 (Jena Bioscience, Jena, Germany) in a 3:1 molar ratio for 7 h in 100 mM phosphate pH 8.6 and 150 mM NaCl. Subsequently 7D12[DBCO] was incubated with PS-N_3 in a 1:2 molar ratio o/n at RT. 7D12[PS] was purified by filter centrifugation in a 10 kDa MWCO filter unit using 50 mM Tris-HCl pH 7.5 and 150 mM NaCl. Protein purity was analyzed with SDS-PAGE gel electrophoresis, and concentration was determined by measuring ultraviolet absorbance at 495 or 689 nm for FL and PS conjugates, respectively. Aliquots were stored at -80°C.

7D12[FL]-ELP[DB] and Fc5[FL]-ELP[DB]

7D12-ELP[DB] and Fc5-ELP[DB] were dialyzed to 0.1 M phosphate buffer pH 7.0. TCEP was added in a ratio of 20:1 to reduce the introduced cysteine. Fluorescein-5-maleimide was dissolved in DMSO and added to 7D12-ELP[DB] at a ratio of 10:1. Unbound Fluorescein-5-maleimide was removed by dialysis using Amicon Ultra-0.5 spin filter units (Millipore, 10 kDa MWCO). Labeling efficiency and protein concentration were determined by integration of the absorbance at 280 and 495 nm after separation with a Bio-Sec 5 300 Å column on an Agilent Bio-Inert HPLC with a flow rate of 1 mL/min 0.1 M NH_4HCO_3 pH 8.62 (Table 1). Mass was determined by ESI TOF. 7D12[FL]-ELP[DB] and Fc5[FL]-ELP[DB] were flash-frozen in liquid nitrogen and stored at -80°C.

Dynamic light scattering and stability of ELP particles in human serum

Samples were diluted to a final concentration of 2 µM in PBS. Measurements were performed on a Malvern Zetasizer Nano. Samples were incubated for 5 minutes at 37°C before data collection. Reported values are averages of 3 independent measurements. For particle stability, 10 µM of 2% 7D12[FL]-ELP[DB], 98% PS-ELP[DB] was added to human serum. Human serum alone,

to which an equal volume of PBS alone was added, was taken as control. Light scattering data was collected at 4°C and 37°C. Aggregation was inspected visually. Reported values are averages of 3 independent measurements.

Cell culture

Human epidermoid carcinoma A431 cells with amplification of EGFR and high grade astrocytoma E98 cells without EGFR expression were cultured in DMEM (Lonza, Basel, Switzerland), supplemented with 10% FCS (Gibco) and 40 µg/ml gentamycin (Centrafarm, Etten-Leur, The Netherlands). Cells were cultured at 37°C in 5% CO_2 in a humidified atmosphere.

Flow cytometry

To determine functionality of 7D12[FL]-ELP[DB] monomers, binding to A431 and E98 cells was determined under non-internalizing conditions at 4°C. A431 and E98 cells were dissociated from culture flasks using 10 mM EDTA in PBS and transferred to V-bottom shaped 96-wells microplates (BD Biosciences, Franklin Lakes, NJ, USA) at 5 x 10^{5} cells per well. Cells were blocked with PBA (PBS, 0.5% BSA and 2% FCS) for 10 minutes at 4 °C, after which they were incubated with 1 µM 7D12[FL]-ELP[DB] or controls Fc5[FL]-ELP[DB] and 7D12[FL] in PBA for 30 min at 4°C. After washing twice with cold PBA, cell-associated fluorescence was quantified on the Cyan flow cytometer (Beckman Coulter, Fullerton, CA, USA) with parameter FL-1. To determine uptake of VHH functionalized ELP nanoparticles and compare this to monomeric VHHs, A431 and E98 cells were grown to 80% confluency in 8 well chambered Lab-Tek chambers (NUNC) after which cells were incubated with a concentration range of pre-warmed 7D12[FL]; 10% 7D12[FL]-ELP[DB], 5% Alexa647-ELP[DB], 85% ELP[DB] particles or 10% Fc5[FL]-ELP[DB], 5% Alexa647-ELP[DB], 85% ELP[DB] particles in DMEM with 10% FCS for 30 min at 37°C. Cells were washed twice with warm DMEM with 10% FCS, dissociated with trypsin and taken up in PBA, and cell associated fluorescence was quantified on the Cyan flow cytometer with parameters FL-1 and FL-8. Experiments were performed in triplicate and statistical significance was tested with an unpaired Student's T-test. Furthermore, cells were imaged after incubation with ELP[DB] particles (or equimolar VHH of 7D12[FL]) on the EVOS microscope using LED cubes GFP (Fluorescein) and Cy5 (Alexa647).

In vitro PDT assays

A431 and E98 cells were cultured in clear 96 wells plates till 80% confluency. Then cells were incubated with a concentration range of pre-warmed 7D12[PS] or 2% 7D12[FL]-ELP[DB], 98% PS-ELP[DB] particles or 2% Fc5[FL]-ELP[DB], 98% PS-ELP[DB] particles in DMEM with 10% FCS for 30 min at 37°C. Cells were washed twice with warm DMEM with 10% FCS, and subsequently cells were illuminated with 100 mW/cm^{2} for 600 sec, reaching a total light dose of 60 J/cm^{2}, using a standardized light emitting diode device (690 ± 10 nm). Cells were incubated with 729 nM of 10% 7D12-ELP[DB] 10% PS-ELP[DB], 10% Fc5-ELP[DB] 10% PS-ELP[DB] particles or 72.9 nM

7D12[PS] without subsequent illumination to determine dark toxicity. Cell viability was quantified using sulforhodamine B (SRB) colorimetric assays, and results were expressed as cell viability relative to untreated illuminated cells.

To examine selectivity of PDT-induced cytotoxicity, 5×10^5 cells were labeled with DiO (A431) or DID (E98) dye (Life technologies, Thermo Fisher Scientific, Waltham, MA, USA) according to manufacturers' protocol. A431, E98 or 1:1 mixtures of the cells were plated and subjected to PIT with 30 nM of the particles or equimolar VHH concentrations of the 7D12[PS] control as described above. Four hours after illumination, cells were incubated with 1 µg/ml propidium iodide (Thermo Fisher Scientific, Waltham, MA, USA) in PBS for 15 min. Cells were visualized with the EVOS microscope using the RFP channel (Propidium Iodide), the GFP channel (DiO labeled cells) and the Cy5 channel (DiD labeled cells).

Stability of ELP[DB] particles in human serum

Stability of ELP[DB] particles in serum was evaluated further by incubating 96 nM [ELP] 2 % 7D12[FL]-ELP[DB], 98 % PS-ELP[DB] or 2 % Fc5[FL]-ELP[DB], 98 % PS-ELP[DB] in freshly obtained human serum (HS) for either 30 minutes, 2 hours and 4 hours at 37°C. Subsequently the 96 nM stocks were diluted in DMEM with 10% FCS and PDT assays were performed with A431 cells as described earlier. Cell viability was compared to controls incubated with diluted serum without PS-ELP[DB] micelles and with PS-ELP[DB] micelles directly diluted in DMEM with 10 % FCS.

8

REFERENCES

1. Muyldermans, S., Nanobodies: Natural Single-Domain Antibodies. *Annu. Rev. Biochem.* **2013,** *82*, 775-797.

2. Wesolowski, J.; Alzogaray, V.; Reyelt, J.; Unger, M.; Juarez, K.; Urrutia, M.; Cauerhff, A.; Danquah, W.; Rissiek, B.; Scheuplein, F.; Schwarz, N.; Adriouch, S.; Boyer, O.; Seman, M.; Licea, A.; Serreze, D. V.; Goldbaum, F. A.; Haag, F.; Koch-Nolte, F., Single domain antibodies: promising experimental and therapeutic tools in infection and immunity. *Med. Microbiol. Immunol.* **2009,** *198* (3), 157-174.

3. Muyldermans, S.; Baral, T. N.; Retarnozzo, V. C.; De Baetselier, P.; De Genst, E.; Kinne, J.; Leonhardt, H.; Magez, S.; Nguyen, V. K.; Revets, H.; Rothbauer, U.; Stijemans, B.; Tillib, S.; Wernery, U.; Wyns, L.; *Hassanzadeh-Ghassabeh, G.; Saerens, D., Camelid immunoglobulins and nanobody technology. Vet. Immunol. Immunopathol.* **2009,** *128* (1-3), 178-183.

4. van Driel, P. B.; Boonstra, M. C.; Slooter, M. D.; Heukers, R.; Stammes, M. A.; Snoeks, T. J.; de Bruijn, H. S.; van Diest, P. J.; Vahrmeijer, A. L.; van Bergen En Henegouwen, P. M.; van de Velde, C. J.; Lowik, C. W.; Robinson, D. J.; Oliveira, S., EGFR targeted nanobody-photosensitizer conjugates for photodynamic therapy in a pre-clinical model of head and neck cancer. *Journal of controlled release : official journal of the Controlled Release Society* **2016**.

5. van der Meel, R.; Oliveira, S.; Altintas, I.; Haselberg, R.; van der Veeken, J.; Roovers, R. C.; van Bergen en Henegouwen, P. M.; Storm, G.; Hennink, W. E.; Schiffelers, R. M.; Kok, R. J., Tumor-targeted Nanobullets: Anti-EGFR nanobody-liposomes loaded with anti-IGF-1R kinase inhibitor for cancer treatment. *J. Controlled Release* **2012,** *159* (2), 281-9.

6. Arias, J. L.; Unciti-Broceta, J. D.; Maceira, J.; Del Castillo, T.; Hernandez-Quero, J.; Magez, S.; Soriano, M.; Garcia-Salcedo, J. A., Nanobody conjugated PLGA nanoparticles for active targeting of African Trypanosomiasis. *Journal of controlled release : official journal of the Controlled Release Society* **2015,** *197*, 190-8.

7. Zhu, M.; Hu, Y.; Li, G.; Ou, W.; Mao, P.; Xin, S.; Wan, Y., Combining magnetic nanoparticle with biotinylated nanobodies for rapid and sensitive detection of influenza H3N2. *Nanoscale Res. Lett.* **2014,** *9* (1), 528.

8. Van de Broek, B.; Devoogdt, N.; D'Hollander, A.; Gijs, H. L.; Jans, K.; Lagae, L.; Muyldermans, S.; Maes, G.; Borghs, G., Specific cell targeting with nanobody conjugated branched gold nanoparticles for photothermal therapy. *ACS Nano* **2011,** *5* (6), 4319-28.

9. Smits, F. C. M.; Castelijns, W. W. A.; van Hest, J. C. M., Crosslinked ELP-based nanoparticles, using the strain promoted azide-alkyne cycloaddition. *Eur. Polym. J.* **2015,** *62*, 386-393.

10. Lee, T. A. T.; Cooper, A.; Apkarian, R. P.; Conticello, V. P., Thermo-reversible self-assembly of nanoparticles derived from elastin-mimetic polypeptides. *Adv. Mater.* **2000,** *12* (15), 1105-+.

11. Soon, A. S. C.; Smith, M. H.; Herman, E. S.; Lyon, L. A.; Barker, T. H., Development of Self-Assembling Mixed Protein Micelles with Temperature-Modulated Avidities. *Adv. Healthcare Mater.* **2013,** *2* (7), 1045-1055.

12. Urry, D. W.; Gowda, D. C.; Parker, T. M.; Luan, C. H.; Reid, M. C.; Harris, C. M.; Pattanaik, A.; Harris, R. D., Hydrophobicity Scale for Proteins Based on Inverse Temperature Transitions. *Biopolymers* **1992,** *32* (9), 1243-1250.

13. Zibouche, N.; Philipsen, P.; Heine, T.; Kuc, A., Electron transport in MoWSeS monolayers in the presence of an external electric field. *Phys. Chem. Chem. Phys.* **2014,** *16* (23), 11251-5.

14. Urry, D. W., Physical chemistry of biological free energy transduction as demonstrated by elastic protein-based polymers. *J. Phys. Chem. B* **1997,** *101* (51), 11007-11028.

15. Urry, D. W.; Trapane, T. L.; Sugano, H.; Prasad, K. U., Sequential Polypeptides of Elastin - Cyclic Conformational Correlates of the Linear Polypentapeptide. *J. Am. Chem. Soc.* **1981,** *103* (8), 2080-2089.

16. Gross, P. C.; Possart, W.; Zeppezauer, M., An alternative structure model for the polypentapeptide in elastin. *Z. Naturforsch., C: J. Biosci.* **2003,** *58* (11-12), 873-878.

17. McDaniel, J. R.; Radford, D. C.; Chilkoti, A., A unified model for de novo design of elastin-like polypeptides with tunable inverse transition temperatures. *Biomacromolecules* **2013**, *14* (8), 2866-72.

18. Phan, H. T.; Conrad, U., Membrane-based inverse transition cycling: an improved means for purifying plant-derived recombinant protein-elastin-like polypeptide fusions. *Int. J. Mol. Sci.* **2011,** *12* (5), 2808-21.

19. Pinedo-Martin, G.; Castro, E.; Martin, L.; Alonso, M.; Rodriguez-Cabello, J. C., Effect of surfactants on the self-assembly of a model elastin-like block corecombinamer: from micelles to an aqueous two-phase system. *Langmuir* **2014,** *30* (12), 3432-40.

20. van Eldijk, M. B.; Smits, F. C. M.; Vermue, N.; Debets, M. F.; Schoffelen, S.; van Hest, J. C. M., Synthesis and Self-Assembly of Well-Defined Elastin-Like Polypeptide-Poly(ethylene glycol) Conjugates. *Biomacromolecules* **2014,** *15* (7), 2751-2759.

21. Floss, D. M.; Mockey, M.; Zanello, G.; Brosson, D.; Diogon, M.; Frutos, R.; Bruel, T.; Rodrigues, V.; Garzon, E.; Chevaleyre, C.; Berri, M.; Salmon, H.; Conrad, U.; Dedieu, L., Expression and immunogenicity of the mycobacterial Ag85B/ESAT-6 antigens produced in transgenic plants by elastin-like peptide fusion strategy. *J. Biomed. Biotechnol.* **2010,** *2010*, 274346.

22. Urry, D. W.; Parker, T. M.; Reid, M. C.; Gowda, D. C., Biocompatibility of the Bioelastic Materials, Poly(Gvgvp) and Its Gamma-Irradiation Cross-Linked Matrix - Summary of Generic Biological Test-Results. *J. Bioact. Compat. Polym.* **1991,** *6* (3), 263-282.

23. Roovers, R. C.; Vosjan, M. J.; Laeremans, T.; el Khoulati, R.; de Bruin, R. C.; Ferguson, K. M.; Verkleij, A. J.; van Dongen, G. A.; van Bergen en Henegouwen, P. M., A biparatopic anti-EGFR nanobody efficiently inhibits solid tumour growth. *Int. J. Cancer* **2011,** *129* (8), 2013-24.

24. Roovers, R. C.; Laeremans, T.; Huang, L.; De Taeye, S.; Verkleij, A. J.; Revets, H.; de Haard, H. J.; van Bergen en Henegouwen, P. M., Efficient inhibition of EGFR signaling and of tumour growth by antagonistic anti-EFGR Nanobodies. *Cancer immunology, immunotherapy : CII* **2007**, *56* (3), 303-317.

25. Abulrob, A.; Sprong, H.; Van Bergen en Henegouwen, P.; Stanimirovic, D., The blood-brain barrier transmigrating single domain antibody: mechanisms of transport and antigenic epitopes in human brain endothelial cells. *J. Neurochem.* **2005,** *95* (4), 1201-14.

26. Hirel, P. H.; Schmitter, J. M.; Dessen, P.; Fayat, G.; Blanquet, S., Extent of N-Terminal Methionine Excision from Escherichia-Coli Proteins Is Governed by the Side-Chain Length of the Penultimate Amino-Acid. *Proc. Natl. Acad. Sci. U. S. A.* **1989,** *86* (21), 8247-8251.

27. Liu, Y. D.; Goetze, A. M.; Bass, R. B.; Flynn, G. C., N-terminal Glutamate to Pyroglutamate Conversion in vivo for Human IgG2 Antibodies. *J. Biol. Chem.* **2011,** *286* (13), 11211-11217.

28. Brewer, A. K.; Striegel, A. M., Characterizing the size, shape, and compactness of a polydisperse prolate ellipsoidal particle via quadruple-detector hydrodynamic chromatography. *Analyst* **2011,** *136* (3), 515-519.

29. Burchard, W., Static and Dynamic Light-Scattering from Branched Polymers and Bio-Polymers. *Adv. Polym. Sci.* **1983**, *48*, 1-124.

30. Bhunia, D.; Chowdhury, R.; Bhattacharyya, K.; Ghosh, S., Fluorescence fluctuation of an antigen-antibody complex: circular dichroism, FCS and smFRET of enhanced GFP and its antibody. *Phys. Chem. Chem. Phys.* **2015,** *17* (38), 25250-9.

31. Schmitz, K. R.; Bagchi, A.; Roovers, R. C.; van Bergen en Henegouwen, P. M.; Ferguson, K. M., Structural evaluation of EGFR inhibition mechanisms for nanobodies/VHH domains. *Structure* **2013,** *21* (7), 1214-24.

32. Keefe, K. A.; Tadir, Y.; Tromberg, B.; Berns, M.; Osann, K.; Hashad, R.; Monk, B. J., Photodynamic therapy of high-grade cervical intraepithelial neoplasia with 5-aminolevulinic acid. *Lasers Surg. Med.* **2002,** *31* (4), 289-93.

8

33. Abulrob, A.; Sprong, H.; Henegouwen, P. V. B. E.; Stanimirovic, D., The blood-brain barrier transmigrating single domain antibody: mechanisms of transport and antigenic epitopes in human brain endothelial cells. *J. Neurochem.* **2005,** *95* (4), 1201-1214.

34. McDaniel, J. R.; Mackay, J. A.; Quiroz, F. G.; Chilkoti, A., Recursive directional ligation by plasmid reconstruction allows rapid and seamless cloning of oligomeric genes. *Biomacromolecules* **2010,** *11* (4), 944-52.

35. Zhao, H.; Brown, P. H.; Schuck, P., On the distribution of protein refractive index increments. *Biophys. J.* **2011,** *100* (9), 2309-17.
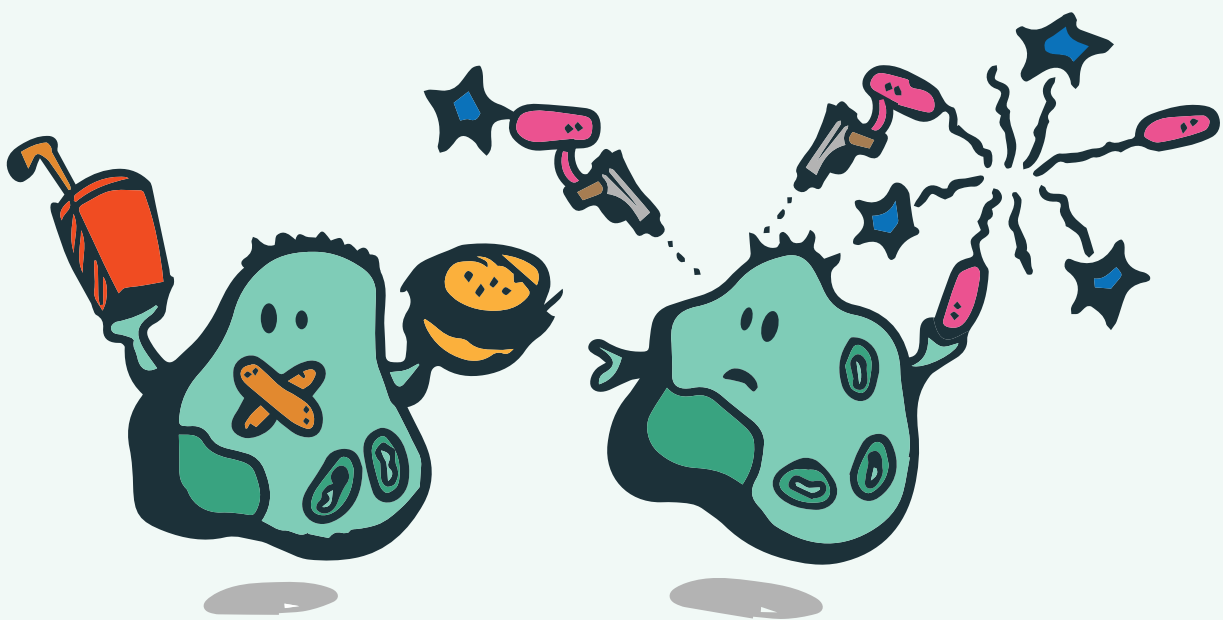
CHAPTER 9

General discussion

METABOLISM IN CANCER

Alterations in cancer metabolism

Research into the metabolism of cancer cells dates back almost a century, when Otto Warburg found that cancer cells divert to glycolysis over oxidative phosphorylation, even in the presence of oxygen (Warburg effect)[1-2]. A number of theories were proposed to explain this phenomenon, like adaptation to hypoxia and inability to perform oxidative phosphorylation due to mitochondrial defects[1,3]. However, now it has become increasingly clear, that the glycolytic switch is the result of oncogenic transformation, involving activation of oncogenes and inactivation of tumor suppressor genes. Like for non-malignant cells that need to support high proliferation rates (e.g. activated T-cells), tumors have increased uptake of glucose and glutamine that are needed for efficient biosynthesis of macromolecules. Activation of key oncogenic signaling pathways (e.g. PI3K/Akt/mTORC, Myc), or inactivation of tumor suppressors (e.g. p53) due to mutations affect cancer cell metabolism by direct upregulation of nutrient transporters and enzymes in key anabolic growth pathways, including glycolysis and glutaminolysis[4].

In addition, metabolic enzymes themselves can act directly as oncogenes or tumor suppressors. Inactivating mutations in fumarate hydratase (*FH*) and succinate dehydrogenase (*SDH*) cause an accumulation of the enzyme substrates fumarate and succinate, and mutations in isocitrate dehydrogenase 1 and 2 (*IDH1* and *IDH2*) cause depletion of α-ketoglutarate (α-KG) and accumulation of the oncometabolite D-2-hydroxyglutarate (D-2-HG). The mechanism of enhanced tumorigenesis is thought to be the effect of these changed metabolite concentrations which alter epigenetic modulation. The exact mechanisms are, however, difficult to unravel, since besides changes in these metabolite concentrations, other compensatory mechanisms come into play to supply cells with nutrients that are needed for survival and proliferation. In **chapter 2,** we described a novel R314C mutation in IDH1, that is defective in isocitrate processing, but unlike the well-known IDH1-R132H mutation, lacks D-2-HG production. Studies using the enzyme that is the result of this mutation could be helpful in distinguishing between the effects of D-2-HG and the induced metabolic rewiring to compensate impaired α-KG production.

9

Identification and inhibition of altered metabolic pathways

Better understanding of the metabolic dependencies of cancer cells is essential to identify the aspects of metabolism that are most suitable for therapeutic interference. Accurate techniques that measure levels of metabolites are based on cutting-edge analytic platforms that include high-performance liquid chromatography (HPLC), liquid chromatography mass spectrometry (LC-MS) and nuclear magnetic resonance (NMR) for metabolic profiling, and stable isotope labeling to study fluxes of labeled metabolites. Cancer cells cannot be considered as isolated metabolic units as there are extensive interactions between cancer cells and non-neoplastic cells in the tumor stroma. As it is challenging to model an accurate tumor microenvironment in cell culture, direct analysis of metabolic fluxes in intact tumors is increasingly considered as important. Fluor-18-deoxyglucose positron emission tomography (^{18}F-FDG-PET) is widely used in clinical practice and allows for direct assessment of tumor glucose uptake. More recently, newer PET tracers have been developed to monitor additional metabolites, including glutamine and choline. D-2-HG levels in patients with gliomas harboring an *IDH1* mutation can be quantified noninvasively using magnetic resonance spectroscopy[5]. Besides quantification of metabolites and metabolite fluxes as a read-out of pathway activity, RNA expression data have also been used for prediction of active pathways in a non-targeted[6] or targeted fashion[7].

Synthetic lethality

Alterations in cell metabolism may be the result of oncogenic events as decribed, and vice versa classical features of cancer such as increased proliferation and migration may be a consequence of altered metabolism. Therefore inhibition of oncogenic alterations may reverse metabolism of cancer cells, and inhibition of metabolic enzymes may reverse the neoplastic phenotype[8]. Furthermore blocking metabolic pathways with specific inhibitors may sensitize cells to toxic therapies in a synthetic lethality approach. As an example, increasing oxidative stress in a cancer cell with metabolic inhibitors (e.g. of enzymes that produce NADPH) may enhance the efficacy of radiotherapy or chemotherapy, as we have described for EGCG and radiotherapy in RCC in **chapter 3**. Furthermore inhibition of autophagy could inhibit the catabolic pathways that cancer cells upregulate as a response to chemotherapy. Lastly, cells with an altered metabolic state can become dependent on certain tyrosine kinase pathways, and synthetic lethality can be achieved by inhibiting this pathway, as has been described for *IDH1*-mutant cholangiocarcinomas and inhibition of the Src family kinases by dasatinib[9].

NANOMEDICINE

VHHs as tumor targeting agents

Monoclonal antibodies and antibody-drug conjugates (ADCs) have found their way in clinical practice as effective tumoricidal compounds. Examples are trastuzumab, the antibody against

human epidermal growth factor receptor 2 (HER2), that significantly improved the prognosis for women with HER2-positive breast cancer, and the anti-CD30 antibody brentuximab coupled to vedotin, ABT-414, described to be effective for relapsed Hodgkin lymphoma and systemic anaplastic large cell lymphoma. Full potential of such molecules is hampered since their large size of about 150 kDa restricts tumor penetration after intravenous infusion and therefore results in a suboptimal biodistribution[10-11]. Development of bispecific antibodies, binding two different epitopes, opens up a wide range of applications, such as direction of specific immune cells to tumor cells or simultaneous inhibition of two oncogenic pathways. Currently, over 50 bispecific antibodies are evaluated in clinical trials, and catumaxomab (targeting EpCAM and CD3) and blinatumomab (targeting CD19 and CD3) are already approved for clinical use[12-13]. However, there are still critical hurdles that have to be overcome, such as large-scale production, purity and immunogenicity.

For these reasons, the variable heavy chain domains of single chain llama antibodies, (VHHs), which are approximately 10 times smaller and consist of only one domain, are interesting alternatives. Basically, anti-tumor VHHs can be categorized into four groups.

1. Monomeric VHHs with intrinsic therapeutic activity

In the context of cancer therapy, mostly VHHs targeting growth factor receptors have been developed. Binding of the VHHs to these receptors or their ligands can inhibit oncogenic signaling and thereby inhibit cell proliferation, as has been described for epidermal growth factor receptor (EGFR)[14-15], tyrosine-protein kinase Met (c-Met)[16-17] and vascular endothelial growth factor receptor (VEGFR)[18]. Next to inhibition of growth factor receptors, allosteric inhibition of protein function could also be of use in tumor targeting. An example is a VHH that neutralizes carbonic anhydrase-IX (CAIX) enzymatic activity by binding to the catalytic site of this pH-regulating enzyme[19].

Though most research has been performed on targeting of extracellular proteins, intracellular proteins are promising therapeutic targets as well, especially since VHHs can withstand the reducing environment of the cytosol. An important limitation is that VHHs generally are not able to penetrate the cell membrane, and therefore other strategies are being developed to transport VHHs into cells. VHHs could be expressed as intrabodies[20-21] by transfection of cells, however, such a gene therapy-approach presents with serious safety concerns *in vivo* and therefore is so far restricted to a preclinical research setting. Other possibilities for intracellular delivery of proteins include the use of nanocarriers[22], nanoparticles[23] and supercharged proteins. Furthermore, systems as used by bacteria, such as the type III secretion system (T3SS), to translocate proteins into eukaryotic host cells can be employed[24-25]. In **chapter 6** we describe increased internalization via clathrin-mediated endocytosis of the anti-EGFR VHH 7D12, conjugated to a cell-penetrating peptide (CPP). Besides CPP-induced depletion of the EGFR-7D12-CPP complex at the cell surface and associated inhibition of EGFR receptor signaling, the CPP-based approach could also be used for internalization of a VHH

with an intracellular target. A major challenge, however, is that entrapment in the endosomes could lead to lysosomal hydrolysis of the protein before it reaches its target. To overcome this limitation, various approaches are being investigated, like pH-sensitive endosomolytic peptides to achieve endosomal escape[26], or conjugation to cyclic deca-arginine, which was found to directly transduce large cargo into the cytosol[27].

2. Multimeric VHHs

Because of the single-domain characteristic, molecular manipulation for generating multivalent of multispecific VHHs is relatively easy. In tandem cloning of two VHHs with a linker peptide yields a bivalent molecule with higher avidity for the antigen[28], and crosslinking of a target by a VHH multimer can induce apoptosis and other signaling cascades[29]. Furthermore, simultaneous inhibition of two tumor targets with bispecific VHHs has been shown to increase anti-tumor efficacy[30]. Redirection of T-cell activity with bispecific constructs is a promising cancer-immunotherapy approach[31-32], however, up to now only combinations of a tumor targeting VHH with a T-cell targeting single-chain variable fragment have been made. Since anti-CD8[33] and anti-PD-1 VHHs have been developed, combination of these with a tumor targeting VHH would be an interesting approach. Besides genetic engineering, VHHs can also be equipped with a LPETG amino acid sequence which can be employed to make tail-to-tail specific constructs as we have described in **chapter 5**. In this situation both N-terminal domains are fully functional, which ensures full binding capacity.

3. VHHs coupled to effector domains

Since not all VHHs have an inherent therapeutic effect, and since treatment with conventional anti-cancer drugs often leads to development of resistance by the tumor cells, coupling of VHHs to a toxic protein, peptide or chemical group to induce immediate cell killing may be advantageous. This approach combines the advantages of the high tumor-specificity of the VHH with the cytotoxic effects mediated by the effector group. Genetic fusion of VHHs with protein-toxins[34-35] or peptide tags as marker for cytotoxic CAR-T cells[36] have been shown to induce cell death in *in vitro* systems.

A widely applied strategy for introduction of effector groups is random conjugation to the amino group of lysine side chains. Since multiple lysines are present in the VHH sequence, this strategy is difficult to control and therefore leads to heterogeneous end-products. Furthermore, interference with lysines in the binding site could compromise functionality. A more site-specific labeling strategy involves introduction of a C-terminal cysteine, since with maleimide chemistry only this residue is labeled[37], as we have confirmed in **chapter 5**. Furthermore we and others[38-39] have employed sortase A mediated transpeptidation for introduction of GGG-X or polyethylene glycol (PEG)x-X molecules. Using this toolbox with conjugation strategies, virtually any compound can be conjugated site-specifically to a VHH.

Conjugates can be tailor-made for specific therapeutic applications, such as photodynamic therapy. Preclinical studies have shown that 7D12-photosensitizer (PS) conjugates rendered EGFR-expressing cells sensitive to light-induced death *in vitro*[40] and in an orthotopic mouse model *in vivo*[41]. In **chapter 7**, we introduced a PS molecule site-specifically at the C-terminus of 7D12, and we confirmed effectivity of these conjugates *in vitro*. Furthermore we have shown that subcellular localization influences activity, since membrane bound 7D12-PS induced cell killing with higher efficacy than internalized 7D12-CPP-PS. To examine if this is a general concept, this approach should be applied to VHHs targeting other membrane proteins. Furthermore, various VHH-radionuclide conjugates are being developed for both alpha and beta radionuclide therapy. An *in vivo* study with ^{177}Lu-labeled anti-HER2 VHH efficiently prevented tumor growth in a xenograft model of HER2-positive breast cancer[42]. Though fast kidney clearance is advantageous for imaging, it can cause nephrotoxicity and suboptimal absolute tumor uptake which is disadvantageous for therapy. Diminishing kidney clearance is therefore of great importance, and this can partly be done by eliminating the C-terminal histidine-tag which normally is present in the sequence[42]. Since we have introduced an LPETG amino acid tag preceding the 8xHistidine-tag in the VHH sequences, this can easily be realized by sortase A mediated cleavage.

The small size of VHHs enables fast tumor accumulation and blood clearance, both contributing to a high tumor-to-background ratio at early time points after injection, which is advantageous for imaging purposes. Conjugation of VHHs to near infrared fluorescent groups enables optical imaging[43-44] as early as 30 minutes post injection. Furthermore labeling with radionuclides is employed for nuclear imaging. This has successfully been done with VHHs targeting EGFR[45-46] and HER2[47]. Currently bimodal VHH agents for combined nuclear and optical imaging are being developed, which could be used for image guided surgery.

4. VHH-targeted nanoparticles

Another way for specific drug delivery is encapsulation of drugs in VHH-targeted nanoparticles. These can act as carriers for hydrophobic drugs, overcoming problems such as poor solubility, limited stability and rapid clearance. Surface modification with targeting moieties such as VHHs can enhance selective delivery to tumor cells. Functionality of VHH- targeted liposomes[48-49], micelles[50], polymersomes[51] and albumin-based nanoparticles[23, 52] has been assessed. In **chapter 8** we describe effective *in vitro* cell killing induced by an ELP-based micelle functionalized with both 7D12 and PS. Though these results are encouraging, *in vivo* complete tumor eradication is probably not reached with photodynamic therapy as the only modality, since the efficacy of the technique is highly dependent on an optimal biodistribution of the PS-conjugate in combination with optimal light-accessibility of the cancer cells to be killed. Therefore dual therapies with e.g. PDT and chemotherapy could be advantageous, and these ELP-based micelles would provide a system to transport both agents selectively to the tumor cells.

9

IS THERE A FUTURE FOR COMBINATION OF METABOLIC INHIBITION AND NANOMEDICINE?

Next generation sequencing supplies us with enormous amounts of data on the molecular events causing cancer. Numerous drugs are available that target specific pathways, facilitating personalized medicine. Although such personalized therapies may prolong survival, the inherent genetic instability of tumors ultimately leads to therapy resistance in most cancers. To overcome this, multiple therapies could be combined to induce synthetic lethality, or compounds should induce immediate cell death so cells simply do not have time to develop resistance. There are several applications in which combinations of metabolic inhibition and nanomedicine could be useful:

- Since oncogenic signaling and altered metabolism are highly intertwined, adjuvant targeting of metabolism might improve efficacy of VHH-mediated inhibition of oncogenic signaling.
- The majority of interesting metabolic targets is localized intracellularly, and therefore therapies are focusing on the use of small molecule inhibitors or metabolic analogs. However, VHHs are also very suitable for inhibition of specific metabolic enzymes, since they are able to bind to sites that are normally not accessible to antibodies (e.g. enzymatic pockets) due to their small size [53-54]. One hurdle that has to be taken is efficient intracellular delivery of VHHs.
- One of the pitfalls of metabolic inhibition is that it also affects healthy cells. Therefore, to diminish delivery of metabolic inhibitors to healthy tissues, they could be encapsulated in nanoparticles decorated with tumor specific VHHs.

To conclude, many challenges and applications lie ahead for both unraveling cancer metabolism and development of VHHs as a theranostic platform. Though cancer metabolism is a widely studied field, the degree and variety of ways in which tumor cells rewire their metabolism is not fully known. In the future we will gain more knowledge about drivers of the altered metabolism, and about ways to deprive cells from their essential metabolites. The conjugation platform that we optimized for VHHs, can be expanded with all kinds of targeting vehicles (e.g. DARPins, affibodies) and therapeutic or diagnostic compounds (e.g. other PSs, radionuclides, CPPs). Ultimately both targeting of rewired metabolism and a nanomedicine based platform could be combined for development of efficient cancer therapies.

REFERENCES

1. Warburg, O., On the origin of cancer cells. *Science* **1956,** *123* (3191), 309-14.

2. Warburg, O., On respiratory impairment in cancer cells. *Science* **1956,** *124* (3215), 269-70.

3. Gatenby, R. A.; Gillies, R. J., Why do cancers have high aerobic glycolysis? *Nat Rev Cancer* **2004,** *4* (11), 891-9.

4. Levine, A. J.; Puzio-Kuter, A. M., The control of the metabolic switch in cancers by oncogenes and tumor suppressor genes. *Science* **2010,** *330* (6009), 1340-4.

5. Choi, C.; Ganji, S. K.; DeBerardinis, R. J.; Hatanpaa, K. J.; Rakheja, D.; Kovacs, Z.; Yang, X. L.; Mashimo, T.; Raisanen, J. M.; Marin-Valencia, I.; Pascual, J. M.; Madden, C. J.; Mickey, B. E.; Malloy, C. R.; Bachoo, R. M.; Maher, E. A., 2-hydroxyglutarate detection by magnetic resonance spectroscopy in IDH-mutated patients with gliomas. *Nature medicine* **2012,** *18* (4), 624-9.

6. Raskevicius, V.; Mikalayeva, V.; Antanaviciute, I.; Cesleviciene, I.; Skeberdis, V. A.; Kairys, V.; Bordel, S., Genome scale metabolic models as tools for drug design and personalized medicine. *PloS one* **2018,** *13* (1), e0190636.

7. de Bitter, T.; van de Water, C.; van den Heuvel, C.; Zeelen, C.; Eijkelenboom, A.; Tops, B.; Oosterwijk, E.; Kolev, D.; Mulders, P.; Ter Laan, M.; van Lith, S.; Leenders, W., Profiling of the metabolic transcriptome via single molecule molecular inversion probes. *Scientific reports* **2017,** *7* (1), 11402.

8. Kroemer, G.; Pouyssegur, J., Tumor cell metabolism: cancer's Achilles' heel. *Cancer Cell* **2008,** *13* (6), 472-82.

9. Saha, S. K.; Gordan, J. D.; Kleinstiver, B. P.; Vu, P.; Najem, M. S.; Yeo, J. C.; Shi, L.; Kato, Y.; Levin, R. S.; Webber, J. T.; Damon, L. J.; Egan, R. K.; Greninger, P.; McDermott, U.; Garnett, M. J.; Jenkins, R. L.; Rieger-Christ, K. M.; Sullivan, T. B.; Hezel, A. F.; Liss, A. S.; Mizukami, Y.; Goyal, L.; Ferrone, C. R.; Zhu, A. X.; Joung, J. K.; Shokat, K. M.; Benes, C. H.; Bardeesy, N., Isocitrate Dehydrogenase Mutations Confer Dasatinib Hypersensitivity and SRC Dependence in Intrahepatic Cholangiocarcinoma. *Cancer discovery* **2016,** *6* (7), 727-39.

10. Minchinton, A. I.; Tannock, I. F., Drug penetration in solid tumours. *Nat Rev Cancer* **2006,** *6* (8), 583-92.

11. Xenaki, K. T.; Oliveira, S.; van Bergen En Henegouwen, P. M. P., Antibody or Antibody Fragments: Implications for Molecular Imaging and Targeted Therapy of Solid Tumors. *Frontiers in immunology* **2017,** *8*, 1287.

12. Fan, G.; Wang, Z.; Hao, M.; Li, J., Bispecific antibodies and their applications. *J Hematol Oncol* **2015,** *8*, 130.

13. Krishnamurthy, A.; Jimeno, A., Bispecific antibodies for cancer therapy: A review. *Pharmacology & therapeutics* **2018,** *185*, 122-134.

14. Schmitz, K. R.; Bagchi, A.; Roovers, R. C.; van Bergen en Henegouwen, P. M.; Ferguson, K. M., Structural evaluation of EGFR inhibition mechanisms for nanobodies/VHH domains. *Structure* **2013,** *21* (7), 1214-24.

15. Roovers, R. C.; Laeremans, T.; Huang, L.; De Taeye, S.; Verkleij, A. J.; Revets, H.; de Haard, H. J.; van Bergen en Henegouwen, P. M., Efficient inhibition of EGFR signaling and of tumour growth by antagonistic anti-EFGR Nanobodies. *Cancer immunology, immunotherapy : CII* **2007,** *56* (3), 303-317.

16. Vosjan, M. J.; Vercammen, J.; Kolkman, J. A.; Stigter-van Walsum, M.; Revets, H.; van Dongen, G. A., Nanobodies targeting the hepatocyte growth factor: potential new drugs for molecular cancer therapy. *Mol Cancer Ther* **2012,** *11* (4), 1017-25.

17. Slordahl, T. S.; Denayer, T.; Moen, S. H.; Standal, T.; Borset, M.; Ververken, C.; Ro, T. B., Anti-c-MET Nanobody - a new potential drug in multiple myeloma treatment. *Eur J Haematol* **2013,** *91* (5), 399-410.

18. Farajpour, Z.; Rahbarizadeh, F.; Kazemi, B.; Ahmadvand, D., A nanobody directed to a functional epitope on VEGF, as a novel strategy for cancer treatment. *Biochem. Biophys. Res. Commun.* **2014,** *446* (1), 132-6.

9

19. Araste, F.; Ebrahimizadeh, W.; Rasooli, I.; Rajabibazl, M.; Mousavi Gargari, S. L., A novel VHH nanobody against the active site (the CA domain) of tumor-associated, carbonic anhydrase isoform IX and its usefulness for cancer diagnosis. *Biotechnol. Lett* **2014,** *36* (1), 21-8.

20. Muyldermans, S., Nanobodies: natural single-domain antibodies. *Annu. Rev. Biochem* **2013,** *82,* 775-97.

21. De Meyer, T.; Muyldermans, S.; Depicker, A., Nanobody-based products as research and diagnostic tools. *Trends Biotechnol.* **2014,** *32* (5), 263-70.

22. Gu, Z.; Biswas, A.; Zhao, M.; Tang, Y., Tailoring nanocarriers for intracellular protein delivery. *Chem. Soc. Rev.* **2011,** *40* (7), 3638-55.

23. Heukers, R.; Altintas, I.; Raghoenath, S.; De Zan, E.; Pepermans, R.; Roovers, R. C.; Haselberg, R.; Hennink, W. E.; Schiffelers, R. M.; Kok, R. J.; van Bergen en Henegouwen, P. M., Targeting hepatocyte growth factor receptor (Met) positive tumor cells using internalizing nanobody-decorated albumin nanoparticles. *Biomaterials* **2014,** *35* (1), 601-10.

24. Blanco-Toribio, A.; Muyldermans, S.; Frankel, G.; Fernandez, L. A., Direct injection of functional single-domain antibodies from E. coli into human cells. *PloS one* **2010,** *5* (12), e15227.

25. Ittig, S. J.; Schmutz, C.; Kasper, C. A.; Amstutz, M.; Schmidt, A.; Sauteur, L.; Vigano, M. A.; Low, S. H.; Affolter, M.; Cornelis, G. R.; Nigg, E. A.; Arrieumerlou, C., A bacterial type III secretion-based protein delivery tool for broad applications in cell biology. *J. Cell Biol.* **2015,** *211* (4), 913-31.

26. Akishiba, M.; Takeuchi, T.; Kawaguchi, Y.; Sakamoto, K.; Yu, H. H.; Nakase, I.; Takatani-Nakase, T.; Madani, F.; Graslund, A.; Futaki, S., Cytosolic antibody delivery by lipid-sensitive endosomolytic peptide. *Nat Chem* **2017,** *9* (8), 751-761.

27. Herce, H. D.; Schumacher, D.; Schneider, A. F. L.; Ludwig, A. K.; Mann, F. A.; Fillies, M.; Kasper, M. A.; Reinke, S.; Krause, E.; Leonhardt, H.; Cardoso, M. C.; Hackenberger, C. P. R., Cell-permeable nanobodies for targeted immunolabelling and antigen manipulation in living cells. *Nat Chem* **2017,** *9* (8), 762-771.

28. Els Conrath, K.; Lauwereys, M.; Wyns, L.; Muyldermans, S., Camel single-domain antibodies as modular building units in bispecific and bivalent antibody constructs. *J. Biol. Chem.* **2001,** *276* (10), 7346-50.

29. Roovers, R. C.; Vosjan, M. J.; Laeremans, T.; el Khoulati, R.; de Bruin, R. C.; Ferguson, K. M.; Verkleij, A. J.; van Dongen, G. A.; van Bergen en Henegouwen, P. M., A biparatopic anti-EGFR nanobody efficiently inhibits solid tumour growth. *International journal of cancer* **2011,** *129* (8), 2013-24.

30. Zhu, Y.; Bassoff, N.; Reinshagen, C.; Bhere, D.; Nowicki, M. O.; Lawler, S. E.; Roux, J.; Shah, K., Bi-specific molecule against EGFR and death receptors simultaneously targets proliferation and death pathways in tumors. *Scientific reports* **2017,** *7* (1), 2602.

31. Li, L.; He, P.; Zhou, C.; Jing, L.; Dong, B.; Chen, S.; Zhang, N.; Liu, Y.; Miao, J.; Wang, Z.; Li, Q., A novel bispecific antibody, S-Fab, induces potent cancer cell killing. *Journal of immunotherapy* **2015,** *38* (9), 350-6.

32. Harwood, S. L.; Alvarez-Cienfuegos, A.; Nunez-Prado, N.; Compte, M.; Hernandez-Perez, S.; Merino, N.; Bonet, J.; Navarro, R.; Van Bergen En Henegouwen, P. M. P.; Lykkemark, S.; Mikkelsen, K.; Molgaard, K.; Jabs, F.; Sanz, L.; Blanco, F. J.; Roda-Navarro, P.; Alvarez-Vallina, L., ATTACK, a novel bispecific T cell-recruiting antibody with trivalent EGFR binding and monovalent CD3 binding for cancer immunotherapy. *Oncoimmunology* **2017,** *7* (1), e1377874.

33. Rashidian, M.; Ingram, J. R.; Dougan, M.; Dongre, A.; Whang, K. A.; LeGall, C.; Cragnolini, J. J.; Bierie, B.; Gostissa, M.; Gorman, J.; Grotenbreg, G. M.; Bhan, A.; Weinberg, R. A.; Ploegh, H. L., Predicting the response to CTLA-4 blockade by longitudinal noninvasive monitoring of CD8 T cells. *The Journal of experimental medicine* **2017,** *214* (8), 2243-2255.

34. Yu, Y.; Li, J.; Zhu, X.; Tang, X.; Bao, Y.; Sun, X.; Huang, Y.; Tian, F.; Liu, X.; Yang, L., Humanized CD7 nanobody-based immunotoxins exhibit promising anti-T-cell acute lymphoblastic leukemia potential. *International journal of nanomedicine* **2017,** *12,* 1969-1983.

35. Deng, C.; Xiong, J.; Gu, X.; Chen, X.; Wu, S.; Wang, Z.; Wang, D.; Tu, J.; Xie, J., Novel recombinant immunotoxin of EGFR specific nanobody fused with cucurmosin, construction and antitumor efficiency in vitro. *Oncotarget* **2017,** *8* (24), 38568-38580.

36. Albert, S.; Arndt, C.; Feldmann, A.; Bergmann, R.; Bachmann, D.; Koristka, S.; Ludwig, F.; Ziller-Walter, P.; Kegler, A.; Gartner, S.; Schmitz, M.; Ehninger, A.; Cartellieri, M.; Ehninger, G.; Pietzsch, H. J.; Pietzsch, J.; Steinbach, J.; Bachmann, M., A novel nanobody-based target module for retargeting of T lymphocytes to EGFR-expressing cancer cells via the modular UniCAR platform. *Oncoimmunology* **2017,** *6* (4), e1287246.

37. Massa, S.; Xavier, C.; De Vos, J.; Caveliers, V.; Lahoutte, T.; Muyldermans, S.; Devoogdt, N., Site-specific labeling of cysteine-tagged camelid single-domain antibody-fragments for use in molecular imaging. *Bioconjug Chem* **2014,** *25* (5), 979-88.

38. Popp, M. W.; Antos, J. M.; Grotenbreg, G. M.; Spooner, E.; Ploegh, H. L., Sortagging: a versatile method for protein labeling. *Nature chemical biology* **2007,** *3* (11), 707-8.

39. Witte, M. D.; Cragnolini, J. J.; Dougan, S. K.; Yoder, N. C.; Popp, M. W.; Ploegh, H. L., Preparation of unnatural N-to-N and C-to-C protein fusions. *Proc Natl Acad Sci U S A* **2012,** *109* (30), 11993-8.

40. Heukers, R.; van Bergen en Henegouwen, P. M.; Oliveira, S., Nanobody-photosensitizer conjugates for targeted photodynamic therapy. *Nanomedicine : nanotechnology, biology, and medicine* **2014,** *10* (7), 1441-51.

41. van Driel, P. B.; Boonstra, M. C.; Slooter, M. D.; Heukers, R.; Stammes, M. A.; Snoeks, T. J.; de Bruijn, H. S.; van Diest, P. J.; Vahrmeijer, A. L.; van Bergen En Henegouwen, P. M.; van de Velde, C. J.; Lowik, C. W.; Robinson, D. J.; Oliveira, S., EGFR targeted nanobody-photosensitizer conjugates for photodynamic therapy in a pre-clinical model of head and neck cancer. *Journal of controlled release : official journal of the Controlled Release Society* **2016**.

42. D'Huyvetter, M.; Vincke, C.; Xavier, C.; Aerts, A.; Impens, N.; Baatout, S.; De Raeve, H.; Muyldermans, S.; Caveliers, V.; Devoogdt, N.; Lahoutte, T., Targeted radionuclide therapy with A 177Lu-labeled anti-HER2 nanobody. *Theranostics* **2014,** *4* (7), 708-20.

43. Oliveira, S.; van Dongen, G. A.; Stigter-van Walsum, M.; Roovers, R. C.; Stam, J. C.; Mali, W.; van Diest, P. J.; van Bergen en Henegouwen, P. M., Rapid visualization of human tumor xenografts through optical imaging with a near-infrared fluorescent anti-epidermal growth factor receptor nanobody. *Molecular imaging* **2012,** *11* (1), 33-46.

44. Kijanka, M. M.; van Brussel, A. S.; van der Wall, E.; Mali, W. P.; van Diest, P. J.; van Bergen En Henegouwen, P. M.; Oliveira, S., Optical imaging of pre-invasive breast cancer with a combination of VHHs targeting CAIX and HER2 increases contrast and facilitates tumour characterization. *EJNMMI Res* **2016,** *6* (1), 14.

45. Huang, L.; Gainkam, L. O.; Caveliers, V.; Vanhove, C.; Keyaerts, M.; De Baetselier, P.; Bossuyt, A.; Revets, H.; Lahoutte, T., SPECT imaging with 99mTc-labeled EGFR-specific nanobody for in vivo monitoring of EGFR expression. *Molecular imaging and biology : MIB : the official publication of the Academy of Molecular Imaging* **2008,** *10* (3), 167-75.

46. Gainkam, L. O.; Huang, L.; Caveliers, V.; Keyaerts, M.; Hernot, S.; Vaneycken, I.; Vanhove, C.; Revets, H.; De Baetselier, P.; Lahoutte, T., Comparison of the biodistribution and tumor targeting of two 99mTc-labeled anti-EGFR nanobodies in mice, using pinhole SPECT/micro-CT. *Journal of nuclear medicine : official publication, Society of Nuclear Medicine* **2008,** *49* (5), 788-95.

47. Vaneycken, I.; Devoogdt, N.; Van Gassen, N.; Vincke, C.; Xavier, C.; Wernery, U.; Muyldermans, S.; Lahoutte, T.; Caveliers, V., Preclinical screening of anti-HER2 nanobodies for molecular imaging of breast cancer. *FASEB J.* **2011,** *25* (7), 2433-46.

48. Oliveira, S.; Schiffelers, R. M.; van der Veeken, J.; van der Meel, R.; Vongpromek, R.; van Bergen En Henegouwen, P. M.; Storm, G.; Roovers, R. C., Downregulation of EGFR by a novel multivalent nanobody-liposome platform. *Journal of controlled release : official journal of the Controlled Release Society* **2010,** *145* (2), 165-75.

49. van der Meel, R.; Oliveira, S.; Altintas, I.; Haselberg, R.; van der Veeken, J.; Roovers, R. C.; van Bergen en Henegouwen, P. M.; Storm, G.; Hennink, W. E.; Schiffelers, R. M.; Kok, R. J., Tumor-targeted

9

Nanobullets: Anti-EGFR nanobody-liposomes loaded with anti-IGF-1R kinase inhibitor for cancer treatment. *Journal of controlled release : official journal of the Controlled Release Society* **2012,** *159* (2), 281-9.

50. Talelli, M.; Oliveira, S.; Rijcken, C. J.; Pieters, E. H.; Etrych, T.; Ulbrich, K.; van Nostrum, R. C.; Storm, G.; Hennink, W. E.; Lammers, T., Intrinsically active nanobody-modified polymeric micelles for tumor-targeted combination therapy. *Biomaterials* **2013,** *34* (4), 1255-60.

51. Zou, T.; Dembele, F.; Beugnet, A.; Sengmanivong, L.; Trepout, S.; Marco, S.; de Marco, A.; Li, M. H., Nanobody-functionalized PEG-b-PCL polymersomes and their targeting study. *J. Biotechnol.* **2015,** *214*, 147-55.

52. Altintas, I.; Heukers, R.; van der Meel, R.; Lacombe, M.; Amidi, M.; van Bergen En Henegouwen, P. M.; Hennink, W. E.; Schiffelers, R. M.; Kok, R. J., Nanobody-albumin nanoparticles (NANAPs) for the delivery of a multikinase inhibitor 17864 to EGFR overexpressing tumor cells. *Journal of controlled release : official journal of the Controlled Release Society* **2013,** *165* (2), 110-8.

53. Lauwereys, M.; Arbabi Ghahroudi, M.; Desmyter, A.; Kinne, J.; Holzer, W.; De Genst, E.; Wyns, L.; Muyldermans, S., Potent enzyme inhibitors derived from dromedary heavy-chain antibodies. *EMBO J.* **1998,** *17* (13), 3512-20.

54. Desmyter, A.; Spinelli, S.; Payan, F.; Lauwereys, M.; Wyns, L.; Muyldermans, S.; Cambillau, C., Three camelid VHH domains in complex with porcine pancreatic alpha-amylase. Inhibition and versatility of binding topology. *J. Biol. Chem.* **2002,** *277* (26), 23645-50.

9

APPENDIX

SUMMARY

Cancer is a multifactorial disease, involving many processes that drive malignancy, described as the hallmarks of cancer. These hallmarks are the result of a range of mutational events that alter signaling pathways. Drugs inhibiting specific pathways have been developed, however due to tumor heterogeneity and plasticity it is becoming clear that blocking of multiple pathways in a synthetic lethality approach, or immediate cell killing with a cytotoxic therapy is a more practical strategy. Altered metabolism has (re)gained interest and inhibition of metabolic pathways on which tumor cells depend for survival could be employed in tumor targeting. This thesis describes both targeting of tumor metabolism and development of a VHH-based nanomedicine platform for inhibition of altered signaling pathways or induction of direct cytotoxicity.

Deranged metabolism in cancer

Metabolic rewiring in cancer cells can be the result of altered signaling pathways due to mutations in oncogenes and tumor suppressor genes. These mutations often cause increased activity of transcription factors such as HIF, MYC and SREBP, promoting an anabolic program resulting in increased protein synthesis, glycolytic flux and lipid synthesis.

Furthermore, an increasing number of mutations are found in genes encoding metabolic proteins such as the TCA enzymes FH, SDH and IDH. In 2008, heterozygous hotspot mutations in the *IDH1* and *IDH2* genes were found in the majority of low-grade and secondary high-grade gliomas. These mutations mostly involve Arg132 in IDH1 and Arg172 or Arg140 in IDH2, and cause a neomorphic gain-of-function. Whereas IDHs convert isocitrate to α-KG with simultaneous reduction of NADP+ to NADPH, the IDH mutants reduce α-KG to D-2-HG while oxidizing NADPH. D-2-HG is a proposed oncometabolite, acting via competitive inhibition of α-KG-dependent enzymes that are involved in metabolism and epigenetic regulation. In **chapter two** we describe a novel heterozygous mutation in the cytosolic IDH1, IDH1R314C. This mutation was discovered in a high grade glioma by high throughput sequencing. The mutated protein lacks isocitrate-to-α-KG conversion activity due to reduced affinity for NADP+, and differs from the IDH1R132 mutants in that it does not produce the oncometabolite D-2-HG. Therefore it represents a valuable tool to study the effects of IDH1-dysfunction on cellular metabolism in the absence of 2-HG production.

Another mutated protein that causes a rewiring of cellular metabolism is VHL, which is mutated in 80% of renal cell carcinomas, resulting in stabilization of HIF-1α and/or HIF-2α, even under normoxic conditions. This leads to constitutive expression of metabolic HIF target genes, such as glucose transporters, glycolytic enzymes and lactate exporters, together orchestrating aerobic glycolysis. Furthermore inhibition of pyruvate shuttling into the TCA causes increased glutamine-driven reductive carboxylation to maintain the production of citrate for lipid biosynthesis. Though HIF-1α and HIF-2α are highly similar in structure, they

A

have distinct effects on cellular metabolism. In **chapter three** we investigated the cellular metabolism of two VHL-impaired ccRCC cell lines, SKRC-17 (expressing only HIF-2α) and SKRC-7 (expressing both HIF-1α and HIF-2α). We show that SKRC-17 cells are more dependent on glutamine for cell proliferation compared to SKRC-7 cells. Furthermore we show that the marked differences in cell metabolism translate in differential sensitivity to inhibitors EGCG and 6-AN.

Tumor targeting with VHHs

Besides a deranged metabolism, tumor initiation and progression can be caused by multiple other signaling pathways, like the ones induced by activated tyrosine kinase receptors (e.g. EGFR, MET, PDGF, VEGF). Monoclonal antibodies inhibiting these activated receptors have been developed, and besides passive tumor targeting these antibodies can also be conjugated to drugs to induce direct cytotoxicity. Though these antibodies are shown to have therapeutic potency, they also have several disadvantages like their size (~150 kDa), which limits tumor penetration, and their long circulation half-life. Heavy chain domains of single chain llama antibodies (VHHs or nanobodies) are an interesting alternative. Because of their small size (~15 kDa) they have better tissue penetrating properties, and furthermore they have other advantages such as low production cost, high water solubility, low immunogenicity and high thermo,- and pH stability. A number of VHHs with high affinity and specificity have been developed binding tyrosine kinase receptors such as EGFR, HER2 and MET, which are all expressed on tumor cells. An alternative approach is targeting of the tumor neo-vasculature in order to stop tumor growth. In **chapter four** we describe identification of a novel tumor targeting VHH, C-C7, via in vivo biopanning of a llama VHH phage display library in an orthotopic mouse model of diffuse glioma. We showed that C-C7 recognizes a subpopulation of tumor blood vessels in clinical glioma samples, and furthermore it recognizes activated endothelium and macrophages in atherosclerotic lesions. Via yeast-2-hybrid screens we identified dynactin-1-p150Glued as the target of C-C7.

Conjugation of VHHs to diagnostic or therapeutic nanoparticles, peptides, proteins or drugs offers many opportunities for optimized targeted therapy in cancer. In **chapter five**, we aimed to combine several conjugation strategies in a modular approach for bioorthogonal VHH modification and conjugation. We employed sortase-A mediated transpeptidation to introduce chemical click moieties to the C-terminus of VHHs, which then can be used for conjugation to other groups. In this way we were able to make tail-to-tail bispecific VHHs and VHH-targeted nanoparticles. Besides introduction of click chemistry moieties, we also employed sortase-A mediated transpeptidation to introduce a cell pepetrating peptide (CPP) to the C-terminus of andi-EGFR VHH 7D12 in **chapter six**. We found that conjugation to the CPP led to 1) more efficient blocking of ligand binding and 2) increased endocytic optake of the whole 7D12-EGFR receptor complex. The net result was that 7D12-CPP more efficiently blocked ligand activation compared to 7D12 alone.

Besides for inhibition of oncogenic signaling pathways, which often is not curative, VHHs could be used for targeted delivery of cytotoxic agents to cancer cells. A class of interesting cytotoxic moieties are photosensitizers (PS), which cause cell death via induction of reactive oxygen species (ROS) after illumination with light of a specific wavelength. VHHs conjugated to PSs have been described to induce cell death of target expressing cells, however the effect of subcellular localization of the VHH-PS construct is largely unknown. Therefore we compared activity of internalizing 7D12-PS-CPP and the membrane bound 7D12-PS in **chapter seven**. We showed that both of these constructs very efficiently induced cell death of EGFR expressing cells, however the membrane bound construct was more potent.

Another way to deliver toxins or drugs to cells is via conjugation to or encapsulation in nanoparticles like liposomes, micelles and polymersomes. This could not only increase the dose of toxin or drug delivered to the tumor but also overcome other issues like poor solubility or stability. Elastin like peptides (ELPs) are protein polymers which can reversibly transform from a soluble state to an aggregated state above a certain transition temperature. ELP-based nanoparticles can be prepared out of amphiphilic diblock copolymers. In **chapter eight**, we report the use of an ELP diblock (ELPDB) polypeptide for creation of self-assembling theranostic 7D12-PS decorated ELP micelles. We showed that we could make well-defined and stable micelles by combining 7D12-ELPDB with PS-ELPDB and heating the mixture above the transition temperature of the hydrophobic block. The 7D12-PS decorated ELP micelles were able to selectively kill tumor cells that (over)express EGFR.

A

SAMENVATTING

Er zijn verschillende factoren van invloed op het ontstaan van kanker, en deze zijn samengevat in de 8 zogenaamde kenmerken van kanker ("hallmarks of cancer"). Deze kenmerken zijn het resultaat van een reeks van mutaties die ervoor zorgen dat de activiteit van intracellulaire signaleringspaden veranderd. Er zijn medicijnen ontwikkeld die de activiteit van deze signaleringspaden kunnen remmen, maar doordat er een hoop verschillen zijn tussen tumorcellen in één tumor, en gezien tumorcellen zich aan kunnen passen, lijken combinatietherapieën waarbij je meerdere paden tegelijk remt, of therapieën die de cel direct doden in plaats van remmen in groei, meer effectief. In dit proefschrift beschrijven we ten eerste hoe het metabolisme van een tumorcel kan veranderen en hoe je deze verandering aan kunt grijpen om tumorgroei te remmen. Ten tweede beschrijven we de ontwikkeling van een nanogeneeskunde ("nanomedicine") platform gebaseerd op llama antilichaam domeinen (VHHs), en een aantal toepassingen hiervan.

Ontspoord metabolisme in kanker

Kankercellen hebben vaak een aangepast metabolisme zodat ze aan alle bouwstoffen kunnen komen die nodig zijn voor de snelle groei. Dit komt onder andere door mutaties in zogenaamde oncogenen en tumorsuppressorgenen. Vaak komen deze mutaties voor in transcriptiefactoren zoals HIF, MYC en SREBP, en ze zorgen voor een verhoogde omzetting van glucose naar lactaat (glycolytische flux) en een verhoogde productie van eiwitten en vetten. Ook zijn er mutaties gevonden in genen die coderen voor de metabole eiwitten zelf. In 2008 werd er in de meerderheid van laaggradige en secundaire hooggradige gliomen mutaties gevonden in de *IDH1* en *IDH2* genen. De mutaties zorgen ervoor dat het IDH enzym een nieuwe functie krijgt. Normaal zetten IDH enzymen isocitraat om naar α-KG, waarbij $NADP^+$ gereduceerd wordt naar NADPH. De gemuteerde enzymen zetten echter α-KG om naar D-2-HG waarbij ze NADPH oxideren naar $NADP^+$. Er is dus een netto vermindering van α-KG en NADPH levels, en een verhoging van D-2-HG levels. D-2-HG wordt gezien als een oncometaboliet omdat het zorgt voor veranderingen in epigenetica en metabolisme. In **hoofdstuk 2** beschrijven wij een nieuwe heterozygote mutatie in het cytosolische enzym IDH1, IDH1[R314C]. Deze mutatie is ontdekt in een hooggradig glioom middels high throughput sequencing. Het gemuteerde eiwit zet geen isocitraat om naar α-KG doordat het verminderde affiniteit voor $NADP^+$ heeft. Het verschilt van het IDH1[R132] mutante eiwit doordat het geen α-KG omzet naar D-2-HG. Daarom kan het een relevant model zijn om te bestuderen wat het effect is van verminderde α-KG productie zonder dat de effecten van D-2-HG hiermee interfereren.

Een ander gemuteerd eiwit dat zorgt voor veranderingen in het metabolisme van een cel is VHL, dit eiwit is gemuteerd en daardoor inactief in meer dan 80% van de niercelcarcinomen (NCC). Normaal zorgt VHL voor de afbraak van transcriptiefactoren HIF-1α en/of HIF-2α, en bij afwezigheid van VHL zijn deze dus in verhoogde mate aanwezig in de cel. Daardoor is er

constante expressie van target genen van HIF, zoals glucosetransporters, eiwitten die actief zijn in de omzetting van glucose naar lactaat, en lactaat exporters. Deze eiwitten samen zorgen voor een verhoogde glycolytische flux. In de normale situatie wordt glucose omgezet naar pyruvaat, en dat kan in de citroenzuurcyclus gebruikt worden voor productie van energie en citraat, dat belangrijk is bij productie van vetten. Dit proces wordt geremd in cellen met VHL mutatie, en om te compenseren voor de verminderde productie van citraat wordt glutamine opgenomen en omgezet naar citraat. In **hoofdstuk 3** hebben we gekeken naar het metabolisme van twee verschillende niercelcarcinoom cellijnen met een VHL mutatie, SKRC-17 en SKRC-7. We hebben laten zien dat SKRC-17 cellen meer afhankelijk zijn van glutamine dan glucose voor celgroei, en dat dit ertoe leidt dat ze gevoeliger zijn voor remming van paden die glutamine omzetten naar citraat.

Tumor targeting met VHHs

Naast veranderingen in metabolisme, kunnen tumorvorming en tumorgroei ook veroorzaakt worden door activatie van andere signaleringspaden, zoals de paden die aangestuurd worden door zogenaamde tyrosine kinase receptoren (bijvoorbeeld EGFR, MET, PDGF, VEGF). Er zijn verschillende antilichamen ontwikkeld die aan deze receptoren binden en hun functie remmen. Bovendien kunnen er ook stofjes aan deze antilichamen gekoppeld worden waardoor je de cel waaraan ze binden meteen dood maakt. Deze antilichamen zijn veelbelovend in de kliniek, maar omdat ze redelijk groot zijn (~150 kDa), kunnen ze soms niet geheel de tumor binnendringen. Lama antilichaam domeinen, of VHHs, zijn ongeveer 10 keer zo klein (~15 kDa) en om deze reden een interessant alternatief. Ook hebben ze andere voordelen zoals lage kosten voor productie, hoge oplosbaarheid in water, lage immunogeniciteit en hoge thermo,- en pH stabiliteit. Er zijn VHHs ontwikkeld tegen verschillende tyrosine kinase receptoren (EGFR, HER2, MET), die allemaal voor komen op tumorcellen. Je zou behalve tegen de tumorcellen, ook therapien kunnen ontwikkelen tegen de nieuw gevormde bloedvaten in tumoren. In **hoofdstuk 4** beschrijven we de identificatie van een nieuw VHH, C-C7, via een selectieprocedure in een muismodel van glioom. We laten zien dat C-C7 een deel van de bloedvaten in glioom, en daarbij geactiveerde bloedvaten en macrofagen in atherosclerose herkent. We hebben dynactin-1-p150[Glued] geïdentificeerd als het eiwit waar C-C7 aan bindt.

Het koppelen van VHHs aan diagnostische en therapeutische nanodeeltjes, eiwitten of medicijnen biedt vele kansen voor doelgerichte therapieën ("targeted therapies") in kanker. In **hoofdstuk vijf** hebben we verschillende strategieën gecombineerd om bepaalde groepen aan VHHs te koppelen. Ten eerste hebben we het enzym sortase-A gebruikt om zogenaamde click groepen (moleculen die specifiek met elkaar reageren) aan de VHHs te hangen. Deze click groepen hebben we gebruikt om twee VHHs aan elkaar te koppelen, of om nanodeeltjes te maken waarbij VHHs aan het oppervlak gekoppeld zitten. We hebben sortase-A ook gebruikt om een cell penetrating peptide (CPP), een klein eiwit dat makkelijk cellen binnengaat, aan een anti-EGFR VHH 7D12 te koppelen in **hoofdstuk 6**. We hebben de functie van dit 7D12-

CPP vergeleken met het normale 7D12. We hebben gezien dat 7D12-CPP zorgde voor meer efficiënte blokkade van binding van het stofje dat normaal de EGFR activeert. Bovendien zorgde het CPP ervoor dat het hele complex van 7D12-CPP met de EGFR opgenomen werd in de cel, waardoor het ook niet meer geactiveerd kon worden. Het netto resultaat was dus dat 7D12-CPP beter was in het remmen van de EGFR activatie dan 7D12 alleen.

VHHs kunnen dus gebruikt worden voor remming van geactiveerde oncogene paden, zoals voor EGFR, maar dit zorgt vaak alleen voor remming van celgroei en niet voor celdood en dus genezing. Een photosensitizer (PS) is een molecuul dat na belichting met licht van een specifieke golflengte zorgt voor de vorming van zuurstofradicalen, die heel schadelijk zijn voor een cel en daardoor celdood veroorzaken. Andere onderzoeksgroepen hebben al laten zien dat wanneer je een VHH aan een photosensitizer koppelt je celdood van specifiek de tumorcellen kunt veroorzaken. Er is echter nog niet bekend wat het effect is op de localisatie van het VHH-PS eiwit. We hebben daarom in hoofdstuk 7 de effecten van 7D12-PS-CPP, dat opgenomen wordt door cellen, vergeleken met de effecten van 7D12-PS, dat vooral aan de buitenkant van de cel op het membraan blijft zitten. We hebben laten zien dat beide eiwitten zeer effectief celdood kunnen veroorzaken na belichting, maar het membraangebonden eiwit was meer effectief dan de internaliserende variant.

Een andere manier om medicijnen bij tumorcellen te krijgen is door het aan nanodeeltjes te koppelen of in nanodeeltjes in te sluiten. Hierdoor kun je niet alleen de effectieve dosis verhogen, maar het kan ook gebruikt worden voor medicatie die anders slecht oplosbaar is of niet stabiel is in waterige omgeving zoals bloed. Elastin like peptides (ELPs) zijn polymeren die reversibel kunnen transformeren van een oplosbare staat naar een geaggregeerde staat wanneer je ze boven een bepaalde transitietemperatuur verhit. Je kunt ELP nanopartikels maken met polymeren die uit 2 delen met ieder een andere transitietemperatuur bestaan (diblock copolymeren). In **hoofdstuk 8** hebben we een ELP diblock copolymeer gebruikt om nanodeeltjes te maken met 7D12 en PS op het oppervlak. We laten zien dat deze nanodeeltjes in staat waren om alleen cellen met EGFR op hun oppervlak te doden na belichting.

A

LIST OF PUBLICATIONS

Navis AC, Niclou SP, Fack F, Stieber D, van Lith SAM, Verrijp K, Wright A, Stauber J, Tops B, Otte-Holler I, Wevers RA, van Rooij A, Pusch S, von Deimling A, Tigchelaar W, van Noorden CJF, Wesseling P, Leenders WPJ. Increased mitochondrial activity in a novel IDH1-R132H mutant human oligodendroglioma xenograft model: in situ detection of 2-HG and α-KG. Acta Neuropathol Commun. 2013;1:18.

van Lith SAM, Navis AC, Verrijp K, Niclou SP, Bjerkvig R, Wesseling P, Tops B, Molenaar R, van Noorden CJF, Leenders WPJ. Glutamate as chemotactic fuel for diffuse glioma cells: Are they glutamate suckers? Biochim biophys acta. 2014;1846(1):66-74

van Lith SAM, Molenaar R, van Noorden CJF, Leenders WPJ. Tumor cells in search for glutamate: an alternative explanation for increased invasiveness of IDH1 mutant gliomas. Neuro oncol. 2014;16(12):1669-70

Navis AC, van Lith SA, van Duijnhoven SM, de Pooter M, Yetkin-Arik B, Wesseling P, Hendriks WJ, Venselaar H, Timmer M, van Cleef P, van Bergen en Henegouwen P, Best MG, Wurdinger TD, Tops BB, Leenders WP. Identification of a novel MET mutation in high-grade glioma resulting in an auto-active intracellular protein. Acta Neuropathol. 2015;130(1):131-44

Molenaar RJ, Botman D, Smits MA, Hira VV, van Lith SA, Stap J, Henneman P, Khurshed M, Lenting K, Mul AN, Dimitrakopoulou D, van Drunen CM, Hoebe RA, Radivoyevitch T, Wilmink JW, Maciejewski JP, Vandertop P, Leenders WP, Bleeker FE, van Noorden CJ. Radioprotection of IDH1-Mutated Cancer Cells by the IDH1-Mutant Inhibitor AGI-5198. Cancer Res. 2015;75(22):4790-802.

van Lith SAM, Navis AC, Lenting K, Verrijp K, Schepens JTG, Hendriks WJAJ, Schubert NA, Venselaar H, Wevers RA, van Rooij A, Wesseling P, Molenaar RJ, van Noorden CJF, Pusch S, Tops B, Leenders WPJ. Identification of a novel inactivating mutation in Isocitrate Dehydrogenase 1 (IDH1-R314C) in a high grade astrocytoma. Sci Rep. 2016;6:30486.

van Lith SAM, Roodink I, Verhoeff JJC, Makinen PI, Lappalainen JP, Yla-Herttuala S, Raats J, van Wijk E, Roepman R, Letteboer SJ, Verrijp K, Leenders WPJ. In vivo phage display screening for tumor vascular targets in glioblastoma identifies a llama nanobody against dynactin-1-p150Glued. Oncotarget. 2016;7(44):71594-17607

A

van der Steen SC, Raavé R, Langerak S, van Houdt L, van Duijnhoven SM, <u>van Lith SA</u>, Massuger LF, Daamen WF, Leenders WP, van Kuppevelt TH. Targeting the extracellular matrix of ovarian cancer using functionalized drug loaded lyophilisomes. Eur J Pharm Biopharm. 2017;113:229-239

<u>van Lith SAM</u>, van Duijnhoven SMJ, Navis AC, Dolk E, Wennink, JW, van Nostrum CF, van Hest JCM, Leenders WPJ. Legomedicine – A versatile chemo-enzymatic approach for the preparation of targeted dual-labeled llama antibody-nanoparticle conjugates. Bioconjug Chem. 2017;28(2):539-548

<u>van Lith SAM</u>, Pille J, van Hest JCM, Leenders WPJ. Self-assembling VHH-elastin-like peptides for photodynamic nanomedicine. Biomac. 2017;18(4):1302-1310

de Bitter T, van de Water C, van den Heuvel C, Eijkelenboom A, Tops B, Oosterwijk E, Kolev D, <u>van Lith S</u>, Leenders W. Profiling of the metabolic transcriptome via single molecule molecular inversion probes. Sci Rep. 2017;7(1):11402

<u>van Lith SAM</u>, van den Brand D, Wallbrecher R, van Duijnhoven SMJ, Brock R, Leenders WPJ. A conjugate of an anti-EGFR VHH and a cell-penetrating peptide drives receptor internalization and blocks EGFR activation. Chembiochem. 2017;18(24):2390-2394

<u>van Lith SAM</u>, van den Brand D, Wallbrecher R, Wubbeke L, van Duijnhoven SMJ, Makinen PI, Hoogstad-van Evert JS, Massuger L, Yla-Herttuala S, Brock R, Leenders WPJ. The effect of subcellular localization on the efficiency of EGFR-targeted VHH photosensitizer conjugates. Eur J Pharm Biopharm 2018; 124:63-72

Gotthardt M, Eizirik DL, Aanstoot HJ, Korsgren O, Mul D, Martin F, Boss M, Jansen TJP, <u>van Lith SAM</u>, Buitinga M, Eriksson O, Cnop M, Brom M. Detection and quantification of beta cells by PET imaging: why clinical implementation has never been closer. Diabetologia 2018; 61(12):2516-2519

Lenting K, Khurshed M, Peeters TH, van den Heuvel CNAM, <u>van Lith SAM</u>, de Bitter T, Hendriks W, Span PN, Molenaar RJ, Botman D, Verrijp K, Heerschap A, Ter Laan M, Kusters B, van Ewijk A, Huynen MA, van Noorden CJF, Leenders WPJ. Isocitrate dehydrogenase 1-mutated human gliomas depend on lactate and glutamate to alleviate metabolic stress. FASEB J. 2019; 33(1):557-571

Peeters TH, Lenting K, Breukels V, van Lith SAM, van den Heuvel CNAM, van Rooij A, Wevers R, Span PN, Heerschap A, Leenders WPJ. Isocitrate dehydrogenase 1-mutated cancers are sensitive to grean tea polyphenol epigallocatechin-3-gallate. *Accepted*

van Lith SAM, Lenting K, Kramer N, Swanenberg L, Span PN, Oosterwijk E, Leenders WPJ. Differences in cellular metabolism of renal cell carcinoma cell lines translate into differential sensitivity to metabolic inhibitors. *Submitted*

Jansen TJP, van Lith SAM, Boss M, Brom M, Joosten L, Béhé M, Buitinga M, Gotthardt M. Exendin-4 analogs in insulinoma theranostics. J Labelled Comp Radiopharm. 2019; Epub ahead of print

Boss M, Bos D, Frielink C, Sandker GW, Ekim S, Marciniak C, Pattou F, van Dam G, van Lith SAM, Brom M, Gotthardt M, Buitinga M. Targeted optical imaging of the glucagon-like peptide-1 receptor using exendin-4-IRDye800CW. *Submitted*

Boss M, Bos D, Frielink C, Sandker GW, Bronkhorst P, van Lith SAM, Brom M, Buitinga M, Gotthardt M. Targeted photodynamic therapy of glucagon-like peptide-1 receptor positive lesions with exendin-4-IRDye700DX. *Submitted*

A

CURRICULUM VITAE

Sanne Anna Maria was born in Arnhem, the Netherlands, on August 13, 1988. She attended primary school in Elst and high school (VWO) at the Over Betuwe College in Bemmel. In 2006 she started studying Biomedical Sciences at the Radboud University in Nijmegen. She performed internships in the laboratory of prof dr Peter Pickkers at the department of experimental intensive care of the Radboudumc, in the laboratory of dr William Leenders at the department of pathology of the Radboudumc and in the laboratory of prof dr Seppo Yla-Herttuala at the department of molecular medicine of the University of Eastern Finland. In 2012 she received the cum laude masters degree in biomedical sciences. She started her PhD research in the group of dr William Leenders, of which results are described in this thesis. Currently she is working as a post-doc researcher in the group of prof dr Martin Gotthardt at the department of radiology and nuclear medicine of the Radboudumc.

A

DANKWOORD

Het misschien wel meest gelezen, of in ieder geval eerst gelezen, onderdeel van dit boekje. Natuurlijk zijn er erg veel mensen die ik wil bedanken, en ik hoop enorm dat ik niemand vergeet, daar gaat 'ie dan!

Ten eerste natuurlijk het promotieteam. **Pieter**, **Roland**, mijn promotoren, bedankt voor het klaar staan wanneer dat nodig was. Roland, wij hebben met name overleggen gehad voor de VHH-hLF en VHH-PS artikelen, en jouw duidelijke mening over wanneer iets zinnig of juist onzinnig was, en heldere visie over welke proeven nodig waren voor publicatie zijn altijd erg nuttig geweest! **William**, niet voor niets ben ik na een leuke stage op de afdeling pathologie naar Finland gegaan voor een tweede stage met het vooruitzicht op een promotieplek in jouw groep. Ik heb veel bewondering voor jouw passie voor wetenschappelijk onderzoek, en de (bijna) onbegrensde kennis van de meest uiteenlopende onderwerpen. Focus was soms ver te zoeken in overleggen, maar er kwamen altijd tientallen nieuwe ideeën uit een uurtje praten gerold. Soms frusterend, maar vooral erg leerzaam dat out-of-the-box denken. Bedankt voor de leuke tijd!

Kiek, de rots in de branding van de tumor targeting groep. Niet alleen kon ik bij jou terecht voor alle ins en outs over ingewikkelde kleuringen en andere proeven, ook was jij altijd in voor gezellige pauzes (als het even kon buiten in de zon, waanzinnige woensdag), en vrijdagmiddag,- of vierdaagseborrels. **Anneke**, wij vormden in het begin met z'n tweeën het kleine tumor targeting groepje. Ik heb dat altijd heel gezellig gevonden, en bewonderde jouw kennis van het muizenwerk. Verder waren de borrels waarbij jij dronken was na 2 roseetjes ook altijd erg goed. **Sander**, ik schaamde me voor mijn labjournaals toen we jouw precieze bedrijfsmatige systeem van werken te zien kregen. Jouw kennis van chemie heeft het VHH werk een boost gegeven en dankzij jouw voorwerk heb ik leuke artikelen af kunnen maken. **Krissie**, partner-in-crime op het lab maar ook daar buiten. Wij hebben de metabole verschrikking geprobeerd aan te pakken, en goede planningen gemaakt voor het om-en-om uitnemen van SRB platen, zodat er toch iemand kon gaan stappen. Samen stappen geeft soms problemen, omdat we beiden een rem missen, maar dit heeft ook tot onvergetelijke dagen/avonden/nachten geleid in oa Whistler, Vancouver en vooral in Nijmegen. Succes als wetenschappelijke zakenvrouw bij Bayer. **Corina**, het schrijfwonder. Ik ben zo jaloers op jouw plezier in schrijven, en het gemak waarop het lijkt te gaan. Bedankt voor de fijne vervanging van Anneke links van me naast de boom, en heel veel succes met je nieuwe baan bij Charles River. **Rene**, oude kletskous. Nooit was het saai op onze kamer wanneer jij aanwezig was. Enorm verhitte discussies over de meest uiteenlopende onderwerpen, en natuurlijk een dagelijkse update van de achterklap rubriek op nu.nl. Daarnaast was je altijd even behulpzaam, je hoefde maar hardop een vraag te denken en jij stond al achter het bureau mee te kijken, bedankt daarvoor en succes met het

A

groot maken van het onderzoek in de neurochirurgie. **Tessa**, begonnen als stagiaire in de groep maar al snel onmisbaar voor het smMIP werk, heel veel succes met je promotieonderzoek!

Heel veel werk tijdens mijn promotieonderzoek is uit handen genomen door slimme stagiaires, die daarnaast de groep ook nog een extra gezellig hebben gemaakt: **Pauline, Kevin, Luuk, Niels, Jennifer, Rodrigo, Mark, Jordi, Charlotte, Lina**, enorm bedankt voor jullie bijdrage! Daarnaast ook alle **vaste analisten van de vierde verdieping** en medewerkers van de diagnostiek (**electonen microscopie**, **cytologie, immuno**,- en **moleculaire** lab) dank voor de hulp bij eigenlijk alles. **Wiljan**, **Jan, Paul, Bastiaan,** dank voor julllie nuttige input tijdens de wekelijkse meetings. **Mark,** bedankt voor de klinische input, het is altijd fijn om te horen of wat wij bedenken op ons lab ook echt wel nuttig kan zijn voor de patienten die jij ziet.

Verder is het onderzoeksgedeelte van de vierde verdieping enorm gegroeid de laatste tijd, en dat kwam de gezelligheid zeker ten goede. Inmiddels is er een groepsapp genaamd 'Feest" met >20 PhD studenten die elk weekend wel weer in zijn voor een party-photo-showdown. Bedankt voor dit plezier in de avond,- en nachtuurtjes ;)

Veel van het onderzoek is tot stand gekomen uit hele interessante samenwerkingen, en van jullie allemaal heb ik weer iets anders geleerd. Voor het cosmoPHOS project was de samenwerking met het lab waar ik ook mijn masterstage heb gedaan van groot belang. **Panos and Seppo**, thanks voor giving me the chance to work for the interesting cosmoPHOS project and the hospitality in Kuopio, and **Petri** and **Einari**, many thanks for the (technical) support. **Jos** en **Rene** bedankt voor de hulp bij het maken van de micellen. VHHs tot expressie brengen en vooral selecteren is nog niet zo makkelijk. Ik heb hier veel tijd aan besteed maar soms kun je dingen beter over laten aan professionals, en daar wil ik de volgende mensen hartelijk voor bedanken. **Paul** bedankt voor alle algemene VHH kennis. **Mohammed** en **Edward** voor de 2-weekse spoedcursus VHHs tot expressie brengen bij QVQ. **Jos** en **Ilse** voor de mogelijkheid om proeven bij Modiquest uit te voeren. Dan het conjugatiegedeelte van de VHHs, als niet-chemicus weet je dan soms niet waar je moet beginnen. Gelukkig was daar de enorm vruchtbare en soepele samenwerking met **Jan van Hest** en **Jan Pille**. Voor het cell-penetrating peptide werk samen met Roland heb ik net zo'n soepele samenwerking gehad met eerst **Rike** en daarna **Dirk**, **Estel**, en voor de DARPins (die helaas geen onderdeel meer van dit boekje uitmaken maar wel van het onderzoek dat ik nu doe) natuurlijk **Wouter.**

Dan het metabole werk, gezien het mega ingewikkelde karakter van dit onderzoek moesten we om de haverklap bij slimme mensen aankloppen, en allemaal waren ze even behulpzaam. **Stephan,** thanks for the help with the work on the IDH1R314C mutant enzyme in the very beginning. **Arend en Tom**, bedankt voor de samenwerking met ingewikkelde NMR metingen om het metabolisme van tumorcellen in kaart te brengen (leuk he dat cellen kweken ;)). **Ron** en

Arno, bedankt voor jullie interesse in ons soms nogal ingewikkelde onderzoek, en voor alle 13C metingen die ons enorm verder geholpen hebben. Onze metabole wederhelft in Amsterdam, **Ron**, **Remco** en **Mohammed**, bedankt voor de vruchtbare gesprekken. **Egbert**, bedankt voor je onmiddellijke interesse en behulpzaamheid om metabolisme in RCC uit te gaan zoeken. Inmiddels werk ik alweer bijna 2 jaar bij de afdeling nucleaire geneeskunde en wil ik daar **iedereen** bedanken voor een warm welkom, ik weet dat jullie ook erg uitkijken naar dit boekje (lees: een feestje).

Naast mensen op het werk zijn mensen thuis natuurlijk ook essentieel geweest om de promotietijd leuk door te komen, en die verdienen allemaal een bedankje dus bij dezen! MASLMAIS, **Maartje**, **Anne Marie**, **Sietske**, **Lucie**, **Marloes**, **Amber**, **Ingrid**. Wij kennen elkaar inmiddels zo'n 15 jaar, en nog steeds zien we elkaar regelmatig. Ik vind dit heel bijzonder en ik hoop dat dit altijd zo blijft! Ingrid jij verdient een extra pluim voor de leuke avondjes 'koken' waarbij je altijd geduldig naar mijn gezeur hebt geluisterd en me van nuttige adviezen hebt voorzien. SSSLLLiK, **Sjaak**, **Sas**, **Luus**, **Lau**, **Lies**, en Kel (op jou kom ik later even terug). Deels familie en bovenal allemaal vriendinnen. Heel wat leuke avonturen in en rondom Elst mee meegemaakt, en ook al woont een deel wat verder weg, als we elkaar zien is het altijd goed. Terras,- stap,- Elstermaatje en buurman **Robert**, bedankt voor het lekker samen klagen en stappen. **Lot,** naast dat je mijn leuke nichtje bent, zijn we ook bijna elk weekend samen op pad. Elke week weer iets om naar uit te kijken! **Lis**, wij kennen elkaar inmiddels al meer dan 25(!!) jaar, en ik weet zeker dat wij nooit meer van elkaar af komen.

Opa Doornenbal en **Oma Anne**, **Opa van Lith** en **Oma Liedje.** Opa's en oma's zijn natuurlijk trots op alles wat je doet, maar in dit geval was dat trots in het kwadraat. Opa Doornenbal heeft mijn bachelordiploma 20 keer afgedrukt en ingeseald, geen idee voor wie maar dat zegt wel iets natuurlijk. Alleen Oma Liedje maakt dit nog mee, maar jullie zitten vast ergens anders trots te zijn. **Leef** en **Esli,** kleine babies, nu ik dit schrijf woon ik weer even bij jullie. Lekker naar liedjes luisteren van zingende Levi en het geklets van Esli bij het eten (**May** hoe houd je het vol ;)). Ik kan niet wachten tot ik weer weg ben maar dan kan ik straks jullie vrolijkheid weer extra waarderen! **Kel,** mijn inmiddels Belgische zusje. Twee handen op een buik kan je ook wel zeggen, met telepathische gaven (handig met 30 seconds) en een raar soort humor die alleen wij twee snappen. Ik blijf jou en **Maarten** overhalen om terug te komen naar Elst, be prepared. **Toet** en **Moek,** daar is ie eindelijk, het boekje waarnaar jullie op het eind wijselijk niet meer vroegen, en straks komt het feest waar jullie nog meer zin in hebben dan ik. Bedankt voor jullie onuitputtelijke steun, en wie had dat gedacht, ik blijf waarschijnlijk voor eeuwig gezellig een paar straten bij jullie vandaan wonen! #zinin

A